Spectroscopic Studies On Molecules And Nanomaterials For Potential Applications In Medical Diagnosis And Environmental Pollution Monitoring

THESIS

SUBMITTED FOR THE DEGREE OF

DOCTOR OF PHILOSOPHY (SCIENCE)

IN

NANOSCIENCE AND NANOTECHNOLOGY

BY

PROBIR KUMAR SARKAR

CENTRE FOR RESEARCH IN NANOSCIENCE AND NANOTECHNOLOGY

UNIVERSITY OF CALCUTTA

2019

To My Family

Acknowledgements

Contents

Chapter 2: An Overview of Spectroscopic Techniques and Systems   22-45

Chapter 1

Introduction

1.1. Background

Spectroscopy is the study of the interaction of light with matter. Interaction of light with matter always fascinates human since ancient times. For thousands of years, people marvelled at the multicolour arc of visible light that frequently appears after rain showers. In order to understand the rainbow effect, the term 'spectroscopy' was originated in the 17th century through the study of visible light dispersion according to its specific wavelength, by a prism. The idea was later extended impressively to append any feasible interaction with radiative energy as a function of its frequency or wavelength. Spectroscopy is a fundamental exploratory tool in the fields of physics, chemistry, biomedical science and environmental science, allowing the compositional and structural information of matter to be investigated at atomic or molecular scale.

Application of spectroscopy in the field of medical science is popularised dramatically during early 20th century. However, from the earliest times to till now the diagnosis of medical diseases using spectroscopic tools is unavoidable. Primary medical diagnosis made by an expert physician based on what they could observe with their eyes and ears, which sometimes also included the examination of human specimens. The ancient Greeks believed that the health was affected due to disorders of bodily fluids called humors, and during the Late Middle Ages, doctors routinely performed uroscopy. Later on, the discovery of microscope was a revolution in medical science; it revealed not only the cellular structure of human tissue, but also the organisms that cause disease. After that, lots of sophisticated diagnostic tools and techniques has been discovered and the clinical laboratory would become a standard fixture of medicine in the beginning of the 20th century using these sophisticated spectroscopic tools and techniques [1]. However, the current cost of clinical laboratory test is very high compared to the economic condition of the people in developing countries. Therefore,

the development of low-cost and highly efficient spectroscopic device for disease diagnosis is still necessary to meet the increasing demand of people living in the low-income countries.

On the other hand, optical spectroscopy has been used for centuries to find out the chemical composition of materials and making decisions by sensing properties and converting them into an optical signature. In the early sixteenth century, Georgius Agricola mentioned in the 'Ore Testing' section of his famous *De re metallica* that the differences in colour from heated materials provide the compositional information of the materials [2]. At the same time, in 1565, Nicolàs Monardes examined a species of wood using fluorescence to use in the treatment of urinary and kidney infections. The spectral analysis was proposed to detect if the wood was counterfeited [3]. Since the sixteenth century, the chemical analysis has been carried out by studying the interaction of matter to radiative excitation, such as photo-acoustic spectroscopy, photothermal spectroscopy, Raman scattering and many others. But the invention of the laser by Maiman in 1960 was a revolution in the field of chemical analysis [4]. As a spectroscopic tool it has several advantages and it rapidly has become a useful technology in laboratories, outdoor situations as well as within the industrial context. In order to be applied outside laboratories focusing on fundamental research, laser spectroscopy is confronted with the real world of sensing and chemical analysis. Furthermore, the aforementioned technologies have been used to integrate the instrumentation for both atomic and molecular spectroscopy. Now a days, the developed spectroscopic tools are used to monitor environmental pollutions, the progress of chemical processes and to assess the purity of products. However, the current cost of environmental pollution monitoring technologies, commercially available in the market is very high. Due to increasing human health problems with increasing environmental pollutions, the development of low-cost and highly efficient spectroscopic techniques is essential to monitor environmental pollutions.

Optical spectroscopy holds promise not only as clinical tool for diagnosing at the early stage of diseases but also as sensing tool for the determination of

environmental pollution by combining with available photonic technology and has been utilised throughout this thesis work.

1.2. Spectroscopy in Medical Diagnosis

Spectroscopy is a broad field in which many sub-disciplines exist, each with numerous implementations of specific spectroscopic techniques. From the mid-1800s, the interaction of light with biological tissues and molecules has been used to recognize the disease. Now a days, the contemporary developments of the small detectors, light sources and fiber optic probes provide the great opportunities for the qualitative as well as quantitative estimation of these interactions, which give the information for diagnosis at the structural, biochemical and (patho) physiological level within the intact tissues and molecules [5]. However, during the last quarter of the century, there has been a tremendous revolution in the use of instrumentation and techniques in the field of biomedical instrumentation for clinical and research purpose. The basic changes are in the way or technique of measuring parameters with some medical relevance [6]. The contemporary challenges in the mentioned fields include the design and realization of low-cost techniques without compromising the sensitivity and overall performance of the device.

Application of spectroscopy in diagnosis covers broad field of application from pulse oximetry to non-invasive optical biopsy. In this section, the state of the art diagnostic strategies based on different spectroscopic techniques has been discussed. Ultraviolet/visible (UV/Vis) absorption spectroscopy has been used in the clinical laboratory for many years. Absorption spectroscopy is usually studied on molecules presented within the aqueous medium. The absorbance of a molecule is linearly depended on its concentration. Therefore, absorption spectroscopy is highly reliable for quantitative estimation of some solute. On the other hand, as the molecular absorbance and absorbing wavelengths of a molecule depend not only on the chemical structure but also on the molecular environment of its chromophores. Therefore, the absorption spectroscopy is also an exceptional technique for following the enzyme

3

catalysis, ligand-binding reactions and conformational transitions in proteins and nucleic acids [7]. In this category, the most popular diagnostic tool used in daily life for the oxygen saturation (SpO_2) measurement is pulse oximetry. A pulse oximeter continuously measures the oxygen saturation level of haemoglobin in the arterial blood. Highly specific and precise oxygen balance maintenance in blood of the human body is necessary for the healthy life. Standard blood oxygen saturation levels in humans are considered to be 95 to 100%. If the level is below 90% then it is considered to be low, resulting in hypoxemia. Pulse oximeter works based on the Beer–Lambert law. It utilizes an electronic circuit and a pair of small light-emitting diodes (LEDs) facing a photodiode through a translucent part (usually a fingertip or an earlobe) of the patient's body. Absorbance spectroscopy has also been employed for the estimation of glycated hemoglobin in hemolysate samples of normal individuals and diabetic patients, which does not involve the use of external dyes or reagents. The fiber optic based instrument is used for recording absorption spectra in the spectral range 200–850 nm of glycated hemoglobin (HbA1c). For the quantitative estimation of the HbA1c(%), the parameter "area under the curve" of each recorded absorption spectrum was used. The obtained glycated hemoglobin values with this developed spectroscopic method were compared with the reported values of the standard ion exchange high-performance liquid chromatography (HPLC) method [7]. Due to extremely high potential in practical application, the aforementioned technique may be employed as supplementary technique to other techniques that already exist.

Fluorescence spectroscopy is a high resolution spectroscopic method which is completely complementary of absorption spectroscopy. Fluorescence spectroscopy is primarily concerned with vibrational and electronic states of the molecules. Fluorescence spectroscopy is being used in many medical subspecialties as a diagnostic tool which extends from diagnostic studies for the determination of multisystem cancers with high sensitivity and specificity to atheromatic plaques detection in coronary arteries. Fluorescence spectroscopy minimizes the need for repetitive biopsy, which is routine practice for cancer patient follow-up. There are three main types of

fluorophores used for cancer diagnostic studies: exogenous fluorophores, endogenous fluorophores and fluorophores synthesized in the tissue from a precursor molecule that is given externally [8, 9]. Endogenous fluorophores give rise to auto-fluorescence phenomenon. Examples of endogenous fluorophores include collagen, elastin, nicotinamide adenine dinucleotide (NADH), tryptophan, porphyrins and flavin adenine dinucleotide (FAD) [10]. Collagen and elastin are mainly responsible for spectral changes associated with structural changes within the tissues and cells [10]. Other fluorophores like FAD, NADH, tryptophan and porphyrins are mainly responsible for spectral changes associated with changes in cellular metabolism and functional processes [9]. Steady-state ultraviolet (UV) fluorescence spectroscopy can be utilised to separate malignant tumors from benign and normal breast, cervical, ovarian and uterus tissues and tumors [9-11]. Not only the steady-state fluorescence but also the time resolved fluorescence is also a novel way to obtain fundamental information on cancer. On the other hand, laser-induced fluorescence spectroscopy, a non-invasive real-time technique for evaluating neoplasia, measures the auto-fluorescence of tissue which generally occur form the natural fluorophore of the tissue. The diagnostic algorithms with high specificity and sensitivity for the diagnosis of squamous intraepithelial lesions (SILs) can be derived with fluorescence spectroscopy. The fluorescence spectroscopy can also be useful for the detection of abnormalities of the cervix without any prior information [11]. New medical technologies or devices can be evaluated using various measures, including specificity, sensitivity, negative and positive predictive values, receiver operating characteristic (ROC) curves and areas under the ROC curves. The ROC curves have the advantage of comparing test performance over several thresholds and can be used for both, in screening settings, in which the prevalence of disease is low and in diagnostic settings, in which the prevalence of disease is high. Furthermore, fluorescence dye based detection of different diseases has also been reported. For an instance, fluorescence lifetime imaging of 4',6-diamidino-2-phenylindole (DAPI) stained nuclei has been utilised as a novel diagnostic tool for the detection and classification of B-cell chronic lymphocytic

leukemia [12]. Conversely, the fluorescence probes, 2,7-dichlorodihydrofluorescein diacetate (DCFH-DA) is also the most widely used one for detection of intracellular oxidative stress [13, 14]. Therefore, it has been observed that the spectroscopic based techniques have extremely high potential applications in the field of medical diagnosis.

1.3. Spectroscopy in Environmental Pollution Monitoring

Application of spectroscopy is not limited to medical science only. Spectroscopy has significant role on environmental pollution monitoring also. Environmental pollution is one of the most serious global problems that humanity and other life forms on our planet are facing today. Among all the environmental pollutants, chemical elements are the most hazardous one. Optical spectroscopy has been used for centuries for determining the chemical composition of materials and making decisions by sensing properties and converting them into an optical signature [15]. During the last quarter of the century, there has been a tremendous revolution in the use of instrumentation and spectroscopic techniques in the field of environmental research. The dynamical change of environmental conditions by various pollutions has adverse effects on life, make it extremely important to detect and quantify. Various spectroscopic techniques and interferometers provide us greater insight about the composition of matter and suspended particulates. Therefore, the application of spectroscopy in the field of environmental pollution monitoring is unanimous.

Ultraviolet and visible spectroscopic tools have been employed by environmental scientists for years. Common colorimetric tests that probe different water properties are now available in the market in simple kit forms, using portable colorimeters or visual colour matching [16]. Atomic absorption spectroscopy and emission spectroscopy are highly convenient techniques in the ultraviolet and visible regions to determine the chemical ions in water and solids samples. Sometimes, to analysis the samples using these techniques, immersion of the analyte into the solution is required. However, certain solid or semi-solid samples can be examined directly with atomic absorption spectrometry (by employing electrothermal atomization). Infrared

spectroscopy is also one of the useful technique for environmental pollution monitoring to the environmental analysts [17]. Environmental scientists employed this technique to develop long-range infrared sensors for the determination of certain compounds' concentration in the air mass. In addition, ultraviolet long-path methods are also tremendously used, albeit not as habitually as infrared spectroscopy. On the other hand, fluorescence spectroscopy, such as atomic fluorescence spectroscopy can be employed for the measurement of a compound present in air, water, or other media. In environmental pollution monitoring field, these techniques are extremely used for chemical ions detection, such as mercury, iron, fluoride etc. The X-ray methods (such as X-ray fluorescence spectroscopy) are also useful techniques for the measurement of atomic composition of solid materials. These methods can also be suitable for the detection of metal concentrations in particulate matter from the air, as well as in soil samples. In addition to all, sometime microwave region spectroscopy and magnetic resonance spectroscopy have also been implemented in some environmental research.

On the other hand, even the nanomaterials or nanoparticles are not directly related to the spectroscopic studies but the working of the nanomaterials can be confirmed by means of spectroscopic methods only. Hence, the application of the nanomaterials as environmental pollution monitoring agent is indirectly related to the spectroscopy. However, in some cases the effective application of the nanoparticles could be enhanced through the application of external light or magnetic field which is in the domain of spectroscopy [18]. The nanomaterials or nanoparticles are extensively used in the past few years for the environmental pollution monitoring agent using spectroscopic application. Strong absorption/emission of electromagnetic waves and tunable optical properties induced by small changes in size, shape, surface nature and dielectric properties of the media make them suitable for the environmental pollution monitoring.

Thus, spectroscopy can offer the necessary tools to investigate the relevant structure and function, but the complexity in biological systems as well as in

environmental systems are beyond that usually encountered in the chemical and physical sciences and therefore poses a particular challenge. This challenge is met by extraordinary efforts to improve the specificity, sensitivity, information content and in some cases spatial resolution of spectroscopic methods. The key focus of this thesis is to exploit modern instrumentation and spectroscopic tools for the betterment of human life by developing novel disease diagnosis tools and environmental pollution monitoring techniques, which can further help to shape our understanding of living systems.

1.4. Scope and Objective

Importance of spectroscopy in the field of medical diagnosis and environmental pollution monitoring is unanimous. Advent of nanotechnology further opens up the scope of optical spectroscopic techniques for the medical diagnosis and environmental pollution monitoring applications. In recent years, spectroscopic techniques have come to be regarded as attractive and promising analytical tools for analyses conducted in research and industrial laboratories. These techniques are increasingly considered by researchers as an obvious solution. Daily, new applications of spectroscopic methods in the fields of biomedical and environmental application are being demonstrated and published. The key objective of this thesis is the development of prototype devices and kits for the disease diagnosis and environmental water pollution monitoring to render the better quality of human life.

Spectroscopic investigation has taken an important role in diagnose different diseases including hypoxia [19], anemia [20], jaundice [21], oxidative stress [22] and cancer [23] also. Among these diseases, anemia is one of the most common global health problems affecting both developed and developing countries; it has far-reaching and severe adverse effects on human health and strongly affects socioeconomic development. The 2015 World Health Organization (WHO) fact sheets on the global statistics of anemia show that roughly 273 million (43%) children, 32.4 million (38%) pregnant women, 496 million (29%) non-pregnant women and 29% of all women of

reproductive age are anemic [24]. Therefore, anemia detection and control activities should be an integral part of healthcare services, particularly because an early diagnosis of anemia in the population is one of the proven means of health promotion. To date, the lack of a portable, easily operable, inexpensive and accurate device has hindered the widespread adaption of anemia screening in public health programs [25]. Some methods for point-of-care non-invasive hemoglobin measurements have been described in the literature [26, 27]. Although these devices address many problems encountered in older non-invasive devices, they have their own limitations, such as low precision and accuracy [28]. The accuracy and sensitivity of all non-invasive devices vary across races (specifically, skin color) because of the variation of melanin concentration in skin tissues [29]. So, to overcome the aforementioned limitations and to realize several crucial functions missing in the current non-invasive devices, a highly efficient spectroscopic device is extremely needed. In the above context, we developed a translational spectroscopic technique for noncontact hemoglobin measurement at low-resource point-of-care settings in human subjects, independent of their skin color, age and sex, by measuring the optical spectrum of the blood flowing in the vascular bed of the bulbar conjunctiva.

Among various diseases, oxidative stress is also a major global health problem. Oxidative stress is essentially an imbalance between the production of reactive oxygen species (ROS) and the ability of our body to counteract or detoxify the harmful effects through neutralization by antioxidants. The production of ROS has been implicated in the onset and progression of several diseases (e.g., neurodegeneration, diabetes, cancer and atherosclerosis) [30]. These species were thought only to be released in host defence roles by phagocytic cells; however, it is now clear that at molecular level, ROS exhibit signaling and cell-function-modifying roles for many biological systems [31, 32]. They are easily inter-converted and can subsequently react with larger biological molecules, causing chain reactions to occur, which can lead to changes in both the function and structure of cellular components. Several analytical approaches have been used to detect ROS using nanoparticles, chemiluminescence, various fluorescence

probes, mass spectrometry probes etc. [33, 34]. However, all of the techniques have some relative advantages as well as disadvantages too. Direct in-vivo measurement of oxidative stress using specific fluorescence probes with negligible additional cytotoxicity remains a great challenge. In this project, we have attached DCFH fluorescent probe to the fiber tip surface through DNA matrix assuring negligible discharge of the probe to the solution under investigation for the direct or localized measurement of ROS/oxidative stress in physiologically relevant environments.

Chemical element is one of the most environmental constituent. Chemical element sensing at physically inaccessible locations or locations unfit for human presence has always been a challenge for scientists and technologists. Among the heavy metals, mercury is the most dangerous environmental pollutant and detrimental to human health due to its high toxicity in all oxidation states. Furthermore, mercury is heavily spread out in water, air, soil and our daily food [35-37]. Such mercury exposure has serious detrimental effects on the brain, heart, lungs, kidneys, central nervous system and immune system in humans and animals at all ages [38]. One of the most usual and stable forms of mercury pollution is water-soluble oxidized divalent mercury (Hg^{2+}) ions [39] with the maximum permissible level in drinking water and food being ~ 2 ppb [40]. In this regards, the environmental monitoring and determination of low level (sub ppb) concentrations of aqueous Hg^{2+} heavy metal ions has become a vital as well as essential need for our healthy society. In our environmental pollution monitoring projects, we have developed a low-cost prototype device for mercury detection based on silver nanoparticles-impregnated poly(vinyle alcohol) (PVA-Ag-NPs) nanocomposite.

On the other hand, other metal ions as well as non-meat ions also create health problem in humans. Among the metal ions, iron is one of the most essential trace elements in human body and plays an important role in human health clinically as well as environmentally. However, excess concentration of iron ions in ground/drinking water creates health problems in humans. The maximum permissible limit of Fe^{3+} in drinking water is 5.4 µM by the U.S. Environmental Protection Agency [41]. Like

heavy metal ions, among non-metal ions, small quantity of fluoride (F^-) ions are also an essential component for normal mineralization of bones and formation of dental enamel in human body [42]. However, excessive intake of fluorine compounds may result in slow, progressive scourge known as fluorosis [43]. Around the world, more than 260 million people are suffering from fluorosis [44]. According to WHO the maximum permissible level of fluoride concentration in drinking water is 1.5 mg/L [45]. In the above context, the development of a facile synthesis, photostable, highly efficient, low-cost and environmental friendly fluorescence probe sensor for rapid qualitative as well as quantitative analysis of Fe^{3+} and F^- ions is extremely needed. In one of our nanomaterials based projects, we have prepared highly fluorescent carbon dots (CDs) through a simple and nontoxic one step hydrothermal carbonization of polyvinylpyrrolidone (PVP) for the developed of a highly efficient, selective, extremely low-cost and sensitive dual fluorescence sensors for Fe^{3+} and F^- ions in aqueous medium.

1.5. Summary of the Work Done

1.5.1. Spectroscopic Studies for the Potential Application in Medical Diagnosis of Anemia:

1.5.1.1. Development and Validation of a Noncontact Spectroscopic Device for Hemoglobin Estimation at Point-of-Care [20]: In this study, we describe a translational spectroscopic technique for noncontact hemoglobin measurement at low-resource point-of-care settings in human subjects, independent of their skin color, age and sex, by measuring the optical spectrum of the blood flowing in the vascular bed of the bulbar conjunctiva. We developed software on the LabVIEW platform for automatic data acquisition and interpretation by nonexperts. The device is calibrated by comparing the differential absorbance of light of wavelength 576 and 600 nm with the clinical hemoglobin level of the subject. Our proposed method is consistent with results obtained using the current gold standard, the automated hematology analyzer. The proposed noncontact optical device for hemoglobin estimation is highly efficient,

inexpensive, feasible and extremely useful in low-resource point-of-care settings. The device output correlates with the different degrees of anemia with absolute and trending accuracy similar to those of widely used invasive methods. Moreover, the device can instantaneously transmit the generated report to a medical expert through e-mail, text messaging, or mobile apps.

1.5.2. Development of Optical Fiber-based Diagnostic Strategy for Direct *In-vivo* Measurement of Reactive Oxygen Species (ROS) in Animal Model:

***1.5.2.1. DNA-based Fiber Optic Sensor for Direct In-vivo Measurement of Oxidative Stress* [22]:** In this study, we have developed a DNA-based portable fiber optic sensor for the direct in-vivo measurement of oxidative stress in physiological milieu. Oxidative stress is essentially an inability of our body to counteract or detoxify the harmful effects of ROS through neutralization by antioxidants. Till date direct in-vivo measurements of oxidative stress are challenging. In this work, first we have developed a novel 2,7-dichlorodihydrofluorescein (DCFH) impregnated genomic DNA-based biomaterial, which is completely insoluble in water and forms excellent thin film layers on optical fiber tips. The biomaterial-sensitized fiber tip fluoresces brightly in the proximity of ROS as the entrapped DCFH is oxidized to highly fluorescent DCF. We have demonstrated that an indigenously developed biomaterial-sensitized optical fiber tip can work as an efficient ROS/oxidative stress sensor in an aqueous medium as well as in the blood phantom (hemoglobin solution). A preclinical study on the minimally invasive direct in-vivo oxidative stress detection in mice model has also been successfully demonstrated.

1.5.3. Spectroscopic Studies for the Potential Application in Environmental Pollution Monitoring of Toxic Heavy Metal Ions:

***1.5.3.1. Nanosurface Energy Transfer Based Highly Selective and Ultrasensitive "Turn on" Fluorescence Mercury Sensor* [46]:** In this work, we have developed a silver nanoparticles (Ag-NPs) impregnated poly(vinyle alcohol) capped 4-nitrophenylanthranilate (PVA-NPA) complex for mercury detection. The fluorescence

intensity of the synthesized PVA-NPA is found to be quenched by the impregnated Ag-NPs through dynamic quenching. Moreover, energy transfer (ET) between the acceptor (Ag-NPs) and the donor (PVA-NPA) is observed to follow the nanosurface energy transfer (NSET) mechanism. We have utilized the amalgamation of Ag-NPs with Hg^{2+} to develop a low cost prototype, which is highly efficient NSET based ultrasensitive "turn on" fluorescence mercury sensor. This sensor has high selectivity for Hg^{2+} ions over a wide range of other competing heavy metal ions, generally present in water of natural sources. The sensor response is found to be linear over the Hg^{2+} ions concentration regime from 0 to 1 ppb with a lower detection limit of 100 ppt (0.5 nM). The proposed method demonstrated successfully for monitoring trace Hg^{2+} ions in real world samples.

1.5.3.2. Development of Highly Selective and Efficient Prototype Sensor for Potential Application in Environmental Mercury Pollution Monitoring **[47]:** In this study, we have extended our earlier work towards more practical for the development of low-cost and portable device upon simplifying the experimental technique and setup. In this work, we have proposed a low-cost prototype device based on silver nanoparticles-impregnated poly(vinyle alcohol) (PVA-Ag-NPs) nanocomposite thin film for mercury detection. The thin film, fabricated through a facile protocol, is shown to be a fast, efficient and selective sensor for Hg^{2+} in aqueous medium with a detection limit of 10 ppb. We have utilized the aggregation and amalgamation of Ag-NPs with Hg^{2+} to develop the low-cost, highly efficient and feasible prototype mercury sensor. In the presence of Hg^{2+}, the yellowish thin film turned into colourless due to the loss of intense surface plasmon resonance (SPR) absorption band of the silver nanoparticles (Ag-NPs) through aggregation and amalgamation with mercury. The developed sensor has high selectivity for Hg^{2+} ion over a wide range of other competing heavy metal ions, generally present in water of natural sources. The sensor response is found to be linear over the Hg^{2+} ions concentration regime from 10 ppb to 5 ppm. The developed sensor has shown to determine a trace Hg^{2+} ions in real water samples. Finally, using the proposed

technique, we have developed a simple and inexpensive prototype device for monitoring in field environmental mercury pollution.

1.5.4. Development of a Carbon Nanomaterial-based Detection Technique for the Potential Environmental Monitoring of Toxic Metal and Non-metal Ions:

***1.5.4.1. Development of Highly Efficient Dual Sensor Based on Carbon Dots for Direct Estimation of Iron and Fluoride Ions in Drinking Water* [48]:** In the present work, highly fluorescent nanomaterials carbon dots (CDs) were prepared through a simple and nontoxic one-step hydrothermal carbonization of polyvinylpyrrolidone (PVP). The as-synthesised CDs, without any pre-treatments or post-treatments, show high stability over a broad pH range and have an excellent potential in chemical sensing applications. The as-prepared CDs have been demonstrated to be an excellent nano probe for Fe^{3+} ions sensing in aqueous media based on the fluorescence quenching with high sensitivity (lower limit of detection ~ 1 µM) and selectivity towards Fe^{3+} ions. "Turn off" fluorescence arises due to the formation of CDs-Fe^{3+} nanocomposite complex in the solution. The nanocomposite complex forms by the attachment of Fe^{3+} ions to the surface emissive site of the CDs, resulting in an obvious fluorescence quenching. Here, CDs itself act as a promising nano carrier for loading of Fe^{3+} ions to form the CDs-Fe^{3+} nanocomposite complex in the solution. In addition to all, in this study we are intensely focused to explore the application of CDs-Fe^{3+} nanocomposite complex. We have used the CDs-Fe^{3+} nanocomposite complex as a novel sensor probe for the detection of F^- ions in aqueous media based on "turn on" fluorescence mechanism. "Turn on" fluorescence occurs due to the formation of thermodynamically highly stable $[FeF_6]^{3-}$ complex and bare CDs in the solution. The developed sensor has high sensitivity (lower limit of detection ~ 1 µM) and selectivity towards F^- ions over a wide-ranging other competing anions. Finally, we successfully demonstrate the real life application of the developed sensor by estimating the trace F^- ions in the real world drinking water samples.

1.6. Plan of the Thesis

The plan of the thesis is as follows:

Chapter 1: This chapter gives a brief introduction to the different types of spectroscopic methods used in various kinds of medical diagnosis and environmental pollution monitoring applications. The scope and brief summary of the work done has also been included in this chapter.

Chapter 2: This chapter provides an overview of spectroscopic techniques, both the dynamical and steady-state, the structural aspects of biologically important systems, fluorescent probes and nanomaterials used in the experiments.

Chapter 3: Details of instrumentation, data analysis and experimental procedures have been discussed in this chapter.

Chapter 4: This chapter demonstrates the development and validation of a noncontact spectroscopic device for hemoglobin estimation without using any blood samples or chemical reagents at point-of-care in human subjects with high precision and accuracy. This chapter also demonstrates that the developed device can also generate and instantaneously transmit the report to a medical expert through e-mail, text messaging, or mobile apps.

Chapter 5: In this chapter, we have developed a highly efficient, portable and inexpensive DNA-based fiber optic sensor for direct measurement of ROS/oxidative stress in physiologically relevant environments. The preparation of DCFH entrapped biomaterial and the sensitization of a chemically etched fiber tip by the prepared biomaterial to develop the DNA-based fiber optic sensor has been described. The ROS generation activity of Mn_3O_4 nanoparticles and direct *in-vivo* measurement of oxidative stress in mice model has also been described in this chapter.

Chapter 6: This chapter deals with the spectroscopic studies on nanomaterial for the potential application in environmental mercury pollution monitoring. In this chapter, we have demonstrated a highly efficient, low cost NSET based ultrasensitive "turn on"

fluorescence sensor and polymer thin film-based portable prototype sensor device for Hg^{2+} ions detection in the background of a wide range of competing heavy metal ions. The potential application of the developed sensor in monitoring trace Hg^{2+} ions in real-world water samples has also been described in this chapter.

Chapter 7: In this chapter, we have developed a highly efficient sensor for direct estimation of iron and fluoride in drinking water. Here, we synthesis a highly fluorescent CDs through one step hydrothermal carbonization of Polyvinylpyrrolidone (PVP). Furthermore, we have developed "turn off" and "turn on" dual fluorescence sensors for Fe^{3+} and F^- ions in aqueous media using the as-prepared CDs. Finally, the real life application of the developed sensor has also been described in this chapter by estimating the trace F^- ions in the real world drinking water samples.

References

1. D. Berger; A brief history of medical diagnosis and the birth of the clinical laboratory. Part 1-Ancient times through the 19th century. *MLO Med. Lab. Obs.* 31 (1999), 28.

2. H. C. Hoover and L. H Hoover; De re metallica. *Dover Publications, New York,* (1950).

3. B. Valeur and M. N. Berberan-Santos; A brief history of fluorescence and phosphorescence before the emergence of quantum theory. *J. Chem. Educ.* 88 (2011), 731.

4. T. H. Maiman; Stimulated optical radiation in ruby. *Nature* 187 (1960), 493.

5. R. Richards-Kortum and E. Sevick-Muraca; Quantitative optical spectroscopy for tissue diagnosis. *Annu. Rev. Phys. Chem.* 47 (1996), 555.

6. R. S. Khandpur; Handbook of biomedical instrumentation. *Tata McGraw-Hill Education,* (1994).

7. M. Mallya, R. Shenoy, G. Kodyalamoole, M. Biswas, J. Karumathil and S. Kamath; Absorption spectroscopy for the estimation of glycated hemoglobin (HbA1c) for the diagnosis and management of diabetes mellitus: a pilot study. *Photomed. Laser Surg.* 31 (2013), 219.

8. T. G. Papazoglou; Malignancies and atherosclerotic plaque diagnosis—is laser induced fluorescence spectroscopy the ultimate solution? *J. Photochem. Photobiol.* 28 (1995), 3.

9. A. Shahzad, M. Knapp, M. Edetsberger, M. Puchinger, E. Gaubitzer and G. Köhler; Diagnostic application of fluorescence spectroscopy in oncology field: Hopes and challenges. *Appl. Spectrosc. Rev.* 45 (2010), 92.

10. R. R. Alfano; Advances in ultrafast time resolved fluorescence physics for cancer detection in optical biopsy. *AIP Adv.* 2 (2012), 011103.

11. M. F. Mitchell, S. B. Cantor, N. Ramanujam, G. Tortolero-Luna and R. Richards-Kortum; Fluorescence spectroscopy for diagnosis of squamous intraepithelial lesions of the cervix. *Obstet. Gynecol.* 93 (1999), 462.

12. G. Yahav, A. Hirshberg, O. Salomon, N. Amariglio, L. Trakhtenbrot and D. Fixler; Fluorescence lifetime imaging of DAPI-stained nuclei as a novel diagnostic tool for the detection and classification of B-cell chronic lymphocytic leukemia. *Cytometry Part A* 89 (2016), 644.

13. B. H. Ye, S. J. Lee, Y. W. Choi, S. Y. Park and C. D. Kim; Preventive effect of gomisin J from Schisandra chinensis on angiotensin II-induced hypertension via an increased nitric oxide bioavailability. *Hypertens. Res.* 38 (2015), 169.

14. X. Chen, Z. Zhong, Z. Xu, L. Chen and Y. Wang; 2',7'-Dichlorodihydrofluorescein as a fluorescent probe for reactive oxygen species measurement: Forty years of application and controversy. *Free Radic. Res.* 44 (2010), 587.

15. N. V. Tkachenko; Optical spectroscopy: methods and instrumentations. *Elsevier,* (2006).

16. J. Das and P. Sarkar; A new dipstick colorimetric sensor for detection of arsenate in drinking water. *Environ. Sci.: Water Res. Technol.* 2 (2016), 693.

17. Y. Li, L. Sun, X. Hu and T. Sun; Application and prospect of infrared spectroscopy in environmental science. *Spectrosc. Spect. Anal.* 28 (2008), 2325.

18. L. D. Marzo, A. Miccheli, P. Sapienza, M. Tedesco, A. Mingoli, G. Capuani, T. Aureli, A. Giuliani, F. Conti and A. Cavallaro; 31Phosphorus magnetic resonance spectroscopy to evaluate medical therapy efficacy in peripheral arterial disease. A pilot study. *Panminerva Med.* 41 (1999), 283.

19. R. E. Airley, J. E. Monaghan and I. J. Stratford; Hypoxia and disease: Opportunities for novel diagnostic and therapeutic prodrug strategies. *Pharm. J.* 264 (2000), 666.

20. P. K. Sarkar, S. Pal, N. Polley, R. Aich, A. Adhikari, A. Halder, S. Chakrabarti, P. Chakrabarti and S. K. Pal; Development and validation of a noncontact spectroscopic device for hemoglobin estimation at point-of-care. *J. Biomed. Opt.* 22 (2017), 055006.

21. I. Yamanouchi, Y. Yamauchi and I. Igarashi; Transcutaneous bilirubinometry: preliminary studies of noninvasive transcutaneous bilirubin meter in the Okayama National Hospital. *Pediatrics* 65 (1980), 195.

22. P. K. Sarkar, A. Halder, A. Adhikari, N. Polley, S. Darbar, P. Lemmens and S. K. Pal; DNA-based fiber optic sensor for direct in-vivo measurement of oxidative stress. *Sens. Actuators B: Chem.* 255 (2018), 2194.

23. Z. Huang, A. McWilliams, H. Lui, D. I. McLean, S. Lam and H. Zeng; Near-infrared Raman spectroscopy for optical diagnosis of lung cancer. *Int. J. Cancer* 107 (2003), 1047.

24. World Health Organization; WHA global nutrition targets 2025: Anaemia policy brief. *Geneva: W. H. O.* (2014).

25. J. Brown, L. Theis, L. Kerr, N. Zakhidova, K. O'Connor, M. Uthman, Z. M. Oden and R. Richards-Kortum; A hand-powered, portable, low-cost centrifuge for diagnosing anemia in low-resource settings. *Am. J. Trop. Med. Hyg.* 85 (2011), 327.

26. D. Frasca, C. Dahyot-Fizelier, K. Catherine, Q. Levrat, B. Debaene and O. Mimoz; Accuracy of a continuous noninvasive hemoglobin monitor in intensive care unit patients. *Crit. Care Med.* 39 (2011), 2277.

27. L. Lamhaut, R. Apriotesei, X. Combes, M. Lejay, P. Carli and B. Vivien; Comparison of the accuracy of noninvasive hemoglobin monitoring by spectrophotometry (SpHb) and HemoCue® with automated laboratory hemoglobin measurement. *Anesthesiology* 115 (2011), 548.

28. A. Belardinelli, M. Benni, P. Tazzari and P. Pagliaro; Noninvasive methods for haemoglobin screening in prospective blood donors. *Vox Sang.* 105 (2013), 116.

29. T. Lister, P. A. Wright and P. H. Chappell; Optical properties of human skin. *J. Biomed. Opt.* 17 (2012), 090901.

30. B. Kalyanaraman, V. Darley-Usmar, K. J. A. Davies, P. A. Dennery, H. J. Forman, M. B. Grisham, G. E. Mann, K. Moore, L. J. Roberts Ii and H.

Ischiropoulos; Measuring reactive oxygen and nitrogen species with fluorescent probes: challenges and limitations. *Free Radic. Biol. Med.* 52 (2012), 1.

31. V. J. Hammond, J. W. Aylott, G. M. Greenway, P. Watts, A. Webster and C. Wiles; An optical sensor for reactive oxygen species: encapsulation of functionalised silica nanoparticles into silicate nanoprobes to reduce fluorophore leaching. *Analyst* 133 (2007), 71.

32. J. T. Hancock, R. Desikan and S. J. Neill; Role of reactive oxygen species in cell signalling pathways. *Biochem. Soc. Trans.* 29 (2001), 345.

33. H. M. Cochemé, C. Quin, S. J. McQuaker, F. Cabreiro, A. Logan, T. A. Prime, I. Abakumova, J. V. Patel, I. M. Fearnley and A. M. James; Measurement of H_2O_2 within living Drosophila during aging using a ratiometric mass spectrometry probe targeted to the mitochondrial matrix. *Cell Metab.* 13 (2011), 340.

34. S. Martins, J. P. S. Farinha, C. Baleizão and M. N. Berberan-Santos; Controlled release of singlet oxygen using diphenylanthracene functionalized polymer nanoparticles. *Chem. Comm.* 50 (2014), 3317.

35. Q. Wang, D. Kim, D. D. Dionysiou, G. A. Sorial and D. Timberlake; Sources and remediation for mercury contamination in aquatic systems—a literature review. *Environ. Pollut.* 131 (2004), 323.

36. J. Ke, X. Li, Q. Zhao, Y. Hou and J. Chen; Ultrasensitive quantum dot fluorescence quenching assay for selective detection of mercury ions in drinking water. *Sci. Rep.* 4 (2014), 5624.

37. J. R. Miller, J. Rowland, P. J. Lechler, M. Desilets and L.-C. Hsu; Dispersal of mercury-contaminated sediments by geomorphic processes, Sixmile Canyon, Nevada, USA: Implications to site characterization and remediation of fluvial environments. *Water, Air and Soil Pollut.* 86 (1996), 373.

38. T. A. Baughman; Elemental mercury spills. *Environ. Health Perspect.* 114 (2006), 147.

39. K. Farhadi, M. Forough, R. Molaei, S. Hajizadeh and A. Rafipour; Highly selective Hg^{2+} colorimetric sensor using green synthesized and unmodified silver nanoparticles. *Sens. Actuators B: Chem.* 161 (2012), 880.

40. E. M. Nolan and S. J. Lippard; Tools and tactics for the optical detection of mercuric ion. *Chem. Rev.* 108 (2008), 3443.

41. Y.-Q. Zhang, D.-K. Ma, Y. Zhuang, X. Zhang, W. Chen, L.-L. Hong, Q.-X. Yan, K. Yu and S.-M. Huang; One-pot synthesis of N-doped carbon dots with tunable luminescence properties. *J. Mater. Chem.* 22 (2012), 16714.

42. J.-a. Annie Ho, H.-C. Chang and W.-T. Su; DOPA-mediated reduction allows the facile synthesis of fluorescent gold nanoclusters for use as sensing probes for ferric ions. *Anal. Chem.* 84 (2012), 3246.

43. Y. Dong, R. Wang, G. Li, C. Chen, Y. Chi and G. Chen; Polyamine-functionalized carbon quantum dots as fluorescent probes for selective and sensitive detection of copper ions. *Anal. Chem.* 84 (2012), 6220.

44. J. Chan, S. C. Dodani and C. J. Chang; Reaction-based small-molecule fluorescent probes for chemoselective bioimaging. *Nat. Chem.* 4 (2012), 973.

45. J. Li, Q. Wang, Z. Guo, H. Ma, Y. Zhang, B. Wang, D. Bin and Q. Wei; Highly selective fluorescent chemosensor for detection of Fe^{3+} based on $Fe_3O_4@ZnO$. *Sci. Rep.* 6 (2016), 23558.

46. P. K. Sarkar, N. Polley, S. Chakrabarti, P. Lemmens and S. K. Pal; Nanosurface energy transfer based highly selective and ultrasensitive "turn on" fluorescence mercury sensor. *ACS Sens.* 1 (2016), 789.

47. P. K. Sarkar, A. Halder, N. Polley and S. K. Pal; Development of highly selective and efficient prototype sensor for potential application in environmental mercury pollution monitoring. *Water, Air and Soil Pollut.* 228 (2017), 314.

48. P. K. Sarkar, P. Kar, A. Halder, P. Lemmens and S. K. Pal; Development of highly efficient dual sensor based on carbon dots for direct estimation of iron and fluoride ions in drinking water. *ChemistrySelect* 4 (2019), 4462.

Chapter 2

An Overview of Spectroscopic Techniques and Systems

In order to investigate the various processes involved in course of study on ultrafast spectroscopy, synthesis, functionalization and potential application of the biomedically relevant sensors and environmental pollution monitoring sensors, different steady-state and dynamical tools have been employed. In this chapter, a brief discussion about these tools has been provided. A brief overview of the various systems used has also been discussed.

2.1. Steady-state and Dynamical Tools

2.1.1. Diffuse Reflectance Spectroscopy: Reflectance spectroscopy is very closely related to UV/Vis spectroscopy, as both of these techniques use visible light to excite valence electrons to empty orbitals. The difference in these techniques is that in UV/Vis spectroscopy one measures the relative change of transmittance of light as it passes through a solution, whereas in diffuse reflectance, one measures the relative change in the amount of reflected light from a surface (Figure 2.1). A solution that is completely clear and colorless has essentially 100% transmission of all visible wavelengths of light, which means that it does not contain any dissolved components that have (allowed) electronic transitions over that energy range. By the same line of reasoning, a white powder effectively reflects 100% of all visible wavelengths of light that interacts with it.
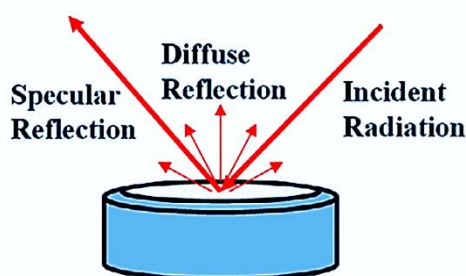
Figure 2.1. *Schematic representation of the diffuse reflection from a solid sample. The diffuse light can be collected for spectroscopic studies.*

However, if the material has electronic energy levels that are separated by energy in the visible region, then it may absorb some of the light energy to move electrons from the filled energy level (valence band) into this empty level (conduction band). This causes a relative decrease in the amount of light at that particular energy, relative to a reference source. In other words, the % transmission/reflectance will decrease.

2.1.2. Förster Resonance Energy Transfer (FRET): Förster Resonance Energy Transfer [1] is an electrodynamic phenomenon involving the non-radiative transfer of the excited state energy from the donor dipole (D) to an acceptor dipole (A) (Figure 2.2a). FRET has got wide uses in all fluorescence applications including medical diagnostics, DNA analysis and optical imaging. Since FRET can measure the size of a protein molecule or the thickness of a membrane, it is also known as "spectroscopic ruler" [2]. FRET is very often used to measure the distance between two sites on a macromolecule. Basically, FRET is of two types: (a) Homo-molecular FRET and (b) Hetero-molecular FRET. In the former case, same fluorophore acts both as energy donor and acceptor, while in the latter case two different molecules act as donor and acceptor.

Each donor-acceptor (D-A) pair participating in FRET is characterized by a distance known as Förster distance (R_0) i.e., the D-A separation at which energy transfer is 50% efficient. The R_0 value ranges from 20 to 60 Å. The rate of resonance energy transfer (k_T) from donor to an acceptor is given by [3],

$$k_T = \frac{1}{\tau_D}\left(\frac{R_0}{r}\right)^6 \tag{2.1}$$

where, τ_D is the lifetime of the donor in the absence of acceptor, R_0 is the Förster distance and r is the donor to acceptor (D-A) distance. The rate of transfer of donor energy depends upon the extent of overlap of the emission spectrum of the donor with the absorption spectrum of the acceptor ($J(\lambda)$), the quantum yield of the donor (Q_D), the relative orientation of the donor and acceptor transition dipoles (κ^2) and the distance between the donor and acceptor molecules (r) (Figure 2.2b). In order to

estimate FRET efficiency of the donor and hence to determine distances of donor-acceptor pairs, the methodology described below is followed [3]. The Förster distance (R_0) is given by,

$$R_0 = 0.211\left[\kappa^2 n^{-4} Q_D J(\lambda)\right]^{1/6} \text{ (in Å)} \tag{2.2}$$

where, n is the refractive index of the medium, Q_D is the quantum yield of the donor and $J(\lambda)$ is the overlap integral. κ^2 is defined as,

$$\kappa^2 = \left(\cos\theta_T - 3\cos\theta_D \cos\theta_A\right)^2 = \left(\sin\theta_D \sin\theta_A \cos\varphi - 2\cos\theta_D \cos\theta_A\right)^2 \tag{2.3}$$

where, θ_T is the angle between the emission transition dipole of the donor and the absorption transition dipole of the acceptor, θ_D and θ_A are the angles between these dipoles and the vector joining the donor and acceptor and φ is angle between the planes of the donor and acceptor (Figure 2.2b). κ^2 value can vary from 0 to 4. For collinear and parallel transition dipoles, $\kappa^2 = 4$; for parallel dipoles, $\kappa^2 = 1$; and for perpendicularly oriented dipoles, $\kappa^2 = 0$. For donor and acceptors that randomize by rotational diffusion prior to energy transfer, the magnitude of κ^2 is assumed to be 2/3. $J(\lambda)$, the overlap integral, which expresses the degree of spectral overlap between the donor emission and the acceptor absorption, is given by,
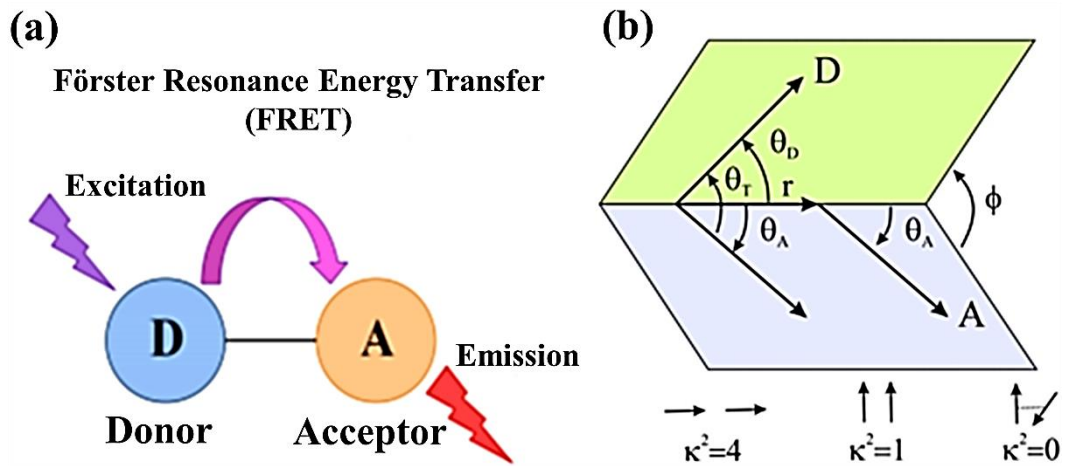
Figure 2.2. *(a) Schematic illustration of the Förster Resonance Energy Transfer (FRET) process. (b) Dependence of the orientation factor κ^2 on the directions of the emission and absorption dipoles of the donor and acceptor, respectively.*

$$J(\lambda) = \frac{\int_0^\infty F_D(\lambda)\varepsilon_A(\lambda)\lambda^4 d\lambda}{\int_0^\infty F_D(\lambda)d\lambda} \qquad (2.4)$$

where, $F_D(\lambda)$ is the fluorescence intensity of the donor in the wavelength range of λ to $\lambda + d\lambda$ and is dimensionless. $\varepsilon_A(\lambda)$ is the extinction coefficient (in $M^{-1}cm^{-1}$) of the acceptor at λ. If λ is in nm, then $J(\lambda)$ is in units of M^{-1} cm^{-1} nm^4.

Once the value of R_0 is known, the efficiency of energy transfer can be calculated. The efficiency of energy transfer (E) is the fraction of photons absorbed by the donor which are transferred to the acceptor and is defined as,

$$E = \frac{k_T(r)}{\tau_D^{-1} + k_T(r)} \qquad (2.5)$$

or $\qquad E = \frac{R_0^6}{r^6 + R_0^6} \qquad (2.6).$

The transfer efficiency is measured using the relative fluorescence intensity of the donor, in absence (F_D) and presence (F_{DA}) of the acceptor as,

$$E = 1 - \frac{F_{DA}}{F_D} \qquad (2.7a).$$

For D-A systems decaying with multiexponential lifetimes, E is calculated from the amplitude weighted lifetimes $\langle\tau\rangle = \sum_i \alpha_i \tau_i$ [3] of the donor in absence (τ_D) and presence (τ_{DA}) of the acceptor as,

$$E = 1 - \frac{\tau_{DA}}{\tau_D} \qquad (2.7b).$$

The D-A distances can be measured using equations (2.6), (2.7a) and (2.7b). The distances measured using Eq. 2.7a and 2.7b are revealed as R^S (steady-state measurement) and R^{TR} (time-resolved measurement), respectively. In one of recent studies from our group [4], we have reported the potential danger of using Eq. 2.7a to conclude the nature of energy transfer as Förster type. The study shows that the energy

transfer efficiency E, calculated from steady-state experiment (Eq. 2.7a) might be due to re-absorption of donor emission, but not due to dipole-dipole interaction (FRET).

2.1.3. Nanosurface Energy Transfer (NSET): The D−A separations can also be calculated using another prevailing technique, NSET [5, 6], in which the energy transfer efficiency depends on the inverse of the fourth power of the D−A separation [7]. The NSET technique is based on the model of Persson and Lang [6], which is concerned with the momentum and energy conservation in the dipole-induced formation of electron−hole pairs. Here the rate of energy transfer is calculated by performing a Fermi golden rule calculation for an excited-state material depopulating with the simultaneous scattering of an electron in the nearby metal to above the Fermi level. The Persson model states that the damping rate to a surface of a noble metal may be calculated by,

$$k_{et} = 0.3(\frac{\mu^2 \omega_{dye}}{\eta \omega_F k_F d^4})$$

(2.8)

which can be expressed in more measurable parameters through the use of the Einstein A_{21} coefficient [8],

$$A_{21} = \frac{\omega^3_{dye}}{3\varepsilon_0 \eta \pi c^3} |\mu^2|$$

(2.9).

To give the following rate of energy transfer in accordance with Coulomb's law $(1/4\pi\varepsilon_0)$:

$$k_{et} = 0.225 \frac{c^3 \phi_{dye}}{\omega^2_{dye} \omega_F k_F d^4 \tau_{dye}}$$

(2.10)

where, c is the speed of light, ϕ_{dye} is the quantum yield of the donor, ω_{dye} is the angular frequency for the donor, ω_F is the angular frequency for acceptor, d is the D−A separation, μ is the dipole moment, τ_{dye} is the average lifetime of the donor and k_F is the Fermi wave-vector [9, 10]. The d_0 value is the distance at which a dye exhibits equal probabilities for energy transfer and spontaneous emission. The d_0 value is given by,

26

$$d_0 = (0.225 \frac{c^3 \phi_{dye}}{\omega_{dye}^2 \omega_F k_F})^{1/4}$$

(2.11).

In our studies, we used k_{et} as $k_{time\text{-}resolved}$,

$$k_{time-resolved} = \frac{1}{\tau_{donor-acceptor}} - \frac{1}{\tau_{dye}}$$

(2.12)

where, $\tau_{donor-acceptor}$ is the average lifetime of the D−A system [11].

Now the donor-acceptor distance d can be calculated by following the given equation,

$$d = \frac{d_0}{(k_{et}\tau_{dye})^{1/4}}$$

(2.13).

2.1.4. Data Analysis of Time-resolved Fluorescence Transients: Curve fitting of the time-resolved fluorescence transients was carried out using a nonlinear least square fitting procedure to a function (2.14) comprised of convolution of the IRF,

$$(X(t) = \int_0^t E(t')R(t-t')dt')$$

(2.14)

(*E(t)*) with a sum of exponentials (2.14) with pre-exponential factors (*B$_i$*),

$$(R(t) = A + \sum_{i=1}^{N} B_i e^{-t/\tau_i})$$

(2.15)

characteristic lifetimes (τ_i) and a background (*A*). Relative concentration in a multiexponential decay is expressed as (2.16),

$$c_n = \frac{B_n}{\sum_{i=1}^{N} B_i} \times 100$$

(2.16).

The average lifetime (amplitude-weighted) of a multiexponential decay is expressed as,

$$\tau_{av} = \sum_{i=1}^{N} c_i \tau_i$$

(2.17).

2.1.5. Dynamic Light Scattering (DLS): According to semi-classical theory of light scattering, when light impinges on matter, the electric field of the light induces an oscillating polarization of electrons in the molecules. Hence, the molecules provide a secondary source of light and subsequently scatter light. The frequency shift, the angular distribution, the polarization and the intensity of scattered light are determined by size, shape and molecular interactions in the scattering material. Dynamic light scattering (DLS) also known as photon correlation spectroscopy (PCS) or quasi-elastic light scattering (QELS) is one of the most popular technique used to determine the size of the particle.

2.1.5.1. Theory: DLS experiments are based on two assumptions:

(a) Particles exhibit Brownian motion (also called 'random walk'). The probability density function is given by the formula,

$$P(r,t|0,0) = (4\pi Dt)^{3/2} \exp(-r^2/4Dt)$$
(2.18)

where, D is the translational diffusion coefficient.

(b) The particles are spherical in shape with particles of molecular dimensions. If it is so, then it is possible to apply the Stoke-Einstein relation and hence have a formula that easily gives the diffusion constant,

$$D = \frac{k_B T}{3\pi\eta d_H}$$
(2.19)

where, d_H is the hydrodynamic diameter of the particles, k_B is the Boltzmann constant, T is the temperature in Kelvin and η is the viscosity of the solvent.

2.1.5.2. Experimental Methods: It has been seen that particles in dispersion are in a constant, random Brownian motion and this causes the intensity of scattered light to fluctuate as a function of time. The correlator used in a DLS instrument constructs the intensity autocorrelation function $G(\tau)$ of the scattered intensity,

$$G(\tau) = \langle I(t) I(t+\tau) \rangle \tag{2.20}$$

where, τ is the time difference (the sample time) of the correlator. For a large number of monodisperse particles in Brownian motion, the correlation function (given the symbol G) is an exponential decaying function of the correlator time delay τ,

$$G(\tau) = A\left[1 + B.\exp(-2\Gamma\tau)\right] \tag{2.21}$$

where, A is the baseline of the correlation function, B is the intercept of the correlation function. Γ is the first cumulant and is related to the translational diffusion coefficient as, $\Gamma = Dq^2$, where q is the scattering vector and its magnitude is defined as,

$$q = \left(\frac{4\pi n}{\lambda_0}\right) \sin\left(\frac{\theta}{2}\right) \tag{2.22}$$

where, n is the refractive index of dispersant, λ_0 is the wavelength of the laser and θ, the scattering angle. For polydisperse samples, the equation can be written as,

$$G(\tau) = A\left[1 + B\left|g^{(1)}(\tau)\right|^2\right] \tag{2.23}$$

where, the correlation function $g^{(1)}(\tau)$ is no longer a single exponential decay and can be written as the Laplace transform of a continuous distribution $G(\Gamma)$ of decay times,

$$g^{(1)}(\tau) = \int_0^\infty G(\Gamma)\exp(-\Gamma\tau)d\Gamma \tag{2.24}.$$

The size distribution of the particles are obtained by fitting, using non-linear least square fitting or CONTIN program, the autocorrelation function to multiexponential function. The size distribution obtained is a plot of the relative intensity of light scattered by particles and is therefore known as an intensity size distribution. However, in the intensity distribution graph, the area of the peak for the larger particle appears at least 10^6 times larger than the peak for the smaller particle. This is because large particles scatter much more light than small particles, as the intensity of light scattering by a particle is proportional to the sixth power of its diameter (Rayleigh's approximation).

2.1.6. Transmission of Light through Optical Fiber: An optical fiber is a cylindrical dielectric waveguide (nonconducting waveguide) that transmits light along its axis, by the process of total internal reflection. The fiber consists of a core surrounded by a cladding layer, both of which are made of dielectric materials [48]. To confine the optical signal in the core, the refractive index of the core must be greater than that of the cladding. The boundary between the core and cladding may either be abrupt, in step-index fiber, or gradual, in graded-index fiber. When the light (electromagnetic wave) travels to the boundary between the core and the clad (with an angle greater than the critical angle) a localized attenuating electromagnetic field is generated which is called the evanescent field.

Evanescent wave is a near-field wave with an intensity that exhibits exponential decay without absorption as a function of the distance from the core-clad boundary of the optical fiber as shown in Figure 2.3. The standard practice for the estimation of penetration depth (d_p) of the evanescent field in a "non-absorbing" medium can be illustrated in the following way [12]. In a fiber optic cable, the optical signal is transmitted by total internal reflection of the light. The light from the silica core with refractive index n_1 is incident on the clad with refractive index n_2, where $n_1 > n_2$. As a result, the light is internally reflected totally, depending upon the incident angle θi, where $\theta i > \theta_c$ (θ_c is the critical angle). In practice, the light does not reflect back from the exact plane of separation between core and clad, rather it has certain penetration depth in the clad region. The penetration depth or depth of penetration d_p is defined as [12],

$$d_p = \frac{\lambda}{2\pi\sqrt{(n_1^2 \sin^2\theta - n_2^2)}} \qquad (2.25).$$

The estimated penetration depth for our case is in the range of few hundreds of nm. However, if any portion of clad is removed or etched (as in our case) the depth of penetration would change. It is also worth mentioning that evanescent field strongly interacts with the environment outside the fiber and carry spectroscopic information,

and is the key of all the waveguide-based sensors [12]. The scenario would change in the case of an environment, which offers strong optical absorption to the light responsible for the evanescent field [13, 14]. This can be conveniently taken into account by defining a complex refractive index [13],

$$\tilde{n} = n + i\varkappa \qquad (2.26)$$

where, the real part of the refractive index n indicates the phase speed, while imaginary part $\varkappa$ indicates the amount of absorption loss when electromagnetic wave propagates through the medium. Both the real and imaginary parts of the refractive index are the functions of wavelength of the light propagating through the optical fiber. One way to incorporate attenuation of the evanescent field in the absorbing medium is via an absorption coefficient (α_{abs}) [13, 14] in the following way,

$$I(z) = I_0 e^{-\alpha_{abs} z} \qquad (2.27)$$

where, $I(z)$ is the intensity of the evanescent field at a distance of z from the interface having field intensity of I_0. α_{abs} denotes absorption coefficient of the medium and equal to twice the magnitude of the imaginary component of the refractive index ($2 \mathsf{X} \varkappa$) [13]. In this formulation, the penetration depth, d_p would be just inverse of the absorption coefficient ($1/\alpha_{abs}$) [13]. From the above formulation it is clear that the penetration depth of the evanescent field in an absorbing medium very much depends on the concentration of the analyte in the medium.
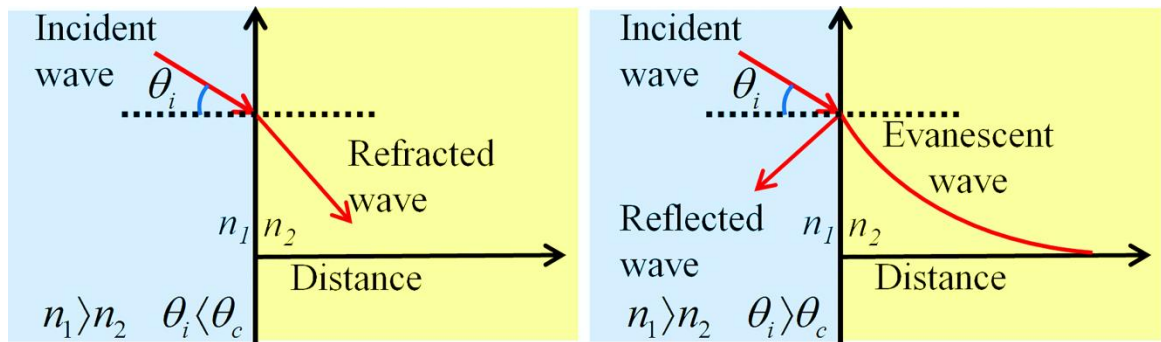
Figure 2.3. *Schematic representation of light refraction from medium with higher to lower refractive index and the evanescent wave in the medium with lower refractive index when $\theta i > \theta_c$ (right).*

2.1.7. Statistical Analysis: Comparison of different parameters between the groups in animal studies was performed using one-way analysis of variance (ANOVA) followed by Tukey's multiple comparison test using a computer program GraphPad Prism (version 5.00 for Windows), GraphPad Software, La Jolla California USA, www.graphpad.com. P values <0.05 were considered significant.

2.2. Systems

2.2.1. Materials and Molecular Probes: In this section, we have discussed about the different materials and probe molecules that have been used in the course of study.

2.2.1.1. Nanomaterials: Nanomaterials represent a special class of materials whose structural features lie intermediate between those of individual atoms and bulk materials, with at least one dimension in the nanometer region. The interest in nanomaterials stems from the fact that new properties are acquired at this length scale and equally important, that these properties change with their size or shape. In recent years, metal, non-meatal and semiconductor nanoparticles have been a prime center of attention for research and development during the past few decades due to their widespread applications in optoelectronics, catalysts, biological sciences, detectors and sensors which mainly arises from their unique size and morphology-dependent optical and electrical properties.

2.2.1.1.1. Metal Nanoparticles (NPs): Metal nanoparticles (10-100 nm) have recently attracted much interest because of their unique properties, including large optical field enhancements resulting in the strong scattering and absorption of light. The interesting optical attributes of metal nanoparticles are due to their unique interaction with light. In the presence of the oscillating electromagnetic field of the light, the free electrons of the metal nanoparticle undergo a collective coherent oscillation with respect to the positive metallic lattice. This process is resonant at a particular frequency of the light and is termed the surface plasmon resonance (SPR) absorption which can be simply visualized as a photon confined to the small size of the nanostructure, constituting an

intense electric field around the particle. The surface plasmon oscillation decays by radiating its energy resulting in light scattering or decays nonradiatively as a result of conversion of absorbed light to heat [15]. The electric field intensity and the scattering and absorption cross-sections are all strongly enhanced at the SPR frequency which for gold, silver and copper lies in the visible region. Since copper is easily oxidized, gold and silver nanostructures are most attractive for optical applications.

Because of surface plasmon enhancement, optical cross-sections of metal nanoparticles are 5 orders of magnitude or much larger than those of dye molecules for various applications including sensing application. Each metal nanoparticle can be considered as an optical probe equivalent to a million dye molecules. This provides a large margin for enhancing the probing sensitivity. Unlike dyes, metal nanoparticles are photostable and do not undergo photobleaching, allowing higher light excitation energies and longer probing times. There is a range of enhanced radiative and nonradiative attributes associated with the SPR. The optical probing strategy can thus be chosen depending on the specific application. Different strategies may also be combined. Another unique property of SPR is that it can be tuned by changing the nanostructure size, shape, composition, environment or dielectric properties of the media [16, 17] in order to suit for different applications.

The spectral position and shape of the plasmon band for a given particle has been determined by Gustav and Mie [18] and can be represented in the following way,

$$E(\lambda) = \frac{24\pi^2 N a^3 \varepsilon_{ex}^{3/2}}{\lambda \ln(10)} \left[\frac{\varepsilon_i(\lambda)}{(\varepsilon_r(\lambda) + \chi \varepsilon_{ex})^2 + \varepsilon_i(\lambda)^2} \right] \tag{2.28}$$

where ε_r and ε_i are respectively, the real and imaginary components of the dielectric function of the metal, ε_{ex} is the external environment dielectric function, r is the radius of the particle, χ is factor related to the eccentricity of the particle and N is the number of atoms present in the particle. Using equation 2.28 one can reasonably predict the position and shape of plasmon absorption for spherical and spheroidal metal nanoparticles which have sizes comparable to the wavelength of the incident light (i.e. R≈λ) [19]. Optical responses of such larger metal nanoparticles (R≈λ) to external

electromagnetic fields are simply dependent on their sizes, free electron density and therefore their dielectric function relative to that of the surrounding medium. This size-dependent effect is extrinsic because optical properties such as dielectric functions (i.e. refractive indices) of the nanoparticles are similar to those of bulk metals [20]. When particle size approaches the second characteristic length, i.e. the electron mean free path (the average distance an electron travels between two adjacent collisions), the dielectric function and refractive indices become size dependent. This is known as an intrinsic size effect [20, 21]. As a result, the optical responses such as plasmon absorptions of small metal nanoparticles ($R<<\lambda$) have different size-dependences compared with large nanoparticles. It is in fact well established that the surface plasmon bandwidth is inversely proportional to the radius r of the particle for sizes smaller than about 20 nm [20, 22]. The increased broadening with decreasing size enhances both the low and high-energy absorbance of the smallest clusters, causing the plasmon to be completely damped below a size of $d=$ 2.2 nm for Au but still observable at the size of $d=$ 1.55 nm for Ag [23]. However, Mie theory can still be extended into this quasi-static regime. Eventually, when particle size becomes comparable to the third characteristic length− Fermi wavelength of an electron (i.e. de Broglie's wavelength of an electron at the Fermi energy, or ~0.5 nm for gold and silver), [24, 25] optical, electronic and chemical properties of metal clusters are dramatically different from the other two size regimes. In this smallest size regime, metal clusters become "molecular species" [26, 27] and discrete states with strong florescence can be observed [28, 29].

2.2.1.1.2. Carbon Dots (CDs): As a new class of fluorescent carbon nanomaterials, carbon dots (CDs) have been a prime center of attention for research and development during the past few decades. CDs have several novel properties like size-tunable emission, narrow spectral line widths, continuous absorption profiles [30], high luminescence, high chemical stability [31], low toxicity [32], high quantum yield [33] and excellent biocompatibility [34-36]. Due to these unique properties, CDs have been applied widely in the fields of drug delivery [37], catalysis [38], chemical sensors [39,

40], biomedical application [41, 42], biological sensors [43], nano-biotechnology [44]. On the other hand, these unique properties allow for excitation of multiple species of CDs utilizing a single light source for multiplexed fluorescence detection without substantial signal cross-coupling. Using suitable capping agents, CDs can be conjugated with biological molecules in order to "match" them with biological environments. By changing the particle size and composition, the photoluminescence emission maximum can be manipulated and attaching nanocrystals to the molecules gives a fluorescent labeling method [45]. The large surface area-to-volume ratio of CDs makes them appealing for the design of more complex nanosystems. Also, the long luminescent lifetime of CDs diminishes interference from background autofluorescence in live cell imaging. Unlike conventional organic dyes, CDs are extremely resistant to photobleaching, which makes them useful for continuous monitoring of biological phenomena and environmental pollution.

2.2.1.2. Poly(vinyl alcohol) (PVA): PVA (Figure 2.4a) is a water-soluble nontoxic and biodegradable synthetic hydrophilic linear polymer that generally exists as a copolymer of vinyl alcohol and vinyl acetate. PVA was first synthesized by Hermann and Haehnel in 1924 via saponification of poly(vinyl ester) in sodium hydroxide solution [46]. The "n" in PVA, -(C$_2$H$_4$O)n-, varies from 500 to 5000, which resembles change in molecular weight from about 20,000 to about 200,000 Daltons. It is white (colourless) and odorless and available as beads or as powder. The polymer melt at around 180-228 °C and display glass to rubber transition at 75-85 °C. Due to the reactive structural functional groups, the polymer undergoes chemical changes such as esterification and etherification, as well as physical changes such as crystallization and ion-polymer complexation. The polymer has high tensile strength and flexibility, as well as high oxygen and aroma barrier properties. PVA has excellent film forming, emulsifying and adhesive properties also. Due to their simple structure and unique properties such as adhesiveness, strength, film forming, swelling, biocompatibility, nontoxic and non-carcinogenicity, polymer has found applications in different industries including

papermaking, textiles, vinylon fiber production, food, biomedical, environmental pollution monitoring and pharmaceutical in particular [47-49].

2.2.1.3. 4-Nitrophenyl Anthranilate (NPA): NPA (Figure 2.4b) is a well-known fluorescence probe having an anthranilate group as fluorescence moiety. NPA also has an active p-nitro-phenyl ester group that can react with nucleophiles.
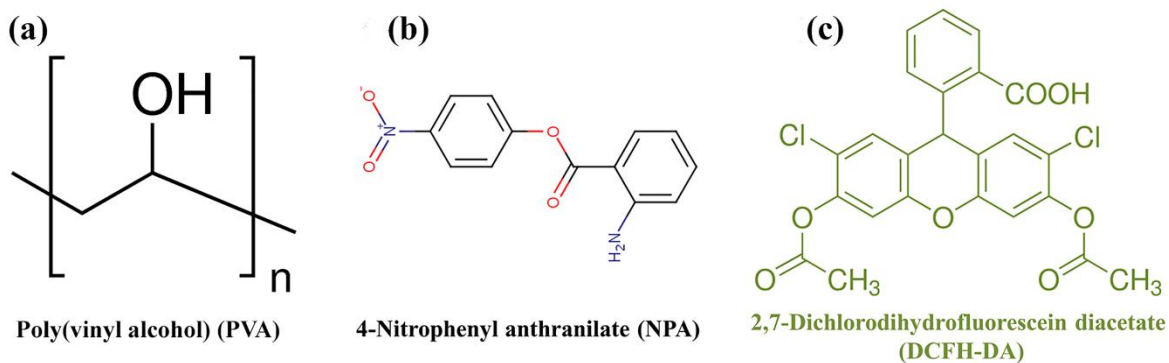
Figure 2.4. *Molecular structures of the molecular probes: (a) Poly(vinyl alcohol) (PVA) (b) 4-Nitrophenyl anthranilate (NPA), (c) 2,7-Dichlorodihydrofluorescein diacetate (DCFH-DA).*

2.2.1.4. 2,7-Dichlorodihydrofluorescein Diacetate (DCFH-DA): DCFH-DA (Figure 2.4c) is a cell-permeable non-fluorescent probe. 2',7'-Dichlorofluorescin diacetate is de-esterified intracellularly and turns to highly fluorescent 2',7'-dichlorofluorescein upon oxidation. This fluorescence probes is the most widely used one for detection of intracellular oxidative stress, including sensitive and rapid quantitation of oxygen-reactive species in response to oxidative metabolism. The probe is added to cells in culture and the intracellular oxidation of 2,7-dichlorodihydrofluorescein (DCFH) results in formation of a fluorescent product, 2,7-dichlorofluorescein (DCF) [50, 51].

2.2.2. Biological Macromolecules: In this section, we have discussed about the different biological macromolecules that have been used in the course of study.

2.2.2.1. Hemoglobin: Found in red blood cells, hemoglobin (Figure 2.5) is globular protein that ferry oxygen (O_2) molecules and carbon dioxide (CO_2) molecules throughout the body. Each hemoglobin protein structure consists of four polypeptide

subunits, which are held together by ionic bonds, hydrogen bonds, hydrophobic interactions and van der Waals forces, as well as four heme pigments, one in each of the subunits [52, 53]. These heme groups contain positively-charged iron (Fe^{2+}) molecules which can reversibly bind to oxygen molecules and transport them to various areas of the body [52, 53]. As the heme groups bind or release their oxygen loads, the overall hemoglobin undergoes conformational changes which alters their affinity for oxygen. Hemoglobin tetramers are comprised of the four subunits, two α-globin chains and two β-globin chains all of which take the form of alpha helices [52]. which is typically hidden within the various subunits, is covalently bound to yet a
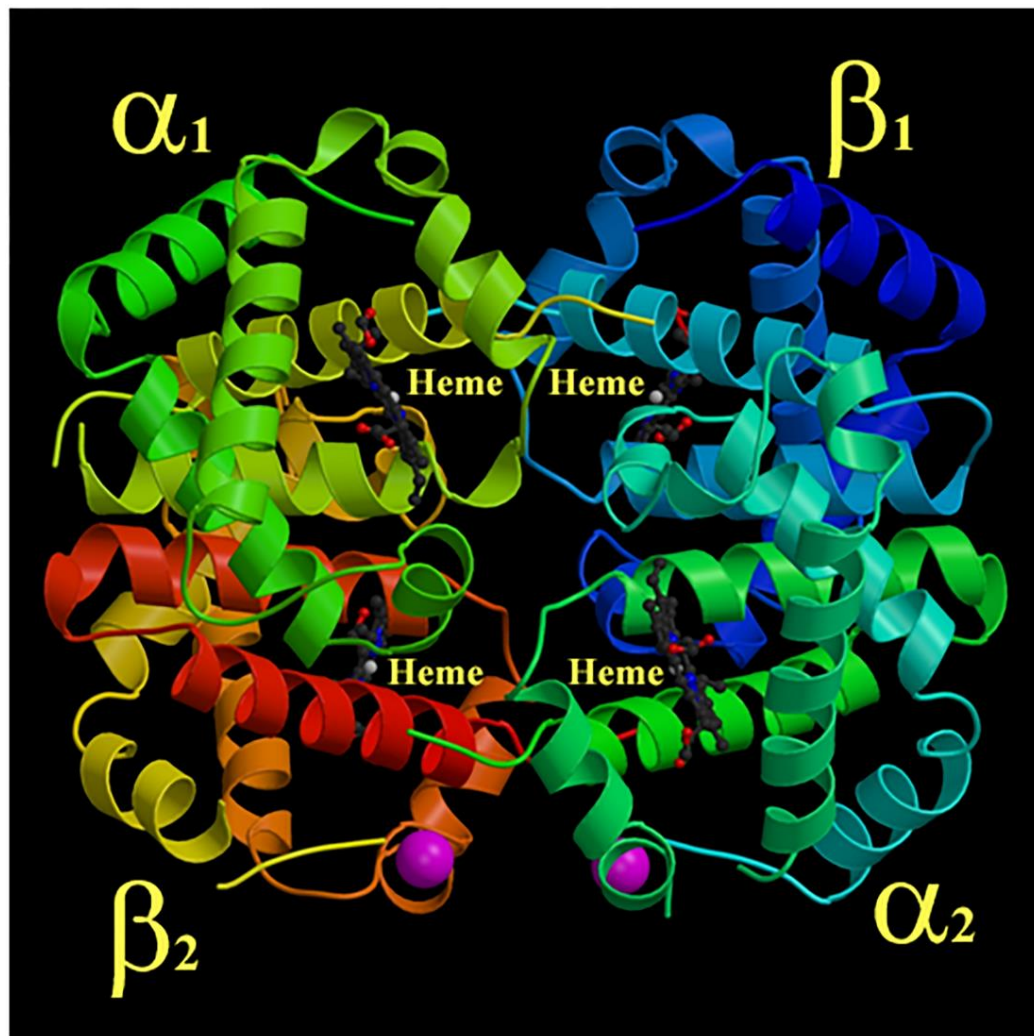
Figure 2.5. *Structure of hemoglobin. There are four subunits as shown by the various colors. The heme groups are shown in predominantly gray. Protein Data Bank ID-4hhb.*

different nitrogen atom that belongs to a nearby histidine group. This histidine chain, combined with other hydrophobic interactions, stabilize the heme group within each subunit. Oxygen molecules bind to the side of the iron ion that is opposite of the proximal histidine. Located near this opposite side is a different histidine chain, which serves two important function even though it is not directly bound to the heme group [54].

2.2.2.2. Deoxyribonucleic Acid (DNA): Nucleic acids form the central molecules in transmission, expression and conservation of genetic information. DNA serves as carrier of genetic information [55]. The classic example of how biological function follows from biomolecular structure comes from the elucidation of double helical structure of DNA by Watson and Crick [56]. DNAs are polynucleotides with each nucleotide comprising of deoxyribose sugar, purine and pyrimidine bases and phosphate groups. The main bases whose intermolecular hydrogen bonding holds the DNA strands together are adenine, guanine, thymine and cytosine. There are generally three forms of DNA: The A, B and Z-form. Native DNA, however, exists in B-form.
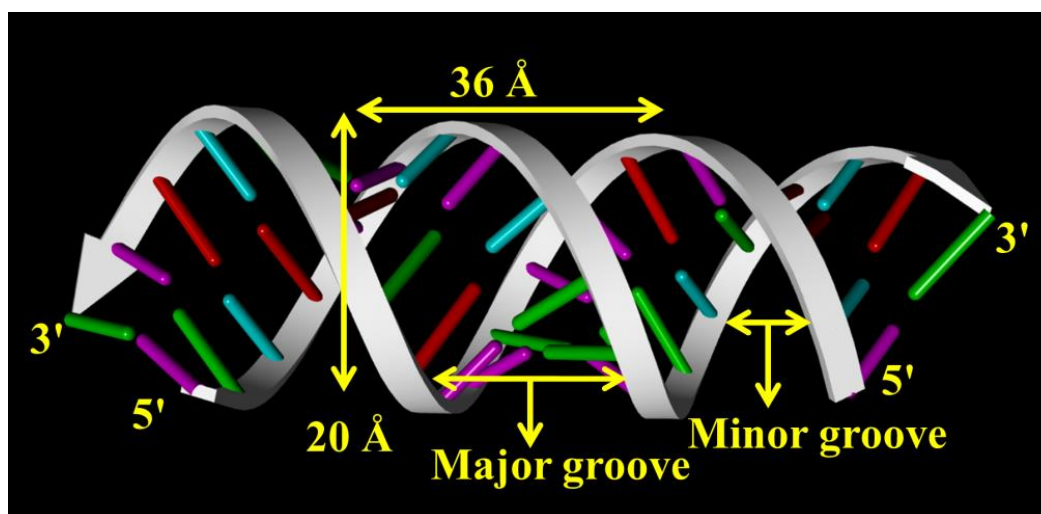
Figure 2.6. *Schematic representation of deoxyribonucleic acid (DNA).*

Native DNA is about a metre long and comprises of hundreds of base pairs. The distance between two base pairs in B-DNA is 3.4 Å [57]. In about 4 M NaCl, B-form is converted into Z-form. DNA structures consist of major and minor grooves and

intercalation spaces through which DNA interacts with ligands. There are two modes of interaction of DNA with ligands: (i) intercalation, where the planar polycyclic heteroaromatic ligands occupy the space in between the base pairs of DNA (Figure 2.6) and interact through π-π interaction [58, 59] and (ii) groove binding where the ligands bind in the major and minor grooves of DNA [60]. The water molecules at the surface of DNA are critical to the structure and to the recognition by other molecules, proteins and drugs. In one of our study, a synthetic DNA oligomer having sequence CTTTTGCAAAAG was used.

References

1. T. Förster; Intramolecular energy migration and fluorescence. *Ann. Phys.* 2 (1948), 55.

2. L. Stryer; Fluorescence energy transfer as a spectroscopic ruler. *Annu. Rev. Biochem.* 47 (1978), 819.

3. J. R. Lakowicz; Principles of fluorescence spectroscopy. Edn. 3rd, *Springer, New York,* (2006).

4. P. Majumder, R. Sarkar, A. K. Shaw, A. Chakraborty and S. K. Pal; Ultrafast dynamics in a nanocage of enzymes: Solvation and fluorescence resonance energy transfer in reverse micelles. *J. Colloid Interface Sci.* 290 (2005), 462.

5. M. Montalti, N. Zaccheroni, L. Prodi, N. O'Reilly and S. L. James; Enhanced sensitized nir luminescence from gold nanoparticles via energy transfer from surface-bound fluorophores. *J. Am. Chem. Soc.* 129 (2007), 2418.

6. B. N. J. Persson and N. D. Lang; Electron-hole pair quenching of excited states near a metal. *Phys. Rev. B* 26 (1982), 5409.

7. J. Gersten and A. Nitzan; Spectroscopic properties of molecules interacting with small dielectric particles *J. Chem. Phys.* 75 (1981), 1139.

8. D. Craig and T. Thirunamachandran; Molecular quantum electrodynamics. *Academic Press, London,* (1984).

9. T. L. Jennings, M. P. Singh and G. F. Strouse; Fluorescent lifetime quenching near d = 1.5 nm gold nanoparticles: Probing NSET validity. *J. Am. Chem. Soc.* 128 (2006), 5462.

10. M. A. H. Muhammed, A. K. Shaw, S. K. Pal and T. Pradeep; Quantum clusters of gold exhibiting fret. *J. Phys. Chem. C* 112 (2008), 14324.

11. A. Makhal, S. Sarkar, S. K. Pal, H. Yan, D. Wulferding, F. Cetin and P. Lemmens; Ultrafast excited state deactivation of doped porous anodic alumina membranes. *Nanotechnology* 23 (2012), 305705.

12. A. Leung, P. M. Shankar and R. Mutharasan; A review of fiber-optic biosensors. *Sens. Actuators B: Chem.* 125 (2007), 688.

13. D. J. Griffiths; Introduction to electrodynamics. *Prentice Hall,* (1999).

14. J. D. Jackson; Classical electrodynamics. *Wiley,* (1975).

15. C. Burda, X. Chen, R. Narayanan and M. A. El-Sayed; Chemistry and properties of nanocrystals of different shapes. *Chem. Rev.* 105 (2005), 1025.

16. P. K. Jain, K. S. Lee, I. H. El-Sayed and M. A. El-Sayed; Calculated absorption and scattering properties of gold nanoparticles of different size, shape and composition: Applications in biological imaging and biomedicine. *J. Phys. Chem. B* 110 (2006), 7238.

17. S. Link and M. A. El-Sayed; Shape and size dependence of radiative, non-radiative and photothermal properties of gold nanocrystals. *Int. Rev. Phys. Chem.* 19 (2000), 409.

18. G. Mie; Beiträge zur optik trüber medien, speziell kolloidaler metallösungen. *Ann. Phys.* 330 (1908), 377.

19. J. A. Creighton and D. G. Eadon; Ultraviolet–visible absorption spectra of the colloidal metallic elements. *J. Chem. Soc.-Faraday Trans.* 87 (1991), 3881.

20. U. Kreibig and M. Vollmer; Optical properties of metal clusters. *Springer, Berlin,* (1995).

21. N. W. Ashcroft and N. D. Mermin; Solid state physics. *HOLT, Rinehart and Winston, New York,* (1976).

22. U. Kreibig and L. Genzel; Optical absorption of small metallic particles. *Surf. Sci.* 156 (1985), 678.

23. J. P. Wilcoxon, J. E. Martin and P. Provencio; Optical properties of gold and silver nanoclusters investigated by liquid chromatography. *J. Chem. Phys.* 115 (2001), 998.

24. R. Kubo; Electronic properties of metallic fine particles. *J. Phys. Soc. Jpn* 17 (1962), 975.

25. T. G. Schaaff, G. Knight, M. N. Shafigullin, R. F. Borkman and R. L. Whetten; Isolation and selected properties of a 10.4 kDa gold: Glutathione cluster compound. *J. Phys. Chem. B* 102 (1998), 10643.

26. W. T. Wallace and R. L. Whetten; Coadsorption of CO and O_2 on selected gold clusters: Evidence for efficient room-temperature CO_2 generation. *J. Am. Chem. Soc.* 124 (2002), 7499.

27. C. T. Campbell, S. C. Parker and D. E. Starr; The effect of size-dependent nanoparticle energetics on catalyst sintering. *Science* 298 (2002), 811.

28. L. A. Peyser, T. H. Lee and R. M. Dickson; Mechanism of Ag_n nanocluster photoproduction from silver oxide films. *J. Phys. Chem. B* 106 (2002), 7725.

29. J. Zheng, C. Zhang and R. M. Dickson; Highly fluorescent, water-soluble, size-tunable gold quantum dots. *Phys. Rev. Lett.* 93 (2004), 077402.

30. A. P. Alivisatos; Perspectives on the physical chemistry of semiconductor nanocrystals. *J. Phys. Chem.* 100 (1996), 13226.

31. Q.-L. Zhao, Z.-L. Zhang, B.-H. Huang, J. Peng, M. Zhang and D.-W. Pang; Facile preparation of low cytotoxicity fluorescent carbon nanocrystals by electrooxidation of graphite. *Chem. Commun.* 41 (2008), 5116.

32. K. Wang, Z. Gao, G. Gao, Y. Wo, Y. Wang, G. Shen and D. Cui; Systematic safety evaluation on photoluminescent carbon dots. *Nanoscale Res. Lett.* 8 (2013), 122.

33. S. Zhu, Q. Meng, L. Wang, J. Zhang, Y. Song, H. Jin, K. Zhang, H. Sun, H. Wang and B. Yang; Highly photoluminescent carbon dots for multicolor patterning, sensors and bioimaging. *Angew. Chem.* 125 (2013), 4045.

34. G. Leménager, E. De Luca, Y.-P. Sun and P. P. Pompa; Super-resolution fluorescence imaging of biocompatible carbon dots. *Nanoscale* 6 (2014), 8617.

35. M. Zhou, Z. Zhou, A. Gong, Y. Zhang and Q. Li; Synthesis of highly photoluminescent carbon dots via citric acid and Tris for iron (III) ions sensors and bioimaging. *Talanta* 143 (2015), 107.

36. T.-Y. Wang, C.-Y. Chen, C.-M. Wang, Y. Z. Tan and W.-S. Liao; Multicolor functional carbon dots via one-step refluxing synthesis. *ACS Sens.* 2 (2017), 354.

37. T. Sun, Y. S. Zhang, B. Pang, D. C. Hyun, M. Yang and Y. Xia; Engineered nanoparticles for drug delivery in cancer therapy. *Angew. Chem., Int. Ed.* 53 (2014), 12320.

38. L. Cao, S. Sahu, P. Anilkumar, C. E. Bunker, J. Xu, K. S. Fernando, P. Wang, E. A. Guliants, K. N. Tackett and Y.-P. Sun; Carbon nanoparticles as visible-light photocatalysts for efficient CO_2 conversion and beyond. *J. Am. Chem. Soc.* 133 (2011), 4754.

39. P. J. S. Rana, P. Singh and P. Kar; Carbon nanoparticles for ferric ion detection and novel HFCNs–Fe^{3+} composite for NH_3 and F^- estimation based on a "turn on" mechanism. *J. Mater. Chem. B* 4 (2016), 5929.

40. S. Bhattacharya, R. Sarkar, B. Chakraborty, A. Porgador and R. Jelinek; Nitric oxide sensing through azo-dye formation on carbon dots. *ACS Sens.* 2 (2017), 1215.

41. S.-T. Yang, X. Wang, H. Wang, F. Lu, P. G. Luo, L. Cao, M. J. Meziani, J.-H. Liu, Y. Liu and M. Chen; Carbon dots as nontoxic and high-performance fluorescence imaging agents. *J. Phys. Chem. C* 113 (2009), 18110.

42. W. Yang, H. Zhang, J. Lai, X. Peng, Y. Hu, W. Gu and L. Ye; Carbon dots with red-shifted photoluminescence by fluorine doping for optical bio-imaging. *Carbon* 128 (2018), 78.

43. Z. Qian, J. Ma, X. Shan, H. Feng, L. Shao and J. Chen; Highly luminescent N‐doped carbon quantum dots as an effective multifunctional fluorescence sensing platform. *Chem. Eur. J.* 20 (2014), 2254.

44. J. Shen, Y. Zhu, X. Yang and C. Li; Graphene quantum dots: Emergent nanolights for bioimaging, sensors, catalysis and photovoltaic devices. *Chem. Commun.* 48 (2012), 3686.

45. M. J. Bruchez, M. Moronne, P. Gin, S. Weiss and A. P. Alivisatos; Semiconductor nanocrystals as fluorescent biological labels. *Science* 281 (1998), 2013.

46. S. Muppalaneni and H. Omidian; Polyvinyl alcohol in medicine and pharmacy: A perspective. *J. Dev. Drugs* 2 (2013), 112.

47. J. Kundu, L. A. Poole-Warren, P. Martens and S. C. Kundu; Silk fibroin/poly (vinyl alcohol) photocrosslinked hydrogels for delivery of macromolecular drugs. *Acta Biomater.* 8 (2012), 1720.

48. P. K. Sarkar, N. Polley, S. Chakrabarti, P. Lemmens and S. K. Pal; Nanosurface energy transfer based highly selective and ultrasensitive "turn on" fluorescence mercury sensor. *ACS Sens.* 1 (2016), 789.

49. P. K. Sarkar, A. Halder, N. Polley and S. K. Pal; Development of highly selective and efficient prototype sensor for potential application in environmental mercury pollution monitoring. *Water, Air and Soil Pollut.* 228 (2017), 314.

50. M. Karlsson, T. Kurz, U. T. Brunk, S. E. Nilsson and C. I. Frennesson; What does the commonly used DCF test for oxidative stress really show? *Biochem. J.* 428 (2010), 183.

51. J. M. Burns, W. J. Cooper, J. L. Ferry, D. W. King, B. P. DiMento, K. McNeill, C. J. Miller, W. L. Miller, B. M. Peake, S. A. Rusak, A. L. Rose and T. D. Waite; Methods for reactive oxygen species (ROS) detection in aqueous environments. *Aquat. Sci.* 74 (2012), 683.

52. D. Sadava, D. M. Hillis, H. C. Heller and M. R. Berenbaum; Life: The science of biology. Edn. 10th, *Sinauer Associates Inc. and W.H. Freeman and Company, USA,* (2008).

53. E. J. Neer, W. Konigsberg and G. Guidotti; The interactions between α and β chains of human hemoglobin. *J. Biol. Chem.* 243 (1968), 1971.

54. M. F. Perutz; Mechanisms regulating the reactions of human hemoglobin with oxygen and carbon monoxide. *Annu. Rev. Physiol.* 52 (1990), 1.

55. A. D. Hershey and M. Chase; Independent functionas of viral protein and nucleic acid in growth of bacteriophage. *J. Gen. Physiol.* 36 (1952), 39.

56. J. D. Watson and F. H. C. Crick; Molecular structure of nucleic ccids: A structure for deoxyribose nucleic acid. *Nature* 171 (1953), 737.

57. D. L. Nelson and M. M. Cox; Lehninger principles of biochemistry. Edn. 3rd *Worth, New York,* (2000).

58. L. S. Lerman; The structure of the DNA-acridine complex. *Proc. Natl. Acad. Sci.* 49 (1963), 94.

59. M. B. Lyles and I. L. Cameron; Interactions of the DNA intercalator acridine orange, with itself, with caffeine and with double stranded DNA. *Biophys. Chem.* 96 (2002), 53.

60. P. B. Dervan; Molecular recognition of DNA by small molecules. *Bioorg. Med. Chem.* 9 (2001), 2215.

Chapter 3

Instrumentation and Sample Preparation

In this chapter we will describe the details of instrumental setup for the spectroscopic investigation of biomedically and environmentally relevant samples and corresponding preparation techniques used in our studies.

3.1. Instrumental Setup

3.1.1. Steady-state Absorption and Fluorescence Spectroscopy: Steady-state UV-Vis absorption and emission spectra of the probe molecules were measured with Shimadzu UV-2450 spectrophotometer and JobinYvon Fluorolog fluorometer, respectively. Schematic ray diagrams of these two instruments are shown in Figures 3.1 and 3.2.
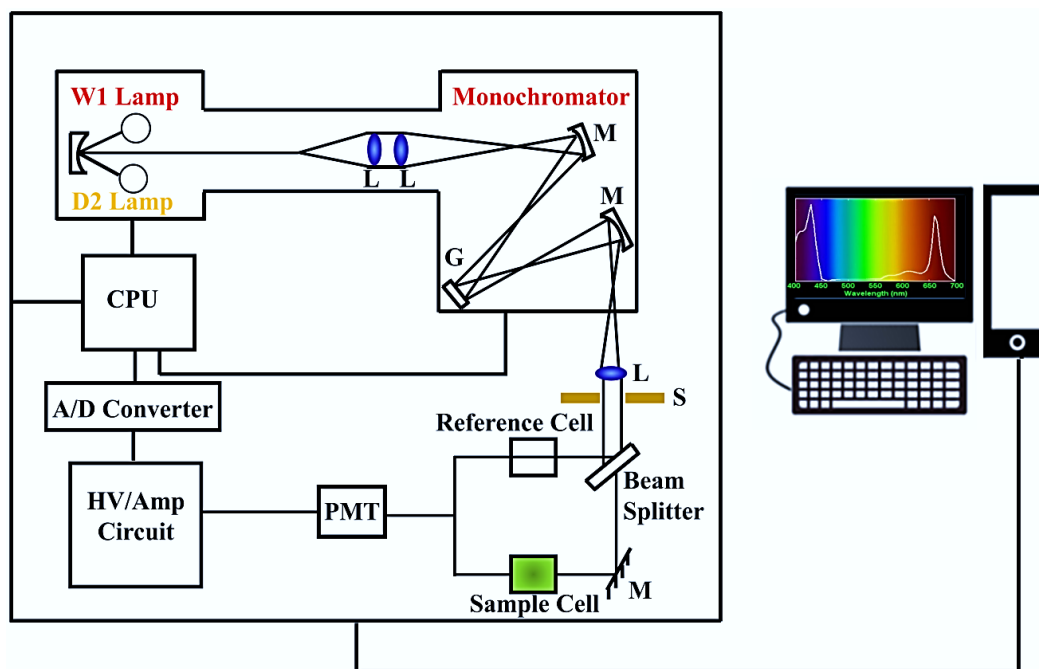
Figure 3.1. *Schematic ray diagram of an absorption spectrophotometer. Tungsten halogen (W1) and deuterium lamps (D2) are used as light sources in the visible and UV regions, respectively. M, G, L, S, PMT designate mirror, grating, lens, shutter and photomultiplier tube, respectively. CPU, A/D converter and HV/amp indicate central processing unit, analog to digital converter and high-voltage/amplifier circuit, respectively.*
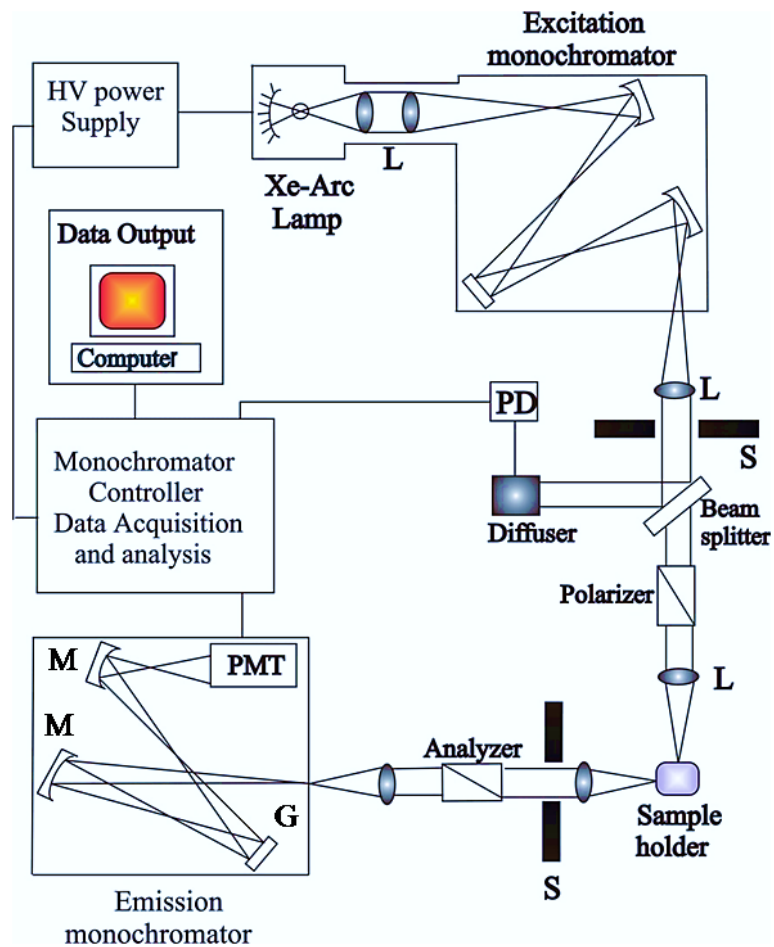
Figure 3.2. *Schematic ray diagram of an emission spectrofluorimeter. M, G, L, S, PMT and PD represent mirror, grating lens, shutter, photomultiplier tube and reference photodiode, respectively.*
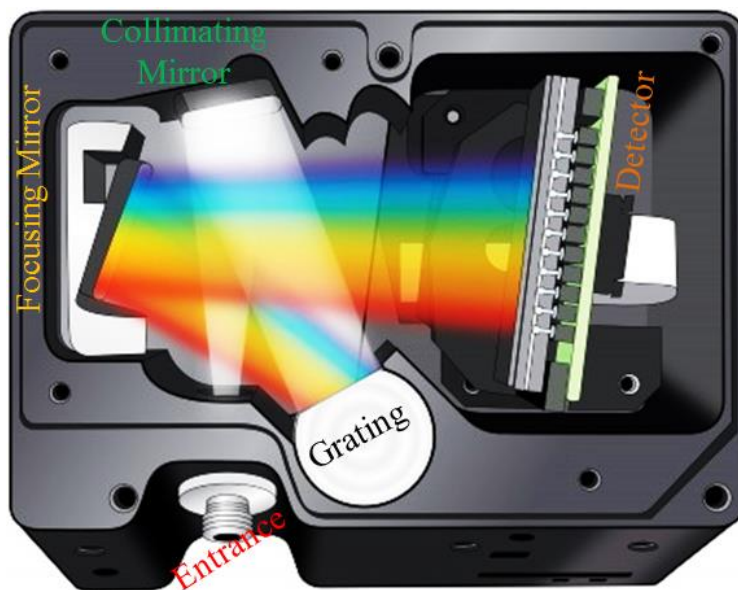
Figure 3.3. *Basic internal ray diagram of CCD array detector based STS-VIS.*

For the studies on development of a noncontact device for monitoring hemoglobin level in human subjects [1] we have used STS-VIS spectrograph from ocean optics. The basic ray diagram of the devices is represented in the Figure 3.3.

3.1.2. Fourier Transform Infrared (FTIR) Measurement: FTIR spectroscopy is a technique that can provide very useful information about functional groups in a sample. An infrared spectrum represents the fingerprint of a sample with absorption peaks which correspond to the frequencies of vibrations between the bonds of the atoms making up the material. Because each different material is a unique combination of atoms, no two compounds produce the exact same infrared spectrum. Therefore, infrared spectroscopy can result in a positive identification (qualitative analysis) of every different kind of material. In addition, the size of the peaks in the spectrum is a direct indication of the amount of material present. The two-beam Michelson interferometer is the heart of FTIR spectrometer. It consists of a fixed mirror (M4), a moving mirror (M5) and a beam-splitter (BS1), as illustrated in Figure 3.4. The beam-splitter is a laminate material that reflects and transmits light equally. The collimated IR beam from the source is partially transmitted to the moving mirror and partially reflected to the fixed mirror by the beam-splitter. The two IR beams are then reflected back to the beam-splitter by the mirrors. The detector then sees the transmitted beam from the fixed mirror and reflected beam from the moving mirror, simultaneously. The two combined beams interfere constructively or destructively depending on the wavelength of the light (or frequency in wavenumbers) and the optical path difference introduced by the moving mirror. The resulting signal is called an interferogram which has the unique property that every data point (a function of the moving mirror position) which makes up the signal has information about every infrared frequency which comes from the source. Because the analyst requires a frequency spectrum (a plot of the intensity at each individual frequency) in order to make identification, the measured interferogram signal cannot be interpreted directly. A means of "decoding" the individual frequencies is required. This can be accomplished via a well-known mathematical technique called the Fourier transformation. This transformation is

performed by the computer which then presents the user with the desired spectral information for analysis. FTIR measurements were performed on a JASCO FTIR-6300 spectrometer (transmission mode). For the FTIR measurements, samples were mixed with KBr powder and pelletized. The background correction was made using a reference blank of KBr pellet. In situ-FTIR study was carried out using a FTIR spectrometer (Bruker Vertex 70v) which is connected to a potentiostatgalvanostat (PGSTAT30, AUTOLAB).
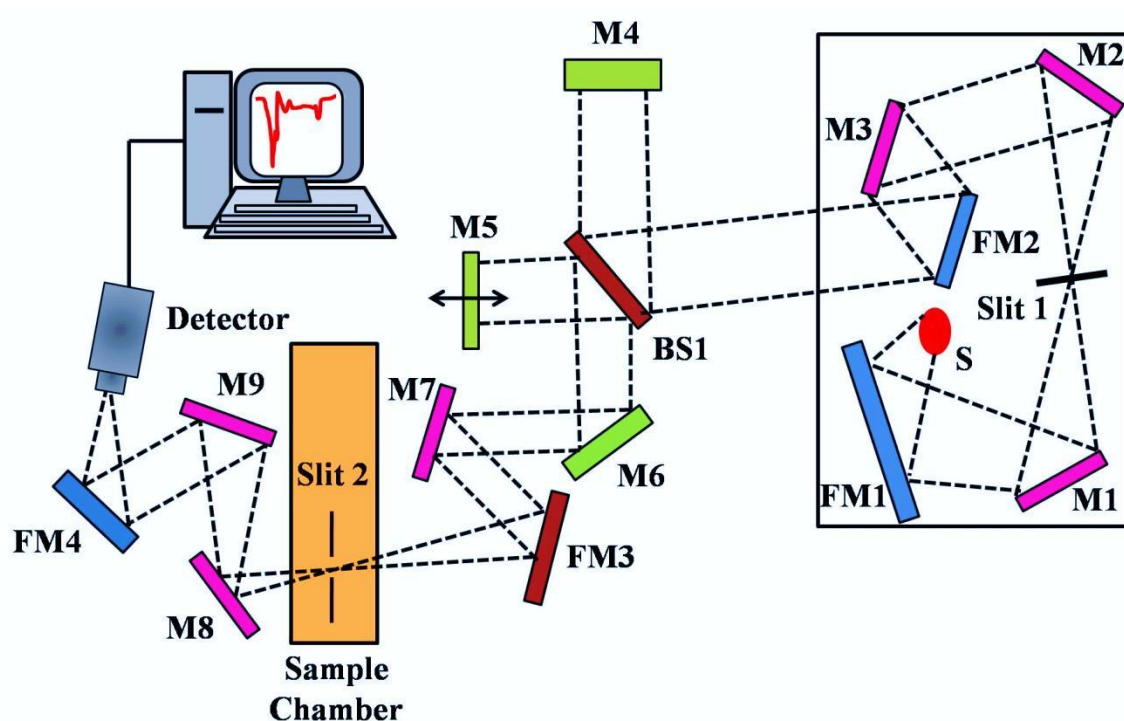
Figure 3.4. *Schematic of Fourier transform infrared (FTIR) spectrometer. It is basically a Michelson interferometer in which one of the two fully-reflecting mirrors is movable, allowing a variable delay (in the travel-time of the light) to be included in one of the beams. M, FM and BS1 represent the mirror, focusing mirror and beam splitter, respectively. M5 is a moving mirror.*

3.1.3. Dynamic Light Scattering (DLS): DLS also known as photon correlation spectroscopy (PCS) or quasi-elastic light scattering (QELS) is one of the most popular techniques used to determine the hydrodynamic size of the particle. DLS measurements were performed on a Nano S Malvern instrument, (U.K.) employing a 4 mW He-Ne laser (λ=632.8 nm) and equipped with a thermostatted sample chamber. The instrument allows DLS measurements in which all the scattered photons are

collected at 173⁰ scattering angle (Figure 3.5). The instrument measures the time dependent fluctuation in intensity of light scattered from the particles in solution at a fixed scattering angle [2]. The scattering intensity data were processed using the instrumental software to obtain the hydrodynamic diameter and the size distribution of the scatterer in each sample. In a typical size distribution graph from the DLS measurement, X-axis shows a distribution of size classes in nm, while the Y-axis shows the relative intensity of the scattered light. The ray diagram of the DLS setup is shown in Figure 3.5.
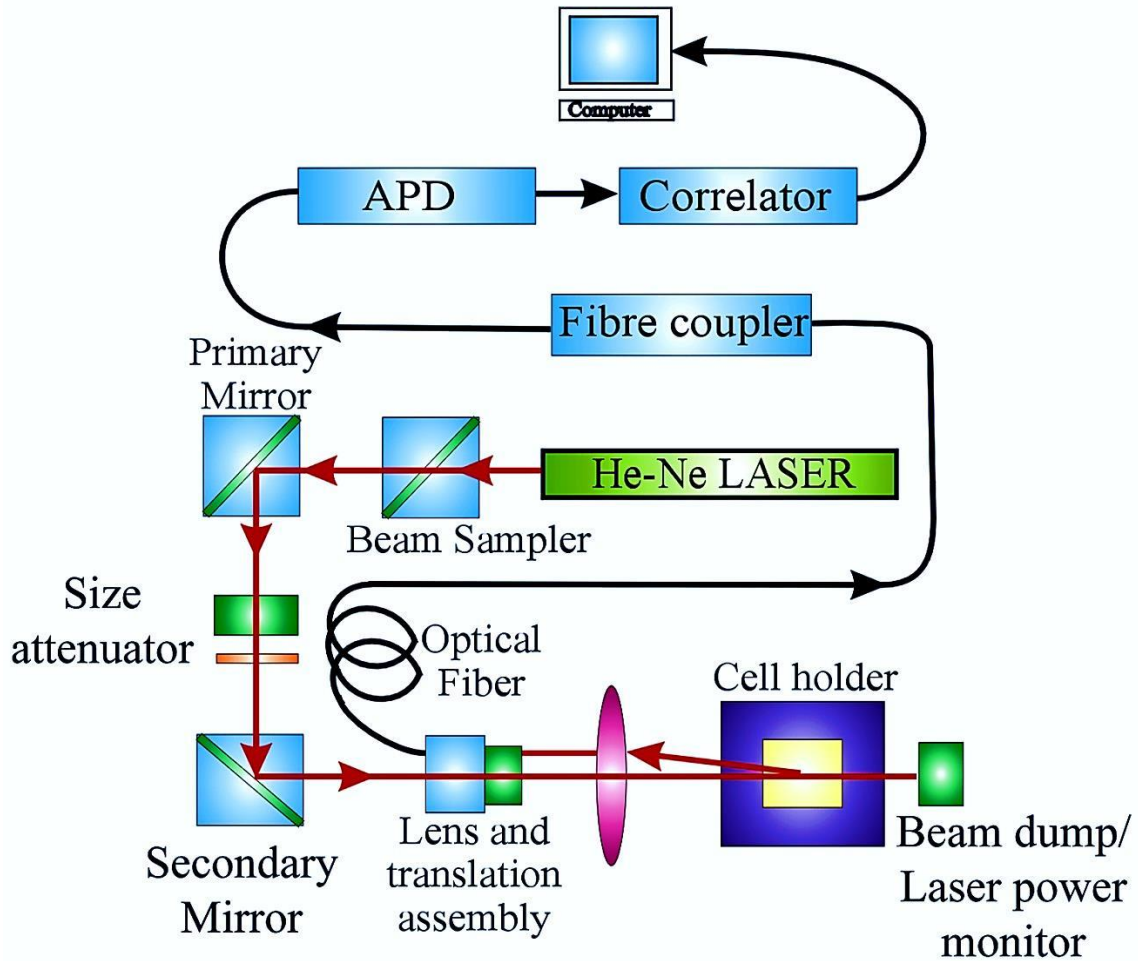
Figure 3.5. *Schematic ray diagram of dynamic Light Scattering (DLS) instrument. The avalanche photo diode (APD) is connected to preamplifier/amplifier assembly and finally to correlator. It has to be noted that lens and translational assembly, laser power monitor, size attenuator, laser are controlled by the computer.*

3.1.4. Time Correlated Single Photon Counting (TCSPC): All the picosecond-resolved fluorescence transients were recorded using TCSPC technique. The schematic block diagram of a TCSPC system is shown in Figure 3.6. Primarily, TCSPC setup from Edinburgh instruments, U.K., was used during fluorescence decay acquisitions. The instrument response functions (IRFs) of the laser sources at different excitation wavelengths varied between 70 ps to 80 ps. The fluorescence from the sample was
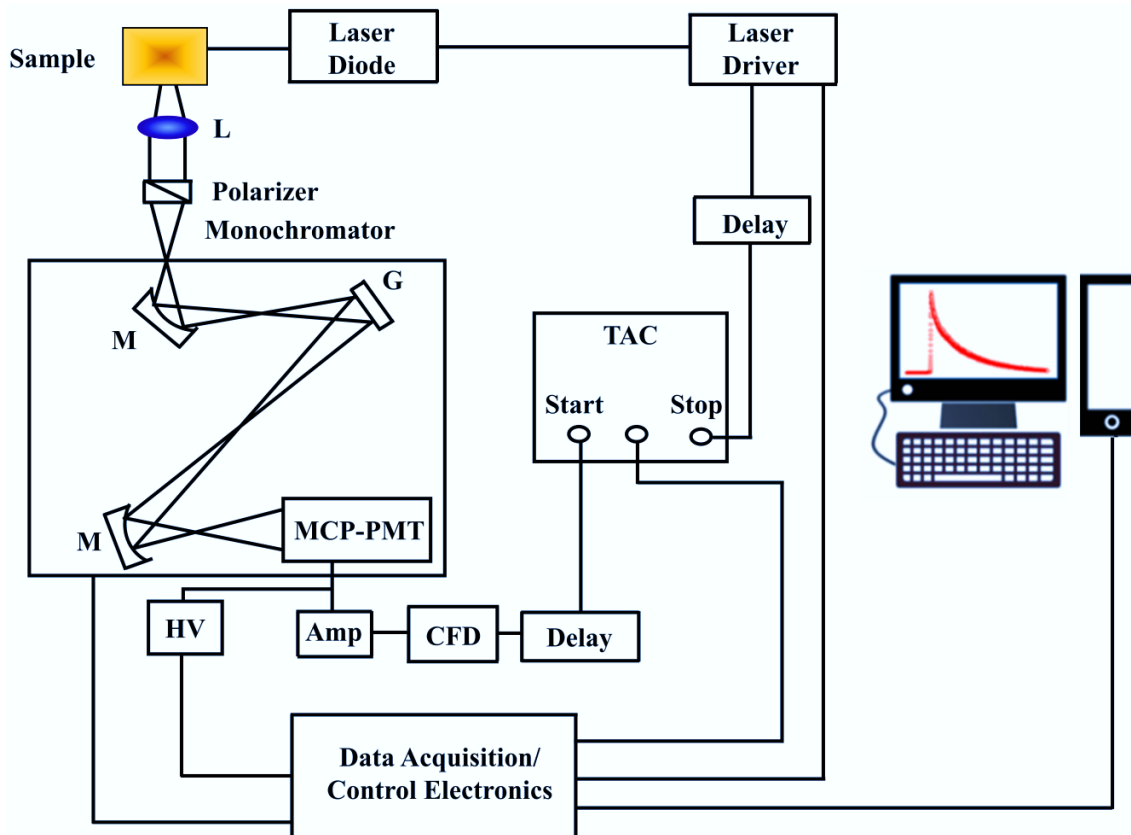
Figure 3.6. *Schematic ray diagram of a time correlated single photon counting (TCSPC) spectrophotometer. A signal from 16 channel photomultiplier tube (PMT) is amplified (Amp) and connected to start channel of time to amplitude converter (TAC) via constant fraction discriminator (CFD) and delay. The stop channel of the TAC is connected to the laser driver via a delay line. L, M, G and HV represent lens, mirror, grating and high voltage source, respectively.*

detected by a photomultiplier after dispersion through a grating monochromator. For all transients, the polarizer in the emission side was adjusted to be at 54.7^0 (magic angle) with respect to the polarization axis of excitation beam. For tryptophan excitation of protein, femtosecond-coupled TCSPC setup were employed in which the sample was excited by the third harmonic laser beam (300 nm) of the 900 nm (0.5 nJ

per pulse) using a mode-locked Ti-sapphire laser with an 80 MHz repetition rate (Tsunami, spectra physics), pumped by a 10 W Millennia (Spectra physics) followed by a third harmonic generator (Spectra-physics, model 3980). The third harmonic beam was used for excitation of the sample inside the TCSPC instrument and the second harmonic beam was collected as for the start pulse.

3.1.5. Transmission Electron Microscope (TEM): An FEI Tecnai TF20 field-emission high-resolution transmission electron microscope (HRTEM) (Figure 3.7) equipped with an Energy Dispersive X-ray (EDAX) spectrometer was used to characterize the microscopic structures of samples and to analyze their elemental composition. The size of the nanoparticles was determined from the TEM images
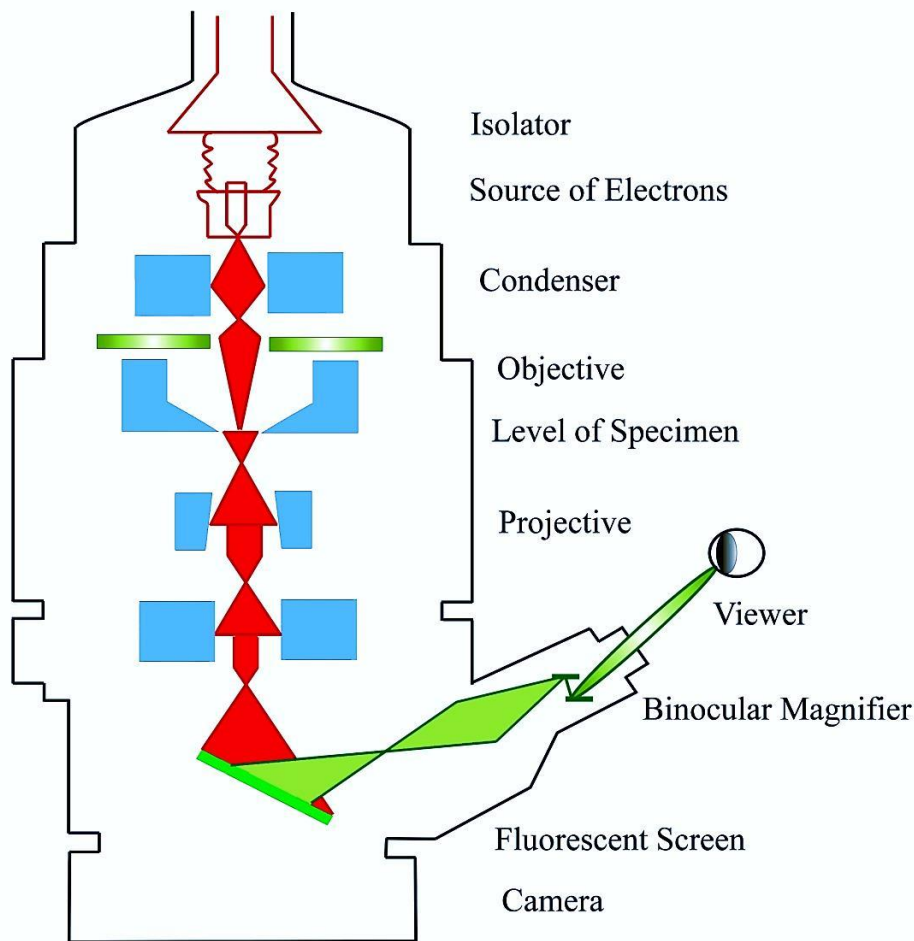
Figure 3.7. *Schematic diagram of a typical transmission electron microscope (TEM). After the transmission of electron beam through a specimen, the magnified image is formed either in the fluorescent screen or can be detected by a CCD camera.*

obtained at 200 kV. Samples for TEM were prepared by placing a drop of the colloidal solution on a carbon-coated copper grid and allowing the film to evaporate overnight at room temperature.

3.1.6. Scanning Electron Microscope (SEM): Surface characteristics of Porous silicon samples were done by scanning electron microscope FE-SEM; JEOL. Ltd., JSM-6500F. An electron-gun is attached to SEM and the electrons from filament triggered by 0 KV to 30 KV. These electrons go first through a condenser lens and then through an objective lens, then through an aperture and finally reach to the specimen. The high energy electrons go a bit in the sample and back again give secondary electrons. The signal from secondary electrons are detected by detector and amplified. The ray diagram of the SEM setup is shown in Figure 3.8.
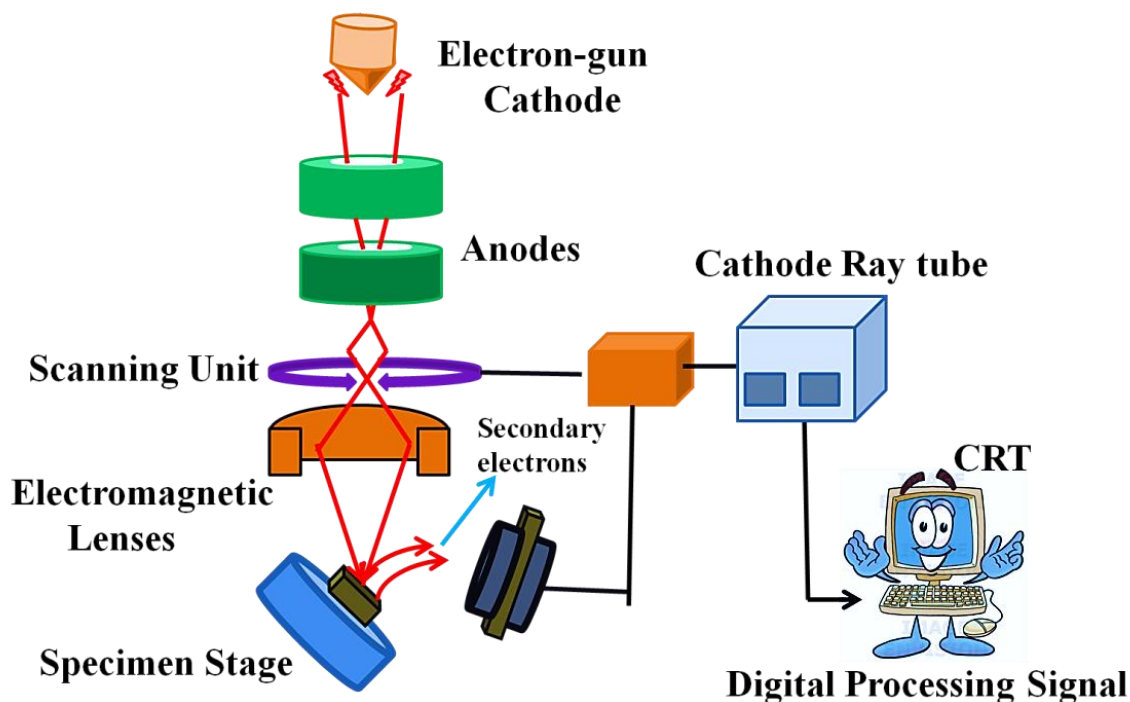
Figure 3.8. *Schematic diagram of typical scanning electron microscope (SEM).*

3.1.7. Fluorescence Microscope: A fluorescence microscope is much the same as a conventional light microscope with added features to enhance its capabilities. The conventional microscope uses visible light (400nm-700nm) to illuminate and produce a magnified image of a sample. A fluorescence microscope, on the other hand, uses a

much higher intensity light source which excites a fluorescent species in a sample of interest. This fluorescent species in turn emits a lower energy light of a longer wavelength that produces the magnified image instead of the original light source. In most cases the sample of interest is labelled with a fluorescent substance known as a fluorophore and then illuminated through the lens with the higher energy source. The illuminating light is absorbed by the fluorophores (now attached to the sample specimen) and causes them to emit a longer lower energy wavelength light. This fluorescent light can be separated from the surrounding radiation with filters designed
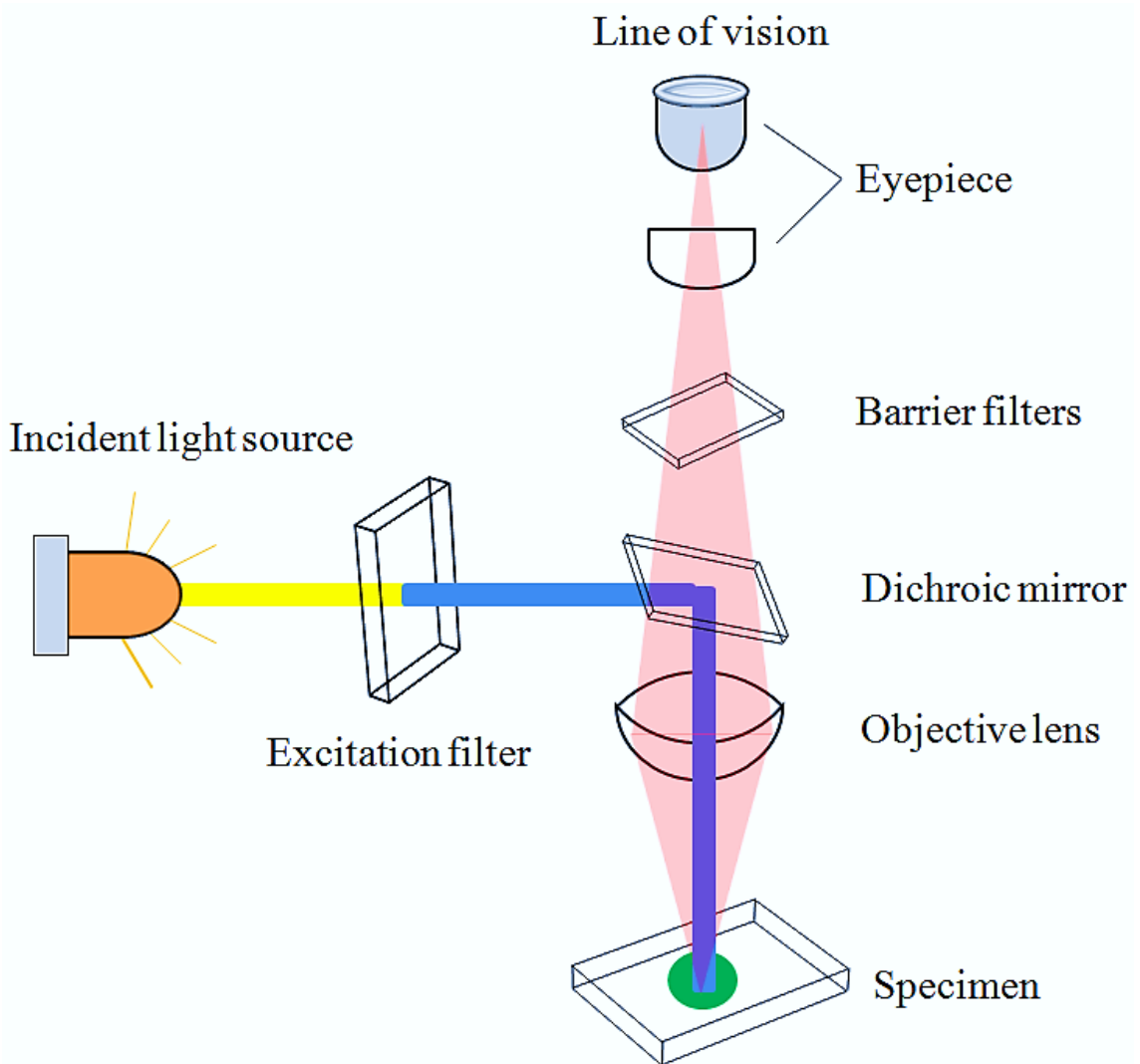
Figure 3.9. *Optical system of a fluorescence microscope.*

for that specific wavelength allowing the viewer to see only the fluorescence. The basic task of the fluorescence microscope is to let excitation light radiate the specimen and then sort out the much weaker emitted light from the image. First, the microscope has a filter that only lets through radiation with the specific wavelength that matches your fluorescing material. The radiation collides with the atoms of the sample specimen and electrons are excited to a higher energy level. When they relax to a lower level, they emit light. Fluorescence from the sample is separated from the excitation light by a second filter (Figure 3.9) to make it detectable (visible to the human eye). Most of the fluorescence microscopes used in biology today are epi-fluorescence microscopes, meaning that both the excitation and the observation of the fluorescence occur above the sample. Most use a Xenon or Mercury arc-discharge lamp for more intense light.

3.1.8. Hydrothermal Technique: The hydrothermal technique was the most popular one, gathering interest from scientists and technologists of different disciplines, for the synthesis of different nanomaterials. Hydrothermal reaction was defined for any heterogenous chemical reaction in the presence of a solvent (whether aqueous or non-aqueous) above room temperature and at pressure greater than 1 atm in a closed system. Crystal growth under hydrothermal conditions requires a reaction vessel called an autoclave. The autoclave must be capable of sustaining highly corrosive salt, which are used to synthesis inorganic materials at high temperature and pressure for a longer duration of time. For selecting a suitable autoclave, the first and foremost parameter is the experimental temperature, pressure conditions and the corrosion resistance in that pressure-temperature range in a given solvent or hydrothermal fluid. To avoid corrosion of autoclave material it should coated with non-reactive material called Teflon from inside. Due to the larger coefficient of thermal expansion of Teflon versus metal, the Teflon will expand and contract much more upon heating and cooling cycles than its enclosure material. For the synthesis of nanomaterials, we have used teflon-lined stainless steel autoclave of 30 mL capacity (Figure 3.10). The autoclave was tested at desired temperature under autogenous pressure for the desired period of time.
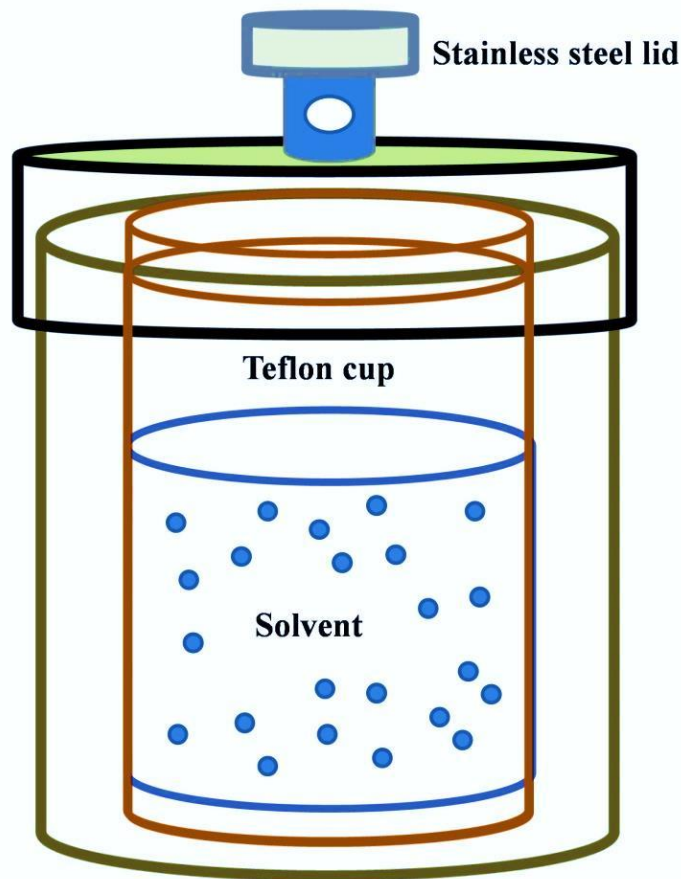
Figure 3.10. *Schematic representation of teflon-lined stainless steel autoclave.*

3.1.9. Experimental Setup for Sensing Studies: In the following section, we have elaborated the experimental setup used in optical fiber based spectroscopic detection techniques. In our study "DNA-based fiber optic sensor for direct *in-vivo* measurement of oxidative stress" [2] we used a commercially available FluoroLog system with a minute modification of the sample chamber. For the fluorescence-based study an 'F-3000 Fiber Optic Mount' was attached externally to the FluoroLog for transmitting the excitation from the fluorometer and to collect the fluorescence from the tip of the sensitized fiber, which was connected through a SMA connector on the end of the Fiber Optic Mount. Through one end of the Fiber Optic Mount, the excitation wavelength introduced into the sensitized fiber to excite the samples of interest. The fluorescence of the samples of interest was collected from another end of the Fiber Optic Mount, which was the signal measured by the fluorometer. All studies were carried out after continuous dipping of the functionalized fiber tip in the samples of

interest. The detailed experimental setup using F-3000 Fiber Optic Mount is shown schematically in Figure 3.11b.

3.1.10. Light Sources and Optical Components: Light emitting diode (LED) light sources ware used in fiber optic based detection systems. For the studies on development and validation of a noncontact spectroscopic device for hemoglobin estimation at point-of-care [1], a white LED source [LS-450, with the preinstalled blue LED replaced with a white LED (196-00000-WHT)] with wavelength range 430–700 nm (Ocean Optics, FL, USA) was used in our study. All the optical parts used in our studies including optical fiber, collimator, fiber couplers etc. are from Ocean Optics. Whereas, the basic components like front surface reflecting mirrors, dichroic mirrors, parabolic mirrors, multimode silica core fiber (FT1000UMT) and optical stands are from Thorlabs.

3.2. Sample Preparation

In this section the different sample preparation and data collection methods have been discussed.

3.2.1. Chemicals Used: The chemicals and spectroscopic probes were procured from the following sources. Analytical-grade chemicals were used for synthesis without further purification. All the aqueous solutions were prepared using deionized water from Millipore system. Sodium azide (NaN_3), calf thymus DNA, CTAB (cetyltrimethyl ammonium bromide; lipid), silicon oil, trisodium citrate ($Na_3C_6H_5O_7$), hemoglobin human, copper sulfate pentahydrate ($CuSO_4 \cdot 5H_2O$), hydro fluoric acid (HF), silver nitrate ($AgNO_3$ - 99.99 %), sodium citrate, sodium borohydride, sodium hydroxide, 4-nitrophenylanthranilate (NPA), poly(vinyl alcohol) (MW- 89000-98000) (PVA), polyvinylpyrrolidone (MW- 10,000) (PVP) as well as the nitrates and chlorides salts of various metal ions were purchased from Sigma-Aldrich (USA). Ethanol, hydrogen peroxide (H_2O_2; 30%), Acetonitrile and sulfuric acid (H_2SO_4) were obtained from Merck (USA). 2,7-dichlorodihydrofluorescein diacetate (DCFH-DA) was obtained

from Calbiochem. All the different anions used in our study, NaCl, AsI, KBr, NaNO$_3$, Na$_2$SO$_4$, NaCOOCH$_3$, Na$_3$PO$_4$, Na$_2$HPO$_4$, Na$_2$H$_2$PO$_4$, NaHCO$_3$ and NaNO$_2$ were purchased from Sigma-Aldrich (USA). Groundwater (from S. N. Bose National Centre for Basic Sciences, Kolkata, India) was used as a real water samples. All the kits for measurement of serum biochemical parameters were purchased from Autospan Liquid Gold, Span Diagnostics Ltd. (IND). All hematological tests were performed spectrophotometrically following the protocols described by the corresponding manufacturers.

3.2.2. Synthesis of Citrate Functionalized-Mn$_3$O$_4$ Nanoparticles: Synthesis of bulk Mn$_3$O$_4$ nanoparticles (NPs) was carried out following a reported ultrasonic-assisted approach for preparation of colloidal Mn$_3$O$_4$ NPs at room temperature and pressure without any additional surfactants or templates [3]. We followed earlier reports [4-6] for surface functionalization of the bulk NPs with citrate ligand. In brief, as prepared bulk Mn$_3$O$_4$ NPs were added to 0.5 M aqueous ligand (citrate) solution of pH 7.0 (∼20 mg Mn$_3$O$_4$ NPs/mL ligand solution) and were extensively mixed for 12 hours in a cyclomixer. A syringe filter of 0.22 μm pore diameter was used to eliminate the non-functionalized bigger-sized NPs. The resulting filtrated solution was used for all successive experiments without further dilution. The final concentration of the as prepared functionalized NPs was estimated to be 250 μM [7]. Our earlier studies showed the average particle size distribution of the prepared citrate functionalized NPs to be around 3.6 nm ± 0.15 nm [4, 5, 7].

3.2.3. Preparation of DNA-based Biomaterial: The DNA-based biomaterial (DNA-DCFH-CTAB) was prepared with minute modification of the procedure reported earlier [8]. For preparation of biomaterial, firstly DCFH was prepared from the DCFH-DA by mixing 0.5 mL of 1.0 mM DCFH-DA in methanol with 2.0 mL of 10 mM NaOH at room temperature for 30 minutes, then the mixture was neutralized with 10 mL of 25 mM NaH$_2$PO$_4$ [9]. After that, the DNA stock was prepared by dissolving the fiber-like NaDNA in 50mM phosphate buffer (6.5g/mL) and incubated

overnight at room temperature in stirring condition. For the preparation of the DNA-DCFH-CTAB complex, the as-prepared 2 mL DCFH was added to a 10 mL volumetric flask containing 3 mL of stock DNA solution and 5 mL Mili-Q water. The
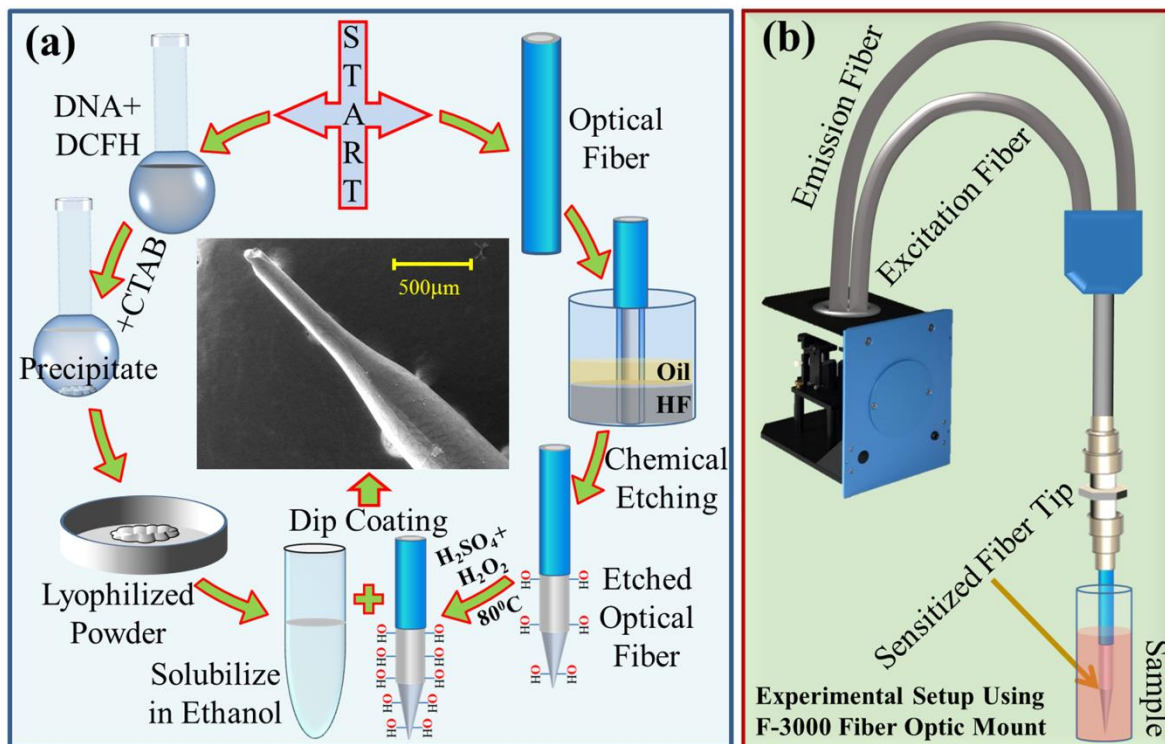
Figure 3.11. *(a) Schematic representation of the DNA-Biomaterial preparation, Optical fiber etching and fiber tip sensitization. Inset shows the SEM image of sensitized fiber tip. (b) Experimental setup using F-3000 Fiber Optic Mount.*

DNA, DCFH mixture was kept in dark for 60 minutes under stirring condition at room temperature for complete complexation reaction. Under continuous stirring condition 500 μL of 40 mM CTAB solution (in water) was added into the DNA-DCFH mixture. The DNA-DCFH-CTAB complex started to form spontaneously and accumulated around the stirring bid. The precipitate was collected by filtration, washed with Mili-Q water and then lyophilized overnight. The resultant biomaterial was dissolved in ethanol through vortexing for 30-60 minutes. The water insoluble DNA-DCFH-CTAB complex was formed due to the binding of CTAB cationic polar head to the negative phosphate sugar chain of the DNA strands. The prepared biomaterial was stored at -20 ^{0}C and used without further modifications. For dip coating an alcohol

solution of the biomaterial was prepared for further use. The preparation of DNA-based biomaterial is shown schematically in Figure 3.11a.

3.2.4. Fiber Tip Preparation and Sensitization with DNA-Biomaterial: The optical fibers of 10 cm length were taken for the sensitization with biomaterial. After removal of jacket (manual etching) from the tip (~ 1 cm), the fibers were dipped (the tip portion) into HF solution with a layer of silicone oil atop the solution and kept overnight [10, 11]. The chemical etching of the fibers led to a sharp needle like fiber tip as shown in Figure 3.11a. The etched fiber tip was then coated with the biomaterial by dipping into the biomaterial alcohol solution and dried in air for a minute (dip-coating). The overall fiber tip preparation and sensitization with the biomaterial is shown schematically in Figure 3.11a. Furthermore, the SEM image of the biomaterial coated fiber tip (sensor tip) confirmed the sharp needle like shape of the sensitized fiber tip (Figure 3.11a).

3.2.5. Mice Treatment Protocol: Swiss albino mice of both sexes (4–6 weeks old, weighing 23 ± 4 g) in good physical conditions were used for this study. Animals were kept in standard, clean polypropylene cages (temperature 22 ± 3° C; relative humidity 45–60%; 12 hours light/dark cycle). Water and standard laboratory pellet diet for mice (Hindustan Lever, Kolkata, India) were available *ad-libitum*. One week of acclimatization was provided to all of them before the experiment. All animals received human care according to the criteria outlined by the Committee for the Purpose of Control and Supervision of Experiments on Animals (CPCSEA), New Delhi, India, and the study was approved by the Institutional Animal Ethics Committee (approval number IAEC/RES/DEY'S – 12/S/2016 Under Animal Welfare Board, Ministry of Environment Forest and Climate Change, Govt. of India).

In total eight animals were randomized into two groups (n = 4 in each group). Group-1 served as sham control and was treated with olive oil (0.5 ml/kg body weight (BW)) in alternative days for a period of 4 weeks. For induction of oxidative stress, Group-2 received carbon tetrachloride solution (25% CCl_4 in olive oil) 1 ml/kg BW in

every alternative days for a period of 4 weeks. All inductions were carried out through intraperitoneal injection. At the end of the experiment, the animals were kept in fasting condition overnight and sacrificed by cervical dislocation. Blood samples were collected in sterile tubes (nonheparinized) from retro orbital plexus just before sacrifice and allowed to clot for 45 minutes. Serum was separated by centrifugation at 5000 rpm for 15 minutes. AST and total bilirubin were measured using commercially available test kits (Autospan Liquid Gold, Span Diagnostics Ltd., Gujarat, India) following the protocols described by the corresponding manufacturers. MDA content was determined following the protocol described elsewhere [6]. SOD and Catalase activity were measured using commercially available test kit (Sigma, USA) following the included protocol.

3.2.6. Direct *In-vivo* Oxidative Stress Measurement Procedure in Mice Model: For the purpose of this study, first the sensitized fiber tip was fixed in an anticoagulated capillary tube. Then for the comparative study, data were collected from both normal (control) as well as CCl$_4$ induced mice. General anaesthesia was used before performing direct ROS measurement in mice model. For the measurement, the mouse was restrained in such a manner that it cannot move, but was breathing well. Then the eyelid was gently pulled back from the globe and the capillary tube with sensitized fiber tip was gently inserted between the lid and the globe, pushing backward with even pressure, puncturing the conjunctiva and gaining access to the retro orbital plexus. The blood was then allowed to drip on the surface of sensor tip, inside the capillary tube, by capillary action.

3.2.7. Data Collection for Noninvasive Hemoglobin Measurement in Human Subject: The study included a total of 493 patients (including 276 males, 74 of whom were children) with a variety of age group ranging from 4 to 76 years (mean age $\pm$ standard deviation (SD) = 27 $\pm$ 13 years). All data were collected using our device in the blood collection room of the outpatient department of Nil Ratan Sircar Medical College and Hospital, Kolkata, following the standard ethical guideline approved by

the local medical ethics committee (No/NMC/443, Dated – 25/01/2016). A duly signed consent form was obtained from the patients or their legal guardians stating their acceptance, involvement and full understanding of the study. All ethical guidelines, including participant confidentiality and legitimacy, were followed.

The study was conducted in two stages. In the first stage, the device was calibrated, and in the second, the accuracy of the software-driven device was measured and compared with that of the gold standard (i.e., the standard biochemical method). Because the study was conducted over a period of 120 days, the dark and reference spectra were acquired each day before starting the data collection to avoid the potential effects of variation in ambient light. We also re-acquired both spectra in case of a change in the measurement location. Before acquisition of the dark and reference spectra, the light source was run for 5 minutes (according to manufacturer instructions, <1.0% variation after 2 minutes of warm up). After completing the instrumental setup and preliminary legal and ethical formalities, the patient was instructed to sit on a chair and look in the direction opposite to that of the probe without head and eye movement. Data were acquired from the vascular bed of the bulbar conjunctiva by placing the probe close to (∼1.5 cm away from) the patient's eye, approximately perpendicular to the surface of the conjunctiva. Because the exposure of light to the conjunctiva is low (∼5 sec), no intervention (manual holding) was needed for most of the subjects. For more accurate measurement we requested the subjects not to blink for a longer time (usually <10 sec), and they all succeed not to blink for that extended period. However, in some cases, we had to manually hold the eye open to avoid interference from eyelashes. As the total measurement time was very short (~15 sec), the light intensity was low (~20 μW); many times lower than that in an ophthalmoscope used during regular eye check-up), and the light was incident on the white portion of the eye (i.e., not on the eyeball), the subject neither sensed the light nor reported any irritation or discomfort. Furthermore, the noninvasive and noncontact nature of our method eliminated the need for disinfecting the measuring probe. Immediately after the acquisition of spectral data, blood samples were collected

from the subjects, and the complete blood count (CBC) was analyzed using an automated hematology analyzer (Sysmex KX-21). These data were later used for calibration and comparison.

3.2.7.1. Stage I: For Calibration: In this stage, the data of 302 (including 134 females and 48 children) participants were randomly selected for device calibration; the collected spectral response, as generated in the spectrograph and processed in the LabVIEW software, were stored in the tablet computer for further processing in terms of calibration.

3.2.7.2. Stage II: Assessment of the Device: In this stage, the clinical assessment output of the calibrated device was compared with that of a standard hematology analyzer by using a statistically significant number of samples (n = 191). To demonstrate the repeatability and reproducibility of the proposed device, 56 and 50 patients in this stage were repetitively examined using our device by the same observer and by two independent observers, respectively.

3.2.8. Synthesis of Silver Nanoparticles (Ag-NPs): Citrate capped Ag-NPs were prepared in aqueous solution (pH = 6.5) by reduction of $AgNO_3$ with $NaBH_4$ [12]. Briefly, first a 1 mM stock solution of sodium citrate, 5 mM stock solution of $NaBH_4$ and 5 mM stock solution of $AgNO_3$ were prepared in an aqueous medium. One millilitre aliquot of stock $AgNO_3$ solution was added to 16 mL of 1 mM aqueous sodium citrate solution under stirring condition in an ice bath at around 0 °C. Then, 150 μL of a freshly prepared 5 mM aqueous $NaBH_4$ solution was added dropwise over 5 minutes. The initially colourless solution gradually turned to intense yellow in colour and was stirred for 2 h and 30 minutes. The formation of Ag-NPs was confirmed by the SPR band at around 400 nm in aqueous media [12].

3.2.9. Preparation of PVA Capped NPA Solution: The PVA capped NPA solution was synthesized by mixing aqueous solution of PVA with acetonitrile solution of NPA at a weight ratio of PVA/NPA of 1200 : 1. The aqueous PVA solution was prepared

by dissolving 0.9g of PVA in 30 mL of water under stirring condition upon heating at temperature around 70 ^{0}C. The pH of the solution was adjusted to 7.5 by adding aqueous solution of NaOH. Then 4 mL of 1 mM acetonitrile solution of NPA was prepared at room temperature. A 3 mL aliquot of stock NPA solution was added in a 30 mL PVA aqueous solution at room temperature under stirring condition, in six aliquots with an interval of 30 minutes. The greenish yellow solution was washed extensively with ethanol (Merck) to remove free NPA and side product. After that, the precipitated PVA capped NPA was dissolved in a 30 mL water. The formation of PVA capped NPA was confirmed by the strong emission band at around 420 nm.

3.2.10. Procedure for Hg^{2+} Ions Detection in Real World Samples: Groundwater samples were collected from the campus and used as model real world samples. The collected samples were spiked with various known concentration ranges of mercury and filtered using 0.22 μm pore size filters. For sensing, 800 μL of Hg^{2+} spiked water samples was taken for the analysis using our developed sensor (final concentrations of mercury in the solution were prepared to be 1 ppb, 1 ppm and 10 ppm).

3.2.11. Preparation of Silver Nanoparticles Impregnated Polymer Thin Film: In order to fabricate the polymer thin film, first the aqueous PVA solution was prepared by dissolving 1.6 g PVA in 10 mL of water under stirring condition upon heating at temperature around 70 ºC. Then 3 mL aliquot of stock Ag-NPs solution was added in 1 mL PVA solution at room temperature under stirring condition. The resulting mixture solution is stirred for 15 minutes. Now, to prepare the sensor film, first of all, we make sure the glass slide size is 4.5 cm long and 1 cm wide. The prepared glass substrates (glass slides) were cleaned using soap solution and water followed by sonication with isopropyl alcohol for 30 minutes and dried in a hot air oven. After that, 50 μL of the well mixed PVA-Ag-NPs mixture solution was casted on the cleaned glass substrates and subsequently heated in a hot air oven at 100 ºC for 2 h. The thin film was formed on the glass substrates by encapsulating Ag-NPs in the host polymer

matrix. Thereafter, the characterization studies of the fabricated sensor films were performed for further sensing application.

3.2.12. Procedure for Hg^{2+} Sensing Experiments by Thin Film Sensor: All the sensing experiments were carried out at room temperature. The Ag-NPs impregnated polymer thin film was immersed into a beaker with Millipore water for a short period of time and taken out for the measurement of absorption spectrum of the sensor film. The spectrum was marked as initial or zero-minute spectrum for comparison study. This process has been repeated at 3 minutes interval consecutively for 30 minutes with the same sensor film. To observe the effect of Hg^{2+} on the films, the beaker was filled with known amount of the aqueous mercury ion (Hg^{2+}) solution (required amount of mercury nitrate monohydrate (Hg(NO$_3$)$_2$ ·H$_2$O) was dissolved in Millipore water to prepare aqueous mercury ion (Hg^{2+}) solution). Similar to the aforementioned way, the spectrum of the sensor films was monitored with 3 minutes interval for up to 12 minutes. A fresh thin film was used for each new experiment.

3.2.13. Procedure for Hg^{2+} Sensing in Real Samples by Thin Film Sensor: Tap water samples were collected from the laboratory and used as a model of real world water samples. The used tap water samples were analysed in a National Accreditation Board for Testing and Calibration Laboratory in the city and found no trace of mercury in the samples. All the collected samples were filtered using 0.22 μm pore size nylon disk and spiked with mercury at different concentration levels by dissolving required amount of mercury nitrate monohydrate (Hg(NO$_3$)$_2$·H$_2$O) salt. Final concentrations of mercury ions in the spiked tap water samples were 500 ppb, 1 ppm, 5 ppm and 10 ppm. For sensing, mercury contamination of the spiked tap water samples were measured as described earlier using our developed sensor and a correlation was traced between the measured and the expected results (obtained from the calibration equation) by comparing the differential absorbance intensity with respect to the reference sample measured at zero minute.

3.2.14. Synthesis of Carbon Dots (CDs): The highly fluorescent CDs were prepared in aqueous solution through one-step hydrothermal carbonization of PVP, which is similar to chemical reactions of chitosan under hydrothermal conditions [13], where PVP served a dual role as both the source of CDs and as a passivating agent. First, the aqueous PVP solution was prepared by dissolving 300 mg of PVP in 10 mL of water under a stirring condition at room temperature. Then, the solution was transferred into a 15 mL Teflon-lined stainless-steel autoclave and was placed into an oven to react at 200 ^{0}C for 6 hours. After the reaction, the system was then cooled down to ambient temperatures naturally. The deep-brown aqueous product was collected and centrifuged at high speed (10,000 rpm/min) for 15 minutes in order to remove any insoluble or bigger particulates. Then the upper deep-brown aqueous solution was collected and stored in the room temperature for further study. The formation of CDs (pH – 6.5) were confirmed by the strong multiple emission.

3.2.15. Determination of the Standard Solution of Fe^{3+} Ions: The determination of Fe^{3+} ions concentrations in the given aqueous solution was carried out as follows: 100 μL of the as-prepared CDs solution was added into 50 mL Millipore water to prepare the stock solution (Fe^{3+} ions sensor). A 2 mL aliquot of the stock solution was taken in the cuvette to measure the emission spectra without and with different concentrations of Fe^{3+} ions, respectively.

3.2.16. Determination of the Standard Solution of F$^-$ Ions: The determination of F$^-$ ions concentrations in the given aqueous solution were carried out as follows: The CDs-Fe^{3+} nanocomposite complex (F$^-$ ions sensor) was prepared by mixing the known concentration of the Fe^{3+} ions in the stock solution of CDs (final concentration of the Fe^{3+} ions in the CDs-Fe^{3+} nanocomposite complex was 150 μM). A 2 mL aliquot of stock CDs-Fe^{3+} nanocomposite complex was taken in the cuvette to measure the emission spectra without and with different concentration F$^-$ ions, respectively.

3.2.17. Procedure for F⁻ Ions Detection in Real World Water Samples:

Groundwater samples were collected from different drinking water tap in our institute and used as model real world water samples. The collected samples were filtered using 0.22 μm pore size filters and spiked with various known concentration ranges of fluoride ions. For sensing, 10 μL of every F⁻ spiked water samples were taken for the analysis using our developed F⁻ ions sensor (final concentrations of F⁻ ions in the solution were 10 μM, 50 μM, 150 μM, 300 μM and 450 μM respectively).

References

1.	P. K. Sarkar, S. Pal, N. Polley, R. Aich, A. Adhikari, A. Halder, S. Chakrabarti, P. Chakrabarti and S. K. Pal; Development and validation of a noncontact spectroscopic device for hemoglobin estimation at point-of-care. *J. Biomed. Opt.* 22 (2017), 055006.

2.	P. K. Sarkar, A. Halder, A. Adhikari, N. Polley, S. Darbar, P. Lemmens and S. K. Pal; DNA-based fiber optic sensor for direct in-vivo measurement of oxidative stress. *Sens. Actuators B: Chem.* 255 (2018), 2194.

3.	S. Lei, K. Tang, Z. Fang and H. Zheng; Ultrasonic-assisted synthesis of colloidal Mn₃O₄ nanoparticles at normal temperature and pressure. *Cryst. Growth Des.* 6 (2006), 1757.

4.	N. Polley, S. Saha, A. Adhikari, S. Banerjee, S. Darbar, S. Das and S. K. Pal; Safe and symptomatic medicinal use of surface-functionalized Mn₃O₄ nanoparticles for hyperbilirubinemia treatment in mice. *Nanomedicine* 10 (2015), 2349.

5.	A. Giri, N. Goswami, M. Pal, M. T. Zar Myint, S. Al-Harthi, A. Singha, B. Ghosh, J. Dutta and S. K. Pal; Rational surface modification of Mn₃O₄ nanoparticles to induce multiple photoluminescence and room temperature ferromagnetism. *J. Mater. Chem. C* 1 (2013), 1885.

6.	A. Adhikari, N. Polley, S. Darbar, D. Bagchi and S. K. Pal; Citrate functionalized Mn₃O₄ in nanotherapy of hepatic fibrosis by oral administration. *Future Sci. OA* 2 (2016), FSO146.

7.	A. Giri, N. Goswami, C. Sasmal, N. Polley, D. Majumdar, S. Sarkar, S. N. Bandyopadhyay, A. Singha and S. K. Pal; Unprecedented catalytic activity of Mn₃O₄ nanoparticles: potential lead of a sustainable therapeutic agent for hyperbilirubinemia. *RSC Adv.* 4 (2014), 5075.

8.	N. Polley, P. K. Sarkar, S. Chakrabarti, P. Lemmens and S. K. Pal; DNA biomaterial based fiber optic sensor: Characterization and application for monitoring in situ mercury pollution. *ChemistrySelect.* 1 (2016), 2916.

9. S. Sardar, S. Chaudhuri, P. Kar, S. Sarkar, P. Lemmens and S. K. Pal; Direct observation of key photoinduced dynamics in a potential nano-delivery vehicle of cancer drugs. *Phys. Chem. Chem. Phys.* 17 (2015), 166.

10. B. A. F. Puygranier and P. Dawson; Chemical etching of optical fibre tips — experiment and model. *Ultramicroscopy* 85 (2000), 235.

11. W. Pak Kin, U. Ulmanella and H. Chih-Ming; Fabrication process of microsurgical tools for single-cell trapping and intracytoplasmic injection. *J. Microelectromech. Syst.* 13 (2004), 940.

12. C. Y. Flores, C. Diaz, A. Rubert, G. A. Benítez, M. S. Moreno, M. A. Fernández Lorenzo de Mele, R. C. Salvarezza, P. L. Schilardi and C. Vericat; Spontaneous adsorption of silver nanoparticles on Ti/TiO_2 surfaces. Antibacterial effect on pseudomonas aeruginosa. *J. Colloid Interface Sci.* 350 (2010), 402.

13. Y. Yang, J. Cui, M. Zheng, C. Hu, S. Tan, Y. Xiao, Q. Yang and Y. Liu; One-step synthesis of amino-functionalized fluorescent carbon nanoparticles by hydrothermal carbonization of chitosan. *Chem. Commun.* 48 (2012), 380.

Chapter 4

Spectroscopic Studies for the Potential Application in Medical Diagnosis of Anemia

4.1. Introduction

Anemia is one of the most common global health problems affecting both developed and developing countries; it has far-reaching and severe adverse effects on human health and strongly affects socioeconomic development [1]. Approximately two billion people-nearly 30% of the world population-are estimated to be currently anemic [2-4], and women of reproductive age, pregnant and breastfeeding women and children are the most vulnerable populations [5-7]. The 2015 World Health Organization (WHO) fact sheets on the global statistics of anemia show that roughly 273 million (43%) children, 32.4 million (38%) pregnant women, 496 million (29%) nonpregnant women and 29% of all women of reproductive age are anemic [8, 9]. Therefore, anemia detection and control activities should be an integral part of healthcare services, particularly because an early diagnosis of anemia in the population is a proven means of health promotion.

Hemoglobin measurement is usually dependent on the services of a well-equipped clinical laboratory. The current gold standard, automated hematology analyzers, use blood samples for precisely estimating hemoglobin concentration in a laboratory setting [7]. Although this method is effective, it has several drawbacks. Numerous other methods, such as HemoCue, hemoglobin color scale, copper sulfate method, are available, but all of these methods require a high level of technical skills to interpret and at least one drop of blood [10]. Invasive blood sampling is stressful and painful for the patients and results in blood loss, which may induce anemia in infants and infection at the sampling site [11]. In addition, the accuracy of the results are heavily dependent on the skills of the operators [12]. Moreover, hematology analyzers

are expensive [10] and the cost per sample is significantly high compared with older manual techniques.

To date, the lack of a portable, easily operable, inexpensive and accurate device has hindered the widespread adaption of anemia screening in public health programs [13]. Most anemic women live in low-resource areas, where cost-effective and accurate diagnosis of anemia is unavailable. These factors have encouraged researchers and manufacturers to develop an economic and accurate noninvasive device for anemia detection in point-of-care settings; such a device would increase the accessibility of anemia screening and increase early diagnosis and treatment [14]. Some methods for point-of-care noninvasive hemoglobin measurements, such as Pronto-7™ and Pulse CO-Oximeter developed by Masimo Corporation (Irvine, CA), NBM-200 developed by OrSense (Israel) and spectrophotometry, have been described in the literature [14-18]. Most of these devices use a finger probe, and the technology is analogous to noninvasive pulse oximetry, which measures the total hemoglobin level within a few minutes. However, although these devices address many problems encountered in older noninvasive devices, they have their own limitations [14], such as low precision and accuracy [19] The accuracy and sensitivity of all noninvasive devices vary across races (specifically, skin color) because of the variation of melanin concentration in skin tissues [17, 20]. Moreover, they are not highly efficient and reliable as they frequently produce erroneous results because of the limitations associated with direct access to the blood or blood vessels and change in tissue morphology, shape and blood content in the targeted area [17].

To overcome the aforementioned limitations and to realize several crucial functions missing in the current noninvasive devices, we applied a spectroscopic method and addressed many unavoidable requirements that are missing in the previous noninvasive devices. In this paper, we present a noninvasive, noncontact and portable device for hemoglobin estimation at point-of-care in human subjects. Our innovation is based on the measurement of the spectroscopic signal emanating from the vascular bed of the bulbar conjunctiva [21]. As the conjunctiva in all humans is transparent and

71

has white sclera as background [22], the accuracy and sensitivity of the proposed device are independent of the skin color of the subjects. The easy access to the conjunctiva and its high vascular visibility ensures that the proposed device has high accuracy and sensitivity. The other distinguishing features of this device include the following: (1) Direct measurements of the hemoglobin level with extremely high precision and accuracy and without interference from pathological conditions. (2) The noninvasive and noncontact nature of the device, which is essential for use in neonates and virus-infected maternal subjects. (3) Online monitoring and compatibility with mobile-phone platforms for data transceiving, which facilitates the quick development of treatment plans. (4) Almost zero maintenance costs. (5) Operable by minimally trained or nearly untrained healthcare workers. Moreover, the proposed device can efficiently estimate hemoglobin levels with high precision and accuracy and without requiring any blood samples or chemical reagents at point-of-care. Furthermore, the generated report can be instantaneously transmitted to a medical expert through e-mail, text messaging, or mobile apps. Thus, the proposed device has high potential for further development and commercialization.

4.2. Result and Discussion

4.2.1. Development and Validation of a Noncontact Spectroscopic Device for Hemoglobin Estimation at Point-of-Care [23]:

4.2.1.1. Characteristic of the Conjunctival Spectrum: Oxyhemoglobin has a unique characteristic optical spectrum over the visible light range, with absorption peaks at approximately 414, 542 and 576 nm [24, 25]. Figure 4.1a presents an optical fiber and spectroscopy–based absorbance setup for collecting and monitoring the diffused reflectance spectral response of the blood flowing in the vascular bed of the bulbar conjunctiva of human subjects (patent 466/KOL/2009). A spectrograph (STS-VIS) with wavelength resolution of 0.47 nm and a white light-emitting diode (LED) source [LS-450, with the preinstalled blue LED replaced with a white LED (196-00000-WHT)] with wavelength range 430–700 nm (Ocean Optics, FL, USA) was used in our

study. A lab-grade optical fiber probe (Fiber-type UV–VIS; Ocean Optics) were used for transmitting and collecting the light to and from the vascular bed of the bulbar conjunctiva. The light from the light source is carried by the six surrounding fibers of the probe (called excitation fibers) and is incident on the conjunctiva, and the single fiber in the middle of the probe (called the collection/detection fiber) collects the diffused light and transmits it back to the spectrograph [Figure 4.1a]. The collected spectral response generated in the spectrograph is then transferred to a tablet computer through a Universal Serial Bus (USB) connection, where it is processed using
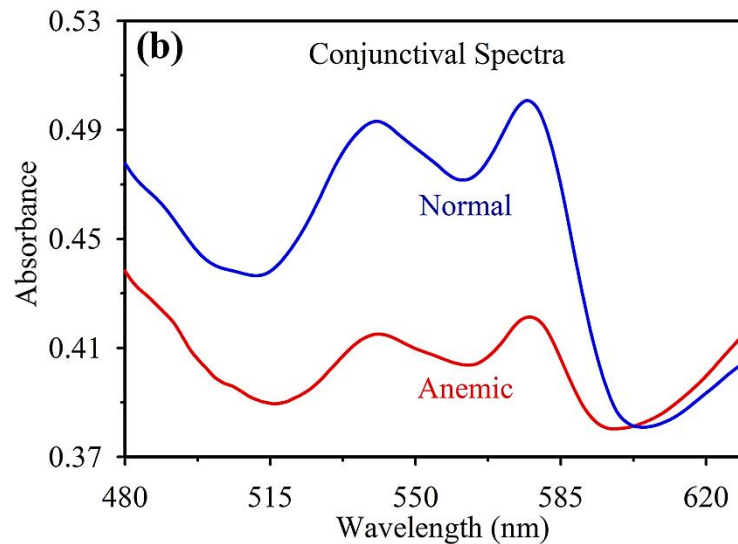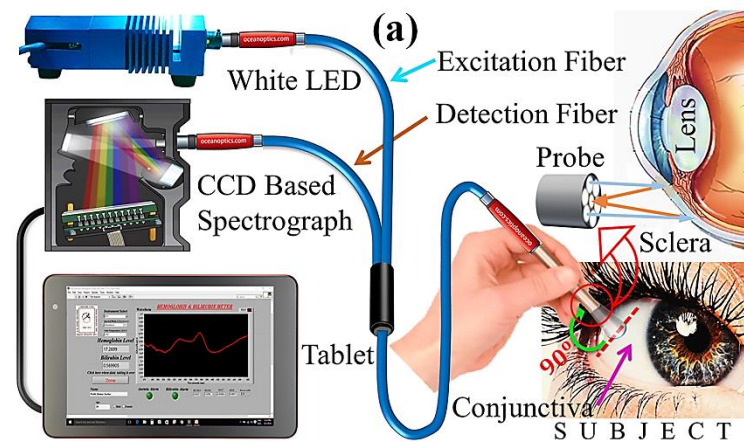
Figure 4.1. *(a) Schematic representation of the proposed device. The light from the source is transmitted through the six-channel excitation fiber and incident on the conjunctiva of the subject. The diffused light from the conjunctiva is collected using the single-channel detection fiber and transmitted to the spectrograph. The corresponding spectral response is processed and generated in the tablet. (b) Comparative spectral response of the conjunctiva of a normal volunteer and anemic patient.*

the custom-developed LabVIEW software. Figure 4.1b presents the collected comparative spectral response of a normal volunteer with hemoglobin level 16.6 g/dL and an anemic patient with hemoglobin level 8.7 g/dL.

4.2.1.2. Software Development: For automatic data acquisition and visualization of the acquired spectra, the supporting software was designed on a LabVIEW platform. First, the collected spectral response as generated in the spectrograph is transferred to a tablet computer through a USB connection, where it is processed and displayed by custom-designed LabVIEW software. The measured spectrum from the conjunctiva of the patient is displayed online and can be used to analyze the medical condition of the patient. Finally, the calculated hemoglobin level of the patient is displayed along with suggested medical attention on the screen of the tablet computer. Figure 4.2a illustrates the sequential program flow diagram of the developed software. The instrument is first initialized to its power-on status. Then, the software creates a folder for a given subject name to store the data and hemoglobin level of the subject. To achieve sufficient signal-to-noise (S/N) ratio in the collected data (spectrum), we set 2 sec as the integration time throughout this study. The integration time was determined at the time of reference-spectrum collection. The reference spectrum is collected using a standard scatterer (WS-1 Reflectance Standards, Ocean Optics) with a spot size of diameter approximately 0.7 cm; the perpendicular distance between the reference surface and the probe tip was maintained at approximately 1.5 cm by adjusting the integration time (2 sec). The dark spectrum is acquired in the presence of ambient light by turning off the source LED. The length of the optical spectrum intensity array is fixed on the basis of the pixel number of the detector. Accordingly the corresponding wavelength array (one-dimensional array) is determined. The pre-acquired dark spectrum and reference spectrum, which were acquired each day before starting the data collection, are then read from the preloaded file location for spectrum processing and baseline correction. The software is then ready to read the optical spectrum processing and baseline correction. The software is then ready to read the optical
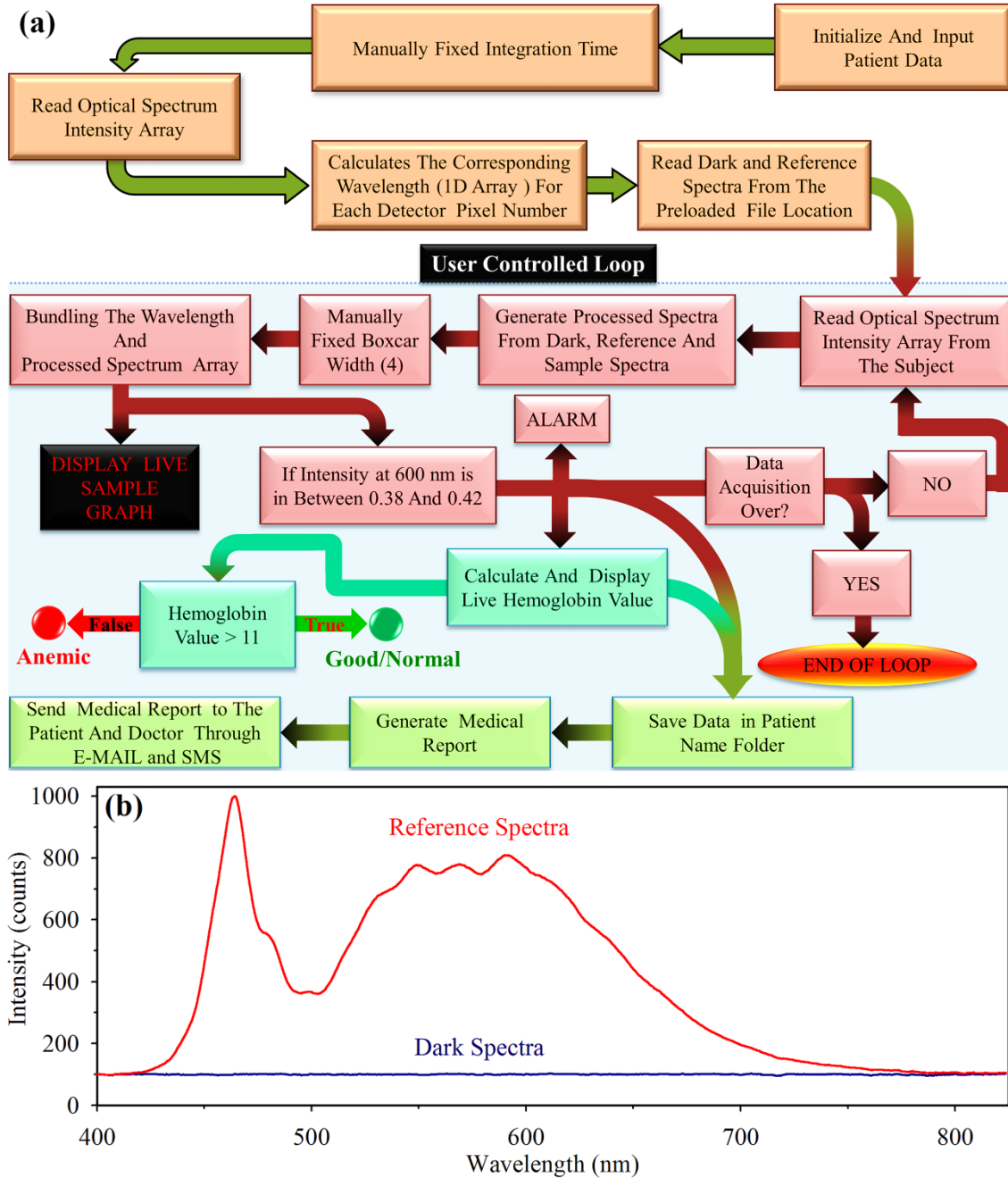
Figgure 4.2. *(a) Sequential program flow diagram of the developed software designed on a LabVIEW platform for noncontact online monitoring of hemoglobin level in humans. (b) Typical reference and dark spectra.*

spectrum intensity array from the subject and generate the processed spectrum array from the dark, reference and sample spectra by using the below equation.

$$\text{Processed spectrum} = -log_{10}\left[\frac{\text{Sample spectrum}-\text{Dark spectrum}}{\text{Reference spectrum}-\text{Dark spectrum}}\right] \quad (4.1)$$

Figure 4.2b shows the typical dark and reference spectra. The boxcar width (= 4) is then fixed to generate a smooth online graph by bundling the wavelength and processed spectrum array; this processing removes noise by averaging the values of the adjacent pixels and therefore improves the S/N ratio at the expense of optical resolution. The online graph and data are automatically saved in the folder location with a sound alarm only when the absorbance intensity of the spectrum at 600 nm is between 0.38 and 0.42. Setting this narrow range of absorption ensures the collection of spectral data from the spot size of diameter approximately 0.7 cm on the conjunctiva. This spot size is the same as that used to acquire the reference spectrum. Subsequently, the software asks the user to either end the data acquisition by ending the loop or to repeat the measurement on the same subject.

Using this developed software we collected 302 participants' data to calibrate our instrument for hemoglobin measurements. The calibration equation was incorporated into the software [Figure 4.2a] for calculating the hemoglobin level from the acquired spectrum. Now the software can also display and save the calculated hemoglobin value following the earlier data saving conditions. The hemoglobin level of the patient is calculated using the differential absorption of light of wavelength 576 and 600 nm. On the basis of the calculated hemoglobin level, the online display indicator classifies the data of the patient as being within or outside the anemic region. Finally, the acquired absorbance spectrum and the displayed hemoglobin level are stored in a folder (labelled with the name of the patient), and a comprehensive medical report is instantaneously generated and sent to the doctor and patient through e-mail and text messaging for offline use. We have ensured that the user interface of the software is appropriate for use by personnel with zero or minimal medical and instrumentation knowledge.

4.2.1.3. Calibration and Validation of the Device: The study included a total of 493 patients (including 276 males, 74 of whom were children) with a variety of age group ranging from 4 to 76 years (mean age ± standard deviation (SD) = 27 ± 13 years). All data were collected using our device in the blood collection room of the outpatient

department of Nil Ratan Sircar Medical College and Hospital, Kolkata, following the standard ethical guideline approved by the local medical ethics committee (No/NMC/443, Dated – 25/01/2016). A duly signed consent form was obtained from the patients or their legal guardians stating their acceptance, involvement and full understanding of the study. All ethical guidelines, including participant confidentiality and legitimacy, were followed. The study was conducted in two stages. In the first stage (Stage I), the device was calibrated, and in the second (Stage II), the accuracy of the software-driven device was measured and compared with that of the gold standard.

The proposed device collects the spectroscopic signal of the blood from the human conjunctiva. We choose the conjunctiva of human eyes as the target organ to estimate the hemoglobin concentration as it is easily accessible, hosts well-oxygenated blood containing high-density vascular bed [26] and has high vascular visibility with a white background in all human subjects. In addition, the noncontact nature of our method ensures no change in tissue morphology, shape and blood content in the target area. Although, the effects of low hemoglobin saturation on our measurements are unknown, the study by MacKenzie et al. showed that the blood in the bulbar conjunctival microvasculature is always highly saturated with oxygen [26]. These advantages ensure that the proposed device can measure hemoglobin concentration with high accuracy and precision and without any interference from the other pathological conditions in subjects from all races. Figure 4.1b presents the spectral response of a normal volunteer and an anemic patient. There was an obvious difference in their absorbance spectra, clearly indicating the concentration of hemoglobin is much higher for the normal volunteer compared to the anemic patient.

For device calibration (Stage I), 302 patients (including 168 males, 48 of whom were children) of all age groups with hemoglobin levels ranging from 3.4 to 17.9 g/dL were randomly selected for data collection; their information is listed in Table 4.1. The acquired data were then processed to enable quantitative comparisons with the blood hemoglobin levels obtained using the automated hematology analyzer. It has already been reported that the absorbance maxima of the blood at around 576 nm wavelength

is directly related to the hemoglobin concentration present in the blood [24, 25]. Different characteristic wavelengths over the collected spectrum were selected for assessment, and the differential absorbance of light of wavelength 576 and 600 nm was found to be highly consistent with the blood hemoglobin levels of the patients. Figure 4.3 presents the dependency of the instrument index values (i.e., differential absorbance at 576 and 600 nm) with blood hemoglobin levels. Clearly, there is a linear
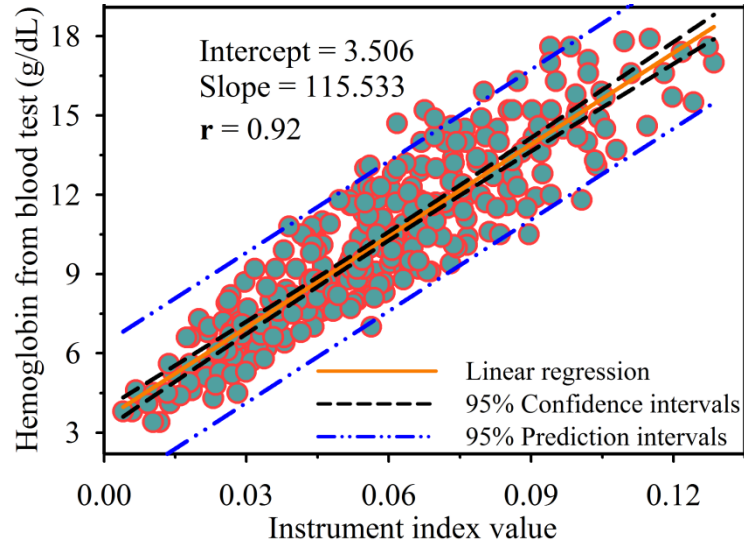
Figure 4.3. *Device calibration: linear regression of the hemoglobin level from the blood test and the instrument index value from our device (r = 0.92) with 95% CI and 95% prediction intervals.*

dependency between the instrument index values and blood hemoglobin levels. To calibrate the device and to determine the direct correlation with blood hemoglobin levels, the clinically measured hemoglobin levels (measured using a standard automated hematology analyzer) were plotted against the instrument index values. The linear regression curve with the 95% confidence intervals (CI) and 95% prediction intervals is shown in Figure 4.3. The Pearson correlation coefficient r = 0.92 and the statistical parameters P value < 0.0001 and F value = 1407.49 indicate a strong correlation between the hemoglobin levels and the instrument index values. The calibration equation obtained from the linear regression curve was $y_i = 115.533x_i + 3.507$, where y_i represents the hemoglobin level and x_i represents the instrument index value. We used this equation in the LabVIEW software to estimate the hemoglobin level from the spectral information obtained using our device.

Table 4.1. *Statistics of the patients' information.*

	For Calibration	For Validation
Patients	N=302	N=191
Age (Yr.)	27±13 (95% CI: 25; 28, CV: 49.15%)	26±12 (95% CI: 25; 28, CV: 49.15%)
Sex Ratio M/F	168/134	108/83
Hb Value (g/dL)	10.15±3.43 (95% CI: 9.76; 10.53; CV: 33.77%)	10.46±3.36 (95% CI: 9.98; 10.94; CV: 32.15%)
Stage of Anaemia		
Severely Anaemic (3-7)	N=63 (20.8%)	N=31 (16.2%)
Anaemic (7-11)	N=120 (39.7%)	N=78 (40.8%)
Normal (11-18)	N=119 (39.4%)	N=82 (42.9%)
Diagnosis		
Iron Deficiency Anaemia	N=18 (5.9%)	N=11 (5.7%)
Thalassemia	N=17 (5.6%)	N=17 (8.9%)
Leukemia	N=25 (8.3%)	N=14 (7.3%)
Other Anaemia (aplastic etc.)	N=20 (6.6%)	N=15 (7.9%)
Other Disorders	N=18 (5.9%)	N=12 (6.3%)
Not Diagnosed (Screening)	N=114 (37.7%)	N=72 (37.7%)
Normal Volunteer	N=90 (29.8%)	N=50 (26.2%)
Transfusion (within 6 months)	N=22 (7.3%)	N=18 (9.4%)

N: Sample Size; 95% CI: 95% confidence interval of Mean, CV: Coefficient of variation, Hb: Hemoglobin concentration (g/dL).

In the field of clinical measurement, a new measurement technique must often be compared with an established technique to evaluate whether the outputs of technique are sufficiently consistent for the new technique to replace the old one. Such investigations are often conducted through the Bland–Altman method [27]. Hence, to the statistical significance of the proposed noncontact and noninvasive optical device for online assessment of the hemoglobin level, correlation and regression analyses were used following the reported literature [28-30]. For assessing the agreement between the outputs of the conventional technique (automated hematology

analyzer) and the proposed optical device, the Bland-Altman method was used to determine the correlation coefficient [27].

To compare the proposed point-of-care noninvasive hemoglobin detection method with an established conventional technique (the Stage II), a total of 191 patients (including 108 males, 26 of whom were children) of all age groups with hemoglobin levels ranging from 3.9 to 17.9 g/dL were randomly selected. Their information is listed in Table 4.1. Figure 4.4a represents the linear regression analysis
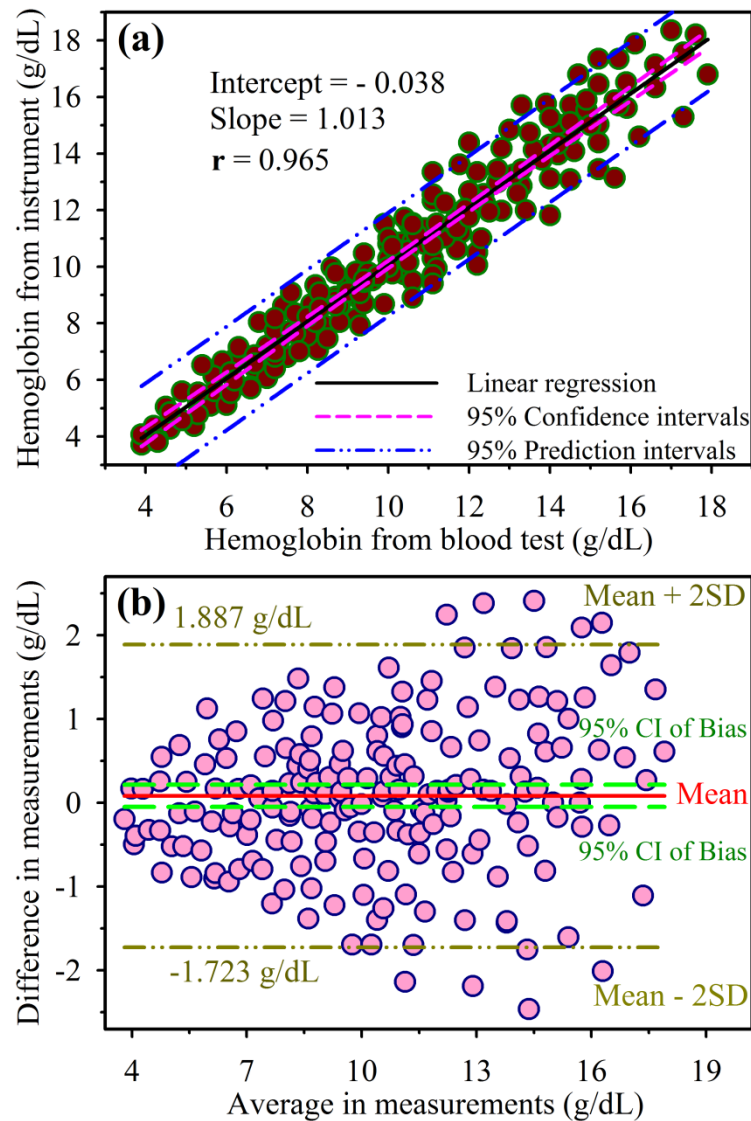
Figure 4.4. *Device validation: (a) Linear regression of the hemoglobin level from blood test and the hemoglobin level from our device (r = 0.965) with 95% CI and 95% prediction intervals. (b) Bland–Altman analysis of the hemoglobin level from the blood test and that from our device with mean bias (continuous line), 95% CI of bias (dashed green lines) and 95% limits of agreement (bias ± 2SD, dot-dashed lines).*

with the 95% CI and 95% prediction intervals. The linear regression results (Pearson correlation coefficient r = 0.965, P value < 0.0001, F value = 2562.86, slope = 1.013 and intercept = −0.038) indicate a strong correlation between the two methods. For a more adequate comparison of the two methods, we applied the Bland-Altman method, which measures the agreement between two repeated measurements and the strength of the relationship between the measurements by using a plot of the difference between the methods against their average value [Figure 4.4b] [31, 32]. A direct comparison of the two methods using this method yielded a bias of 0.082 g/dL and SD of 0.921; 95% CI for the bias was −0.049 to 0.214 and 95% limits of agreement [mean ± 2SD] were −1.723 to 1.887 g/dL [Figure 4.4b]; 95% limits of agreement means that 95% of the differences are assumed to lie within these limits and how far apart the measurements obtained using the two methods are likely to be for most individuals. The accuracy of the proposed method relative to the reference method was calculated using the accuracy root mean square (A_{RMS}) as $\sqrt{[\text{mean bias}]^2 + [\text{SD}]^2}$ [15]. The obtained A_{RMS} of our method throughout the hemoglobin range was 0.924 g/dL, which indicate the high accuracy of the method. These results exhibit strong agreement between the conventional method and the proposed noninvasive as well as noncontact method of anemia detection.

Compared with laboratory reference values, the overall bias ± the limits of agreement was 0.082 ± 1.805 g/dL for the proposed device, which is significantly lower than that the commercially available noninvasive and invasive hemoglobin monitoring devices such as Radical-7® Pulse CO-Oximetry (−0.02 ± 2.724 g/dL), HemoCue®201+ (−0.17 ± 2.058 g/dL), HemoCue point-of-care device (−0.4 ± 2.6 g/dL) and hemoglobin monitoring using capillary blood (−0.4 ± 2.6 g/dL) [15, 16, 33]. Compared with laboratory reference values, noninvasive hemoglobin measurement with the proposed device has absolute and trending accuracy similar to those of widely used noninvasive and invasive methods of hemoglobin measurement. The proposed method is especially useful in low-resource settings, where conventional hematology analyzers are cost-prohibitive.

Furthermore, the proposed device can efficiently classify anemia in the patient into the different stages defined by the WHO, the severe anemia, <7 g/dL; mild anemia, 7–11 g/dL; and normal rage above 11 g/dL [6, 25]. Therefore, for effective screening test, detection of hemoglobin level upto 11 g/dL with high precision and
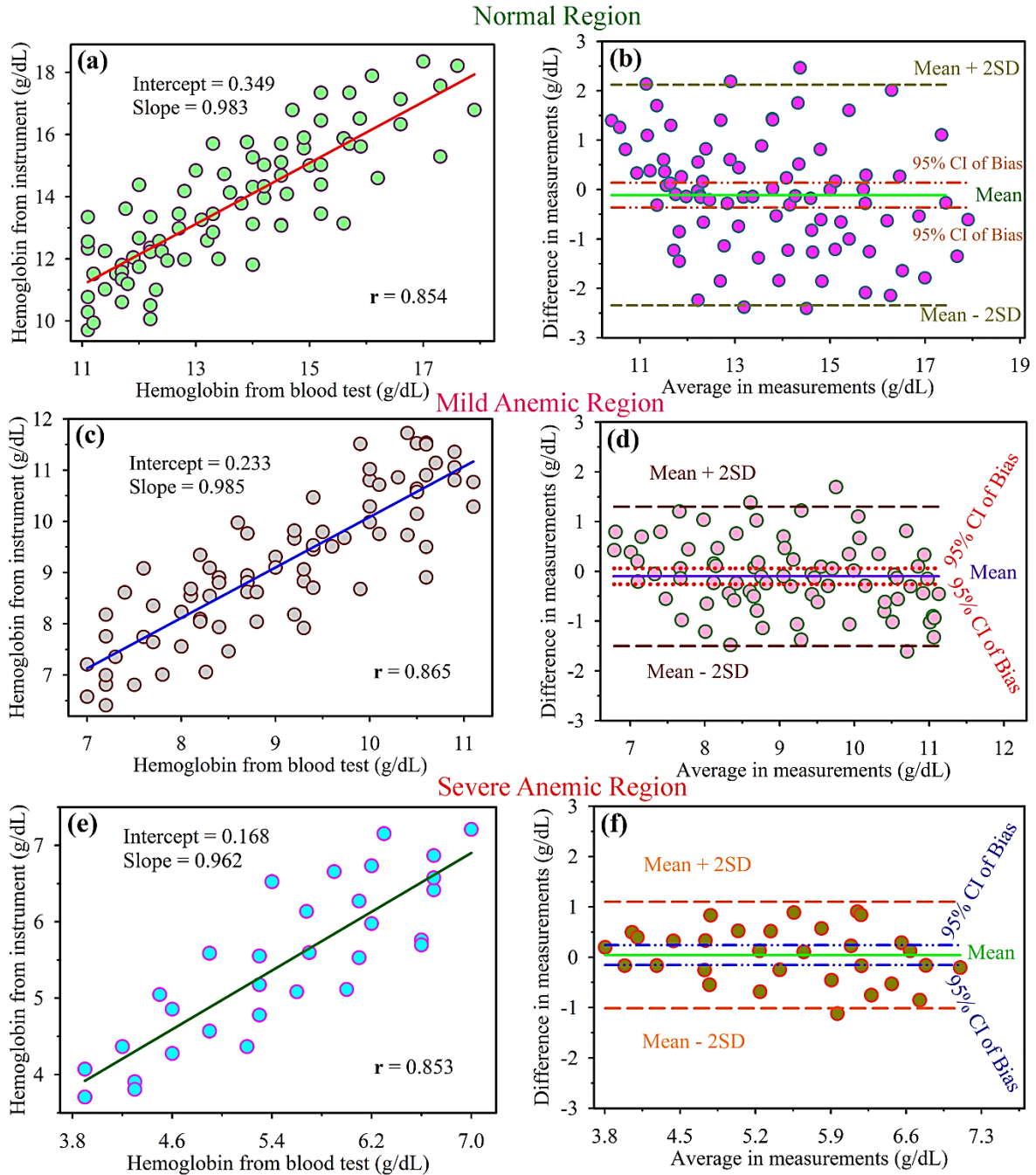
Figure 4.5. *Linear regression and Bland–Altman analysis of the hemoglobin level from the blood test and that from our device with mean bias (continuous line), 95% CI of bias and 95% limits of agreement for (a) and (b) normal region, (c) and (d) mild anemic region and (e) and (f) severe anemic region.*

82

accuracy is the main goal of our invention. According to the defined anemic range we classified our all the results into three regions according to the aforementioned ranges [Figure 4.5]. Figure 4.5a presents the linear regression analysis for the samples in which the hemoglobin level exceeds 11 g/dL (n = 82; r = 0.854, *P* value < 0.0001, *F* value = 198.10, slope = 0.983 and intercept = 0.349), and Figure 4.5b depicts the Bland–Altman plot of two successive measurements made using the two different methods (mean =−0.112 g/dL, SD = 1.138 and the calculated accuracy (A_{RMS}) is = 1.143 g/dL). The correlation coefficient between the proposed device and laboratory-measured hemoglobin is the indication of good agreement between the two methods of measurement. The promising results imply that the device can detect and differentiate hemoglobin levels ranging from 11 g/dL to onwards with high accuracy.

On the other hand the CBC results revealed that the hemoglobin levels were 7–11 g/dL in 78 samples; Figure 4.5c presents the corresponding linear regression, which confirms that the clinical hemoglobin level measured using the automated hematology analyzer correlates strongly with the hemoglobin level measured using our noncontact device (r = 0.865, *P* value < 0.0001, *F* value = 206.12, slope = 0.985 and intercept = 0.233). In addition, the Bland–Altman method yielded a bias of −0.099 g/dL and SD of 0.713; the 95% CI for the bias was −0.260 to 0.061 and 95% limits of agreement were −1.498 to 1.298 g/dL [Figure 4.5d]. The high accuracy of the device (A_{RMS} = 0.719 g/dL) in this region highlight the strong potential of the device. These results indicate that the output of the noncontact anemia detection device is highly consistent with that of the conventional method. The 95% limits of agreement suggest that the device is relatively more sensitive in the anemic region.

Lastly, to establish the performance of the device in the severe anemia region, 31 samples were analyzed. Figure 4.5e and f presents the linear regression analysis (r = 0.853, *P* value < 0.0001, *F* value = 77.25, slope = 0.962 and intercept = 0.168) and the Bland–Altman plot (bias 0.043 g/dL, SD 0.542, 95%, CI for the bias, −0.154 to 0.241 and 95% limits of agreement, −1.014 to 1.101 g/dL), both of which reveal a strong correlation and agreement between the two methods. The accuracy of the device (A_{RMS}

= 0.54 g/dL) in this region is highly comparable with commercially available devices. These promising results validate the ability of device to detect severe anemia with extremely high accuracy. The Bland-Altman analysis confirmed that the proposed device is highly sensitive in the anemic region, more than that in the normal region, meaning that the device can accurately diagnose even the mildest forms of anemia as well as nonanemic participants' hemoglobin level and different degrees of polycythemia.

Finally, according to the CBC results, of the 191 samples with hemoglobin level in the 3.9–17.9 g/dL range, 109 had anemia (<11 g/dL); among the 109 anemic samples, 31 were severe anemia. The corresponding results, obtained using our method are as follows: 112 patients were classified as anemic, among whom 35 were classified as having severe anemia. These results indicate that in the clinically most significant region (i.e., in the anemic region, <11 g/dL), the performance of the proposed device is highly consistent with that of the current gold standard and that the device can determine anemia efficiently with extremely high accuracy. This device thus has the potential to provide CBC-quality measurement of total hemoglobin in point-of-care and austere medical environments, which do not have direct access to laboratory equipment. Moreover, the device is useful for diagnosing patients with any degree of anemia in low-resource settings in any region of the world.

4.2.1.4. Repeatability Test: To demonstrate repeatability, the hemoglobin levels of 56 patients were measured repetitively using the proposed device. We found the outstanding precision between the two back-to-back measurements in the same subject by the same observer. The calculated SD and mean were almost the same in both measurements, with highly significant intraclass correlation (correlation coefficient r = 0.983, P value < 0.0001). Linear regression analysis as shown in the Figure 4.6a further confirmed that the accuracy of the two measurements (*F* value = 1498.26, slope = 0.994 and intercept = 0.084). Figure 4.6b presents the Bland-Altman plots of the measurements, wherein each point represents one patient (throughout the hemoglobin
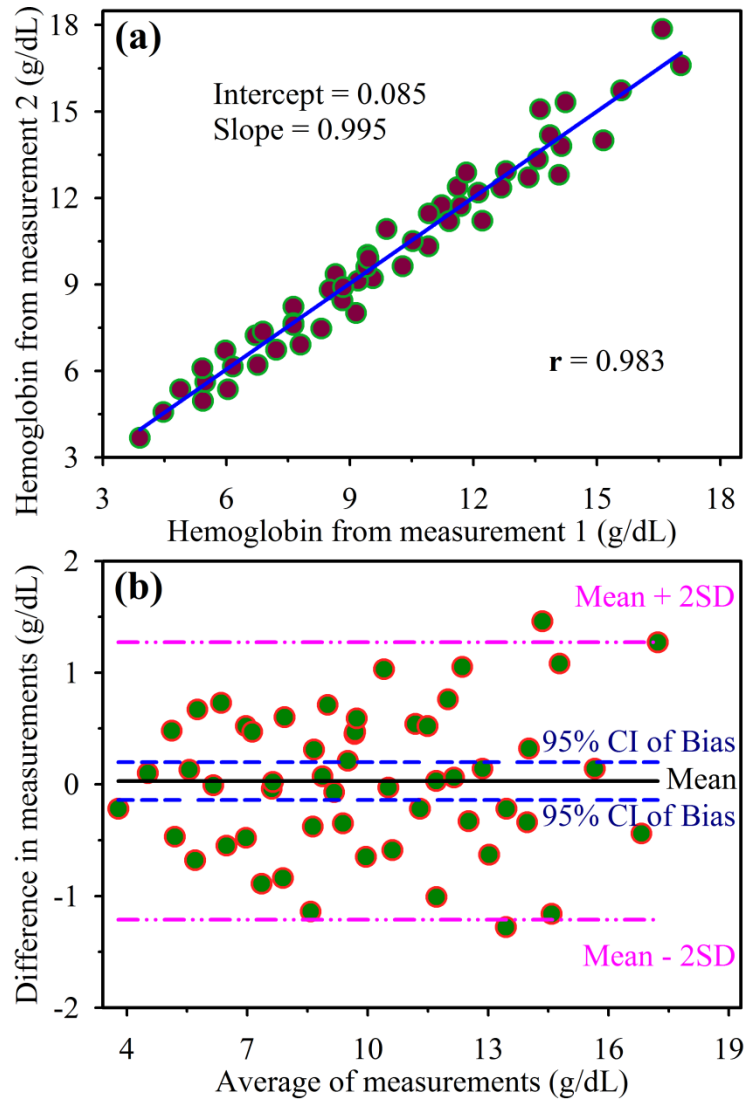
Figure 4.6. *Device repeatability: (a) linear regression analysis for two successive hemoglobin measurements in the same subject by the same observer and (b) the corresponding Bland-Altman analysis.*

range, mean bias = 0.03, SD = 0.633, 95 % limits of agreement = −1.212 to 1.272 g/dL and A_{RMS} = 0.634 g/dL). Ideally, the bias should be zero; the instrumental bias for our device was 0.03 g/dL, which is close to zero and exerts nearly no effect on the clinical hemoglobin measurement. These results suggest that the proposed non-invasive as well as noncontact device has excellent repeatability.

4.2.1.5. Reproducibility Test: Reproducibility of the device was assessed by measuring the clinically significant samples of 50 patients' hemoglobin levels two times in the
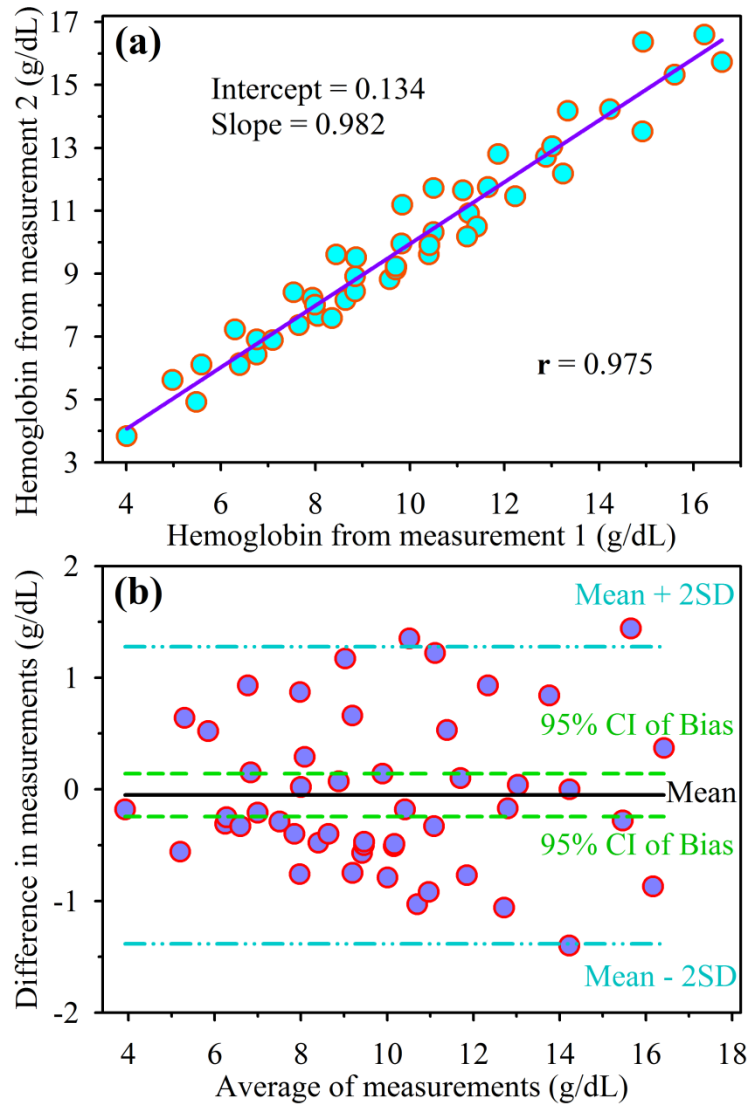
Figure 4.7. *Device reproducibility: (a) linear regression analysis for two successive hemoglobin measurements in the same subject by two independent observers and (b) the corresponding Bland-Altman analysis.*

same subject by two independent observers. We found marvelous precision between two back-to-back measurements in the same subject by two independent observers. The measurements were highly precise, with nearly the same SD and mean values in both measurements and a significant correlation in the linear regression analysis (correlation coefficient r = 0.975, P value < 0.0001, *F* value = 993.68, slope = 0.982 and intercept = 0.134) [Figure 4.7(a)]. Moreover, the Bland–Altman analysis yielded a bias of −0.052 g/dL, SD of 0.679, 95 % limits of agreement of −1.382 to 1.278 g/dL and A_{RMS} = 0.681 g/dL [Figure 4.7(b)]. The two measurements exhibited a

nonsignificant bias and a close agreement. These results indicate that the proposed noncontact device has high reproducibility.

4.3. Conclusion

We proposed a simple diffused reflection measurement technique for assessing hemoglobin levels and demonstrated that the vascular bed of bulbar conjunctiva is an ideal target area for this device. Through this spectroscopic method, which is invariable to skin color, age and sex of the subject, we developed an inexpensive, noncontact, highly reliable and efficient practical device for the online monitoring of hemoglobin levels in low-resource point-of-care settings. Moreover, the device can instantaneously transmit the generated report to a medical expert through e-mail, text messaging, or mobile apps. Furthermore, the device can classify the measured data into different degrees of anemia. In the clinically most significant regions [i.e., in the severe anemic region (<7 g/dL) and mild anemic region (7–11 g/dL)], the device has absolute and trending accuracy similar to those of widely used invasive methods of hemoglobin measurement. Moreover, this proposed noncontact, feasible and inexpensive device for rapid anemia screening with extremely high precision and accuracy has high potential for further development and commercialization.

References

1. Y. Balarajan, U. Ramakrishnan, E. Özaltin, A. H. Shankar and S. V. Subramanian; Anaemia in low-income and middle-income countries. *Lancet* 378 (2011), 2123.

2. World Health Organization; Micronutrient deficiencies. *W. H. O.* *https://www.who.int/nutrition/topics/vad/en/* (accessed on 2016).

3. J. Punter-Villagrasa, J. Cid, C. Páez-Avilés, I. Rodríguez-Villarreal, E. Juanola-Feliu, J. Colomer-Farrarons and P. Miribel-Català; An instantaneous low-cost point-of-care anemia detection device. *Sensors* 15 (2015), 4564.

4. M. M. Sirdah, A. Yaghi and A. R. Yaghi; Iron deficiency anemia among kindergarten children living in the marginalized areas of Gaza Strip, Palestine. *Rev. Bras. Hematol. Hemoter.* 36 (2014), 132.

5. PATH; Anemia detection in health services: Guidelines for program managers. *PATH* (1996).

6. E. McLean, M. Cogswell, I. Egli, D. Wojdyla and B. De Benoist; Worldwide prevalence of anaemia, WHO vitamin and mineral nutrition information system, 1993–2005. *Public Health Nutr.* 12 (2009), 444.

7. World Health Organization; Iron deficiency anaemia: Assessment, prevention and control: A guide for programme managers. *Geneva: W. H. O.* (2001).

8. World Health Organization; The global prevalence of anaemia in 2011. *Geneva: W. H. O.* (2015).

9. World Health Organization; Global nutrition targets 2025: Anaemia Policy brief. *Geneva: W. H. O.* (2014).

10. T. Srivastava, H. Negandhi, S. B. Neogi, J. Sharma and R. Saxena; Methods for hemoglobin estimation: a review of "what works.". *J. Hematol. Transfus.* 2 (2014), 1028.

11. L. D. Lilien, V. J. Harris, R. S. Ramamurthy and R. S. Pildes; Neonatal osteomyelitis of the calcaneus: Complication of heel puncture. *J. Pediatr.* 88 (1976), 478.

12. R. Neville; Evaluation of portable haemoglobinometer in general practice. *Br. Med. J. (Clin Res Ed)* 294 (1987), 1263.

13. J. Brown, L. Theis, L. Kerr, N. Zakhidova, K. O'Connor, M. Uthman, Z. M. Oden and R. Richards-Kortum; A hand-powered, portable, low-cost centrifuge for diagnosing anemia in low-resource settings. *Am. J. Trop. Med. Hyg.* 85 (2011), 327.

14. PATH; Noninvasive technology for anemia detection. *PATH* (2013).

15. D. Frasca, C. Dahyot-Fizelier, K. Catherine, Q. Levrat, B. Debaene and O. Mimoz; Accuracy of a continuous noninvasive hemoglobin monitor in intensive care unit patients. *Crit. Care Med.* 39 (2011), 2277.

16. L. Lamhaut, R. Apriotesei, X. Combes, M. Lejay, P. Carli and B. Vivien; Comparison of the accuracy of noninvasive hemoglobin monitoring by spectrophotometry (SpHb) and HemoCue® with automated laboratory hemoglobin measurement. *Anesthesiology* 115 (2011), 548.

17. J. W. McMurdy, G. D. Jay, S. Suner, F. M. Trespalacios and G. P. Crawford; Diffuse reflectance spectra of the palpebral conjunctiva and its utility as a noninvasive indicator of total hemoglobin. *J. Biomed. Opt.* 11 (2006), 014019.

18. N. B. Hampson, E. D. Ecker and K. L. Scott; Use of a noninvasive pulse CO-oximeter to measure blood carboxyhemoglobin levels in bingo players. *Respiratory care* 51 (2006), 758.

19. A. Belardinelli, M. Benni, P. L. Tazzari and P. Pagliaro; Noninvasive methods for haemoglobin screening in prospective blood donors. *Vox Sang.* 105 (2013), 116.

20. T. Lister, P. A. Wright and P. H. Chappell; Optical properties of human skin. *J. Biomed. Opt.* 17 (2012), 0909011.

21. J. Ditzel and R. W. ST. Clair; Clinical method of photographing the smaller blood vessels and the circulating blood in the bulbar conjunctiva of human subjects. *Circulation* 10 (1954), 277.

22. N. Polley, S. Saha, S. Singh, A. Adhikari, S. Das, B. R. Choudhury and S. K. Pal; Development and optimization of a noncontact optical device for online monitoring of jaundice in human subjects. *J. Biomed. Opt.* 20 (2015), 067001.

23. P. K. Sarkar, S. Pal, N. Polley, R. Aich, A. Adhikari, A. Halder, S. Chakrabarti, P. Chakrabarti and S. K. Pal; Development and validation of a noncontact spectroscopic device for hemoglobin estimation at point-of-care. *J. Biomed. Opt.* 22 (2017), 055006.

24. C. E. Carnicom; Morgellons: Altered blood. *Carnicom Institute* (2011).

25. E. A. Tyburski, S. E. Gillespie, W. A. Stoy, R. G. Mannino, A. J. Weiss, A. F. Siu, R. H. Bulloch, K. Thota, A. Cardenas, W. Session, H. J. Khoury, S. O'Connor, S. T. Bunting, J. Boudreaux, C. R. Forest, M. Gaddh, T. Leong, L. A. Lyon and W. A. Lam; Disposable platform provides visual and color-based point-of-care anemia self-testing. *J. Clin. Invest.* 124 (2014), 4387.

26. L. E. MacKenzie, T. R. Choudhary, A. I. McNaught and A. R. Harvey; In vivo oximetry of human bulbar conjunctival and episcleral microvasculature using snapshot multispectral imaging. *Exp. Cell. Res.* 149 (2016), 48.

27. J. Martin Bland and D. Altman; Statistical methods for assessing agreement between two methods of clinical measurement. *Lancet* 327 (1986), 307.

28. J. M. Bland and D. G. Altman; Calculating correlation coefficients with repeated observations: Part 2—correlation between subjects. *BMJ* 310 (1995), 633.

29. M. J. Gardner and D. G. Altman; Confidence intervals rather than P values: estimation rather than hypothesis testing. *Br. Med. J. (Clin. Res. Ed.)* 292 (1986), 746.

30. J. M. Bland and D. G. Altman; Statistics Notes: Correlation, regression and repeated data. *BMJ* 308 (1994), 896.

31. J. M. Bland and D. G. Altman; Comparing methods of measurement: why plotting difference against standard method is misleading. *Lancet* 346 (1995), 1085.

32. J. M. Bland and D. G. Altman; Applying the right statistics: analyses of measurement studies. *Ultrasound. Obstet. Gynecol.* 22 (2003), 85.

33. G. Lindner and A. K. Exadaktylos; How noninvasive haemoglobin measurement with pulse CO-Oximetry can change your practice: an expert review. *Emerg. Med. Int.* 2013 (2013), 701529.

Chapter 5

Development of Optical Fiber-based Diagnostic Strategy for Direct *In-vivo* Measurement of Reactive Oxygen Species (ROS) in Animal Model

5.1. Introduction

Molecular oxygen is one of the most important elements for living beings on the earth because almost all living organisms utilize oxygen for respiration and energy generation. But oxygen's derivatives, reactive oxygen species (ROS), can be very detrimental. The generation of ROS has been implicated in the onset and progression of several diseases (e.g., neurodegeneration, diabetes, cancer and atherosclerosis) [1]. These species were thought only to be released in host defense roles by phagocytic cells; however, it is now clear that at molecular level, ROS exhibit signaling and cell-function-modifying roles for many biological systems [2, 3]. They are easily inter-converted and can subsequently react with larger biological molecules, causing chain reactions to occur, which can lead to changes in both the function and structure of cellular components. Oxidative stress is essentially an imbalance between the production of ROS and the ability of our body to counteract or detoxify the harmful effects through neutralization by antioxidants. Several analytical approaches have been used to detect ROS using nanoparticles, chemiluminescence, various fluorescence probes, mass spectrometry probes etc. [4, 5]. However, all of the techniques have some relative advantages as well as disadvantages too. Among these fluorescence probes, 2,7-dichlorodihydrofluorescein diacetate (DCFH-DA) is the most widely used one for detection of intracellular oxidative stress. The probe is added to cells in culture and the intracellular oxidation of 2,7-dichlorodihydrofluorescein (DCFH) results in formation of a fluorescent product, 2,7-dichlorofluorescein (DCF), which can be monitored by several fluorescence-based techniques (confocal microscopy, spectroscopic

fluorescence detection, flow cytometry etc.) [6, 7]. This type of fluorescence techniques using some specific fluorophores are usually applied for detecting oxidative stress in cellular environment [8, 9]. However, use of these fluorescent probes in applications such as *in-vivo* measurement of oxidative stress is sparse in the literature. Direct *in-vivo* measurement of oxidative stress using specific fluorescence probes with negligible additional cytotoxicity remains a great challenge to the researchers. Some other analytical techniques for oxidative stress detection such as nuclear magnetic resonance (NMR), electron paramagnetic resonance (EPR), derivatization with attendant mass spectrometric (MS) analysis and liquid scintillation counting can also be quite useful but are less portable and often require highly trained technical expertise making the techniques to be highly expensive [7]. The aforementioned factors encourage us to develop a cost effective, simple, efficient and non-invasive or minimally-invasive technique for direct oxidative stress measurement.

The combination of optical fiber-based probes and DNA-based biomaterial offers an attractive non-invasive or minimally-invasive novel approach for various applications in biomedical and environmental sensor design [10, 11]. In this study we have attached a fluorescent probe to the fiber tip surface through DNA-based biomaterial matrix assuring negligible discharge of the probe to the solution under investigation for the direct or localized measurement of ROS [10, 11]. DNA, 'the molecule of life' has been used extensively for biomaterials development in the last few decades [12]. Among different types of DNA based biomaterials the DNA–lipid (surfactant) complex is most popular [13]. On the other hand, Fiber-Optic Sensors (FOS) are popular since 1987 [14] as FOS based system can be handled by any non-expert with little or no knowledge of instrument handling. In some recent reviews the development of Fiber-Optic Biosensors (FOBS) and Chemical Sensors (FOCS) has also been summarized [15-18]. However, reports on the direct *in-vivo* measurement of ROS or oxidative stress in biological systems are limited in the contemporary literature. There are few reports on potential FOS tools for the detection of hydrogen peroxide [19], with limited portability, cost-effectiveness and versatility. On the other hand,

there are several reports on the offline measurement of ROS [7, 20, 21]. However, cost effectiveness and versatility in the measurement capability, which are essential for the conclusive diagnosis of oxidative stress in a physiological condition have been profoundly compromised in the reports. In the given context, development of a highly efficient, portable and inexpensive DNA-based FOS for direct measurement of ROS/oxidative stress in physiologically relevant environments is the motivation of the present work.

In this work, salmon sperm DNA, a waste product of fish-processing industry, is used to produce sensor biomaterial. The highly water soluble DNA forms complex polymers upon interaction with cationic surfactants. The complex is insoluble in water but completely soluble in alcohol [22], which is not only privileged in terms of casting DNA thin-films over any surface but also supreme for sensing applications. We have utilized the exceptional affinity of DNA towards different dyes in order to encapsulate DCFH into the DNA-complex matrix [23]. The DCFH is impregnated into the DNA matrix during the complexation reaction with a cationic surfactant, CTAB (cetyltrimethyl ammonium bromide) in aqueous solution. The DCFH entrapped biomaterial (DNA-DCFH-CTAB complex) eventually dried and re-solubilized in alcohol. We have sensitized a chemically etched fiber tip by dipping the tip into the biomaterial in alcohol solution and dried in air for a minute (dip-coating) for direct measurement of ROS/oxidative stress in physiologically relevant environments. The regenerative use of the fiber tip can be achieved by wiping the fiber tip using ethanol followed by further dip-coating of the tip. Here, we have followed the increase in fluorescence intensity and quenching of fluorescence intensity of the sensitized fiber tip upon interaction with well-known ROS generator (Mn_3O_4 nanoparticles: NPs [24]) and ROS quencher (sodium azide: NaN_3 [25]), respectively. The effects of blood phantom (aqueous hemoglobin solution) and real blood (mice model) on the sensitized fiber tip have also been studied. The fluorescence of sensitized fiber tip gets increased depending upon the concentration of ROS present in the blood phantom/blood samples. Picosecond time-resolved studies on the sensitized fiber tip in presence of

94

ROS with hemoglobin (Hb)/blood samples have confirmed the reabsorption of fluorophores' energy by Hb/blood. In order to assess the effectiveness of the sensor fiber tip, ROS was monitored directly in anaesthetized mice.

5.2. Result and Discussion

5.2.1. DNA-based Fiber Optic Sensor for Direct *In-vivo* Measurement of Oxidative Stress [26]:

5.2.1.1. ROS Generation Activity of Mn₃O₄ Nanoparticles: In this study, we used citrate functionalized Mn_3O_4 nanoparticles as a ROS generating agent[27]. The UV-Vis spectra of the as prepared NPs (200 µL in 2 mL water: 25 µM) is shown in the Figure 5.1a (blue color). The absorbance maxima at around 290 nm (data not shown) and 429 nm correspond to the high-energy ligand-to-metal charge transfer transition (LMCT) involving citrate-Mn^{4+} interaction and Jahn-Teller (J-T) distorted d-d transitions centered over Mn^{3+} ions respectively [24]. In order to observe the ROS generation ability of the NPs in aqueous media a fluorescent probe DCFH was employed. Oxidation of DCFH by ROS, converts the molecules to DCF, is which highly fluorescent. The prepared DCFH solution was characterized by the absorbance as well as the fluorescence spectra. Figure 5.1a shows that the absorbance of DCFH at around 500 nm is increasing with time from zero to finite values in presence of NPs. For more convenience the time dependant change in absorbance of DCFH at 500 nm in presence and absence of NPs are shown in the inset of the Figure 5.1a. In addition the excitation spectra of DCFH monitored at 530 nm with time is shown in Figure 5.1b. Figure 5.1b also reveals the strong emission of DCFH at around 520 nm, upon excitation at 480 nm, in presence of NPs. The above results indicate that the NPs are efficient generator of ROS, which oxidise the non-fluorescent DCFH to highly fluorescent DCF. In order to investigate the ROS generation efficiency of the NPs, the time dependant fluorescence at 520 nm of the DCFH in presence and absence of NPs is observed (inset of Figure 5.1b). The observed result indicates that the NPs can efficiently generate ROS for more than 15 minutes.

95
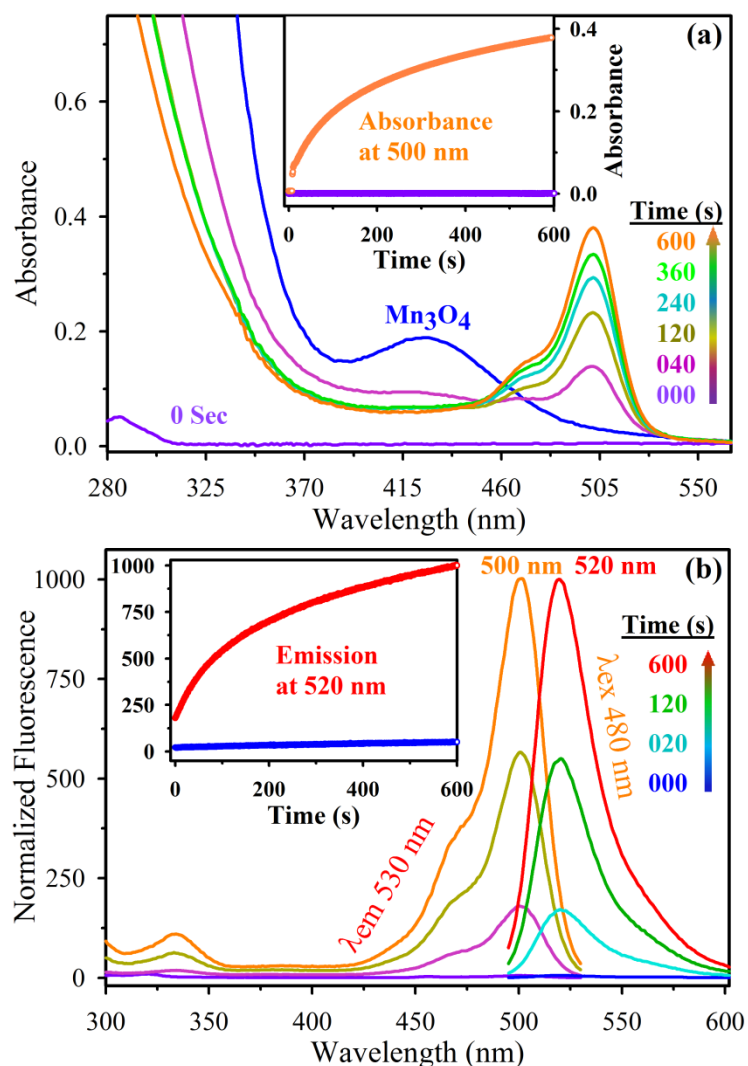
Figure 5.1. *(a) UV-vis absorption spectra of DCFH in presence of Mn_3O_4 NPs with time and Mn_3O_4 NPs (Blue) in aqueous medium. Inset shows the reaction kinetics of DCFH in presence and absence of Mn_3O_4 NPs. (b) Steady-state fluorescence emissions (λ_{ex} = 480 nm) and excitation (λ_{em} = 530 nm) spectra of DCFH in absence and presence of ROS generator NP_S (Mn_3O_4) with time. It has to be noted that the emission peak of DCFH appears at 520 nm. The excitation spectra are collected at detection wavelength of 530 nm to measure complete pattern. Inset shows the reaction kinetics of DCFH in absence and presence of ROS generator NPs.*

5.2.1.2. Characterization of the DNA-based Biomaterial Coated Fiber Tips:

After preparation of the biomaterial and the fiber tip, the DNA-based biomaterial was coated on the etched fiber tip by dip-coating. The overall fiber tip preparation and sensitization with the biomaterial is shown schematically in Figure 3.11a. The SEM image of the biomaterial coated fiber tip (sensor tip) confirmed the sharp needle like shape of the sensitized fiber tip (Figure 3.11a). The comparative microscopic images of
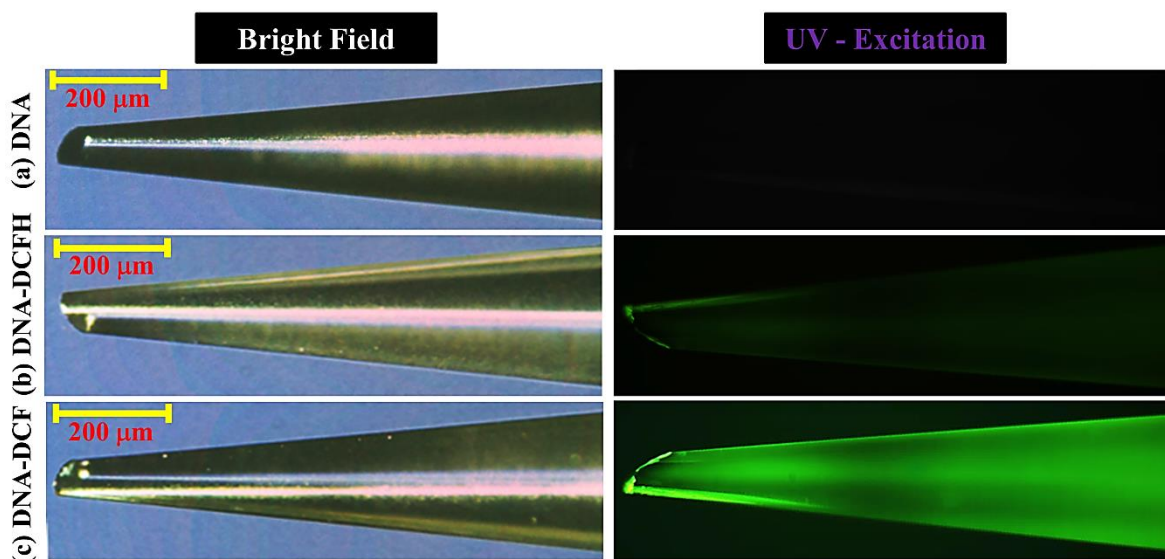
Figure 5.2. *The comparative study of different biomaterial coated fiber tips under bright field (Integration time (t) = 50 ms) and UV excitation (t = 500 ms): (a) DNA coated fiber tip, (b) DNA-Biomaterial coated fiber tip before interaction with NPs, (c) DNA-Biomaterial coated fiber tip after interaction with NPs.*

different biomaterial coated fiber tips under bright field (Integration time (t) = 50 ms) and UV excitation (t = 500 ms) are presented in Figure 5.2. We considered three variants of the biomaterial for our study namely (a) DNA, (b) DNA-DCFH and (c) DNA-DCF (CTAB was common for all). As shown in Figure 5.2, all the observations under bright field were almost the same. However, under UV excitation the fiber tip in the panel (a) was invisible and those in panels (b) & (c) were visible. Though the concentration of biomaterial present in both the fiber tips ((b) & (c)) were same but tip shown in panel (c) fluoresces exceptionally high due to the interaction with NPs. Because in presence of NPs (ROS generator) very low-fluorescent DNA-DCFH was converted to highly fluorescent DNA-DCF.

The indigenously developed experimental setup was used to collect the spectroscopic signal from the biomaterial coated fiber tip, as shown in Figure 3.11b. The emission and excitation spectra of the biomaterial coated fiber tip were recorded under the experimental setup and represented in Figure 5.3a. A low green (at 530 nm) emission was observed from the sensitized fiber tip upon the excitation at 500 nm wavelength. However, no emission was observed from the fiber tip before sensitization. The excitation spectra corresponding to λ_{em} ~ 540 nm reveals the

97
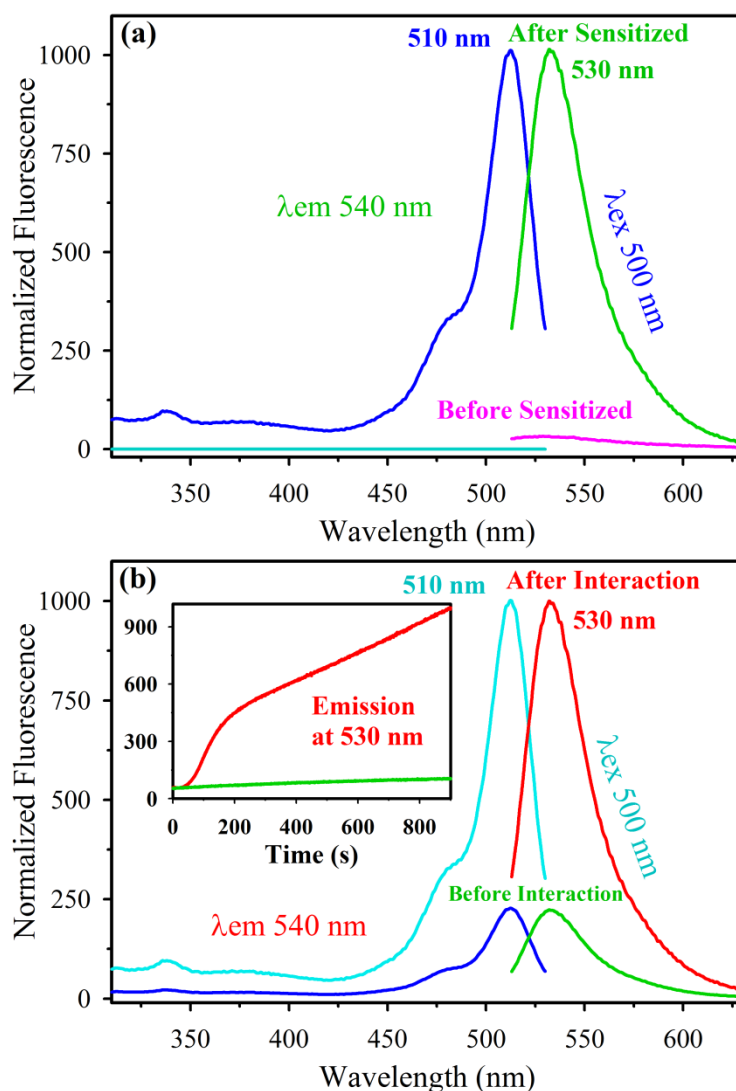
Figure 5.3. *Steady-state fluorescence emissions (λ_{ex} = 500 nm) and excitation (λ_{em} = 540 nm) of: (a) the fiber tip before and after sensitization with DNA-based biomaterial. (b) the sensitized fiber tip before and after interaction with Mn_3O_4 NPs. Inset shows the fluorescence kinetic of the sensitized fiber tip in absence and presence of Mn_3O_4 NPs.*

excitation wavelength maxima to be at around 510 nm. The emission maximum of the DCF was shifted from 520 nm (in methanol) to 530 nm (in DNA-matrix) due to the solvent effect. Significant increase in emission/excitation intensity of the biomaterial coated fiber tip after interaction with Mn_3O_4 NPs was due to the ROS generation in the solution by NPs. DCFH present in the biomaterial on the sensitized fiber tip, on oxidation by ROS forms DCF showing an emission maximum at 530 nm is represented in Figure 5.3b. Inset of the Figure 5.3b reveals that the fluorescence intensity of the sensitized fiber tip is increasing with time due to the continuous

oxidation of DCFH by the NPs in the test solution and is found to increase up to about 8 fold within 15 minutes. The persistent increase in DCF fluorescence represents the continuous ROS measurement ability of the sensor tip.

5.2.1.3. ROS Measurements in Aqueous Media: Different measurement times are reported in the literature for using DCFH assay for ROS measurements, spanning from minutes to hour [28, 29]. As shown in Figure 5.4, we investigated the fluorescence kinetics of the sensor tip over 15 minutes of exposure to ROS generator (NPs) with different concentrations. As demonstrated in Figure 5.4a, we observed an increase in ROS generation with increasing concentrations of NPs in the solution without any saturation in the fluorescence intensity. The observation reveals that the probe fiber tip would be able to monitor the status of ROS of a given medium for at least 15 minutes continuously. A control study on the probe fiber tip dipped into water is also shown in the Figure 5.4a, revealing negligibly small auto-oxidation of DCFH in the biomaterial. In another controlled experiment, we confirmed that the fluorescence kinetics of the sensor tip after dipping into water for 1 hour shows comparable kinetic profile with respect to the un-dipped tip. The observation concludes a negligible leaching of the biomaterial including entrapped DCFH to the solution under investigation. In order to confirm the increased oxidative stress in the solution containing NPs, we used sodium azide (NaN_3), which is a well-known ROS quencher in aqueous solution [25]. As shown in Figure 5.4b, the extent of fluorescence enhancement in the sensor fiber tip decreased with the increase in NaN_3 concentration in the test solution at a fixed NPs concentration (ROS generator). Therefore, the nature of ROS was found to be singlet oxygen, as the oxidation of DCFH decreased significantly in presence of NaN_3, a well-known singlet oxygen quencher [25, 30]. In order to get a quantitative estimation of ROS in various environments including mice blood, we calibrated the fluorescence enhancement of DCF in presence of different measured amounts of H_2O_2, a well-known ROS source in presence of Cu^{2+} ions [25]. Thus, the concentration of ROS measured in our developed sensor tip is essentially equivalent to the concentration of H_2O_2 [31]. Figure 5.4c shows the calibration
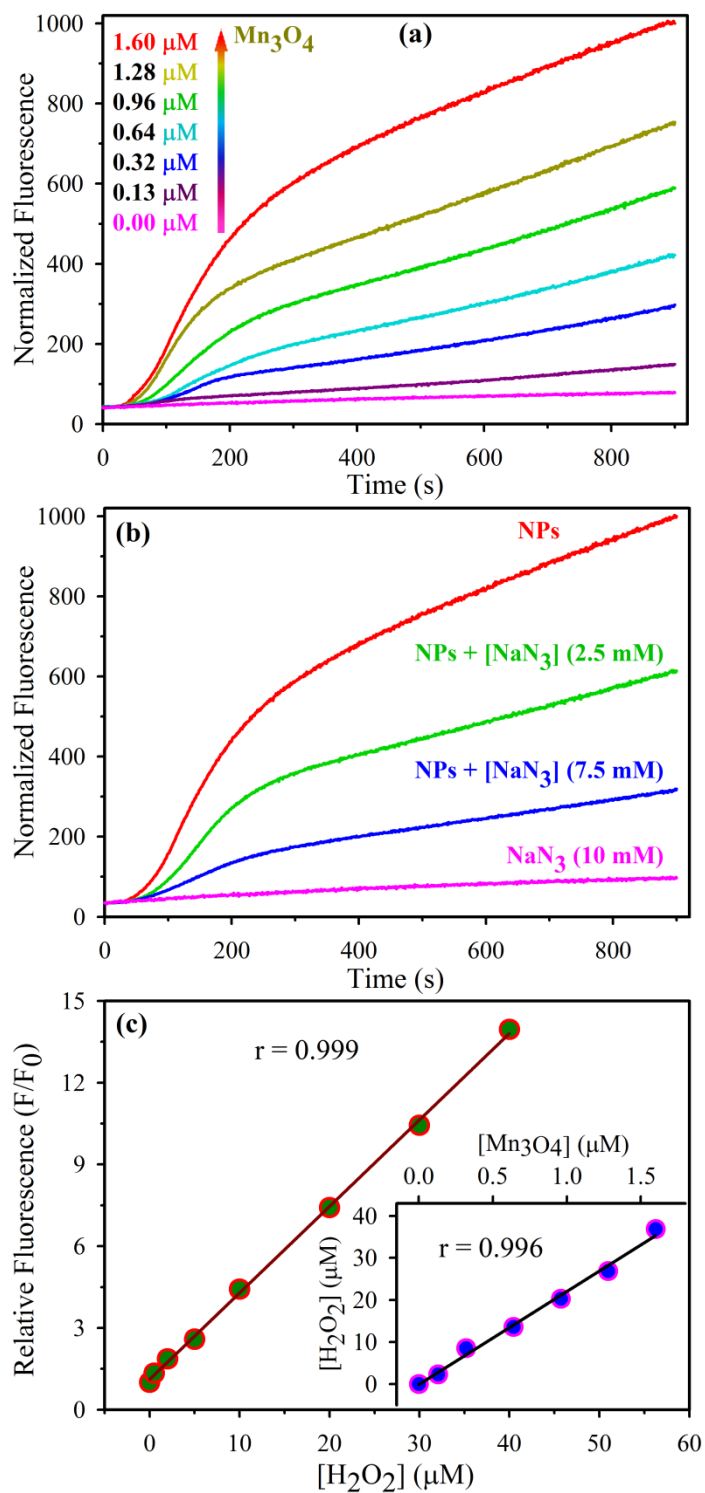
Figure 5.4. *The fluorescence kinetics (emission at 530 nm) of the sensitized fiber tip: (a) with increasing concentrations of NPs (ROS generator), (b) with increasing concentrations of NaN₃ (ROS quencher) keeping fixed NPs concentration (1.60 μM). (c) Calibration curve of relative fluorescent intensity obtained from the reaction between DCFH and H_2O_2 in presence of constant Cu^{2+} ions (150 μM) with incubation time 15 minutes. The linear dependency is remarkable. Inset shows the relation between concentration of NPs and equivalent H_2O_2 concentration estimated from relative DCF fluorescence.*

relationship between the relative fluorescence intensity (F/F_0: F is the fluorescence intensity of DCF in presence of ROS generator and F_0 is the fluorescence intensity of DCF in absence of ROS generator) and H_2O_2 concentration in presence of constant Cu^{2+} ions (150 μM). The calibration equation obtained from the linear regression curve is $F/F_0 = 0.317 \times [H_2O_2] + 1.11$, with the Pearson's correlation coefficient r = 0.999. We also calibrated the concentration of the NPs used in our present study as ROS generator in terms of equivalent H_2O_2 concentration using the relative fluorescence of DCF in the corresponding solution as shown in the inset of Figure 5.4c. As shown in the figure, the estimated ROS concentration values in the aqueous medium generated by 0.13, 0.32, 0.64, 0.96, 1.28 and 1.60 μM NPs are found to be 2.30, 8.48, 13.54, 20.27, 26.84 and 36.85 μM, respectively.

5.2.1.4. ROS/Oxidative Stress Measurement in Blood Phantom and Mice Blood: Direct measurement of oxidative stress in physiological milieu is very difficult due to following two important factors. Firstly, the concerned ROS are having very short lifetime [32] revealing erroneous results upon detachment of test sample (e.g. blood) from the main body. This fact requires an *in-vivo* placement of the sensor probe to the main body. Secondly, the reaction of the sensor probe with the test sample reveals toxicity in the main body during the measurements. *In-vivo* measurements require a non-toxic sensor probe for the measurement of oxidative stress in physiological milieu. Thus, oxidative stress assessment is usually performed by indirect methods measuring ROS-induced oxidative damages on proteins, membrane lipids and DNA, the most vulnerable biological targets for oxidative stress [33]. Although thousands of articles have been attributed for evaluation of oxidative damage by measuring the increase of protein oxidation, direct measurement of ROS in the biological system is still missing. Here, we choose blood as a system for direct monitoring of ROS levels. It is well known that red blood cells (RBC) may exert both antioxidant and pro-oxidant activity because of the high-iron concentration [33]. Keeping this fact in mind we select hemoglobin (Hb) solution as a blood phantom for

examining its pro and antioxidant activity. Figure 5.5a reveals that the fluorescence intensity of the developed sensor tip significantly increases with time in presence of Hb compared to that in control sample (water). The observation is consistent with the pro-oxidant activity of Hb in the proximity of the sensor probe. It is also reported that Hb shows antioxidant properties in environment with high oxidative stress [34]. Figure 5.5a presents how the ROS generation ability of NPs is reduced due to the presence of Hb in the solution. The Figure also shows that even in the presence of fixed concentration of ROS generator NPs (1.28 µM) the oxidation of DCFH was dramatically decreased with increasing concentration of Hb resulting in a decrease in the fluorescence intensity of the sensor tip. The above results reveal that the developed sensor tip is able to efficiently measure the presence of ROS, the major cause of oxidative stress in blood phantom.

In order to measure the oxidative stress in real blood, blood samples were collected from retro-orbital sinus plexus of Swiss albino mice. Freshly obtained blood samples were immediately diluted into two different ways and stored on ice prior to analysis. For sample-1, 5 µL of fresh blood was diluted in 4 mL of phosphate buffered saline water. For sample-2, 5 µL of the same blood was diluted in 4 mL of phosphate buffered saline water in presence of different concentrations of oxidant (NPs). The ROS measurement study was carried out with our indigenously developed setup (Figure 3.11b) using the prepared samples. As shown in Figure 5.5b, the fluorescence intensity (at 530 nm) of the sensor fiber increases significantly in sample-1 compared to that in buffer solution. The study demonstrates the pro-oxidant activity of the whole blood. Figure 5.5b also shows that the fluorescence intensity of the DCF in presence of sample-2 increases with increasing oxidant (NPs) concentration for a fixed concentration of blood in the medium. The observation is consistent with the fact, that the developed sensor would be able to measure oxidative stress and its different extents in real blood sample.
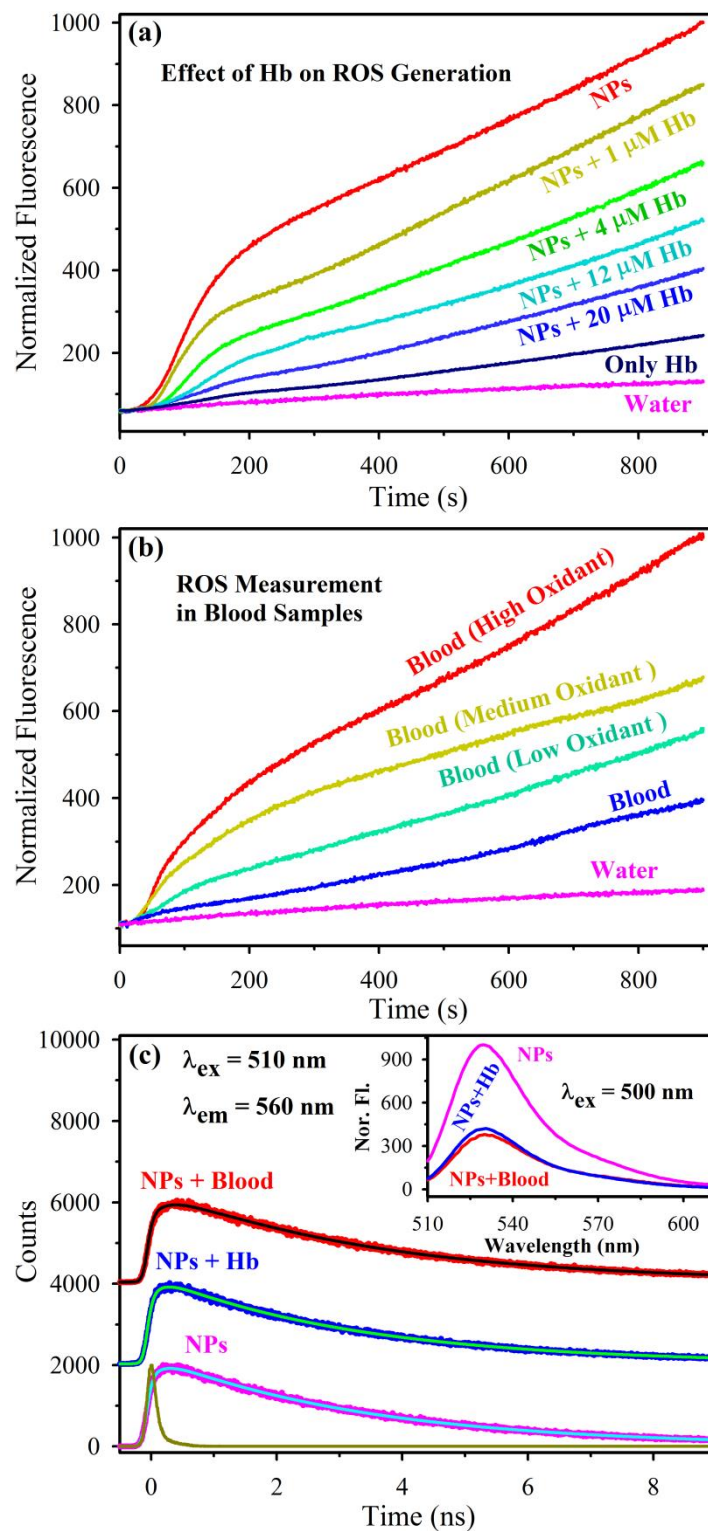
Figure 5.5. *(a) The effect of Hb concentration on fluorescence kinetics of the sensor tip with fixed oxidant (NPs) concentration (1.28 μM). (b) Oxidative stress measurement in mice blood with different concentrations of oxidant (NPs). (c) Picosecond time-resolved fluorescence transients of the sensor tip in presence of NPs, NPs + Hb and NPs + Blood upon excitation at 510 nm wavelength. Inset shows the corresponding steady-state fluorescence spectra upon excitation at 500 nm wavelength.*

The inset of Figure 5.5c presents the steady-state fluorescence of the sensor fiber in presence of NPs (ROS generator), Hb+NPs and whole blood+NPs in aqueous solution. A significant quenching of the florescence intensity in presence of Hb and whole blood is evident. In order to understand the photo-physical basis of the fluorescence quenching, we performed picosecond resolved fluorescence transient measurement monitored at 560 nm (excitation 510 nm) as shown in Figure 5.5c. The fluorescence transients of sensor tip in presence of NPs exposed single-exponential time constants with lifetime (τ) of 3.4 ns, which remained unchanged in the presence of Hb and whole blood. The results rule out any kind of exited state processes including electron transfer and/or complexation of the biomaterial on the fiber tip and Hb/blood in the aqueous medium, other than mere re-absorption of the fiber tip emission by the Hb/whole blood [35].

5.2.1.5. Direct In-vivo Measurement of Oxidative Stress in Mice Model: In order to validate the developed sensor in preclinical model, we induced mice with CCl_4 to generate oxidative stress [30]. To confirm the induction of oxidative stress in the CCl_4 induced mice, we evaluated some serum parameters (SOD, Catalase, AST, Total Bilirubin and Lipid Peroxidation) which are conventionally considered as the potential biomarkers [30]. SOD and Catalase are the two mutually supportive kingmakers of *in-vivo* antioxidant defence system. SOD converts superoxide anions to H_2O_2, which is further converted to H_2O with the help of GPx and CAT. SOD also inhibits hydroxyl radical production. In our study, as shown inset of the Figure 5.6a, CCl_4 caused substantial downregulation of the SOD ($\sim$28.9%) and CAT ($\sim$32.9%) activities, indicating the introduction of high oxidative stress. We further studied the effect of CCl_4 on liver function parameters as the liver serves as the primary target organ of this genotoxic agent. Figure 5.6a presents both AST ($\sim$369.1%) and total bilirubin level ($\sim$266.7%) were much higher than the respective control groups; further signifying that free radicals induced severe liver damage. Rapid lipid peroxidation of the membrane structural lipids was proposed as the basis of CCl_4 liver toxicity. So, we
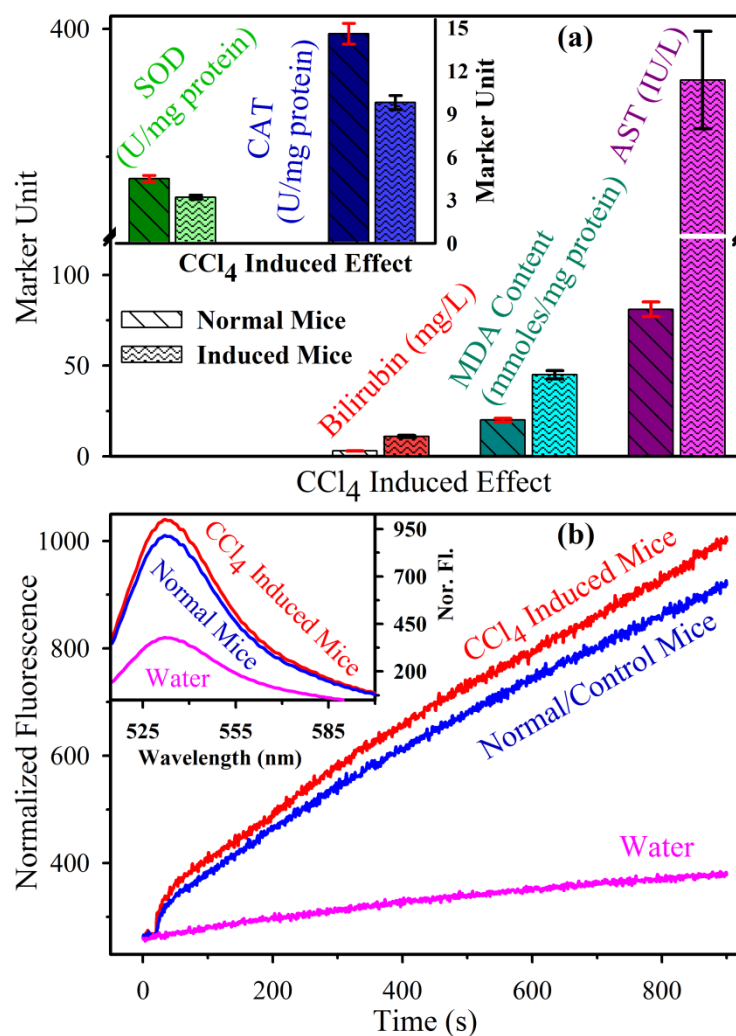
Figure 5.6. *(a) Comparison of conventional biomarker levels (serum and liver function parameters), which are used to evaluate the oxidative damage, between the normal (control) and CCl₄ induced mice. (b) Direct in-vivo measurement of oxidative stress in mice model by the developed fiber optics sensor. Inset shows the corresponding steady-state fluorescence spectra of the direct in-vivo measurement at the end (after 15 minutes).*

monitored the levels of MDA, an index of oxidative damage and one of the decomposition products of the peroxidised polyunsaturated fatty acids, to evaluate the effect of CCl₄ induction. As shown in Figure 5.6a, significant increase of MDA (~125.0%) in the CCl₄-treated group strongly confirmed that the substantial oxidative damage had been induced. All the results are tabulated in Table 5.1. The direct *in-vivo* measurements of oxidative stress in both normal (control) as well as CCl₄ -treated mice were carried out by our developed sensor for the comparisons (data were collected following the describe method using the developed setup (Figure 3.11b). The obtained

Table 5.1: *Comparison of various oxidative stress markers between normal and CCl₄ intoxicated mice.*

Marker	Normal mice	CCl₄ induced mice	Change in %	p value
SOD (U/mg protein)	4.5 ± 0.3	3.2 ± 0.4	28.9	0.0025
CAT (U/mg protein)	14.6 ± 1.2	9.8 ± 1.1	32.9	0.0011
AST (IU/L)	81 ± 5.2	380 ± 40.1	369.1	0.0006
BILIRUBIN (mg/dL)	0.3 ± 0.04	1.1 ± 0.05	266.7	0.0001
MDA Content (mmoles/mg protein)	20 ± 3.1	45 ± 4.2	125.0	0.0014
Measured ROS (µM) using the proposed method	4.16 ± 0.12	5.00 ± 0.20	20.2	0.0009

Data are expressed as mean $\pm$ standard deviation (n = 4). p value computed using unpaired t-test (parametric) with Welch's correction. p <0.01 compared to normal mice.

results were then validated with the conventional biomarker levels which are used to evaluate the oxidative damage as mentioned above. As shown in Figure 5.6b, the collected fluorescence intensity (at 530 nm, up to 15 minutes) of the sensor from the CCl₄ induced mice is significantly different compared to the control one (normal mice) at every time. The difference is evident in the steady-state fluorescence spectra also, as shown inset of the Figure 5.6b. The concentration of ROS in the CCl₄ induced and normal mice are estimated to be 5.00 ± 0.20 µM and 4.16 ± 0.12 µM respectively ($p < 0.01$). The direct *in-vivo* measurement of oxidative stress in mice model is shown
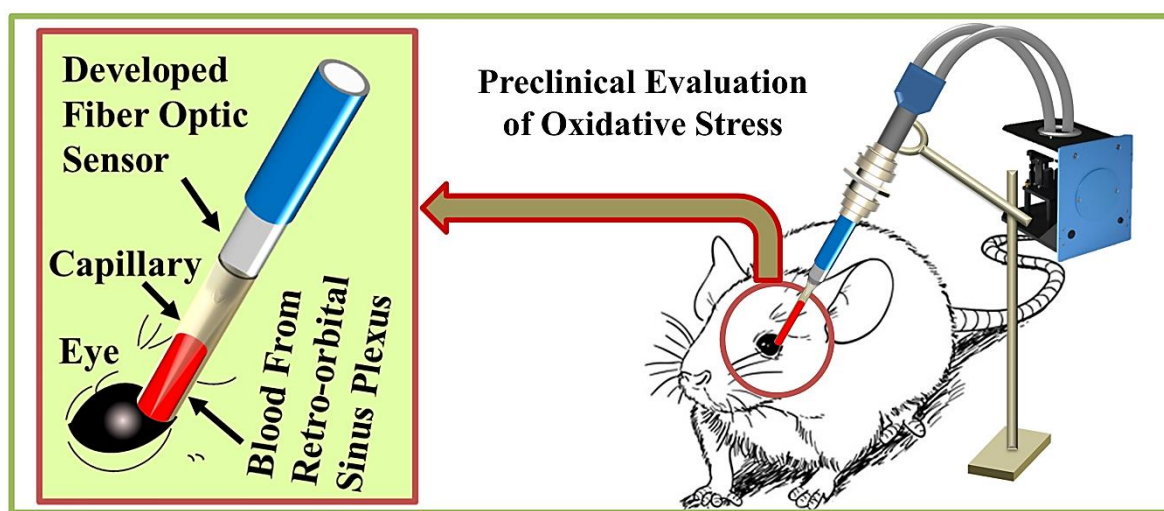
Figure 5.7. *Schematic representation of the direct in-vivo measurement of oxidative stress in mice model by the developed fiber optics sensor.*

schematically in the Figure 5.7. The above facts indicate the sensor result is well consistent with the conventional biomarker levels for evaluation of oxidative stress. The observed results also confirm the direct *in-vivo* oxidative stress measurement ability of the developed sensor in the living animal models. Although a thorough study for direct *in-vivo* oxidative stress measurement is under investigation, the proof of concept experiment clearly showed a promise for the direct *in-vivo* measurement of oxidative stress.

5.3. Conclusion

In summary, we have developed a DNA-based portable fiber optic sensor for the direct *in-vivo* measurement of oxidative stress in physiological milieu. Impregnated DCFH assay in a water insoluble DNA-lipid complex at the sensitized tip of a multimodal optical fiber is shown to play a crucial role in the sensing mechanism. Significant increase in fluorescence intensity of the indigenously developed biomaterial functionalized fiber tip is shown to be a key factor for the aforementioned sensing. Moreover, the sensor is shown to monitor ROS/ oxidative stress efficiently and continuously in the aqueous medium as well as in the biological samples, without forming any complexations or reaction with the biological samples. To our understanding, the scope for further development of the concept is extensive, which offers great potential for the development of economical, portable devices for the direct *in-vivo* measurement of oxidative stress efficiently. In the future, our study is expected to find relevance in the quick measurement of oxidative stress in human subjects in a minimally invasive way.

References

1. B. Kalyanaraman, V. Darley-Usmar, K. J. A. Davies, P. A. Dennery, H. J. Forman, M. B. Grisham, G. E. Mann, K. Moore, L. J. Roberts and H. Ischiropoulos; Measuring reactive oxygen and nitrogen species with fluorescent probes: challenges and limitations. *Free Radic. Biol. Med.* 52 (2012), 1.

2. V. J. Hammond, J. W. Aylott, G. M. Greenway, P. Watts, A. Webster and C. Wiles; An optical sensor for reactive oxygen species: encapsulation of functionalised silica nanoparticles into silicate nanoprobes to reduce fluorophore leaching. *Analyst* 133 (2007), 71.

3. J. T. Hancock, R. Desikan and S. J. Neill; Role of reactive oxygen species in cell signalling pathways. *Biochem. Soc. Trans.* 29 (2001), 345.

4. H. M. Cochemé, C. Quin, S. J. McQuaker, F. Cabreiro, A. Logan, T. A. Prime, I. Abakumova, J. V. Patel, I. M. Fearnley, A. M. James, C. M. Porteous, R. A. J. Smith, S. Saeed, J. E. Carré, M. Singer, D. Gems, R. C. Hartley, L. Partridge and M. P. Murphy; Measurement of H_2O_2 within living drosophila during aging using a ratiometric mass spectrometry probe targeted to the mitochondrial matrix. *Cell Metab.* 13 (2011), 340.

5. S. Martins, J. P. S. Farinha, C. Baleizao and M. N. Berberan-Santos; Controlled release of singlet oxygen using diphenylanthracene functionalized polymer nanoparticles. *Chem. Commun.* 50 (2014), 3317.

6. M. Karlsson, T. Kurz, U. T. Brunk, S. E. Nilsson and C. I. Frennesson; What does the commonly used DCF test for oxidative stress really show? *Biochem. J.* 428 (2010), 183.

7. J. M. Burns, W. J. Cooper, J. L. Ferry, D. W. King, B. P. DiMento, K. McNeill, C. J. Miller, W. L. Miller, B. M. Peake, S. A. Rusak, A. L. Rose and T. D. Waite; Methods for reactive oxygen species (ROS) detection in aqueous environments. *Aquat. Sci.* 74 (2012), 683.

8. J. Chan, S. C. Dodani and C. J. Chang; Reaction-based small-molecule fluorescent probes for chemoselective bioimaging. *Nat. Chem.* 4 (2012), 973.

9.   A. R. Lippert, G. C. Van de Bittner and C. J. Chang; Boronate oxidation as a bioorthogonal reaction approach for studying the chemistry of hydrogen peroxide in living systems. *Acc. Chem. Res.* 44 (2011), 793.

10. N. Polley, P. K. Sarkar, S. Chakrabarti, P. Lemmens and S. K. Pal; DNA biomaterial based fiber optic sensor: Characterization and application for monitoring in situ mercury pollution. *ChemistrySelect.* 1 (2016), 2916.

11. S. Heng, M.-C. Nguyen, R. Kostecki, T. M. Monro and A. D. Abell; Nanoliter-scale, regenerable ion sensor: Sensing with a surface functionalized microstructured optical fibre. *RSC Adv.* 3 (2013), 8308.

12. A. J. Steckl; DNA - a new material for photonics? *Nat. Photon.* 1 (2007), 3.

13. K. Tanaka and Y. Okahata; A DNA−lipid complex in organic media and formation of an aligned cast film1. *J. Am. Chem. Soc.* 118 (1996), 10679.

14. C. A. Villarruel, D. D. Dominguez and A. Dandridge; Evanescent wave fiber optic chemical sensor. *In Proc. SPIE.* 0798 (1987) 225.

15. O. S. Wolfbeis; Fiber-optic chemical sensors and biosensors. *Anal. Chem.* 80 (2008), 4269.

16. X. D. Wang and O. S. Wolfbeis; Fiber-optic chemical sensors and biosensors (2008–2012). *Anal. Chem.* 85 (2013), 487.

17. M. Pospíšilová, G. Kuncová and J. Trögl; Fiber-optic chemical sensors and fiber-optic bio-sensors. *Sensors* 15 (2015), 25208.

18. X. D. Wang and O. S. Wolfbeis; Fiber-optic chemical sensors and biosensors (2013–2015). *Anal. Chem.* 88 (2016), 203.

19. M. Purdey, J. Thompson, T. Monro, A. Abell and E. Schartner; A dual sensor for pH and hydrogen peroxide using polymer-coated optical fibre tips. *Sensors* 15 (2015), 29893.

20. I.-W. Kim, J. M. Park, Y. J. Roh, J. H. Kim, M.-G. Choi and T. Hasan; Direct measurement of singlet oxygen by using a photomultiplier tube-based detection system. *J. Photochem. Photobiol. B* 159 (2016), 14.

21. S. Hosaka, T. Itagaki and Y. Kuramitsu; Selectivity and sensitivity in the measurement of reactive oxygen species (ROS) using chemiluminescent microspheres prepared by the binding of acridinium ester or ABEI to polymer microspheres. *Luminescence* 14 (1999), 349.

22. V. G. Sergeyev, S. V. Mikhailenko, O. A. Pyshkina, I. V. Yaminsky and K. Yoshikawa; How does alcohol dissolve the complex of DNA with a cationic surfactant? *J. Am. Chem. Soc.* 121 (1999), 1780.

23. D. Banerjee and S. K. Pal; Dynamics in the DNA recognition by DAPI: Exploration of the various binding modes. *J. Phys. Chem. B* 112 (2008), 1016.

24. N. Polley, S. Saha, A. Adhikari, S. Banerjee, S. Darbar, S. Das and S. K. Pal; Safe and symptomatic medicinal use of surface-functionalized Mn_3O_4 nanoparticles for hyperbilirubinemia treatment in mice. *Nanomedicine* 10 (2015), 2349.

25. M. Bancirova; Sodium azide as a specific quencher of singlet oxygen during chemiluminescent detection by luminol and cypridina luciferin analogues. *Luminescence* 26 (2011), 685.

26. P. K. Sarkar, A. Halder, A. Adhikari, N. Polley, S. Darbar, P. Lemmens and S. K. Pal; DNA-based fiber optic sensor for direct in-vivo measurement of oxidative stress. *Sens. Actuators B: Chem.* 255 (2018), 2194.

27. S. Lei, K. Tang, Z. Fang and H. Zheng; Ultrasonic-assisted synthesis of colloidal Mn_3O_4 nanoparticles at normal temperature and pressure. *Cryst. Growth Des.* 6 (2006), 1757.

28. A. K. Pal, D. Bello, B. Budhlall, E. Rogers and D. K. Milton; Screening for oxidative stress elicited by engineered nanomaterials: Evaluation of acellular DCFH assay. *Dose-Response* 10 (2012), 308.

29. J. M. Veranth, E. G. Kaser, M. M. Veranth, M. Koch and G. S. Yost; Cytokine responses of human lung cells (BEAS-2B) treated with micron-sized and nanoparticles of metal oxides compared to soil dusts. *Part. Fibre. Toxicol.* 4 (2007), 2.

30. A. Adhikari, N. Polley, S. Darbar, D. Bagchi and S. K. Pal; Citrate functionalized Mn_3O_4 in nanotherapy of hepatic fibrosis by oral administration. *Future Sci. OA* 2 (2016), FSO146.

31. J. Zhao and P. K. Hopke; Concentration of reactive oxygen species (ROS) in mainstream and sidestream cigarette smoke. *Aerosol Sci. Technol.* 46 (2012), 191.

32. K. Krumova and G. Cosa; Overview of reactive oxygen species. *RSC* 1 (2016).

33. S. Mrakic-Sposta, M. Gussoni, M. Montorsi, S. Porcelli and A. Vezzoli; A quantitative method to monitor reactive oxygen species production by electron paramagnetic resonance in physiological and pathological conditions. *Oxid. Med. Cell. Longev.* 2014 (2014), 10.

34. M. Minetti and W. Malorni; Redox control of red blood cell biology: The red blood cell as a target and source of prooxidant species. *Antioxid. Redox Signal.* 8 (2006), 1165.

35. P. K. Sarkar, S. Pal, N. Polley, R. Aich, A. Adhikari, A. Halder, S. Chakrabarti, P. Chakrabarti and S. K. Pal; Development and validation of a noncontact spectroscopic device for hemoglobin estimation at point-of-care. *J. Biomed. Opt.* 22 (2017), 055006.

Chapter 6

Spectroscopic Studies for the Potential Application in Environmental Pollution Monitoring of Toxic Heavy Metal Ions

6.1. Introduction

In concern to the human and ecological health impacts, mercury (Hg) and its compounds are considered as well-known toxic and environmental pollutant. Both elemental and ionic mercury can be converted into organo-mercury species (like methylmercury) by bacteria in the environment. These species can easily be bio-accumulated in the food chain and are detrimental to the health of living beings [1, 2]. The sources from which living organisms can be subjected to mercury exposure include water, air, soil and food [2-7]. Mercury exposure has adverse effects on the cardiovascular system, heart, brain, kidney, lungs, central nervous system and immune system of human beings and animals, as well as organic mercury exposure may cause neurologic and mental disorders [2, 8-11]. One of the most usual and stable forms of mercury pollution is water-soluble oxidized divalent mercury (Hg^{2+}) ions, [9, 12] with the maximum permissible level in drinking water and food being ~ 2 ppb [13, 14]. Therefore, the environmental monitoring and determination of low level (sub ppb) concentrations of aqueous Hg^{2+} heavy metal ions has become a vital as well as essential need for our healthy society due to the potential impact of mercury ions on human health and the environment. Several sensitive and selective methods have been developed for qualitative or quantitative detection of Hg^{2+} ion using various analytical sophisticated instruments. Among many different kinds of sensors, optical sensors have comprehensive advantages over other methods due to their versatility, specificity, sensitivity and real-time monitoring ability with fast response time [13, 15]. In the past decade, the commonly adopted techniques for mercury ion detection include atomic

absorption spectrometry (AAS), atomic fluorescence spectrometry (AFS), inductive coupled plasma mass spectrometry (ICP-MS) [16, 17] and electrochemical methods [18]. However, these methods generally involve complicated operation procedures, time-consuming and high costs, which greatly limit their practical applications for routine assay of mercury ion detection [19, 20]. In recent years, a number of efforts have been devoted to design various kinds of chemo-sensors targeting the detection of mercury ions. Such sensors can be utilized for both qualitative and quantitative detection of mercury ions using various analytical and sophisticated instruments [21-24]. Although, the aforementioned methods are sensitive and selective, they are having limitations in practical involving due to rigorous sample preparation and in certain cases, the methods are unstable or not functional in aqueous medium [25, 26]. To resolve such issues, noble metal nanoparticles (NPs) are extensively used in the past few years for high sensitive, selective and cost-effective fluorescence based sensor development. Recently, with the development of nanotechnology, fluorescence quenching of fluorescent dyes by noble metal NPs have attracted remarkable attention in biophotonics, material sciences, as well as sensor applications [27, 28]. Noble metal NPs, in particular, silver nanoparticles (Ag-NPs), have recently emerged as an important quencher in energy transfer/quenching based fluorescence sensor because of their, strong absorption of electromagnetic waves in the visible region due to Surface Plasmon Resonance (SPR) bands and tunable optical properties induced by small changes in size, shape, surface nature and dielectric properties of the media [9, 29, 30]. Ag-NPs based sensors are relatively most efficient and sensitive compared to Au-NPs based sensors because of the (more than 100 -fold) higher visible region molar extinction coefficient of the Ag-NPs (1×10^8 to 6×10^{10} M^{-1}cm^{-1}) compared to Au-NPs [31, 32]. Although, Au-NPs have been widely employed as colorimetric reporters due to the higher and tunable SPR absorption in the visible region. However, few potential problems including sensitivity, selectivity and cost have also been reported in the practical implementations of Au-NPs-based mercury sensors [5, 29, 33-35]. On the other hand, Ag-NPs in solution have been used for sensing mercury based on the

reduction of the SPR extinction; selectivity would be high as such reactions do not occur with the majority of other transition metal ions. Naked eye visible Ag-NPs are extensively used to alter the emission behavior of dye molecules because of their SPR bands matching with the emission bands of the dyes [27, 36]. In addition, fluorescence quenching is one of the most powerful methods used in medical science and material science due to its sensitive and selective information about interaction between a dye and quencher [26, 37]. Fluorescence intensity of a fluorophore is quenched upon interaction with quencher through excited state reaction, ground state complexation (static quenching), collisional interaction (dynamic quenching) or energy transfer [27, 37]. During the interaction between the dye and the NPs through the process of Förster resonance energy transfer (FRET) or nanosurface energy transfer (NSET), NPs work as an energy acceptor and the dye works as an energy donor [38, 39]. There are various methods based on fluorescence/FRET/NSET described in the literature for Hg^{2+} detection [13, 26, 27, 33, 36]. These are efficient techniques for the determination of Hg^{2+}; however, highly selective and ultrasensitive fluorescence-NSET based "turn on" fluorescence mercury sensors are not frequently reported. In addition, some of the fluorescence-NSET based Hg^{2+} sensors are not highly selective i.e. suffer from cross-sensitivity toward other metal ions, particularly Cu^{2+}, Mn^{2+} and Pb^{2+}, and on the other hand require time-effective, sensitive and economical operation that is limited due to time-consuming and complex sample preparation with relatively high cost of starting materials [40-43]. In the given context, development of a highly efficient, low cost, ultrasensitive and highly selective NSET based Hg^{2+} sensors and polymer thin film based prototype sensor for rapid qualitative as well as quantitative analysis of Hg^{2+} in real world water samples is the motivation of the present work.

In this work, we report a highly efficient, low cost NSET based ultrasensitive "turn on" fluorescence sensor and polymer thin film-based portable prototype sensor device for Hg^{2+} ions detection in the background of a wide range of competing heavy metal ions. This report is devoted to study the steady-state fluorescence quenching of the probe PVA-NPA by Ag-NPs and the interaction between them. "Turn on"

fluorescence depends on the interaction between metal NPs (Ag-NPs) and Hg^{2+} ions in the solution. Picosecond time-resolved NSET studies on the ligands with the metal NPs; confirm the excited-state energy transferred of fluorophores through the nonradiative process to metal NPs. The emission of the fluorescence probe PVA-NPA and Ag-NPs mixture solution is increased following the addition of Hg^{2+} ions with a short response time. The sensing mechanism is found to be based on amalgamation of Hg^{2+} with the NPs excluding the need for special functionalization of the NPs for the development of "turn on" fluorescence mercury sensor and thin film-based mercury sensor. The possible interaction between Ag-NPs and mercury ions within the polymer matrix has been examined by transmission electron microscopic (TEM) studies. Characterization of the thin film thickness is performed by using scanning electron microscope (SEM). To the best of our knowledge, this is the first simple and inexpensive portable sensor and prototype device for Hg^{2+} ion detection in environmental water samples with very high selectivity even in the presence of other relevant transition metal ions.

6.2. Result and Discussion

6.2.1. Nanosurface Energy Transfer Based Highly Selective and Ultrasensitive "Turn on" Fluorescence Mercury Sensor [44]:

6.2.1.1. Characterization and Interaction of Ag-NPs with PVA-NPA: The prepared Ag-NPs were characterized by TEM imaging as well as UV-vis spectra. Figure 6.1a represents the TEM image of the citrate capped Ag-NPs. The TEM images reveal the spherical particles in shape with almost uniform size distribution. The average diameter of particles has been found to be 10 nm (inset of Figure 6.1a). The details crystallographic structural information on Ag-NPs was provided by HRTEM. Figure 6.1b illustrates the HRTEM image of the NPs, showing continuous single directional lattice fringes. The interplanar distance of the fringes measured to be about 0.23 nm corresponds to the interplanar distance of Ag [111] lattice planes [45]. The UV-vis spectra of prepared Ag-NPs are shown in the Figure 6.1c (yellow color). The

observed characteristic absorbance band peaking at around 395 nm due to SPR band of the Ag-NPs also indicates the formed particle size is around 10 nm.[32] As shown in Figure 6.1c, the fluorescent dye PVA capped NPA (PVA-NPA) exhibits an absorption band peaking at around 332 nm. In addition to that, the absorption band of PVA-NPA in the presence of Ag-NPs was shifting toward the absorbance maxima of Ag-NPs but the absorbance due to Ag-NPs was unchanged. The absorbance maxima shift may be due to the very strong and broad absorbance of Ag-NPs compared to PVA-NPA in the overlapping region (pseudoshift) or the complex formation between them. The deconvolution of absorbance spectra of PVA-NPA with Ag-NPs (inset of Figure 6.1c)
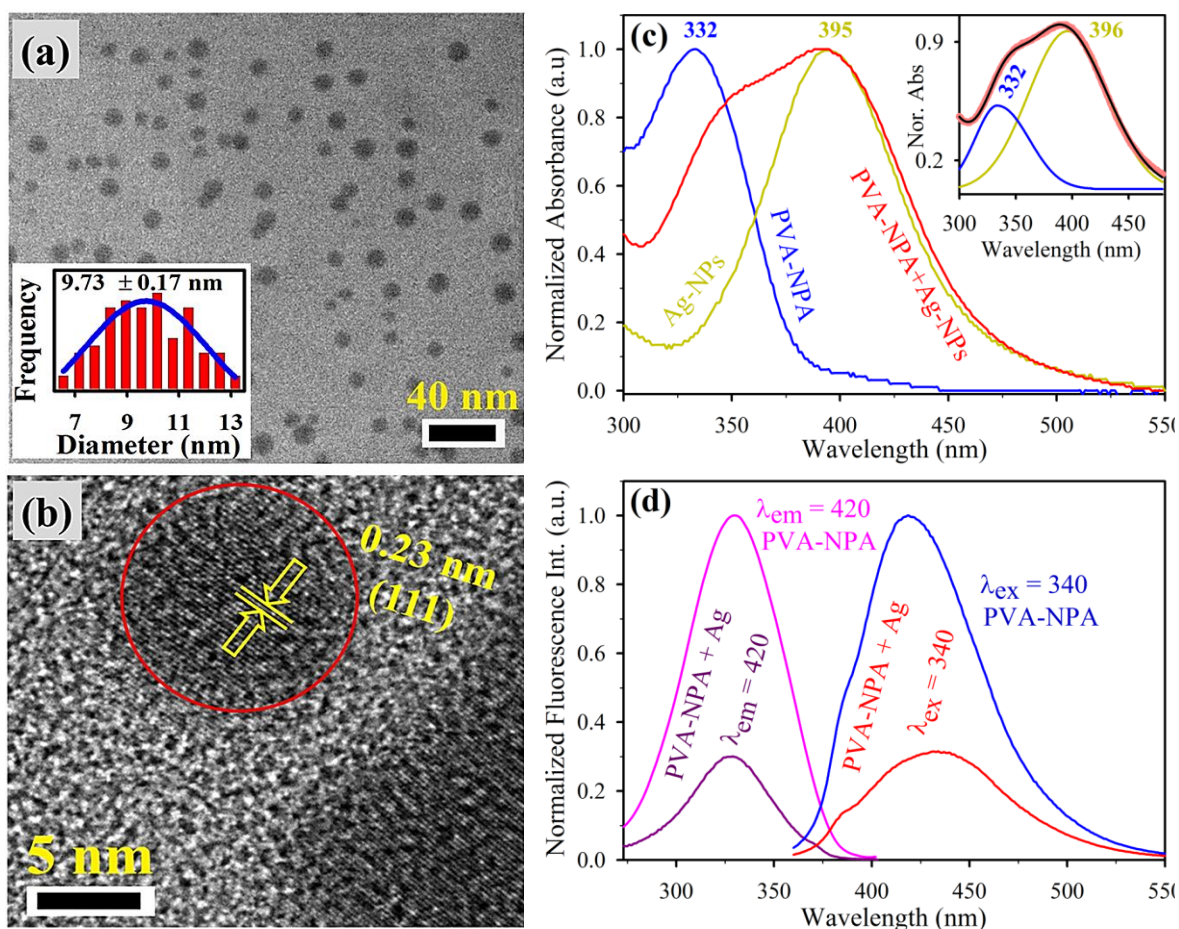
Figure 6.1. *(a) TEM image of Ag-NPs with an average diameter of 10 nm. Inset shows the size distribution of the Ag-NPs. (b) High-resolution TEM (HRTEM) image of Ag-NPs. (c) UV–vis absorption spectra of Ag-NPs (deep yellow), PVA-NPA (blue) and PVA-NPA in the presence of Ag-NPs (red). Inset shows the curve deconvolution of PVA-NPA in the presence of Ag-NPs. (d) Steady-state fluorescence emission (λ_{ex} = 340 nm) and excitation (λ_{em} = 420 nm) spectra of PVA-NPA in the absence and presence of acceptor (Ag-NPs).*

indicates a pseudo shift in the absorbance band of PVA-NPA in the presence of Ag-NPs. All the absorbance spectra are represented after scattering correction following the reported literature [46, 47]. As shown in Figure 6.1d, the strong emission of PVA-NPA was found at around 420 nm, upon 340 nm excitation. A significant quenching of PVA-NPA emission was observed upon addition of Ag-NPs, keeping fixed the concentration of PVA-NPA in the solution. The Figure 6.1d also shows the excitation spectra of PVA-NPA and PVA-NPA with Ag-NPs monitored at the emission peak (420 nm). The excitation spectra for both PVA-NPA and PVA-NPA with Ag-NPs show maxima at around 330 nm. In addition, the excitation spectra for PVA-NPA with Ag-NPs also reveal the pseudo shift which is in accordance to the observations made from the curve deconvolution of absorption spectra.

6.2.1.2. Quenching Mechanisms and Titration Study: Figure 6.2a represents the steady-state fluorescence quenching of PVA-NPA in aqueous solution with increasing concentration of Ag-NPs. Upon 340 nm excitation, the maximum emission wavelength of PVA-NPA was at around 420 nm. In addition, the emission peak is shifting toward higher wavelength with increasing concentration of Ag-NPs. The observed peak shift and decrease in fluorescence intensity of PVA-NPA in the presence of Ag-NPs can arise either due to excited state reaction or collisional interaction (dynamic) or static quenching or both or even through nonmolecular mechanisms where fluorophore itself or other absorbing species attenuates the fluorescence intensity.[48]. The specified quenching mechanism can be determined by lifetime measurements. Figure 6.2b represents the fluorescence transients of PVA-NPA in the absence and presence of different concentrations of Ag-NPs (acceptor) monitored at 445 nm. The fluorescence transients of PVA–NPA exposed multiexponential time constants with an average lifetime (τ_0) of 2.3 ns as tabulated in Table 6.1. Furthermore, it has also been observed that the fluorescence transient for the donor-acceptor system the average lifetime (τ) decreases with the increase in Ag-NPs concentration (Table 6.1) which indicates efficient energy transfer from PVA-NPA donor to Ag-NPs acceptor.

117
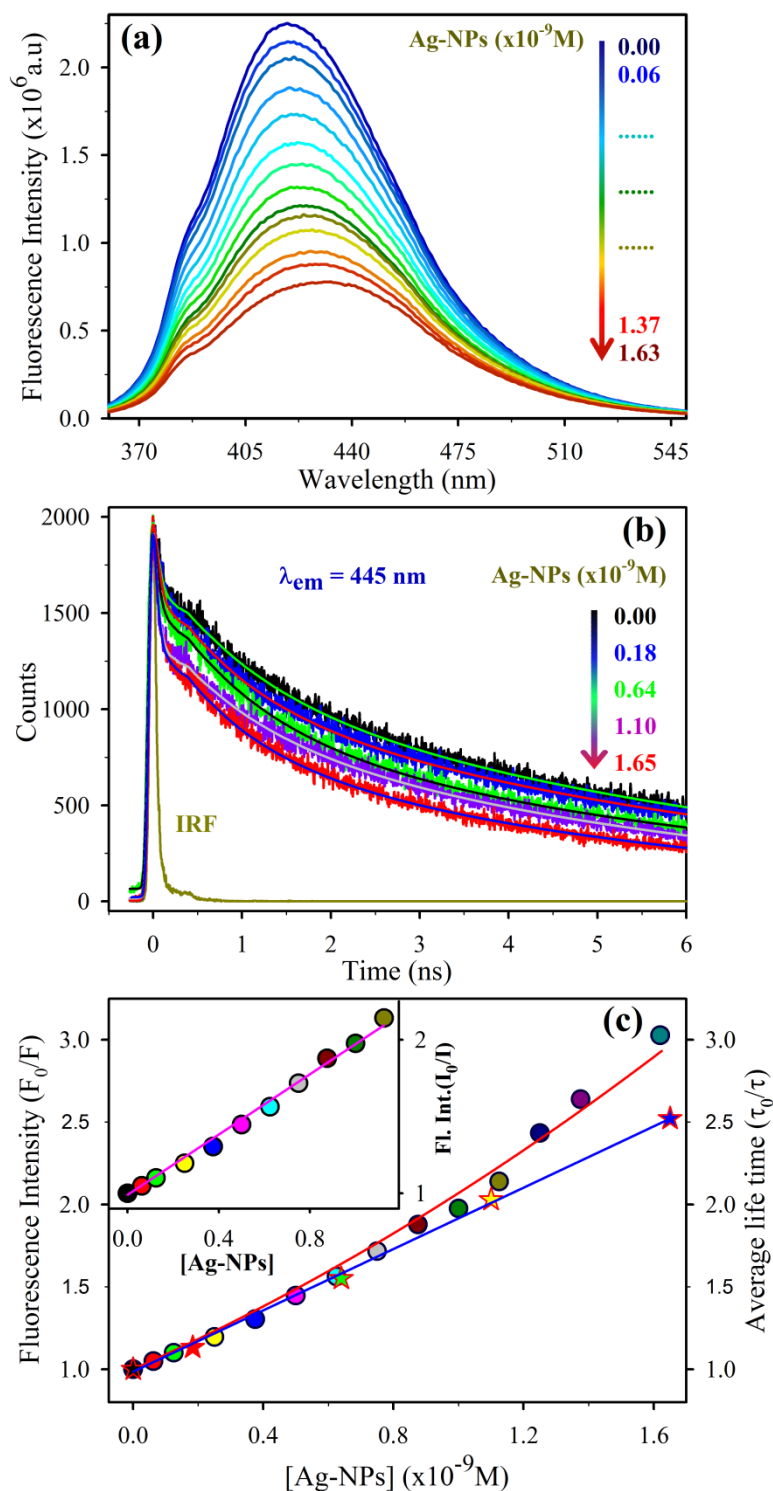
Figure 6.2. *(a) Fluorescence emissions spectra (λ_{ex} = 340 nm) of PVA-NPA with increasing concentrations of Ag-NPs (0.00, 0.06, 0.12, 0.25, 0.37, 0.50, 0.62, 0.75, 0.87, 1.00, 1.13, 1.25, 1.37 and 1.63 $\times 10^9$ M). (b) Picosecond time-resolved fluorescence transients of the donor with increasing concentrations of Ag-NPs (0.00, 0.18, 0.64, 1.10 and 1.65$\times 10^9$ M), upon excitation at 375 nm. (c) Plots of F_0/F vs [Ag-NPs] at 420 nm (red) and τ_0/τ vs [Ag-NPs] (λ_{ex} = 375 nm) (blue). Inset shows the linear part of the plot of F_0/F vs [Ag-NPs].*

118

Table 6.1: *Dynamics of Picosecond Time-Resolved Fluorescence Transients of PVA-NPA in the Absence and Presence of Different Concentrations of Ag-NPs (acceptor), Monitored at 445 nm.*

Figure	Samples	Concentration of Ag-NPs	τ_1(ps)	τ_2(ns)	τ_3(ns)	τ_{avg} (ns)
Figure 6.2(b)	PVA-NPA	0.00	54 (53.4%)	1.0 (16.0%)	6.9 (30.5%)	2.3
	PVA-NPA+Ag-NPs	0.55×10^{-9} M	48 (56.4%)	0.9 (15.7%)	6.6 (27.9%)	2.0
		1.90×10^{-9} M	42 (60.4%)	1.0 (16.9%)	5.7 (22.7%)	1.5
		3.30×10^{-9} M	32 (72.6%)	1.0 (9.4%)	5.6 (18.0%)	1.1
		4.95×10^{-9} M	30 (73.3%)	0.8 (11.3%)	5.1 (15.4%)	0.9

In order to understand the quenching mechanism, the relative change in fluorescence intensity and average lifetime of PVA-NPA has been plotted as a function of the quencher (Ag-NPs) concentration as shown in Figure 6.2c. For the collisional (dynamic) quenching, the relative change in fluorescence intensity and average lifetime is linearly related to the quencher concentration, as described by the well-known Stern–Volmer (SV) equation [49].

$$F_0/F = 1 + k_q\tau_0[Q] = 1 + K_{SV}[Q] \tag{6.1}$$

and
$$\tau_0/\tau = 1 + k_q\tau_0[Q] = 1 + K_D[Q] \tag{6.2}$$

where k_q is the bimolecular quenching constant, τ_0 and τ are the lifetime of the fluorophore in the absence and present of quencher, respectively, [Q] is the quencher concentration, F_0 and F are the fluorescence intensities in the absence and presence of quencher, respectively, K_{SV} is the Stern-Volmer constant and K_D is the dynamic quenching constant. In the case of pure collisional (dynamic) quenching $\tau_0/\tau = F_0/F$ while for static quenching F_0/F increases but τ remains unchanged i.e, $\tau_0/\tau = 1$.[36, 49] As shown in Figure 6.2c for the quencher concentration below 1.13×10^{-9} M a linear SV plot F_0/F vs [Q] (inset of Figure 6.2c) with almost equal slope value of the plot τ_0/τ vs [Q] has been observed. The observed results indicate that the quenching mechanism is purely collisional (dynamic) for the quencher (Ag-NPs) concentration

lower than 1.13×10^{-9} M. Then it is possible to estimate the dynamic quenching constant (K_D) and the Stern-Volmer constant (K_{SV}) based on eqs 6.1 and 6.2. It turns out that K_{SV} and K_D are equal to 0.98×10^9 M^{-1} and 0.93×10^9 M^{-1} respectively. Now, in the case of higher concentrations of Ag-NPs, the nonlinear upward curvature SV plot (Figure 6.2c) suggests that maybe both dynamic and static quenching mechanisms are occurring. When both static and dynamic quenching mechanisms occur, the SV equation gets modified as [49],

$$F_0/F = (1 + k_q \tau_0 [Q])(1 + K_S [Q]) \tag{6.3}$$

where, K_S represents the static quenching constant. In such a case the plot F_0/F vs [Q] will have an upward curvature due to the $[Q]^2$ term, which accounts for the upward curvature in our SV plots shown in Figure 6.2c.

6.2.1.3. FRET and NSET Studies: In order to rationalize the above quenching phenomena picosecond resolved fluorescence spectroscopy was performed. As shown in Figure 6.3a, a huge spectral overlap (overlap integral value [$J(\lambda)$] is equal to 1.06×10^{19} M^{-1} cm^{-1} nm^4) between the emission spectrum of PVA-NPA and absorption spectrum of Ag-NPs makes these two entities excellent donor–acceptor pairs, suggesting an efficient energy transfer (ET) between them. To confirm the resonance type of energy transfer from PVA-NPA to Ag-NPs a picosecond resolved fluorescence study was monitored at 445 nm upon excitation at 375 nm wavelength. The inset of Figure 6.3b represents the steady-state fluorescence spectra of PVA-NPA in the absence and presence of Ag-NPs that indicates the energy transfer occurs between the donor and acceptor. For further confirmation, we measured the excited state lifetime of PVA-NPA with and without Ag- NPs as shown in Figure 6.3b. The time constants of the fluorescence transients at 445 nm for PVA-NPA and PVA-NPA with Ag-NPs revealed multiexponential decay, with an average lifetime of 2.3 and 0.90 ns, respectively. The details of the lifetime components of the transients are tabulated in Table 6.2. A significant faster component observed in donor-acceptor system which indicates efficient ET occurs from PVA-NPA to Ag-NPs. Upon utilization of the FRET scheme [50] the donor-acceptor distance was found to be 18.13 nm. As the

calculated donor-acceptor distance exceeds 100 Å, the appropriate model for our system is NSET, which typically occurs if donors are located too close to acceptors
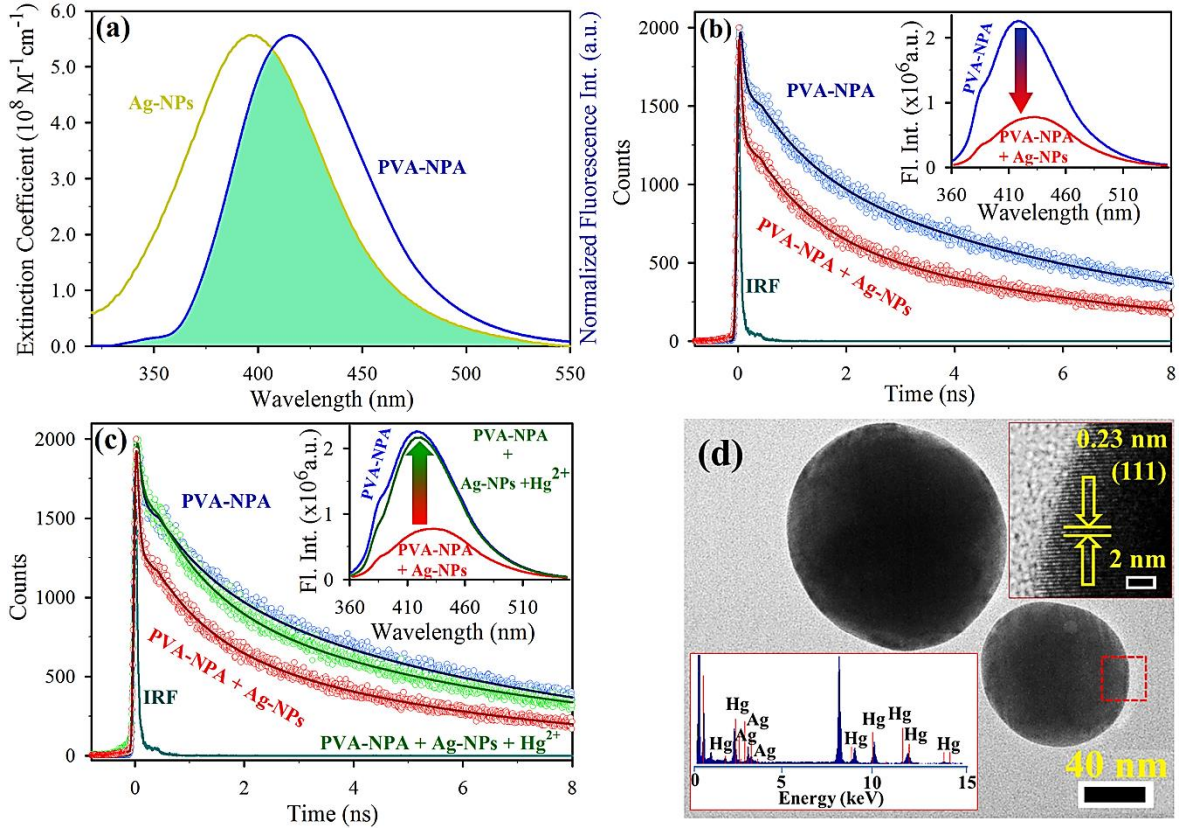
Figure 6.3. *(a) Spectral overlap between emission spectrum of donor (PVA-NPA) and the absorption spectrum of acceptor (Ag-NPs). (b) Picosecond time-resolved fluorescence transients of donor in the absence and presence of the acceptor, monitored at λ_{em} = 445 nm. Inset shows corresponding fluorescence emissions spectra (λ_{ex} = 340 nm). (c) Picosecond time-resolved fluorescence transients of the PVA-NPA+Ag-NPs complex upon interaction with Hg^{2+} metal ions, monitored at λ_{em} = 445 nm. Inset shows corresponding fluorescence emissions spectra (λ_{ex} = 340 nm). (d) TEM image of the complex PVA-NPA+Ag-NPs after interaction with Hg^{2+} ions. Uper inset shows the HRTEM image obtained from the highlighted (red square) region and lower inset shows the EDAX spectra.*

Table 6.2: *Dynamics of Picosecond Time-Resolved Fluorescence Transients of PVA-NPA, PVA-NPA +Ag-NPs and PVA-NPA+Ag-NPs+Hg^{2+}, Monitored at 445 nm.*

Figure	Samples	τ_1(ps)	τ_2(ns)	τ_3(ns)	τ_{avg}(ns)
Figure 6.2(b) & 6.3(c)	PVA-NPA	54 (53.4%)	1.0 (16.0%)	6.9 (30.5%)	2.3
	PVA-NPA+Ag-NPs	30 (73.3%)	0.8 (11.3%)	5.1 (15.4%)	0.9
	PVA-NPA+Ag-NPs+Hg²⁺	54 (49.4%)	1.0 (23.5%)	6.7 (27.1%)	2.1

surface [51]. In order to approve the NSET model, the distance between donor and acceptor is determined to be 5.66 nm (d_0 = 6.27 nm) from eqs 2.11 and 2.13, respectively. Herein, we propose NSET from the donor PVA-NPA to the acceptor Ag-NPs, as the measured donor-acceptor distance is comparable to the radius (~ 5 nm) of the silver NPs. Hence, it is worth emphasizing that the energy transfers from PVA-NPA to Ag-NPs results in the quenching of PVA-NPA emission.

6.2.1.4. Sensing Mechanism for Detection of Hg^{2+} Ions: In order to understand, how the quenching phenomena as well as lifetime of the dye are affected by the metal Hg^{2+} ions, we furthermore performed the picosecond resolved fluorescence transients at 445 nm for the quenched system in the presence of Hg^{2+} ions. The inset of Figure 6.3c shows the drastic emissions of the quenched system in the presence of Hg^{2+} ions, which are almost same as the emissions of the PVA-NPA system, which indicates no energy transfer occurs between the donor (PVA-NPA) and acceptor (Ag-NPs) in the presence of Hg^{2+} ions. For more confirmation we present the fluorescence transient spectra in Figure 6.3c, which shows the decay lifetime of the donor-acceptor system in the presence of Hg^{2+} ions is similar to that in the PVA-NPA system. The detailed lifetime components of the transients are tabulated in Table 6.2. The observed result indicates "turn on" fluorescence as well as "turn off" NSET that is deactivation of NSET phenomena are occurring in presence of Hg^{2+} ions. This "on-off" phenomenon is happening in the presence of Hg^{2+} ions due to the aggregation [52, 53] of metal NPs as well as the amalgam formation of Ag-NPs with Hg^{2+} ions [14, 54, 55]. The amalgam formed by reduction of Hg^{2+} in the presence of silver nanoparticles [14, 56, 57]. Silver nanoparticles reduce Hg^{2+} to form the amalgam at the surface of the nanoparticles within the polymer matrix. The oxidation state of the Ag-nanoparticles is also reported to be changed (from 0 to +1) at the surface, leading to significant reduction and blue shifting of the SPR band (reduction of effective sizes of the Ag-NPs upon Hg^{2+} amalgamation), imparting remarkable selectivity for the sensing response. As such reactions do not occur with the majority of other transition metal ions, high selectivity is expected. In addition to that, in the time of amalgamation, the Ag-NPs lead to

aggregation, leaving free the PVA-NPA dye. Due to aggregation, Ag-NPs lose SPR band and increase the particles size, and as a result the donor-acceptor system behaves like a PVA-NPA system. The overall sensing mechanism is represented schematically in scheme 6.1. The aggregations of metal NPs as well as the amalgam formation of Ag-NPs with Hg are further confirmed by the TEM image and EDAX spectra as shown in Figure 6.3d and the lower inset. The HRTEM image obtained from the square part of the aggregated Ag-NPs, shown in the upper inset of Figure 6.3d. The continuous single directional lattice fringe with measured interplanar distance of about 0.23 nm corresponds to the interplanar distance of Ag [111] lattice planes. The observed result confirms the aggregation of Ag-NPs as well as the amalgam formation of Ag-NPs with Hg.
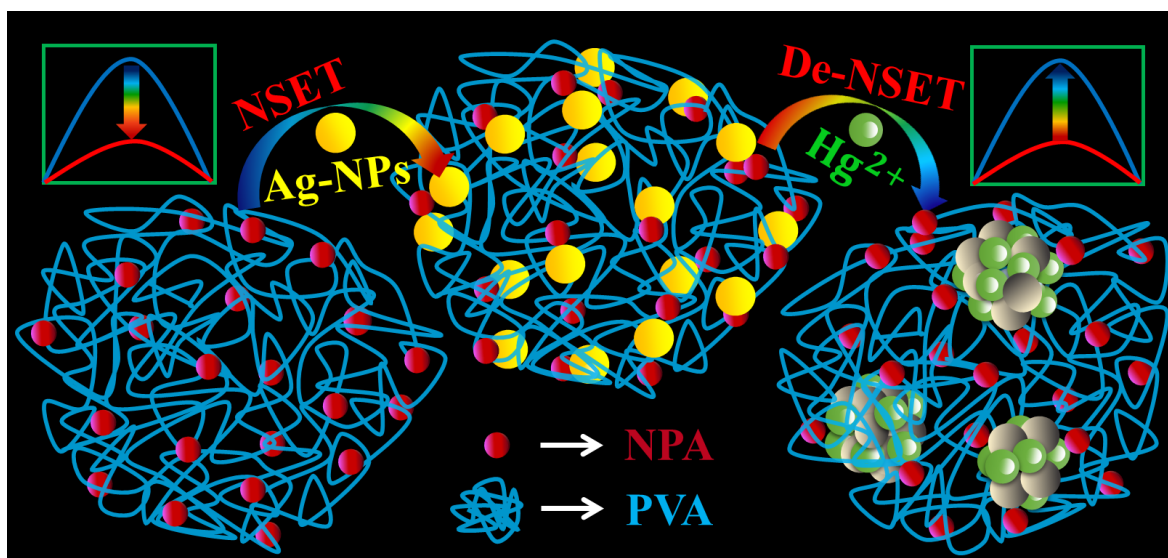
Scheme 6.1. *Schematic representation of the Nano-Surface Energy Transfer (NSET) between PVA-NPA and silver nanoparticles (Ag-NPs) and De-NEST after addition of mercury (Hg^{2+}) ions due to amalgamation of Ag-NPs with Hg^{2+} ions.*

6.2.1.5. Factors Affecting the Sensing of Hg^{2+} Ions: For better analytical performance and in order to obtain a highly sensitive sensor, the experimental conditions were optimized. We first studied the concentration effects of PVA-NPA and Ag-NPs on Hg^{2+} sensing. Three different concentration of as prepared PVA-NPA, likely 10%, 20% and 30% (V/V) were employed for the quenching and titration study with increasing concentration of Ag-NPs. Although the fluorescence intensity

123

(F_0/F) increased with the increase in Ag-NPs concentration but it was independent of PVA-NPA concentration. So, it is obvious that the as prepared PVA-NPA concentration will not affect the detection sensitivity significantly. Linear dependency between the fluorescence intensity (F_0/F) and Ag-NPs concentration (below 1.13×10^{-9} M) has also been observed (Figure 6.2c, inset). So, the preferable concentrations for sensing application should be equal or less than 1.13×10^{-9} M Ag-NPs at 20% (V/V) as prepared PVA-NPA. The effects of pH on the sensing was then investigated. We observed that the fluorescence intensity of as prepared sample with pH = 6.5 was weaker at acidic or basic conditions. So as prepared sample (pH = 6.5) is chosen for sensing application. Finally, the response time was studied. We observed that the interaction of the Ag-NPs and Hg^{2+} is very fast, which can reach a steady condition within 2 minutes. This result indicates that the present method is time-saving.

6.2.1.6. Selectivity Studies: The high selectivity is a matter of necessity for an excellent sensor. It is proved that the synthesized PVA-NPA exhibits a strong emission and quenched by Ag-NPs. After addition of Hg^{2+} ions to the quenched solution (final Hg concentration in the solution is 100 ppm), the emission of the solution dramatically increased within a minute and exhibits the same emission as PVA-NPA (as shown in inset of Figure 6.3c). Now to investigate the response of our sensor to others meta ions, including Cu^{2+}, Cd^{2+}, Ca^{2+}, Co^{2+}, Mg^{2+}, Na^+, K^+, Pb^{2+}, Ni^{2+}, Zn^{2+} and Fe^{3+} were examined under same condition. First, the same concentration (final metal ions concentration in the solution is 100 ppm) of the stock solutions of the as prepared various metals ions were added into sample solution (PVA-NPA + Ag-NPs). These results demonstrate that no significant change in fluorescence intensity in the presence of other metal ions (as indicated in Figure 6.4). Second, all metal ions (including Hg^{2+} and excluding Hg^{2+}) with same concentration were mixed together to form a mixture solution and added into sample solution (PVA-NPA + Ag-NPs) for interference testing. Inset of the Figure 6.4b reveals the dramatic change in fluorescence intensity occurs only when Hg^{2+}-mixed solution was added. The selectivity studies clearly exhibited the high selectivity of our sensor (PVA-NPA + Ag-NPs) to Hg^{2+} ions in
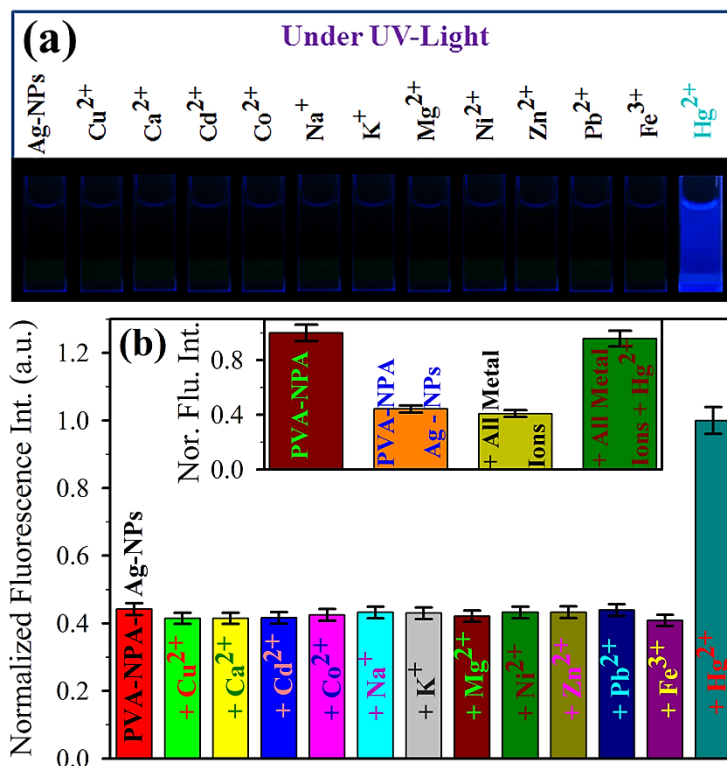
Figure 6.4. *(a) Visual representation of PVA-NPA+Ag-NPs complexes upon interaction with metal ions under UV light. (b) Relative fluorescence intensity of the quenched fluorophore (PVA-NPA+Ag-NPs) in the presence of various metal ions (with same concentration) monitored at 433 nm. Inset shows the relative fluorescence intensity of fluorophore and the quenched fluorophore with all metal (except Hg^{2+}) ions in absent and present of Hg^{2+} ions.*

comparison to the other metal ions. The observed result indicated the potential applications of our method for the detection of Hg^{2+} ions in aqueous medium without any interference of other metal ions.

6.2.1.7. Sensitivity Studies: The sensing and optical properties of the sensor were investigated by various measurements. In this subsection we are demonstrating the qualitative as well as quantitative detection of mercury ions in aqueous medium by our ultrasensitive sensor. Figure 6.5a reveals "turn on" fluorescence signal instantly upon addition of Hg^{2+} ions into the sensor (aqueous PVA-NPA with Ag-NPs) and intensity increased as the concentration of Hg^{2+} ions increased in a dynamic range that spanned 0-40 ppm. Meanwhile, the yellow solution rapidly became colorless and a blue shift was observed in the spectra due to decreasing concentration and the aggregation of the nanoparticles. Inset of Figure 6.5a shows that our highly efficient and ultrasensitive
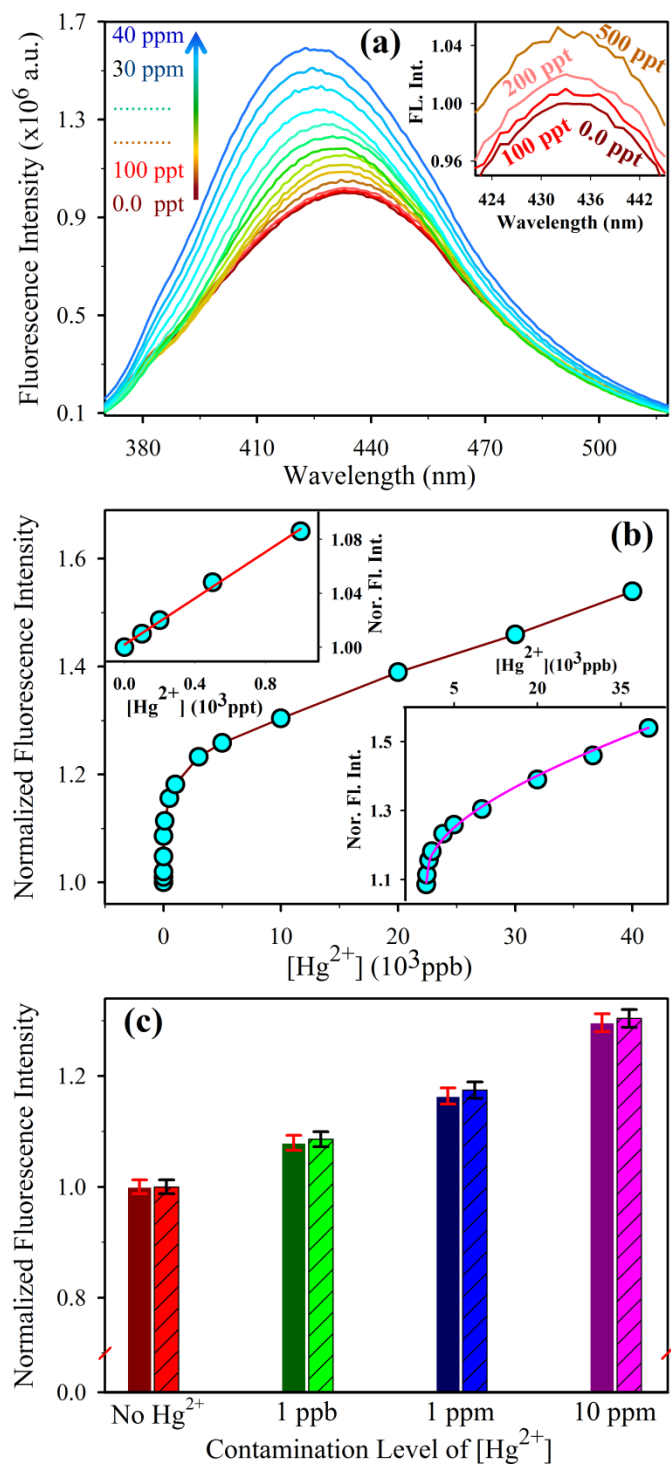
Figure 6.5. *(a) Steady-state fluorescence spectra (λ_{ex} = 340 nm) of the quenched fluorophore (PVA-NPA+Ag-NPs) upon addition of Hg²⁺ ions (0-40 ppm). Inset shows the magnified fluorescence spectra for some low concentration (0, 100, 200 and 500 ppt) of Hg²⁺ ions. (b) The plot of normalized fluorescence intensity vs [Hg²⁺], at 433 nm. Upper inset shows the linear response with [Hg²⁺] from 0 to 1 ppb and the lower inset shows the nonlinear response with [Hg²⁺] from 1 ppb to 40 ppm. (c) Response of the sensor without and with contaminated real water samples and comparison of measured values (solid bars) with proposed values (cross bars).*

126

sensor had a detection limit of 100 ppt (0.5 nM) for Hg^{2+} ions, which was in the same range or at a lower value compared to recently reported colorimetric as well as fluorescence and energy transfer base sensor [26, 33, 58-65]. Upper inset of Figure 6.5b exhibits the linear response (with slope = 0.086) of the sensor for very low concentration (0-1 ppb) of Hg^{2+} ions. For high concentration (1 ppb-40 ppm) of Hg^{2+} ions, the sensor follows nonlinearity by the equation $Y = (0.916 - 0.004*X^{0.4})^{-1}$, where Y is the normalized fluorescence intensity and X (in ppb) is the Hg^{2+} ions concentration (shown in the lower inset of the Figure 6.5b). These results imply that this highly selective, cost-effective and ultrasensitive novel sensor can be applied to the direct detection of Hg^{2+} ions in real world water samples as well as drinking water.

6.2.1.8. Determination of Hg²⁺ Ions in Real World Samples: Application of our proposed method has been evaluated for the determination of Hg^{2+} in a real world samples. We choose groundwater as a real sample. In such environmental samples, the concentration of other metal ions and some unknown contamination are significantly higher than that of Hg^{2+} ions, so it is highly challenging to detect mercury in real world samples. Figure 6.5c represents the comparative analysis between the value obtained from calibration curve and instrumental data for different concentration of Hg^{2+} contaminated groundwater. It has been found that the real world sample was free from Hg^{2+} ions contaminations. Upon addition of the Hg^{2+} ions contamination in the water samples with various known concentrations, it has been observed that the value obtained from the calibration curve and the values measured were within the 10% error range. This result suggests that the proposed sensor has potential for sensing of Hg^{2+} ions in environmental real world samples.

6.2.2. Development of Highly Selective and Efficient Prototype Sensor for Potential Application in Environmental Mercury Pollution Monitoring [66]:

6.2.2.1. Characterization of PVA-Ag-NPs Thin Film: The film was characterized by the UV-Vis spectrophotometer. The SPR spectrum of the prepared PVA-Ag-NPs thin film is shown in Figure 6.6a. The observed characteristic absorbance band peaking at
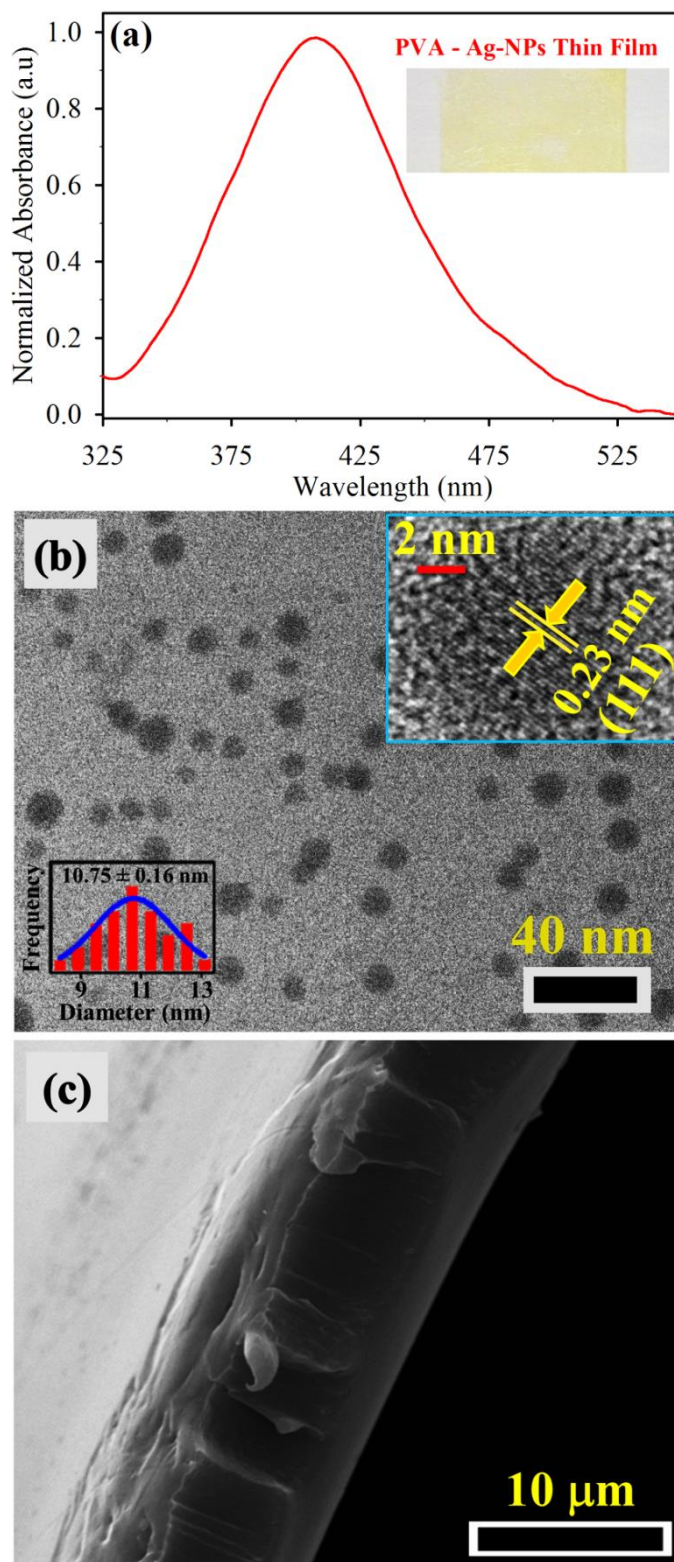
Figure 6.6. *(a) Normalized UV–Vis absorbance spectrum of PVA-Ag-NPs thin film. Inset shows the image of the thin film on glass slide. (b) TEM images of PVA-Ag-NPs thin film. Lower inset shows the size distribution of the Ag-NPs and upper inset shows the high-resolution TEM (HRTEM) image of Ag-NPs. (c) SEM image of Ag-NPs impregnated PVA thin film (cross-sectional).*

around 405 nm is due to SPR band of the Ag-NPs. The absorbance band of the NPs indicates the synthesized particle size is around 11 nm [32]. The photographic image of the sensor film is shown in the inset of Figure 6.6a. For further confirmation on the consistency of the sensor film, we have used electron microscopy (TEM, SEM) on the PVA-Ag-NPs thin film. Figure 6.6b represents the TEM image of the as prepare citrate capped Ag- NPs within the polymer matrix. The TEM images reveal that the particles are spherical in shape with almost uniform size distribution. The average diameter of the particles is found to be around 11 nm (lower inset of Figure 6.6b). The particle size distribution is further reconfirmed by DLS study also (data not shown). The crystal structure of the metal NPs is also confirmed from the fringe-distance in the HRTEM image. Upper inset of Figure 6.6b shows continuous single directional lattice fringes. The measured interplanar distance of the fringes (~0.23 nm) corresponds to Ag [111] lattice planes [45]. Figure 6.6c presents the SEM image of the Ag-NPs impregnated PVA thin film (cross-sectional) revealing average thickness of sensor film to be around 12-13 μm.

***6.2.2.2. Sensing Mechanism and Sensitivity Studies for Hg^{2+} Detection:*** In order to understand how the SPR band of the nanoparticle is affected by the metal Hg^{2+} ions, a control study on the prepared thin film was performed. The absorbance spectrum of the wet sensor film remains constant for more than 30 minutes (Figure 6.7a), demonstrating that even though the polymer swells in the aqueous medium, there was absolutely no leaching of Ag-NPs into the wetting medium. Our observation is consistent with the reported literature on the Ag-NPs impregnated PVA thin film [14]. In order to measure the influence of aqueous mercury solutions on the sensor films, the SPR spectra of the films were recorded before and after introducing Hg^{2+} aqueous solutions with known concentrations. The spectra for a selected set of concentrations are shown in Figure 6.7. As shown in Figure 6.7b,c the spectra show small but definite and reproducible decrease in absorbance within a few minutes, even at the lowest Hg^{2+} concentration of 10 ppb. However, for higher concentrations of Hg^{2+} ions like 500 ppb, 1 ppm and 2 ppm (shown in Figure 6.7d-f), the spectra show
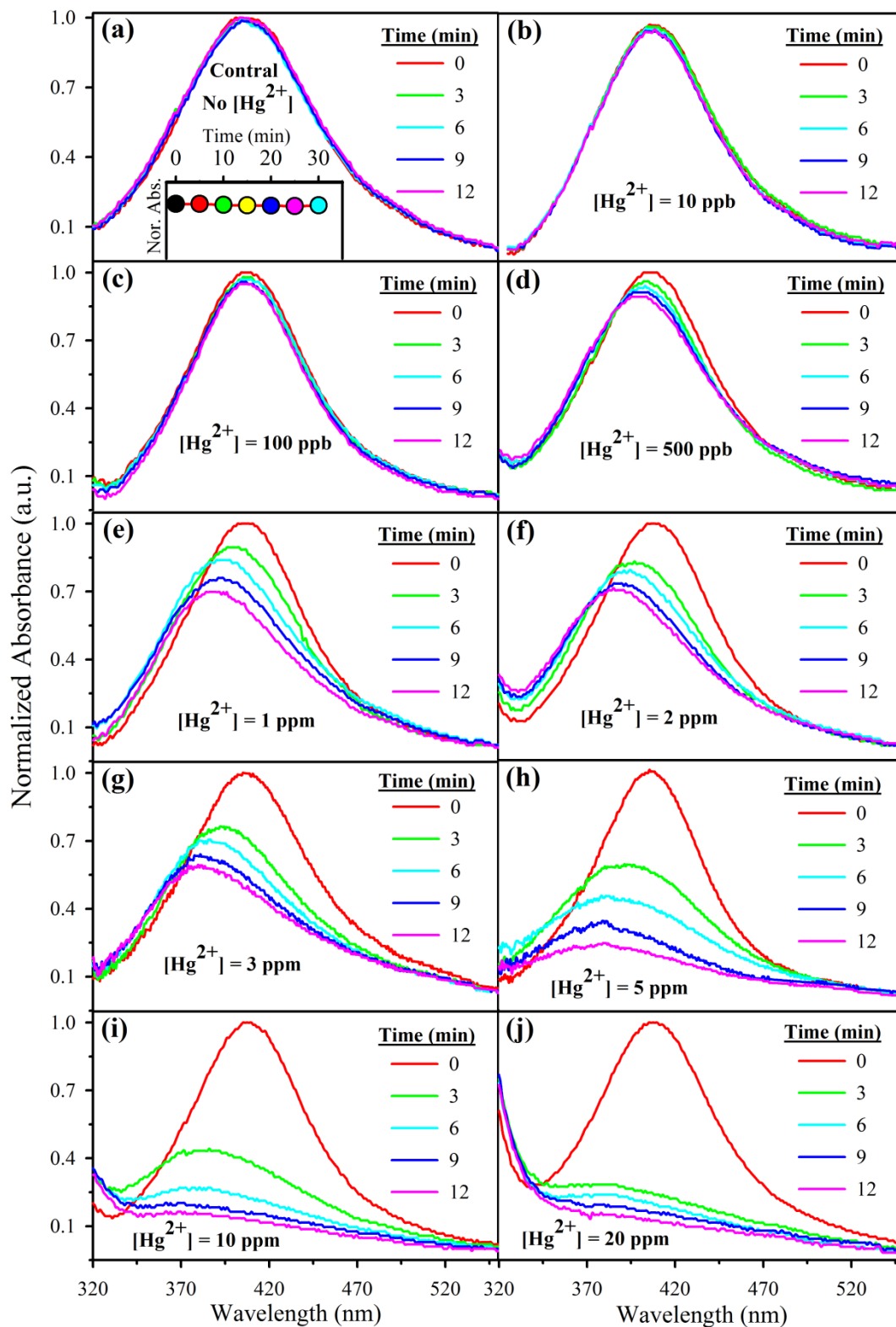
Figure 6.7. *Temporal variation of the SPR spectra of PVA-Ag-NPs thin films immersed in aqueous solutions (pH = 6.5) with different concentrations of Hg^{2+} ions are shown in the panels (a-j). (a) Shows the variation of SPR in longer time window at [Hg^{2+}] = 0 ppb. Absorbance at zero time is normalized to 1.0 in each case.*

significant change within 3 minutes. In addition to the decrease in intensity, the SPR peak undergoes a blue shift which becomes prominent at higher Hg^{2+} concentrations (Figure 6.7g-j). The relative change in absorbance with respect to zero-minute spectrum with different time in presence of various concentrations of mercury ions is shown in Figure 6.8a. Even at Hg^{2+} concentrations below 100 ppb, a small but gradual temporal change in the absorbance with respect to initial spectrum is evident. Although the sensitivity of the sensor increased with incubation time, for sensitivity calibration study 3 minutes of incubation time was chosen in our study as the changes in absorbance in all mercury concentrations in the time window were found to be reasonable. The effect of pH on the sensing was also investigated. We observed that the SPR absorbance of as-prepared sensor film was weaker at acidic or basic conditions compared to that in pH = 6.5. At acidic or basic conditions, the increased H^+ and OH^- in the medium probably interact with the NPs and reduce stability of the SPR of Ag-NPs, which plays significant role in the sensing mechanism. The advantage of our sensor is that the as-prepared film exhibits the highest sensitivity at the ground water's natural pH level (pH = 6.5) revealing the possibility of potential use of the sensor for testing ground water as it is. The overall sensing process is represented schematically in scheme 6.2.
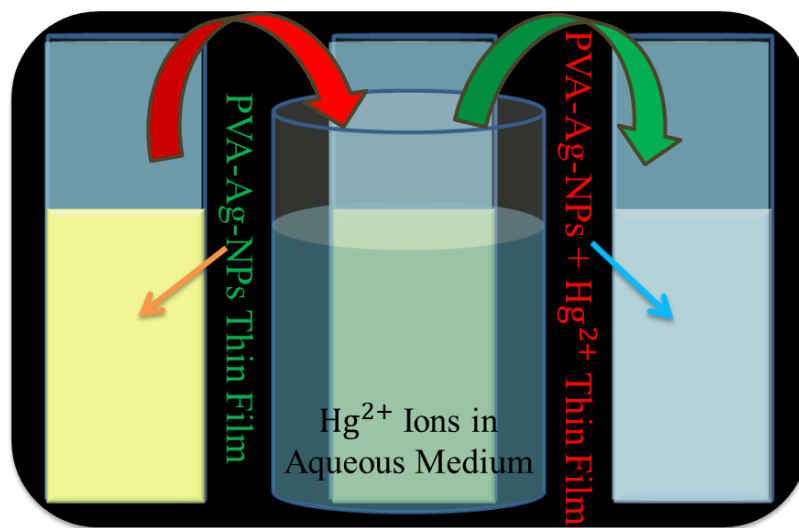
Scheme 6.2. *The experimental procedure and the effect of mercury (Hg^{2+}) ions on the silver nanoparticles (Ag-NPs) are shown schematically.*

Figure 6.8b demonstrates that for all over the concentration (10 ppb-20 ppm) of Hg²⁺ ions, as-prepared sensor film follows non-linearity by eq. $Y = X /(10.63 + 1.4 \times X - 2.66 \times \sqrt{X})$ with 3 minutes incubation time, where Y is the differential absorbance $(I_0 - I)$, X is the Hg²⁺ ion concentration (in ppm) and I_0 and I are the absorbances at 405 nm of the sensor film at 0 and 3 minutes respectively. However, the inset of Figure 6.8b exhibits that the differential absorbance $(I_0 - I)$ and Hg²⁺ ion concentration is in excellent linear correlation ($Y = 0.09 \times X + 0.014$, with correlation
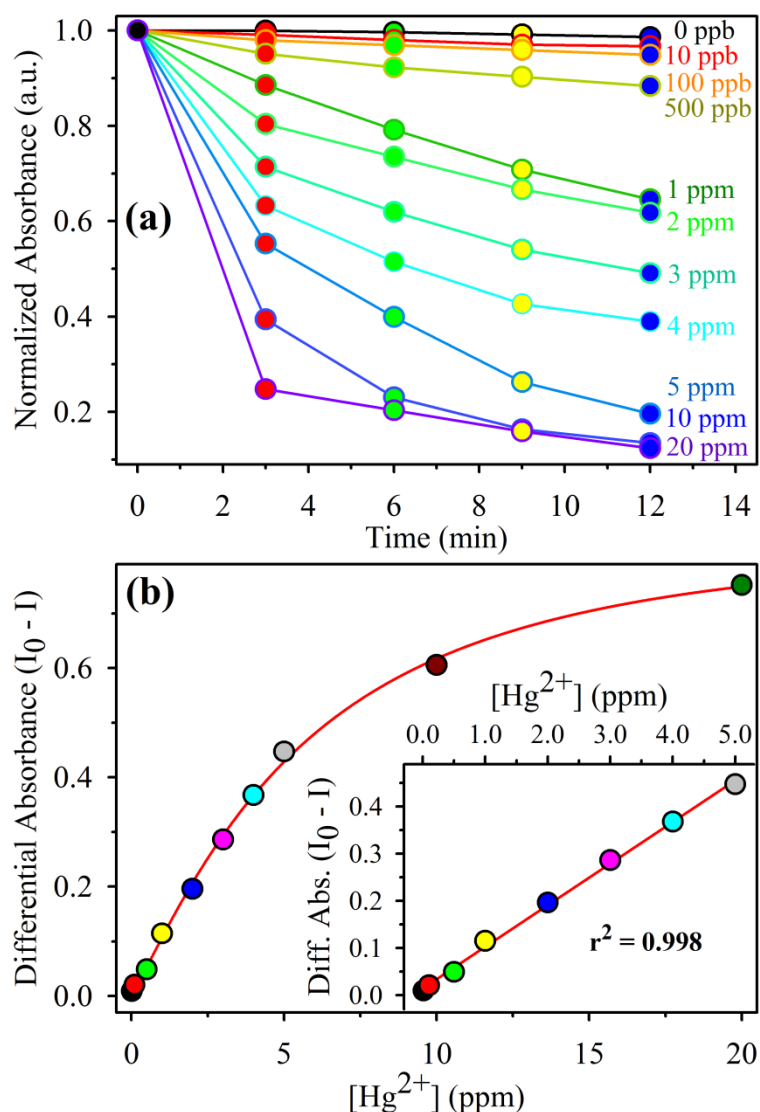
Figure 6.8. *(a) Relative change in absorbance of the thin films as a function of time for different concentrations of Hg^{2+} ions in aqueous medium. (b) The plot of differential absorbance of the thin films at 405 nm with Hg^{2+} ions concentration. Inset shows the linear response of the sensor with $[Hg^{2+}]$ from 10 ppb to 5 ppm.*

coefficient = 0.998) over the range 10 ppb to 5 ppm. Thus, the 3 minutes incubation time can be considered as sufficient duration for Hg^{2+} detection in aqueous media with the lower detection limit of 10 ppb. We also observed that longer incubation time of the sensor with the test sample increased the sensitivity where 10 and 100 ppb could be distinguished confidently (Figure 6.7b and c). Therefore, for longer incubation time the lower detection limit of the sensor can be reduced to lower than 10 ppb.

In order to get insights into the reaction mechanisms of Hg^{2+} sensing, further
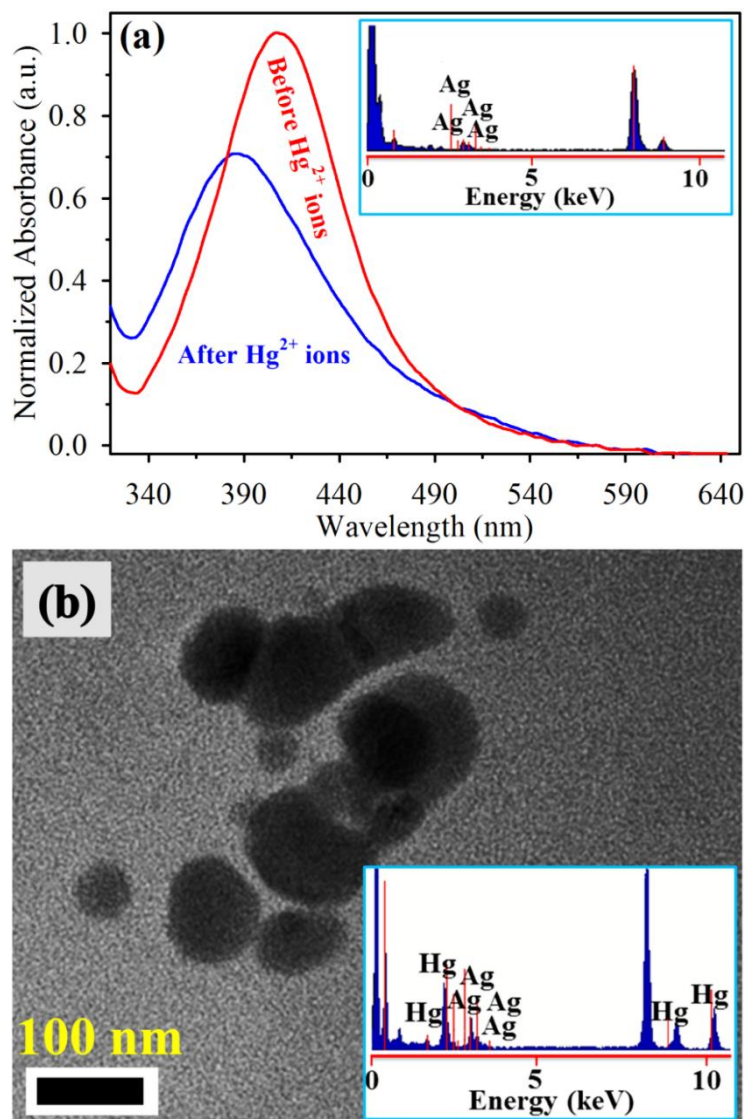
Figure 6.9. *(a) Normalized UV–Vis absorbance spectrum of PVA-Ag-NPs thin film, before and after immersed in aqueous solutions of Hg^{2+} ions. Inset shows the EDAX spectra of the thin film before interaction with Hg^{2+} ions. (b) TEM image of the thin film after interaction with Hg^{2+} ions. Inset shows the EDAX spectra of the thin film after interaction with Hg^{2+} ions.*

experimental results are presented in Figure 6.9. Figure 6.9a shows decrease in absorbance at 405 nm as well as blue shift of SPR band in presence of Hg^{2+} ions. The blue shift of the SPR band might be due to the formation of amalgamation at the surface of Ag-NPs (incomplete amalgamation) effectively reducing the size of the NPs. It has to be noted that complete amalgamation would abolish the SPR of Ag-NPs and subsequently induce agglomeration in order to form bigger-sized Ag-Hg alloy particles. To understand the above phenomena, the TEM and EDAX spectra of the thin film were studied before and after immerging in the aqueous mercury solution. As shown in the EDAX study, before immerging in the aqueous mercury solution, the thin film was completely free from the mercury (inset of the Figure 6.9a) and no aggregation was found among the NPs (Figure 6.6b). However, after immerging the thin film in the aqueous mercury ion solution, TEM studies (Figure 6.9b) confirmed increase of sizes of the observed NPs. Inclusion of Hg in the NPs is evident from EDAX spectrum as shown in the inset of the Figure 6.9b. Our observation is consistent with the reported literature [44]. The amalgam formed at the surface of the silver nanoparticles within the polymer matrix by reduction of Hg^{2+} ions [14, 56, 57]. The amalgamation is unavoidable only in the presence of Hg^{2+} ions because the reduction of Hg^{2+} (to Hg) is most facile by Ag-NPs due to the equivalent redox potential of Hg^{2+} (to Hg) ($E^0 = 0.85$ V) and Ag-NPs (to Ag^{+1}) ($E^0 = 0.80$ V)[14, 67]. The amalgamated/aggregated Ag-NPs lose SPR band (decrease in absorbance) and increase the particles size within the sensor film.

6.2.2.3. Selectivity Studies: From our earlier studies, it is evident that the Ag-NPs impregnated sensor thin film acts as an efficient mercury sensor through amalgamation/aggregation of the NPs within the polymer matrix. Now, to investigate the selectivity of the developed sensor, we have studied the interference of other metal ions including Cu^{2+}, Cd^{2+}, Mg^{2+}, Co^{2+}, Na^+, Ca^{2+}, K^+, Zn^{2+}, Ni^{2+}, Pb^{2+}, Fe^{3+} and Ag^+ in the detection ability of the sensor under the same experimental condition. The changes in absorbance at 405 nm of the sensor films after the interaction (interaction time 12 minute) with different metal ions and mixture of all metal ions (including Hg^{2+}
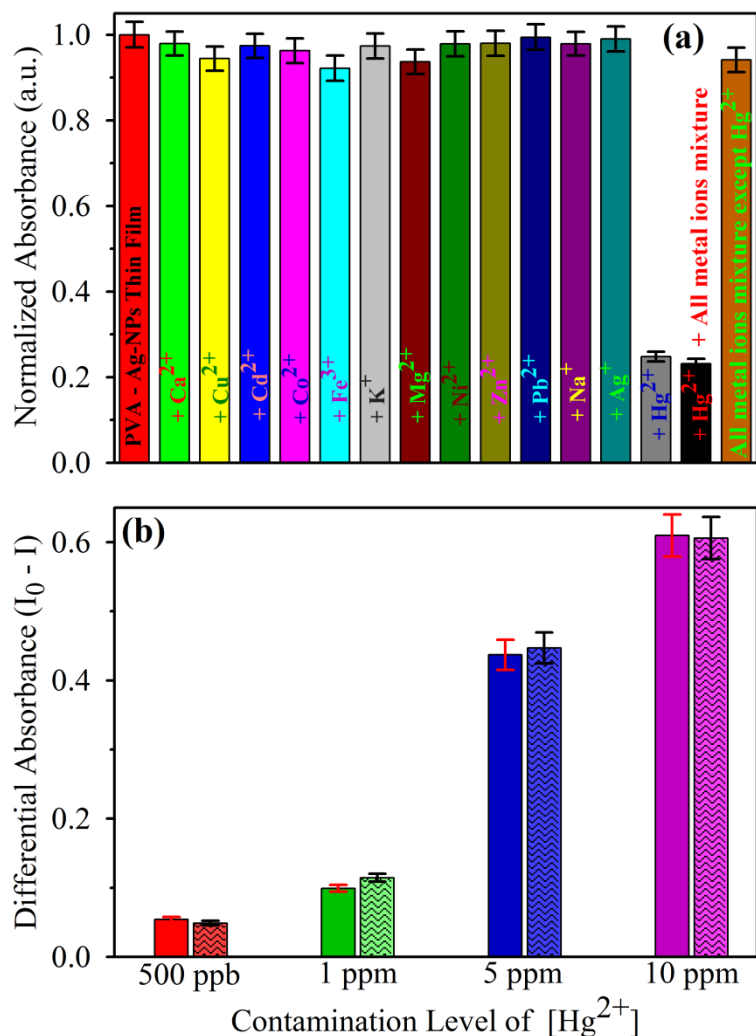
Figure 6.10. *(a) Normalized UV−Vis absorbance spectra of the thin films in the presence of various metal ions, monitored at 405 nm. (b) Response of the sensor with Hg^{2+} ion contaminated real water samples and comparison of measured values (zig-zag bars) with expected values (solid bars).*

and excluding Hg^{2+}) are shown in the Figure 6.10a with a 5% error bar. The results demonstrate that all of those relevant metal ions (except mercury ion) and mixture of all metal ions (excluding Hg^{2+}) have no significant effect on the sensor thin films' optical response (Figure 6.10a). The selectivity studies clearly indicate that the amalgamation/aggregation phenomenon is only evident in the presence of Hg^{2+} ions because the reduction of Hg^{2+} (to Hg) is most facile by Ag-NPs due to the equivalent redox potential of Hg^{2+} and Ag-NPs [14, 67]. Our observation indicates that the sensor has potential in real life applications for monitoring environmental mercury pollution in aqueous medium without any interference from other relevant metal ions.

6.2.2.4. Determination of Hg²⁺ Ions in Real Samples: Potential application of the proposed technique was evaluated for determination of mercury ions in real samples. Laboratory tap water sample was taken for this experiment. As the collected environmental water sample was not fully purified, the metal ions are expected to be present in significant amount. The test report of the tap water from a National Accreditation Board for Testing and Calibration Laboratories test centre is as follows. *Escherichia coli*, MPN/100 ml – Nil, total hardness ($CaCO_3$) – 73.2 mg/L, sulphate – 26.2 mg/L, nitrate – 1.6 mg/L, iron – 0.04 mg/L, arsanic – 0.005 mg/L, fluoride – 0.194 mg/L, chlorine – 17.71 mg/L, lead – 0.002mg/L, calcium – 27.0 mg/L. So, it is highly challenging to detect Hg^{2+} in such environmental water sample. From the experimental data, it is found that the tap water sample is free from Hg^{2+} ions. Figure 6.10b shows that our developed sensor is capable of detecting mercury contamination in real-world samples. The obtained concentration of Hg^{2+} ions from the calibration curve (calculated) and spiked values (expected) are within the 5% error range (for details of the experimental procedure see experimental section). The results are summarized in Table 6.3 and show good agreement with the expected values. It is also observed from Table 6.3 that the recoveries of Hg^{2+} at different concentration levels (ratio between the measured and expected values) are in between 98.0 and 103.8%; the RSDs are in between 0.91 and 2.45%. It is evident from our studies that the developed

Table 6.3: *Determination of Hg²⁺ ions in real water samples using the proposed method.*

Samples	Detection of Hg²⁺ ions	Spiked Hg²⁺ (ppm)	Measured Hg²⁺ (ppm)		Recovery(%)	RSD(%)
			Mean	SD		
Tap water 1	Not detected	0.5	0.49	0.010	98.0	2.04
Tap water 2	Not detected	1.0	1.03	0.025	103.0	2.45
Tap water 3	Not detected	5.0	5.19	0.055	103.8	1.06
Tap water 4	Not detected	10.0	9.89	0.090	98.9	09.1

SD ~ Standard deviation, Recovery(%) = 100×(concentration found/concentration added), RSD(%) = Relative standard deviation of three determination = Coefficient of variation×100.

thin film sensor has extremely high potential for Hg^{2+} ions monitoring in environmental water samples.

6.2.2.5. *Development of the Prototype Device:* Our studies confirmed that the developed technique has high potential application in environmental mercury pollution monitoring in the real-world water samples. By using the technique, we have developed a simple and inexpensive prototype device for monitoring in field environmental mercury pollution. The basic block diagram of the designed prototype device is shown in Scheme 6.3. Here, we have used commonly available two light-emitting diodes (LEDs) with irradiance in the visible region of the electromagnetic spectrum as light sources. The violet irradiance of the LED with wavelength of 405 nm is complementary of the absorbance spectrum peak of the developed sensor thin film. The red LED with wavelength of 600 nm is used for baseline correction (reference). The lenses are used to focus the light on the sample and the LDR (light dependent resistor). Finally, the programmable IC (integrated circuit) which is connected to a digital display is used to convert the LDR signal to digital value. We will present the detailed instrumentation and the validation of the designed portable device for a statistically significant number of real-world water samples in our future work.
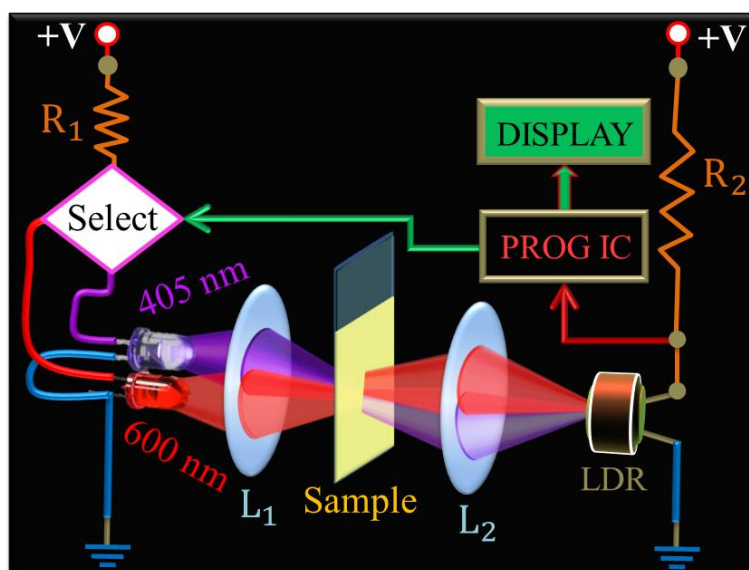
Scheme 6.3. *The block diagram representation of the developed prototype device for potential application in environmental mercury pollution monitoring is shown schematically.*

6.3. Conclusion

In summary, the quenching of dye fluorescence by Ag-NPs was studied using fluorescence spectroscopy. The quenching process was characterized by well-known Stern-Volmer plots which display a dynamic quenching for the quencher concentration bellow 1.13×10^{-9} M. The calculated donor-acceptor distance (d = 5.66 nm) by NSET model confirmed the energy transfer phenomenon between the fluorescent dye and NPs. The present study demonstrates the unique potential of metal nanoparticle in chemical sensing application followed by the nonradiative energy transfer process. We have successfully developed a very low cost, highly selective and ultrasensitive "turn on" fluorescence sensor based on NSET for direct detection of Hg^{2+} in aqueous medium with the detection limit 100 ppt (0.5 nM). The developed sensor is not only insensitive to other metal ions but also highly selective toward Hg^{2+} ions in the presence of other metal ions. The developed sensor has potential applications in monitoring trace Hg^{2+} ions in real world samples. As the scope for further development of this concept is extensive, we extend our study for the development of economical portable devices. To design a simple and inexpensive prototype mercury sensor devices, we first prepared silver nanoparticles-impregnated poly(vinyle alcohol) nanocomposite thin film. The thin film fabricated through a facile protocol is shown to be a fast, efficient and selective sensor for Hg^{2+} in aqueous medium. The study demonstrates the unique potential of Ag-NPs in mercury ion sensing application followed by the reduction and blue shift of the SPR spectrum upon interaction with mercury, enhancing the selectivity of the detection, through amalgamation/aggregation process. The developed sensor is highly selective toward Hg^{2+} ion, even in the presence of other metal ions generally present in water of natural sources. The sensor response exhibits excellent linear correlation with Hg^{2+} ions concentration over the range 10 ppb to 5 ppm. The developed sensor has potential applications in monitoring trace Hg^{2+} ions in real-world water samples. Finally, we have also developed a simple, inexpensive and feasible prototype device using the proposed technique for potential application in environmental mercury pollution monitoring.

References

1. H. H. Harris, I. J. Pickering and G. N. George; The chemical form of mercury in fish. *Science* 301 (2003), 1203.

2. J. Ke, X. Li, Q. Zhao, Y. Hou and J. Chen; Ultrasensitive quantum dot fluorescence quenching assay for selective detection of mercury ions in drinking water. *Sci. Rep.* 4 (2014), 5624.

3. Q. Wang, D. Kim, D. D. Dionysiou, G. A. Sorial and D. Timberlake; Sources and remediation for mercury contamination in aquatic systems—a literature review. *Environ. Pollut.* 131 (2004), 323.

4. R. Eisler; Health risks of gold miners: A synoptic review. *Environ. Geochem. Health* 25 (2003), 325.

5. H. Wang, Y. Wang, J. Jin and R. Yang; Gold nanoparticle-based colorimetric and "turn-on" fluorescent probe for mercury(II) ions in aqueous solution. *Anal. Chem.* 80 (2008), 9021.

6. J. R. Miller, J. Rowland, P. J. Lechler, M. Desilets and L.-C. Hsu; Dispersal of mercury-contaminated sediments by geomorphic processes, Sixmile Canyon, Nevada, USA: Implications to site characterization and remediation of fluvial environments. *Water, Air and Soil Pollut.* 86 (1996), 373.

7. G. E. Glass, J. A. Sorensen, K. W. Schmidt, G. R. Rapp, D. Yap and D. Fraser; Mercury deposition and sources for the upper great lakes region. *Water, Air and Soil Pollut.* 56 (1991), 235.

8. P. B. Tchounwou, W. K. Ayensu, N. Ninashvili and D. Sutton; Review: Environmental exposure to mercury and its toxicopathologic implications for public health. *Environ. Toxicol.* 18 (2003), 149.

9. K. Farhadi, M. Forough, R. Molaei, S. Hajizadeh and A. Rafipour; Highly selective Hg^{2+} colorimetric sensor using green synthesized and unmodified silver nanoparticles. *Sens. Actuators B: Chem.* 161 (2012), 880.

10. T. A. Baughman; Elemental mercury spills. *Environ. Health Perspect.* 114 (2006), 147.

11.   Z. Yan, M.-F. Yuen, L. Hu, P. Sun and C.-S. Lee; Advances for the colorimetric detection of Hg^{2+} in aqueous solution. *RSC Adv.* 4 (2014), 48373.

12.   O. T. Butler, J. M. Cook, C. F. Harrington, S. J. Hill, J. Rieuwerts and D. L. Miles; Atomic spectrometry update. Environmental analysis. *J. Anal. At. Spectrom* 21 (2006), 217.

13.   E. M. Nolan and S. J. Lippard; Tools and tactics for the optical detection of mercuric ion. *Chem. Rev.* 108 (2008), 3443.

14.   G. V. Ramesh and T. P. Radhakrishnan; a universal sensor for mercury (Hg, Hg(I), Hg(II)) based on silver nanoparticle-embedded polymer thin film. *ACS Appl. Mater. Interfaces* 3 (2011), 988.

15.   S. A. El-Safty and M. Shenashen; Mercury-ion optical sensors. *Trends. Analyt. Chem.* 38 (2012), 98.

16.   H. N. Kim, W. X. Ren, J. S. Kim and J. Yoon; Fluorescent and colorimetric sensors for detection of lead, cadmium and mercury ions. *Chem. Soc. Rev.* 41 (2012), 3210.

17.   M. Ghaedi, M. Reza Fathi, A. Shokrollahi and F. Shajarat; Highly selective and sensitive preconcentration of mercury ion and determination by cold vapor atomic absorption spectroscopy. *Anal. Lett.* 39 (2006), 1171.

18.   N. Wang, M. Lin, H. Dai and H. Ma; Functionalized gold nanoparticles/reduced graphene oxide nanocomposites for ultrasensitive electrochemical sensing of mercury ions based on thymine–mercury–thymine structure. *Biosens. Bioelectron.* 79 (2016), 320.

19.   Y. Ma, Z. Zhang, Y. Xu, M. Ma, B. Chen, L. Wei and L. Xiao; A bright carbon-dot-based fluorescent probe for selective and sensitive detection of mercury ions. *Talanta* 161 (2016), 476.

20.   M. Pepi, D. Reniero, F. Baldi and P. Barbieri; A comparison of MER::LUX whole cell biosensors and moss, a bioindicator, for estimating mercury pollution. *Water, Air and Soil Pollut.* 173 (2006), 163.

21. I. T. Somé, A. K. Sakira, D. Mertens, S. N. Ronkart and J.-M. Kauffmann; Determination of groundwater mercury (II) content using a disposable gold modified screen printed carbon electrode. *Talanta* 152 (2016), 335.

22. L. Chen, L. Yang, H. Li, Y. Gao, D. Deng, Y. Wu and L.-j. Ma; Tridentate lysine-based fluorescent sensor for Hg (II) in aqueous solution. *Inorg. Chem.* 50 (2011), 10028.

23. M. De la Cruz-Guzman, A. Aguilar-Aguilar, L. Hernandez-Adame, A. Bañuelos-Frias, F. J. Medellín-Rodríguez and G. Palestino; A turn-on fluorescent solid-sensor for Hg (II) detection. *Nanoscale Res. Lett.* 9 (2014), 1.

24. D. Wallschläger, H. H. Kock, W. H. Schroeder, S. E. Lindberg, R. Ebinghaus and R.-D. Wilken; Estimating Gaseous Mercury Emissions from Contaminated Floodplain Soils to the Atmosphere with Simple Field Measurement Techniques. *Water, Air and Soil Pollut.* 135 (2002), 39.

25. Y. Wan, W. Niu, W. J. Behof, Y. Wang, P. Boyle and C. B. Gorman; Aminoisoquinolines as colorimetric Hg^{2+} sensors: The importance of molecular structure and sacrificial base. *Tetrahedron.* 65 (2009), 4293.

26. N. Wanichacheva, O. Hanmeng, S. Kraithong and K. Sukrat; Dual optical Hg^{2+}-selective sensing through FRET system of fluorescein and rhodamine B fluorophores. *J. Photochem. Photobiol. A* 278 (2014), 75.

27. G. Rezanejade Bardajee, Z. Hooshyar and M. Khanjari; Dye fluorescence quenching by newly synthesized silver nanoparticles. *J. Photochem. Photobiol. A* 276 (2014), 113.

28. N. N. Horimoto, K. Imura and H. Okamoto; Dye fluorescence enhancement and quenching by gold nanoparticles: Direct near-field microscopic observation of shape dependence. *Chem. Phys. Lett.* 467 (2008), 105.

29. M. Annadhasan, T. Muthukumarasamyvel, V. R. Sankar Babu and N. Rajendiran; Green synthesized silver and gold nanoparticles for colorimetric detection of Hg^{2+}, Pb^{2+} and Mn^{2+} in aqueous medium. *ACS Sustain. Chem. Eng.* 2 (2014), 887.

30. K. L. Kelly, E. Coronado, L. L. Zhao and G. C. Schatz; The optical properties of metal nanoparticles: The influence of size, shape and dielectric environment. *J. Phys. Chem. B* 107 (2003), 668.

31. D. G. Thompson, R. J. Stokes, R. W. Martin, P. J. Lundahl, K. Faulds and D. Graham; Synthesis of unique nanostructures with novel optical properties using oligonucleotide mixed–metal nanoparticle conjugates. *Small* 4 (2008), 1054.

32. D. Paramelle, A. Sadovoy, S. Gorelik, P. Free, J. Hobley and D. G. Fernig; A rapid method to estimate the concentration of citrate capped silver nanoparticles from UV-visible light spectra. *Analyst* 139 (2014), 4855.

33. M. Li, Q. Wang, X. Shi, L. A. Hornak and N. Wu; Detection of mercury(II) by quantum dot/DNA/gold nanoparticle ensemble based nanosensor via nanometal surface energy transfer. *Anal. Chem.* 83 (2011), 7061.

34. Z. Wang, J. Heon Lee and Y. Lu; Highly sensitive "turn-on" fluorescent sensor for Hg^{2+} in aqueous solution based on structure-switching DNA. *Chem. Commun.* (2008), 6005.

35. L. Guo, Y. Xu, A. R. Ferhan, G. Chen and D.-H. Kim; Oriented gold nanoparticle aggregation for colorimetric sensors with surprisingly high analytical figures of merit. *J. Am. Chem. Soc.* 135 (2013), 12338.

36. I. Y. S. Lee and H. Suzuki; Quenching dynamics promoted by silver nanoparticles. *J. Photochem. Photobiol. A* 195 (2008), 254.

37. S. Webber; The role of time-dependent measurements in elucidating static versus dynamic quenching processes. *Photochem. Photobiol.* 65 (1997), 33.

38. S. Chaudhuri, S. Sardar, D. Bagchi, S. S. Singha, P. Lemmens and S. K. Pal; Sensitization of an endogenous photosensitizer: Electronic spectroscopy of riboflavin in the proximity of semiconductor, insulator and metal nanoparticles. *J. Phys. Chem. A* 119 (2015), 4162.

39. A. Giri, A. Makhal, B. Ghosh, A. K. Raychaudhuri and S. K. Pal; Functionalization of manganite nanoparticles and their interaction with

biologically relevant small ligands: Picosecond time-resolved FRET studies. *Nanoscale.* 2 (2010), 2704.

40. B. Biswal and B. Bag; Preferences of rhodamine coupled (aminoalkyl)-piperazine probes towards Hg(ii) ion and their FRET mediated signaling. *Org. Biomol. Chem.* 11 (2013), 4975.

41. Z. Liu, Z. Zhu, Q. Wu, S. Hu and H. Zheng; Dielectric barrier discharge-plasma induced vaporization and its application to the determination of mercury by atomic fluorescence spectrometry. *Analyst* 136 (2011), 4539.

42. Y. H. Lee, M. H. Lee, J. F. Zhang and J. S. Kim; Pyrene excimer-based calix[4]arene FRET chemosensor for mercury(II). *J. Org. Chem.* 75 (2010), 7159.

43. Y. Pang, Z. Rong, R. Xiao and S. Wang; "Turn on" and label-free core−shell $Ag@SiO_2$ nanoparticles-based metal-enhanced fluorescent (MEF) aptasensor for Hg^{2+}. *Sci. Rep.* 5 (2015), 9451.

44. P. K. Sarkar, N. Polley, S. Chakrabarti, P. Lemmens and S. K. Pal; Nanosurface energy transfer based highly selective and ultrasensitive "turn on" fluorescence mercury sensor. *ACS Sens.* 1 (2016), 789.

45. E. Rodriguez-Leon, R. Iniguez-Palomares, R. Navarro, R. Herrera-Urbina, J. Tanori, C. Iniguez-Palomares and A. Maldonado; Synthesis of silver nanoparticles using reducing agents obtained from natural sources (Rumex hymenosepalus extracts). *Nanoscale Res. Lett.* 8 (2013), 318.

46. S. J. Leach and H. A. Scheraga; Effect of light scattering on ultraviolet difference spectra1. *J. Am. Chem. Soc.* 82 (1960), 4790.

47. E. Gratton; Method for the automatic correction of scattering in absorption spectra by using the integrating sphere. *Biopolymers* 10 (1971), 2629.

48. S. Banerjee, S. Sarkar, K. Lakshman, J. Dutta and S. K. Pal; UVA radiation induced ultrafast electron transfer from a food carcinogen benzo[a]pyrene to organic molecules, biological macromolecules and inorganic nano structures. *J. Phys. Chem. B* 117 (2013), 3726.

49. J. R. Lakowicz; Principles of fluorescence spectroscopy. *Springer Science and Business Media,* (2013).

50. M. A. H. Muhammed, A. K. Shaw, S. K. Pal and T. Pradeep; Quantum clusters of gold exhibiting FRET. *J. Phys. Chem. C* 112 (2008), 14324.

51. K.-S. Kim, H. Kim, J.-H. Kim, J.-H. Kim, C.-L. Lee, F. Laquai, S. I. Yoo and B.-H. Sohn; Correlation of micellar structures with surface-plasmon-coupled fluorescence in a strategy for fluorescence enhancement. *J. Mater. Chem.* 22 (2012), 24727.

52. Y. Wang, F. Yang and X. Yang; Colorimetric detection of mercury(II) ion using unmodified silver nanoparticles and mercury-specific oligonucleotides. *ACS Appl. Mater. Interfaces* 2 (2010), 339.

53. L. Li, L. Gui and W. Li; A colorimetric silver nanoparticle-based assay for Hg (II) using lysine as a particle-linking reagent. *Microchim. Acta* 182 (2015), 1977.

54. L. P. Wu, H. W. Zhao, Z. H. Qin, X. Y. Zhao and W. D. Pu; Highly selective Hg (II) ion detection based on linear blue-shift of the maximum absorption wavelength of silver nanoparticles. *J. Anal. Methods. Chem.* 2012 (2012), 856947.

55. M. Rex, F. E. Hernandez and A. D. Campiglia; Pushing the limits of mercury sensors with gold nanorods. *Anal. Chem.* 78 (2006), 445.

56. L. Katsikas, M. Gutiérrez and A. Henglein; Bimetallic colloids: Silver and mercury. *J. Phys. Chem.* 100 (1996), 11203.

57. A. Henglein and C. Brancewicz; Absorption spectra and reactions of colloidal bimetallic nanoparticles containing mercury. *Chem. Mater.* 9 (1997), 2164.

58. F. Long, A. Zhu, H. Shi, H. Wang and J. Liu; Rapid on-site/in-situ detection of heavy metal ions in environmental water using a structure-switching DNA optical biosensor. *Sci. Rep.* 3 (2013), 2308.

59. A. B. Othman, J. W. Lee, J.-S. Wu, J. S. Kim, R. Abidi, P. Thuéry, J. M. Strub, A. Van Dorsselaer and J. Vicens; Calix[4]arene-based, Hg^{2+}-induced intramolecular fluorescence resonance energy transfer chemosensor. *J. Org. Chem.* 72 (2007), 7634.

60. B. N. Ahamed and P. Ghosh; An integrated system of pyrene and rhodamine-6G for selective colorimetric and fluorometric sensing of mercury(II). *Inorg. Chim. Acta* 372 (2011), 100.

61. Y. Liu, X. Lv, Y. Zhao, M. Chen, J. Liu, P. Wang and W. Guo; A naphthalimide–rhodamine ratiometric fluorescent probe for Hg^{2+} based on fluorescence resonance energy transfer. *Dyes Pigments* 92 (2012), 909.

62. L. Wang, T. Yao, S. Shi, Y. Cao and W. Sun; A label-free fluorescent probe for Hg^{2+} and biothiols based on graphene oxide and Ru-complex. *Sci. Rep.* 4 (2014), 5320.

63. H. Zhang and Y. Xia; Ratiometry, wavelength and intensity: Triple signal readout for colorimetric sensing of mercury ions by plasmonic $Cu_{2-x}Se$ nanoparticles. *ACS Sens.* 1 (2016), 384.

64. Q. Zou and H. Tian; Chemodosimeters for mercury(II) and methylmercury(I) based on 2,1,3-benzothiadiazole. *Sens. Actuators B: Chem.* 149 (2010), 20.

65. G. Zhou, J. Chang, H. Pu, K. Shi, S. Mao, X. Sui, R. Ren, S. Cui and J. Chen; Ultrasensitive mercury ion detection using DNA-functionalized molybdenum disulfide nanosheet/gold nanoparticle hybrid field-effect transistor device. *ACS Sens.* 1 (2016), 295.

66. P. K. Sarkar, A. Halder, N. Polley and S. K. Pal; Development of Highly Selective and Efficient Prototype Sensor for Potential Application in Environmental Mercury Pollution Monitoring. *Water, Air and Soil Pollut.* 228 (2017), 314.

67. S. S. Ravi, L. R. Christena, N. SaiSubramanian and S. P. Anthony; Green synthesized silver nanoparticles for selective colorimetric sensing of Hg^{2+} in aqueous solution at wide pH range. *Analyst* 138 (2013), 4370.

Chapter 7

Development of a Carbon Nanomaterial-based Detection Technique for the Potential Environmental Monitoring of Toxic Metal and Non-metal Ions

7.1. Introduction

Fluorescent nanomaterials including semiconductor quantum dots, organic dyes/dye-doped nanoparticles (NPs) and carbon nanomaterials such as carbon nanoclusters (CNCs), carbon dots (CDs), or carbon nanodots (CNDs) have been a prime center of attention for research and development throughout the past few decades for use in field of sensing and bio-imaging. To date, a huge number of high luminescent nanomaterials have been found. However, the applications of these nanomaterials is under question because of their environmental hazards and potential toxicity [1]. Besides an outstanding quantum efficiency, semiconductor quantum dots are less preferred in real life applications due to the involvement of heavy toxic metals and a low chemical stability [2, 3]. On the other hand poor stability of organic dyes/dye-doped NPs prevent their long-term analysis [1]. On account of these, highly fluorescent carbon dots are the best way out of the grid given by the above described dilemma [4]. Recently, CDs have attracted tremendous attention because of their unique physical-chemical characteristics and numerous exceptional advantages such as high chemical stability [5], low toxicity [6], high quantum yield [6], high-fluorescence and excellent biocompatibility [7-9]. Due to these unique properties, CDs have been applied widely in the fields of drug delivery [10], catalysis [11], chemical sensors [4, 12], biomedical application [13, 14], biological sensors [15], nano-biotechnology [16], etc. Although this nanomaterial holds great promise in a wide field of applications, considerable work in the sensing field is still required to develop the advanced smart sensors.

Recently, various simple and environmentally friendly approaches, such as ultrasonic method [17], chemical oxidation method [18], hydrothermal synthesis [19-21], microwave method [22, 23], solvothermal method [24] and laser ablation [25], have been reported to synthesize CDs. However, due to the requirement of high-energy systems and costly starting materials limit the further development of their production. On the other hand, pre-treatments or post-treatments are commonly essential because of the complex and lavish elements of natural bio-resources and high volume strong smoke are usually released after the carbonization [26]. Chemical oxidation of carbohydrates is one of the eye-catching and alternative approaches to produce CDs. However, passivation of carbon dots' surfaces and strong acid or numerous synthesis steps are required for maximum of these synthesis approaches. Moreover, the fluorescence intensity of maximum cooked CDs is affected by the environment, such as temperature, chemical ions, pH of the solution, etc. In this context, we have developed a facile, cost-effective and environmentally friendly technique for one-step hydrothermal synthesis of nontoxic highly fluorescent CDs with high environmental stability, without using any strong acid, surface passivation and pre-treatments or post-treatments.

Due to some unique properties, highly fluorescent CDs can be used as sensor probes in the field of chemical sensing. The development of extremely sensitive and selective fluorescent sensor probes for the selective as well as quantitative estimation of heavy metal and non-metal ions in ground/drinking water has been inspiring the scientific community in the past few decades for concern of human health and environmental safety [27-30]. Among the heavy metal ions, iron is one of the most essential trace elements in the human body and plays an important role in human health clinically as well as environmentally. However, excess concentrations of iron ions in ground/drinking water create health problems in humans. The maximum permissible limit of Fe^{3+} in drinking water is $5.4\,\mu M$ by the U.S. Environmental Protection Agency [31, 32]. Like heavy metal ions, among non-metal ions, small quantities of fluoride (F^-) ions are also an essential component for normal

mineralization of bones and formation of dental enamel in human body [33]. Although, According to WHO the maximum permissible level of fluoride concentration in drinking water is 1.5 mg/L [34]. Because the excessive intake of fluorine compounds may result in slow, progressive scourge known as fluorosis [35]. Two different kinds of fluorosis (skeletal and/or dental) generally observed within human physiology. In skeletal fluorosis, the effect of fluoride can be seen within the bones structure primarily and in dental fluorosis, the teeth enamel is affected mostly by the excess fluoride. Around the world, more than 260 million people are suffering from fluorosis [33]. In addition to these, excessive intake of fluoride can also create neurological problems, thyroid imbalance and nutritional deficiencies in human body. Such chronic F^- toxicity are endemic in over 25 countries, with contamination typically leaching into drinking and irrigation water supplies through rocks rich in F^- minerals, or waste from such industrial processes as aluminum smelting and glass processing. Therefore, research into new solutions for the estimation of low-level concentrations of Fe^{3+} and F^- ions in aqueous medium has become an essential need, aims to surpass existing commercial devices in their accessibility to non-expert users who require regular, laboratory-free sampling, such as remote populations in areas where chronic Fe^{3+} and F^- toxicity is endemic. To date the simultaneous detection of both Fe^{3+} and F^- ions in aqueous media is limited in the literature; however several methods have been reported for detection of Fe^{3+} and F^- ions separately [31, 36-38]. The recently reported methods for the detection of F^- include molecular complexes exhibiting "turn on", "turn off", or ratio-metric color changes. On the other hand few reports have been found in the literature for the quantitative as well as selective estimating of both Fe^{3+} and F^- ions [4, 39]. However, most of the reported methods' have several limitations in real-world use, such as the detection procedures is highly time taking, used sophisticated analytical methods, low sensitivity and in certain cases an instability of the applications [31, 39-45]. Although, among these reported methods, the most favorable method is fluorescence quenching and "turn on" fluorescence based due to

its ease of operation, high sensitivity and selectivity. Therefore, the development of fluorescent probes for detecting Fe^{3+} and F^- ions has attracted increasing attentions. The effective fluorescent probes for Fe^{3+} and F^- ions detection is mainly limited to organic fluorescent molecular, quantum dots, carbon dots and their complexes [46-49]. However, those have several drawbacks for practical applications due to their poor stability, complicated synthesis route, complex sample preparation, relatively high cost of starting materials and high toxicity towards biological system [49-51]. Therefore, the development of a facile synthesis, photostable, highly efficient, low-cost and environmental friendly fluorescence probe sensor for rapid qualitative as well as quantitative analysis of Fe^{3+} and F^- ions in real world water samples is still worthwhile and challenging.

In this work, we report a very simple, facile and cost-effective synthesis of nontoxic highly fluorescent CDs through one step hydrothermal treatment of Polyvinylpyrrolidone (PVP). The novel CDs are synthesis without using any strong acid, base, organic solvent or other post-synthetic surface passivation because PVP serves a dual role as both the source of CDs and as a passivation agent. Herein, we also report a highly efficient, selective, extremely low-cost and sensitive "turn off" and "turn on" dual fluorescence sensors for Fe^{3+} and F^- ions in aqueous media. The proposed sensors exhibit a high selectivity for Fe^{3+} and F^- ions in the background of a wide range of competing heavy metal ions and non-metal ions respectively. This report is devoted to studying the steady-state fluorescence quenching ("turn off" fluorescence) of the CDs by Fe^{3+} ions and the interaction between them. Picosecond time-resolved studies on CDs with various concentrations of Fe^{3+} ions, confirm the static fluorescence quenching. On the other hand, fluorescence "turn on" of the CDs-Fe^{3+} nanocomposite complex depends on the interaction between Fe^{3+} and F^- ions in the solution. The possible interaction between CDs and Fe^{3+} ions and/or CDs-Fe^{3+} nanocomposite complex and F^- ions have been examined by TEM imaging studies. Determination of fluoride contamination in the real life drinking water samples has also been shown using developed sensor. To the best of our knowledge, this is an

extremely simple "turn off" and "turn on" dual fluorescence sensor for Fe^{3+} and F^- ions detection in an aqueous medium with very high sensitivity and selectivity.

7.2. Results and Discussion

7.2.1. Development of Highly Efficient Dual Sensor Based on Carbon Dots for Direct Estimation of Iron and Fluoride Ions in Drinking Water [52]:

7.2.1.1. Characterization of Carbon Dots (CDs): The as-prepared CDs were characterized by UV-Vis spectra, steady-state fluorescence spectra, HRTEM imaging, DLS study as well as FTIR measurement. To confirm the formation of CDs, the absorbance and the fluorescence emission of the as-prepared sample were collected. The UV-Vis spectrum of as-prepared CDs is shown in Figure 7.1a. It is evident from this spectrum that the characteristic absorbance of the CDs is in the UV region, with a tail extending to the visible region. Figure 7.1a also represents the enormous blue luminescence of the CDs under excitation 300 nm. The CDs are completely dissolved into the distil water and show up transparent and a slightly deep-brown colour in daylight, which changes to an enormous blue emission (inset of Figure 7.1a) under the UV light excitation. As shown in Figure 7.1b, the CDs are able to fluoresce highly with different excitation wavelengths (ranging from 300 to 380 nm) and the highest fluorescence is found with 300 nm excitation wavelength. In addition to that the fluorescence of the CDs becomes redshifted with increasing excitation wavelengths. Here, this fluorescence is not only due to the different particle size of CDs but also due to surface defects which act as a capturing centre for excitons [4, 53]. The DLS and HRTEM measurements were performed to investigate the particle size distribution and crystallographic structural information of the CDs. Figure 7.1c represents the HRTEM image of the CDs. It is evident from the HRTEM image that the estimated particles size is around 5-6 nm. The particle size distribution is further reconfirmed by DLS study. The average particles size distribution is estimated to be 3.80 ± 0.11 nm from the DLS study (Figure 7.1d), which exactly reflect the HRTEM result. The detailed crystallographic structural information of CDs is demonstrated by HRTEM

imaging. Inset of the Figure 7.1c shows the continuous single directional lattice fringes. The measured inter-planar distance of the fringes is about 0.32 nm corresponds to [002] lattice planes of graphite [54, 55]. Figure 7.1e shows the FTIR spectrum of the nanomaterials (CDs powder), produced after overnight lyophilization of the
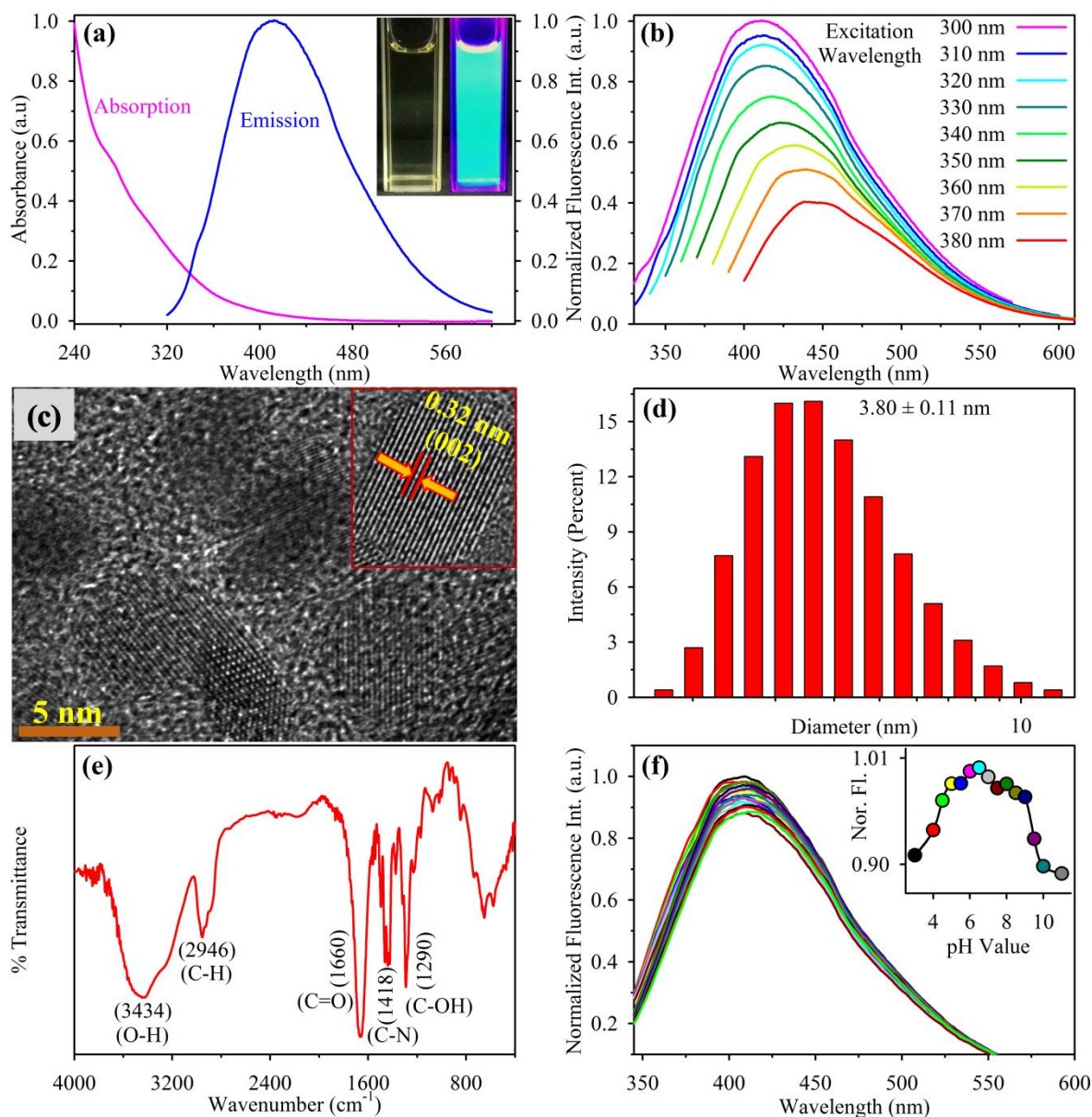
Figure 7.1. *(a) UV–Vis absorption spectrum and fluorescence emission (λ_{ex} = 300 nm) spectrum of the as-synthesised CDs. Inset: Visual representation of the as-synthesised CDs under day light and UV light. (b) Fluorescence emission of the CDs with increasing excitation wavelength. (c) HRTEM image of the CDs. (d) DLS measurement of the CDs. (e) FTIR spectrum of the CDs. (f) Fluorescence spectra of the CDs in a solution with different pH values. Inset shows the change in fluorescence intensity at 410 nm with different pH values ranging from 3 to 11.*

as- prepared CDs. The broad absorption band centered at 3434 cm^{-1} is attributed to the O-H stretching mode of H_2O absorbed on the surface of the materials [56]. On the other hand the absorption bands centered at 1660 cm^{-1} and 1218 cm^{-1} are due to the C=O stretching motion and C-N stretching motion of monomer for PVP, respectively [19, 57]. These results of FTIR spectroscopy confirm that the CDs are produced after hydrothermal carbonization of PVP. The dependence of fluorescence intensity on the amount of PVP, reaction temperature and the reaction time during the hydrothermal treatment for the synthesis of CDs were investigated and optimized to 30 mg/mL, 200 ^{0}C and 6 hours respectively (data not shown). The dependence of fluorescence intensity of the as-prepared CDs on pH values is also investigated. As shown in Figure 7.1f, the fluorescence intensity of the CDs was not only highly stable but also the emission peak did not shift over a wide range of pH from 3 to 11. Inset of the Figure 7.1f revealed that the maximum fluorescence intensity of the CDs was found at pH – 6.5. The observed result indicates that the fluorescence intensity of the as-prepared CDs (pH = 6.5) is maximum. Therefore, the as-prepared high-quality CDs with a high quantum yield (calculated using Harmine as a reference (45%) is about 24.26%), excellent water solubility and good photostability were chosen for our further studies.

7.2.1.2. Interaction between CDs and Fe^{3+} Ions: The fluorescence emission spectrum of CDs in the presence of Fe^{3+} ions was investigated to observe the effect of Fe^{3+} ions on the CDs. As shown in Figure 7.2a, the overall fluorescence intensity of the CDs is quenched dramatically in the presence of Fe^{3+} ions without an obvious change of the peak shape. The huge change in the fluorescence intensity suggests that the quencher Fe^{3+} ions affect the structure/size of the CDs. To gain more insight into the origin of the fluorescence quenching behaviour of CDs in presence of Fe^{3+} ions, HRTEM, EDAX and DLS were performed. It is evident from the Figure 7.2b, the structure/size of the CDs is enhanced after interaction with Fe^{3+} ions and CDs-Fe^{3+} nanocomposite complexes are formed. The formation of CDs-Fe^{3+} nanocomposite complexes is further confirmed by EDAX study, as shown in the inset of Figure 7.2b. The huge presence of carbon and iron in the EDAX spectra relate to the complexation
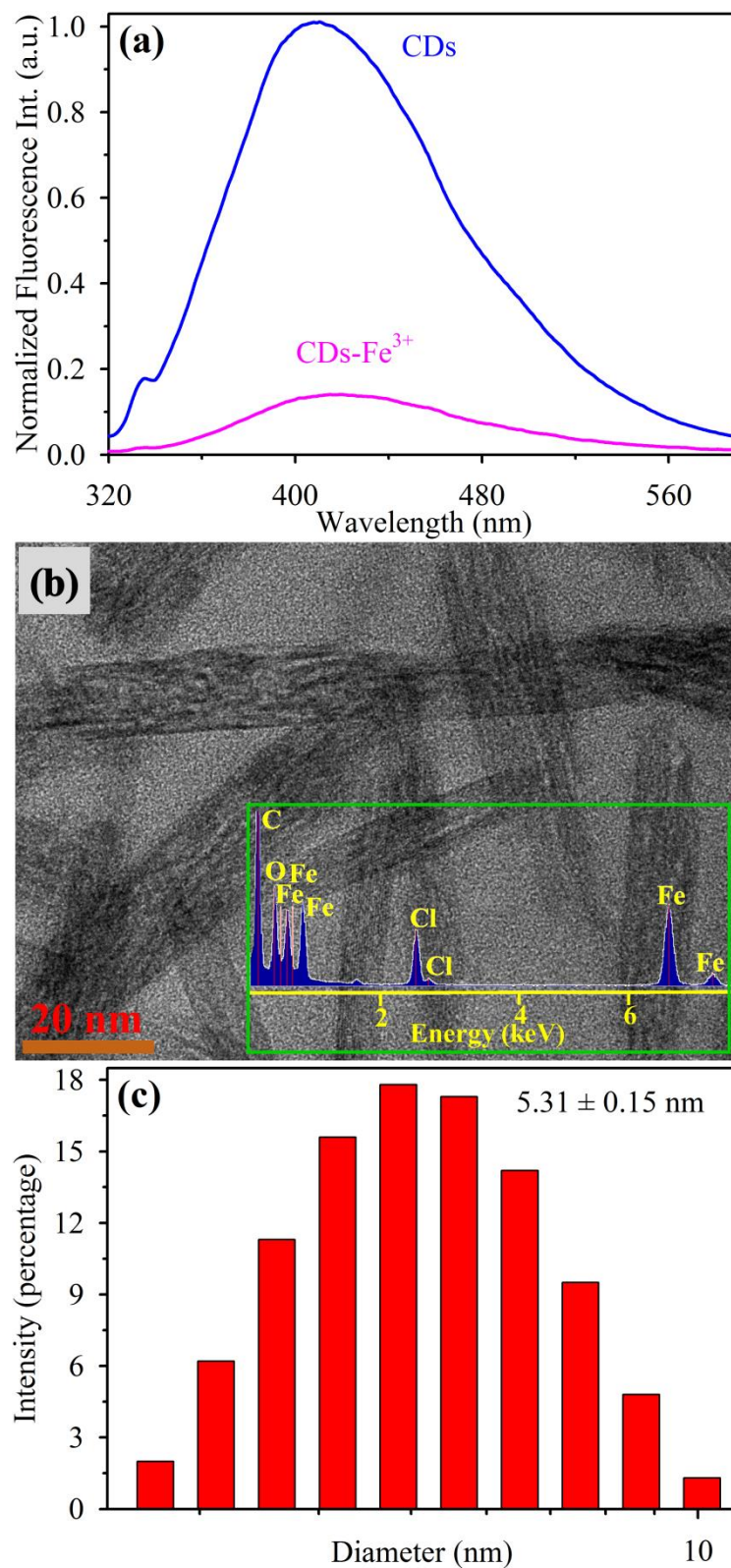
Figure 7.2. *(a) Fluorescence emission spectra of the CDs in presence and absence of Fe^{3+} (300 μM) ions. (b) HRTEM image of the CDs-Fe^{3+} nanocomposite complex. Inset shows the EDAX spectra of the complex. (c) DLS measurement of the CDs-Fe^{3+} nanocomposite complex.*

of CDs with Fe^{3+} ions. From HRTEM it is resolved that the average diameter of CDs-Fe^{3+} nanocomposite complex is approximately 70 nm, while the average diameter of fresh CDs is around 3.80 ± 0.11 nm (Figure 7.1d). The formation of said structure would be due to the metallophilic interaction of Fe^{3+} containing CDs under electron beam irradiation inside the TEM, lead to the self-assembly or aggregation of the complexes. It has to be noted that the larger structural size of the CDs upon impregnation of Fe^{3+} is not found in aqueous solution (average diameter of complex in aqueous solution is around 5.31 ± 0.15 nm), as shown in the DLS measurement (Figure 7.2c). These observations confirm that Fe^{3+} ions actuate strong fluorescence quenching and induce the formation of non-fluorescence complex between the surface functional groups of CDs and Fe^{3+} ions, which results in the strong "turn off" fluorescence arising from the formation of CDs-Fe^{3+} nanocomposite complexes. Here, CDs itself act as a promising nano carrier for loading of Fe^{3+} ions and to form the nanocomposite complexes.

7.2.1.3. Response Time and Selectivity of CDs towards Fe^{3+} Ions: Both short response time and high selectivity are a matter of necessity for an excellent sensor. Therefore, the response time and selectivity of CDs towards Fe^{3+} ions were investigated to find out the incubation time for the further study as well as the effect of other metal ions. Figure 7.3a shows the relative change in fluorescence intensity of the CDs with time with different concentrations of Fe^{3+} ions (0, 5, 10, 20, 30, 50, 75 and 100 μM). The Figure 7.3a reveal that the interaction of the CDs with Fe^{3+} ions is very fast, which can reach a steady condition within 60 sec. Therefore, the fluorescent probe can be appropriate for the rapid analysis of Fe^{3+} ions in real samples. It has been shown that the synthesized CDs exhibits a strong emission and quenched by Fe^{3+} ions.

The selectivity of CDs for Fe^{3+} (300 μM) was investigated by screening its response to relevant other metal ions, including Ca^{2+}, Cd^{2+}, Co^{2+}, Cu^{2+}, Hg^{2+}, Mg^{2+}, Fe^{2+}, As^{3+}, K^+, Na^+, Pb^{2+}, Ag^+, Mn^{2+}, Ni^{2+} and $MeHg^+$ (all other metal ions ~ 10 mM), under the same conditions. As shown in Figure 7.3b, the higher concentrations of other competing metal ions do not affect the fluorescence intensity of the sensor
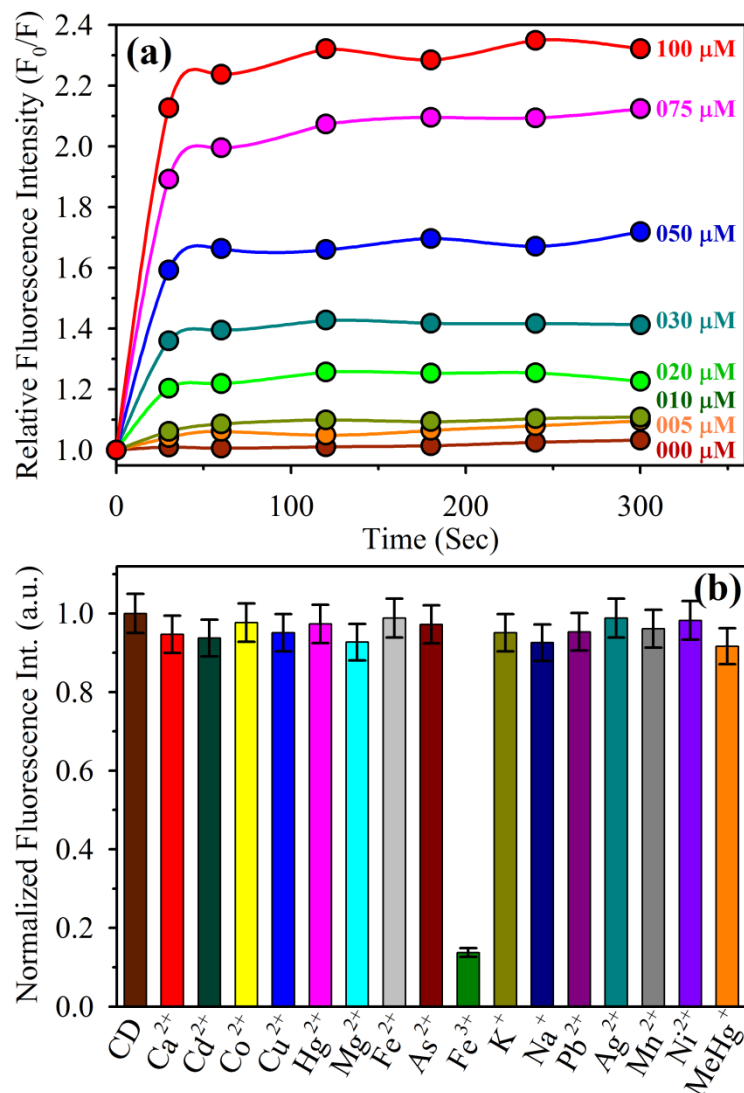
Figure 7.3. *(a) Relative change in fluorescence intensity of the CDs as a function of time for different concentrations of Fe^{3+} ions (0-100 μM) in aqueous media (b) Normalized fluorescence intensity of the CDs in presence of Fe^{3+} ions (300 μM) and other competing heavy metal ions (10 mM).*

probe significantly. The high fluorescence quenching effect of Fe^{3+} may originate from selective coordination and higher binding affinity of Fe^{3+} towards functional group of the CDs. Compared with other cations, the electron-deficient Fe^{3+} is selectively coordinated and has a higher binding affinity towards the electron-rich groups (such as -OH, -C-N, -C=O) on the surface of the CDs [58, 59]. Due to such coordination interaction and higher binding affinity towards functional group of the CDs, the strong fluorescence quenching provoked only by Fe^{3+} compared with that of other metal cations. In addition to all some other metal cations can also react with electron-rich

groups in the CDs but they have weak electrophilic ability compare to Fe^{3+} ions, which may lead to lower or no fluorescence quenching compare to Fe^{3+}. The selectivity studies clearly exhibit a high selectivity of sensor probe towards Fe^{3+} ions in the background of other metal ions. These results demonstrate the reliability of the sensor probe for the detection of Fe^{3+} ions in aqueous media without any interference by other metal ions.

7.2.1.4. Quenching Mechanisms and Determination of Fe^{3+} Ions: High sensitivity is a matter of necessity for an excellent sensor. For the quantitative detection of Fe^{3+} ions and to know the quenching mechanism we record the steady-state fluorescence emission of the CDs with increasing concentration Fe^{3+} ions. Figure 7.4a presents the fluorescence quenching of CDs under different concentration of Fe^{3+} ions. The figure also reveals the quenching effect of iron ions on the fluorescence of CDs upon excitation at 300 nm. The strong fluorescence quenching of the nanomaterials by the Fe^{3+} ions might arise due to ground state complexation (static quenching), collisional interaction/excited state reaction (dynamic quenching), through nonradioactive energy transfer, molecular rearrangements and surface emissive group destruction [4, 60]. To realize the specified quenching mechanism, lifetime measurements of the fluorescence probe were also carried out with different concentration of Fe^{3+} ions. Figure 7.4b presents the fluorescence transients of CDs in the absence and presence of different Fe^{3+} ions concentrations, collected at 460 nm upon excitation 375 nm. The fluorescence transients of CDs showed multi-exponential time constants with the average lifetime (τ_0) of 1.2 ns, which remained unchanged in the presence of various concentrations of Fe^{3+} ions. The results rule out any kind of exited state processes including electron transfer and/or excited state reaction of the CDs and Fe^{3+} ions in the aqueous medium. In order to explain the exact quenching mechanism, the relative change in fluorescence intensity and average lifetime of CDs has been plotted as a function of the quencher (Fe^{3+} ions) concentrations (Figure 7.4c). The relative change in fluorescence intensity and average lifetime of the CDs is proportional to Fe^{3+} ions concentration that was well explained by considering the well-known Stern-Volmer

156
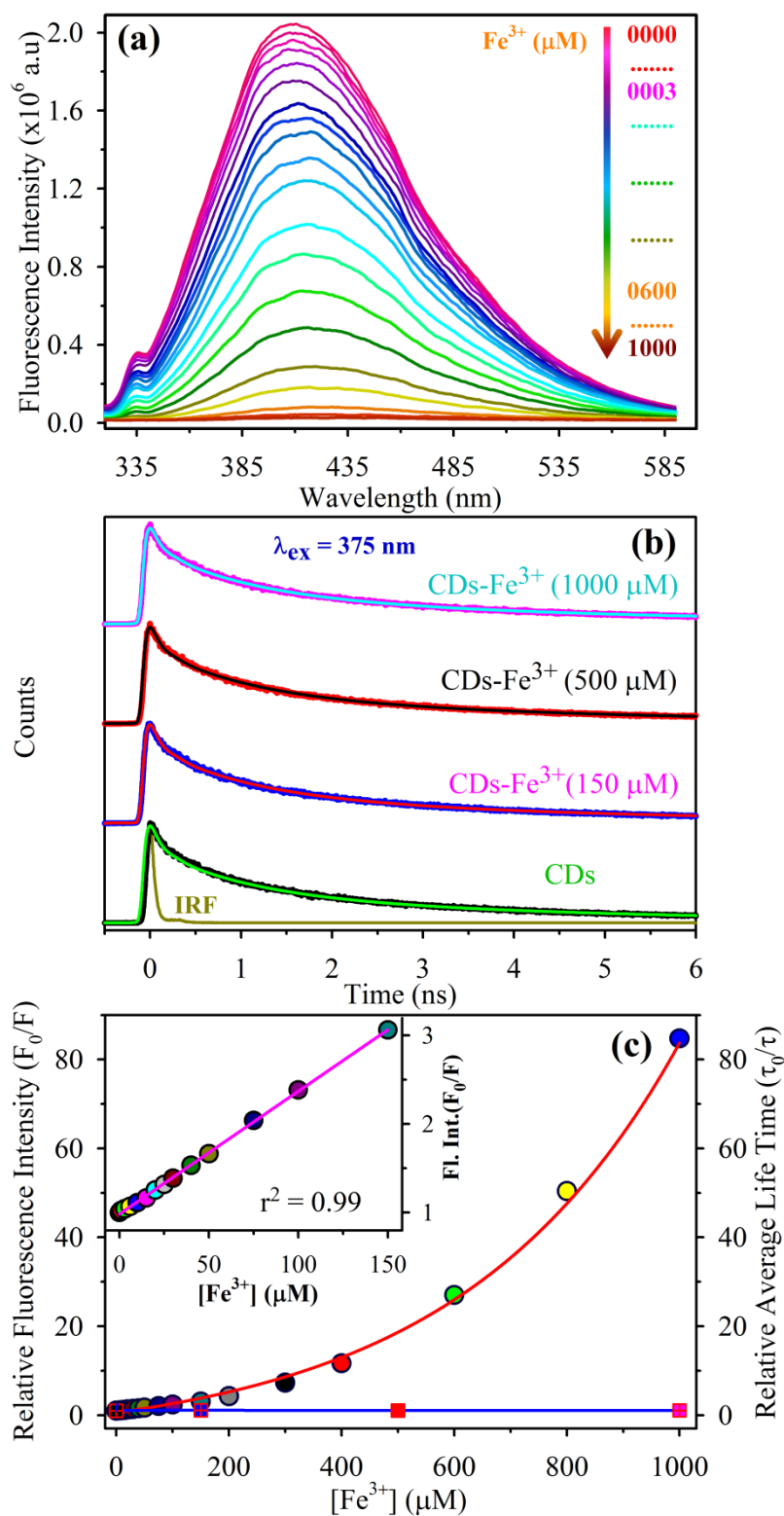
Figure 7.4. *(a) Steady-state fluorescence spectra (λ_{ex} = 300 nm) of the CDs with increasing concentrations of Fe^{3+} ions (0-1000 μM). (b) Picosecond time-resolved fluorescence transients of the CDs with increasing concentrations of Fe^{3+} ions. (c) Plots of F_0/F vs [Fe^{3+}] at 410 nm (red) and τ_0/τ vs [Fe^{3+}] (blue). Inset shows the linear part of the plot of F_0/F vs [Fe^{3+}].*

(SV) equations.

$$\frac{F_0}{F} = 1 + k_q\tau_0[Q] = 1 + K_{SV}[Q] \qquad (7.1)$$

and
$$\tau_0/\tau = 1 + k_q\tau_0[Q] = 1 + K_D[Q] \qquad (7.2)$$

where F_0 and F are the fluorescence intensities of the probe sensor in the absence and presence of quencher (Fe^{3+} ions) respectively, k_q is the bimolecular quenching constant, K_{SV} is the Stern-Volmer quenching constant, τ_0 and τ are the average lifetime of the fluorophore in the absence and present of quencher respectively, K_D is the dynamic quenching constant and $[Q]$ is the quencher concentration. It is well reported that in dynamic quenching, $F_0/F = \tau_0/\tau$, while for static quenching, F_0/F increases but τ_0/τ remains unchanged with quencher concentration, i.e, $\tau_0/\tau = 1$ [60, 61]. As shown inset of the Figure 7.4c, the relative change in fluorescence intensity (F_0/F) increases linearly with quencher concentration (upto 150 μM) and was well explained by SV equations ($K_{SV} = 1.39\times10^4$ M^{-1}). But τ_0/τ remains unchanged even with very high quencher concentration (Figure 7.4c). The observed results indicate that the fluorescence quenching provoked by Fe^{3+} was probably due to static quenching and the strong quenching was arising due to the formation of CDs-Fe^{3+} nanocomposite complex in the solution. The nanocomposite complex was formed by the attachment of Fe^{3+} ions to the surface functional groups of the CDs, result in an obvious fluorescence quenching.

A gradual quenching process in fluorescence intensity of CDs was observed upon progressive addition of Fe^{3+} ions. The plot of relative change in fluorescence intensity (F_0/F) with different concentration of Fe^{3+} ions shows a good linear relationship in the range 0-150 μM with slope = 0.0139, intercept = 0.98 and $r^2 = 0.99$ (inset of the Figure 7.4c). However, the linearity deviates after the quencher concentration 150 μM and shows a nonlinearity followed by the equation $Y = ae^{\frac{X}{t}} + y$ (Figure 7.4c), Y relative fluorescence intensity and X is the Fe^{3+} ions' concentration with the values $a = 6.95, t = 390.35$ and $y = -6.37$. Finally, it is evident from the

Figure 7.4 that our highly efficient fluorescence sensor had a detection limit of 1 μM for Fe^{3+} ions, which is comparable with other reported colorimetric as well as fluorescence based sensor [8, 62, 63]. Hence, this is a highly promising, highly efficient, extremely low-cost and sensitive "turn off" fluorescence sensor for Fe^{3+} ions.

7.2.1.5. *Interaction of CDs-Fe^{3+} Nanocomposite Complex with F^- Ions:*
Interaction of CDs-Fe^{3+} nanocomposite complex with F^- ions was investigated under the same condition as before. Figure 7.5a revealed the ballistic enhancement in fluorescence intensity of CDs-Fe^{3+} nanocomposite complex after interaction with F^- ions. Therefore in the progression we have used the CDs-Fe^{3+} nanocomposite complex as a novel sensor probe for the detection of F^- ions. The remarkable change
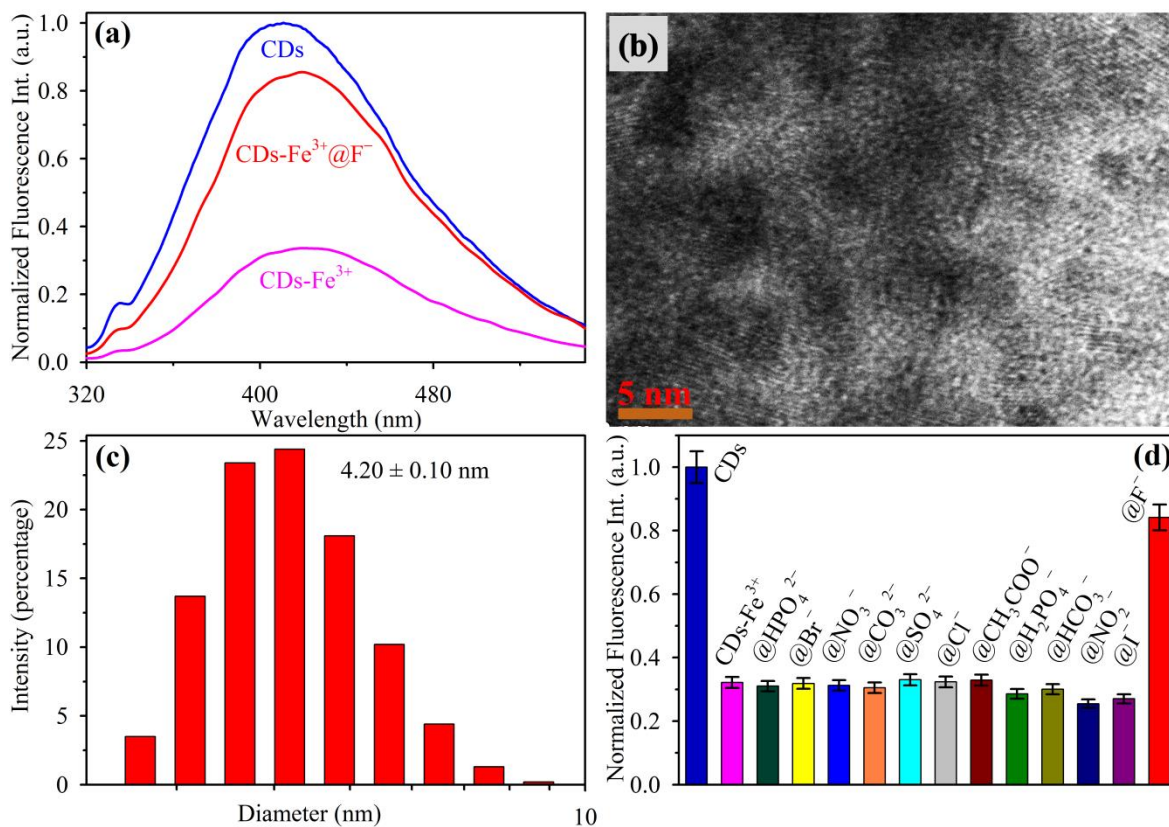
Figure 7.5. *(a) Fluorescence emission spectra of the CDs in presence and absence of Fe^{3+} ions and fluorescence emission spectra of the CDs-Fe^{3+} nanocomposite complex in presence of F^- ions. (b) HRTEM image of the CDs-$Fe^{3+}@F^-$ complex. (c) DLS measurement of the CDs-$Fe^{3+}@F^-$ complex. (d) Normalized fluorescence intensity of the CDs-Fe^{3+} nanocomposite complex in presence of F^- ions and other competing anions (@anions ~ CDs-Fe^{3+}@anions).*

in fluorescence intensity is a consequence of complexation between hard Fe^{3+} with hard and less polarisable F^- ions. Formation of thermodynamically highly stable $[FeF_6]^{3-}$ complex liberate most of the Fe^{3+} ions from the surface emissive site of the CDs which make the surface free from the quencher Fe^{3+} ions, employing "turn on" fluorescence. Fluorescence intensity spectra of CDs-$Fe^{3+}@F^-$ was lower in intensity as compare to as-synthesised CDs because all the entire surface emissive site of the CDs were not get free from Fe^{3+} ions (Figure 7.5a). As the complex CDs-Fe^{3+} was destroyed in presence of F^- ions and CDs were get almost free from Fe^{3+} ions, it is expected that the particles size of the complex in the solution will also reduce in presence of F^- ions. As shown in Figure 7.5b, the size of the CDs-Fe^{3+} nanocomposite complex was decreased after interaction with F^- ions and formed almost Fe^{3+} ions free bare CDs. The estimated particles size from the HRTEM image of CDs-$Fe^{3+}@F^-$ was around 6-7 nm. The particle size reduction was further confirmed by DLS studies (Figure 7.5c). Figure 7.5c revealed that the average diameter of CDs-Fe^{3+} was reduced from 5.31 ± 0.15 nm to 4.20 ± 0.10 nm in presence of F^- ions in the solution, while the average diameter of fresh CDs was around 3.80 ± 0.11 nm (Figure 7.1d). The results clearly indicate that the "turn on" fluorescence occurs due to the formation of bare CDs from CDs-Fe^{3+} nanocomposite complexes in presence of F^- ions in the solution.

7.2.1.6. Selectivity of CDs-Fe³⁺ Nanocomposite Complex towards F⁻ Ions: It is proven that the fluorescence intensity of the CDs-Fe^{3+} nanocomposite complex increases dramatically in presence of F^- ions. Now to investigate the selectivity of the probe towards F^- ions over other anions, including HPO_4^{2-}, Br^-, NO_3^-, CO_3^{2-}, SO_4^{2-}, Cl^-, CH_3COO^-, $H_2PO_4^-$, HCO_3^-, NO_2^- and I^- (all anions ~ 10 mM) were examined under the same conditions. These results demonstrated that no significant change in fluorescence intensity in the presence of other anions even under high concentrations (Figure 7.5d). The observed results reveal the high selectivity of sensor

probe towards F⁻ ions in the background of other competing anions. The results also indicate that the sensor probe might be highly reliable for the detection of F⁻ ions in real world water samples without any interference of other anions.

7.2.1.7. Determination of the Standard Solution of F⁻ Ions: In this subsection, we are presenting the qualitative as well as quantitative detection of F⁻ ions in aqueous medium by our developed sensor, which is extremely low-cost and selective. As shown
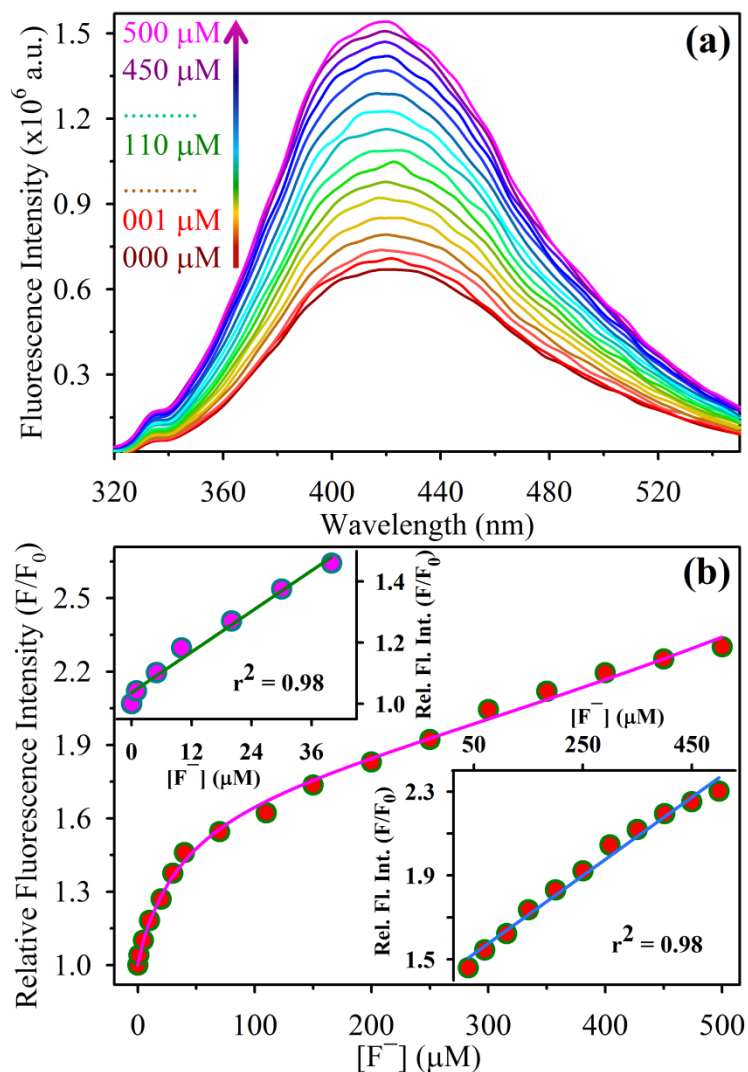
Figure 7.6. *(a) Steady-state fluorescence spectra (λ_{ex} = 300 nm) of the CDs-Fe³⁺ nanocomposite complex with increasing concentrations of F⁻ ions (0-500 μM). (b) The plot of relative change in fluorescence intensity of CDs-Fe³⁺@F⁻ complex against F⁻ ions concentrations (0-500 μM). Upper inset shows the linear response of the sensor with the concentrations of F⁻ ions from 0-40 μM. Lower inset shows the linear response of the sensor with the concentrations of F⁻ ions from 40-500 μM.*

in Figure 7.6a, the fluorescence intensity of the CDs-Fe^{3+} nanocomposite complex was increase dramatically with increasing concentration of F^- ions (range ~ 0–500 μM). The fluorescence intensity of the CDs-Fe^{3+} nanocomposite complex was started "turn on" when the concentration of F^- ions was 1 μM (Figure 7.6a). The result clearly exhibited that the sensor had a detection limit as low as 1 μM for F^- ions, which is much lower than the maximum permissible limit of fluoride and comparable with recently reported colorimetric as well as fluorescence base sensor [4, 37, 39, 64, 65]. The relative change in fluorescence intensity (F/F_0 ~ F and F_0 are the fluorescence intensities of the nanocomposite complex in the presence and absence of F^- ions) with different concentration (0–500 μM) of F^- ions displays a nonlinear relationship followed by the equation $Y=(X + 23.08)*[9.86 + 0.56*(X + 23.08) − 2.99*10^{-4}*(X + 23.08)^2]^{-1}$ (Figure 7.6b), where Y is the relative fluorescence intensity and X is the F^- ions' concentration (in μM). However, the above nonlinearity turned to very good linearity for the two different concentration ranges with different slopes. Upper inset of the Figure 7.6b exhibits the linear response of the sensor for lower concentration range (0–40 μM) of F^- ions with slope = 11.08×10^{-3}, intercept = 1.04 and r^2 = 0.98. For the higher concentration range (40–500 μM) of F^- ions, the sensor follows another linearity with slope = 1.87×10^{-3}, intercept = 1.43 and r^2 = 0.98 (lower inset of the Figure 7.6b). These linear responses increase the feasibility of the sensor for real life applications. These results also imply that this highly selective, extremely cost-effective, sensitive and highly efficient novel "turn on" fluorescence sensor can be applied to the direct detection of F^- ions in real world water samples.

**7.2.1.8. Determination of F^- Ions in Real World Drinking Water Samples:** Potential applications of the developed sensor are appraised for determination of F^- ions in real world water samples. Real world drinking water samples were collected from different drinking water tap in our institute for this experiment. As the collected environmental real world drinking water samples were not fully purified, cations and

anions are likely to be present in significant amounts. Due to the adequate presence of different ions in the collected real world drinking water samples, the measurements of F^- ions in such environmental samples were extremely challenging. However, the proposed sensor can be able to detect F^- ions in such environmental real drinking water samples due to its high sensitivity and selectivity. The measured concentration of

Table 7.1. *Determination of F^- ions in real water samples using the proposed sensor.*

Samples	Concentration of F^- ions before spiked (tested by the sensor)	Spiked F^- ions (μM)	Measured F^- ions (μM)		Recovery (%)	RSD (%)
			Mean	SD		
Sample 1	Not found	10	7.33	1.07	73.30	14.60
Sample 2	Not found	50	41.75	2.36	83.50	5.65
Sample 3	Not found	150	136.75	5.38	91.17	3.93
Sample 4	Not found	300	273.25	7.89	91.08	2.89
Sample 5	Not found	450	427.25	5.97	94.94	1.40

SD ~ Standard deviation (n=4), Recovery(%) = 100×(concentration found/concentration added), RSD(%) = Relative standard deviation of four determination = Coefficient of variation×100.
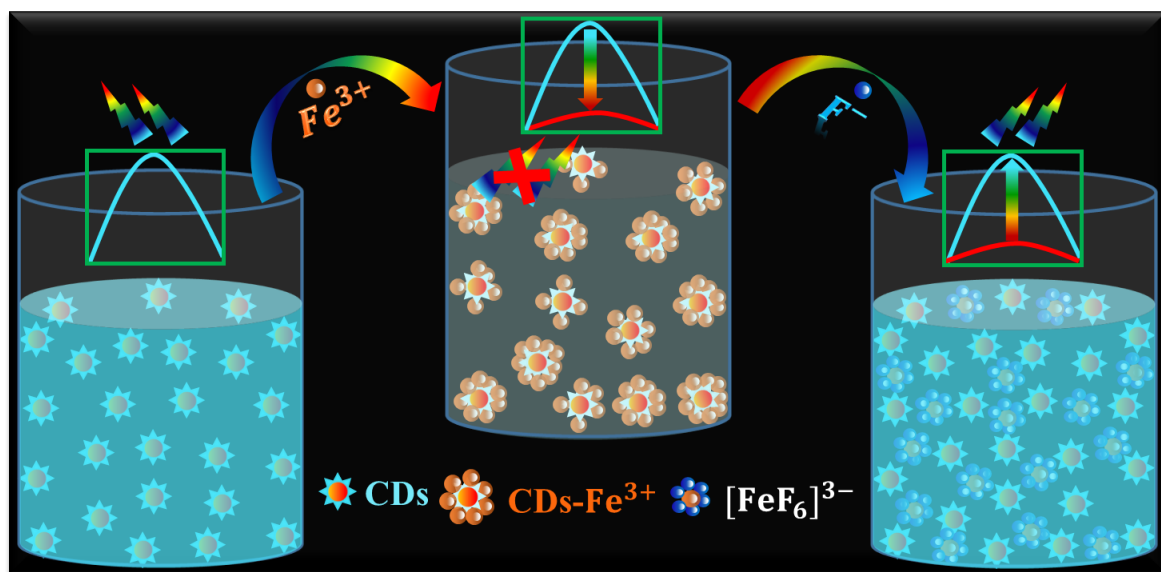
Figure 7.7. *Schematic representation of the overall sensor. "Turn off" fluorescence arises in the presence of Fe^{3+} ions and "turn on" fluorescence occurs in presence of F^- ions due to the formation of bare CDs in the solution.*

F⁻ ions in the collected and spiked real world drinking water samples by the proposed sensor are summarized in Table 7.1. The summarized results display good agreement with the expected values. Table 7.1 also reveals that the recoveries (the ratio of measured value to expected value of F⁻ ions) and the RSDs in the measurement of real water samples with different spiked concentration levels are in between 73.30 – 94.94% and 1.40 – 14.60%. It is clear from our studies that the developed highly selective, sensitive and truly cost-effective "turn on" fluorescence sensor has extremely high potential for the estimating of trace F⁻ ions in environmental real world drinking water samples. The overall sensing procedure is shown schematically in the Figure 7.7.

7.3. Conclusion

In conclusion, we have demonstrated a simple and highly economical method for the preparation of the extremely fluorescent CDs in aqueous media through the one step hydrothermal carbonization of PVP. The as-prepared high-quality CDs were exhibit good stability over a broad pH range. In addition, using the as-prepared CDs we have successfully developed a simple, cost-effective, extremely selective and sensitive "turn off" fluorescence sensor based on the formation of CDs-Fe^{3+} nanocomposite complex for direct estimation of Fe^{3+} ions in water medium. The Stern−Volmer plots ensure that the quenching mechanism is purely static quenching in nature. Further, in the progression we have utilised the CDs-Fe^{3+} nanocomposite complex as a novel sensor probe for the detection of F⁻ ions in aqueous medium based on "turn on" fluorescence mechanism. Fluorescence "turn on" occur due to the formation of bare CDs in the solution from CDs-Fe^{3+} nanocomposite complex in presence of F⁻ ions. The developed sensor has potential applications in estimating trace F⁻ ions in real world drinking water samples. In addition to all, we have successfully developed a highly efficient, selective, extremely low-cost and sensitive "turn off" and "turn on" dual fluorescence sensors for Fe^{3+} and F⁻ ions. The further augmentation of this concept is considerable, which offers great potential for the buildout of economical and efficient portable devices.

References

1. A. Salinas-Castillo, M. Ariza-Avidad, C. Pritz, M. Camprubi-Robles, B. Fernandez, M. J. Ruedas-Rama, A. Megia-Fernandez, A. Lapresta-Fernandez, F. Santoyo-Gonzalez, A. Schrott-Fischer and L. F. Capitan-Vallvey; Carbon dots for copper detection with down and upconversion fluorescent properties as excitation sources. *Chem. Commun.* 49 (2013), 1103.

2. A. M. Derfus, W. C. Chan and S. N. Bhatia; Probing the cytotoxicity of semiconductor quantum dots. *Nano Lett.* 4 (2004), 11.

3. C. Kirchner, T. Liedl, S. Kudera, T. Pellegrino, A. Muñoz Javier, H. E. Gaub, S. Stölzle, N. Fertig and W. J. Parak; Cytotoxicity of colloidal CdSe and CdSe/ZnS nanoparticles. *Nano Lett.* 5 (2005), 331.

4. P. J. S. Rana, P. Singh and P. Kar; Carbon nanoparticles for ferric ion detection and novel HFCNs–Fe^{3+} composite for NH_3 and F^- estimation based on a "turn on" mechanism. *J. Mater. Chem. B* 4 (2016), 5929.

5. Q.-L. Zhao, Z.-L. Zhang, B.-H. Huang, J. Peng, M. Zhang and D.-W. Pang; Facile preparation of low cytotoxicity fluorescent carbon nanocrystals by electrooxidation of graphite. *Chem. Commun.* 41 (2008), 5116.

6. S. Zhu, Q. Meng, L. Wang, J. Zhang, Y. Song, H. Jin, K. Zhang, H. Sun, H. Wang and B. Yang; Highly photoluminescent carbon dots for multicolor patterning, sensors and bioimaging. *Ang. Chem. Int. Ed.* 125 (2013), 4045.

7. G. Leménager, E. De Luca, Y.-P. Sun and P. P. Pompa; Super-resolution fluorescence imaging of biocompatible carbon dots. *Nanoscale* 6 (2014), 8617.

8. M. Zhou, Z. Zhou, A. Gong, Y. Zhang and Q. Li; Synthesis of highly photoluminescent carbon dots via citric acid and Tris for iron (III) ions sensors and bioimaging. *Talanta* 143 (2015), 107.

9. T.-Y. Wang, C.-Y. Chen, C.-M. Wang, Y. Z. Tan and W.-S. Liao; Multicolor functional carbon dots via one-step refluxing synthesis. *ACS Sens.* 2 (2017), 354.

10. T. Sun, Y. S. Zhang, B. Pang, D. C. Hyun, M. Yang and Y. Xia; Engineered nanoparticles for drug delivery in cancer therapy. *Ang. Chem. Int. Ed.* 53 (2014), 12320.

11. L. Cao, S. Sahu, P. Anilkumar, C. E. Bunker, J. Xu, K. S. Fernando, P. Wang, E. A. Guliants, K. N. Tackett and Y.-P. Sun; Carbon nanoparticles as visible-light photocatalysts for efficient CO_2 conversion and beyond. *J. Am. Chem. Soc.* 133 (2011), 4754.

12. S. Bhattacharya, R. Sarkar, B. Chakraborty, A. Porgador and R. Jelinek; Nitric oxide sensing through azo-dye formation on carbon dots. *ACS Sens.* 2 (2017), 1215.

13. S.-T. Yang, X. Wang, H. Wang, F. Lu, P. G. Luo, L. Cao, M. J. Meziani, J.-H. Liu, Y. Liu and M. Chen; Carbon dots as nontoxic and high-performance fluorescence imaging agents. *J. Phys. Chem. C* 113 (2009), 18110.

14. W. Yang, H. Zhang, J. Lai, X. Peng, Y. Hu, W. Gu and L. Ye; Carbon dots with red-shifted photoluminescence by fluorine doping for optical bio-imaging. *Carbon* 128 (2018), 78.

15. Z. Qian, J. Ma, X. Shan, H. Feng, L. Shao and J. Chen; Highly luminescent N-doped carbon quantum dots as an effective multifunctional fluorescence sensing platform. *Chem. Eur. J.* 20 (2014), 2254.

16. J. Shen, Y. Zhu, X. Yang and C. Li; Graphene quantum dots: Emergent nanolights for bioimaging, sensors, catalysis and photovoltaic devices. *Chem. Commun.* 48 (2012), 3686.

17. Z. Ma, H. Ming, H. Huang, Y. Liu and Z. Kang; One-step ultrasonic synthesis of fluorescent N-doped carbon dots from glucose and their visible-light sensitive photocatalytic ability. *New J. Chem.* 36 (2012), 861.

18. H. Peng and J. Travas-Sejdic; Simple aqueous solution route to luminescent carbogenic dots from carbohydrates. *Chem. Mater.* 21 (2009), 5563.

19. X. Ren, J. Liu, X. Meng, J. Wei, T. Liu and F. Tang; Synthesis of ultra‑stable fluorescent carbon dots from polyvinylpyrrolidone and their application in the detection of hydroxyl radicals. *Chem. Asian J.* 9 (2014), 1054.

20. G. Wang, X. Pan, L. Gu, W. Ren, W. Cheng, J. N. Kumar and Y. Liu; Fluorescent carbon dot (C-dot) nanoclusters. *Nanotechnology* 25 (2014), 375601.

21. Y. Liu, Q. Zhou, Y. Yuan and Y. Wu; Hydrothermal synthesis of fluorescent carbon dots from sodium citrate and polyacrylamide and their highly selective detection of lead and pyrophosphate. *Carbon* 115 (2017), 550.

22. T.-N. Pham-Truong, T. Petenzi, C. Ranjan, H. Randriamahazaka and J. Ghilane; Microwave assisted synthesis of carbon dots in ionic liquid as metal free catalyst for highly selective production of hydrogen peroxide. *Carbon* 130 (2018), 544.

23. Y. Liu, N. Xiao, N. Gong, H. Wang, X. Shi, W. Gu and L. Ye; One-step microwave-assisted polyol synthesis of green luminescent carbon dots as optical nanoprobes. *Carbon* 68 (2014), 258.

24. Y.-Q. Zhang, D.-K. Ma, Y. Zhuang, X. Zhang, W. Chen, L.-L. Hong, Q.-X. Yan, K. Yu and S.-M. Huang; One-pot synthesis of N-doped carbon dots with tunable luminescence properties. *J. Mater. Chem.* 22 (2012), 16714.

25. Y.-P. Sun, B. Zhou, Y. Lin, W. Wang, K. S. Fernando, P. Pathak, M. J. Meziani, B. A. Harruff, X. Wang and H. Wang; Quantum-sized carbon dots for bright and colorful photoluminescence. *J. Am. Chem. Soc.* 128 (2006), 7756.

26. Q. Liang, W. Ma, Y. Shi, Z. Li and X. Yang; Easy synthesis of highly fluorescent carbon quantum dots from gelatin and their luminescent properties and applications. *Carbon* 60 (2013), 421.

27. J. Chan, S. C. Dodani and C. J. Chang; Reaction-based small-molecule fluorescent probes for chemoselective bioimaging. *Nat. Chem.* 4 (2012), 973.

28. Y. Dong, R. Wang, G. Li, C. Chen, Y. Chi and G. Chen; Polyamine-functionalized carbon quantum dots as fluorescent probes for selective and sensitive detection of copper ions. *Anal. Chem.* 84 (2012), 6220.

29. D. Santra, S. Mandal, A. Santra and U. K. Ghorai; Cost-effective, wireless, portable device for estimation of hexavalent chromium, fluoride and iron in drinking water. *Anal. Chem.* 90 (2018), 12815.

30. P. K. Sarkar, A. Halder, N. Polley and S. K. Pal; Development of highly selective and efficient prototype sensor for potential application in environmental mercury pollution monitoring. *Water, Air and Soil Pollut.* 228 (2017), 314.

31. J. Li, Q. Wang, Z. Guo, H. Ma, Y. Zhang, B. Wang, D. Bin and Q. Wei; Highly selective fluorescent chemosensor for detection of Fe^{3+} based on Fe_3O_4@ZnO. *Sci. Rep.* 6 (2016), 23558.

32. J. Annie Ho, H.-C. Chang and W.-T. Su; DOPA-mediated reduction allows the facile synthesis of fluorescent gold nanoclusters for use as sensing probes for ferric ions. *Anal. Chem.* 84 (2012), 3246.

33. A. Kumar and V. Kumar; Fluoride contamination in drinking water and its impact on human health of Kishanganj, Bihar, India. *Res. J. Chem. Sci.* 5 (2015), 76.

34. F. Edition; Guidelines for drinking-water quality. *WHO Chronicle* 38 (2011), 104.

35. I. A. Sherwood; Fluorosis varied treatment options. *J. Conserv. Dent.* 13 (2010), 47.

36. X. Zhu, Z. Zhang, Z. Xue, C. Huang, Y. Shan, C. Liu, X. Qin, W. Yang, X. Chen and T. Wang; Understanding the selective detection of Fe^{3+} based on graphene quantum dots as fluorescent probes: The K_{sp} of a metal hydroxide-assisted mechanism. *Anal. Chem.* 89 (2017), 12054.

37. Y. Guo, J. Li, S. Chai and J. Yao; Nanomaterials for the optical detection of fluoride. *Nanoscale* 9 (2017), 17667.

38. J. Shangguan, J. Huang, D. He, X. He, K. Wang, R. Ye, X. Yang, T. Qing and J. Tang; Highly Fe^{3+}-selective fluorescent nanoprobe based on ultrabright n/p codoped carbon dots and its application in biological samples. *Anal. Chem.* 89 (2017), 7477.

39. A. Basu, A. Suryawanshi, B. Kumawat, A. Dandia, D. Guin and S. B. Ogale; Starch (Tapioca) to carbon dots: an efficient green approach to an on–off–on photoluminescence probe for fluoride ion sensing. *Analyst* 140 (2015), 1837.

40. D. Raj and E. Shaji; Fluoride contamination in groundwater resources of Alleppey, southern India. *Geoscience Frontiers* 8 (2017), 117.

41. A. Spolaor, P. Vallelonga, J. Gabrieli, G. Cozzi, C. Boutron and C. Barbante; Determination of Fe^{2+} and Fe^{3+} species by FIA-CRC-ICP-MS in Antarctic ice samples. *J. Anal. At. Spectrom.* 27 (2012), 310.

42. A. Sil, V. S. Ijeri and A. K. Srivastava; Coated-wire iron (III) ion-selective electrode based on iron complex of 1, 4, 8, 11-tetraazacyclotetradecane. *Sens. Actuators B: Chem.* 106 (2005), 648.

43. S. Kage, K. Kudo, N. Nishida, H. Ikeda, N. Yoshioka and N. Ikeda; Determination of fluoride in human whole blood and urine by gas chromatography-mass spectrometry. *Forensic Toxicol.* 26 (2008), 23.

44. A. C. Kalita and R. Murugavel; Fluoride ion sensing and caging by a preformed molecular D4R zinc phosphate heterocubane. *Inorg. Chem.* 53 (2014), 3345.

45. Y. Zhou, J. F. Zhang and J. Yoon; Fluorescence and colorimetric chemosensors for fluoride-ion detection. *Chem. Rev.* 114 (2014), 5511.

46. M. H. Lee, T. Van Giap, S. H. Kim, Y. H. Lee, C. Kang and J. S. Kim; A novel strategy to selectively detect Fe (III) in aqueous media driven by hydrolysis of a rhodamine 6G Schiff base. *Chem. Commun.* 46 (2010), 1407.

47. T. Noipa, K. Ngamdee, T. Tuntulani and W. Ngeontae; Cysteamine CdS quantum dots decorated with Fe^{3+} as a fluorescence sensor for the detection of PPi. *Spectrochim. Acta A* 118 (2014), 17.

48. M. Xu, S. Wu, F. Zeng and C. Yu; Cyclodextrin supramolecular complex as a water-soluble ratiometric sensor for ferric ion sensing. *Langmuir* 26 (2009), 4529.

49.	B. Sui, B. Kim, Y. Zhang, A. Frazer and K. D. Belfield; Highly selective fluorescence turn-on sensor for fluoride detection. *ACS Appl. Mater. Interfaces* 5 (2013), 2920.

50.	T. Jamieson, R. Bakhshi, D. Petrova, R. Pocock, M. Imani and A. M. Seifalian; Biological applications of quantum dots. *Biomaterials* 28 (2007), 4717.

51.	M. Saleem, R. Abdullah, A. Ali, B. J. Park, E. H. Choi, I. S. Hong and K. H. Lee; Facile synthesis, cytotoxicity and bioimaging of Fe^{3+} selective fluorescent chemosensor. *Bioorganic Med. Chem.* 22 (2014), 2045.

52.	P. K. Sarkar, P. Kar, A. Halder, P. Lemmens and S. K. Pal; Development of highly efficient dual sensor based on carbon dots for direct estimation of iron and fluoride ions in drinking water. *ChemistrySelect* 4 (2019), 4462.

53.	R. Wang, K.-Q. Lu, Z.-R. Tang and Y.-J. Xu; Recent progress in carbon quantum dots: synthesis, properties and applications in photocatalysis. *J. Mater. Chem. A* 5 (2017), 3717.

54.	J. Tian, Y. Leng, Z. Zhao, Y. Xia, Y. Sang, P. Hao, J. Zhan, M. Li and H. Liu; Carbon quantum dots/hydrogenated TiO_2 nanobelt heterostructures and their broad spectrum photocatalytic properties under UV, visible and near-infrared irradiation. *Nano Energy* 11 (2015), 419.

55.	H. Ding, P. Zhang, T.-Y. Wang, J.-L. Kong and H.-M. Xiong; Nitrogen-doped carbon dots derived from polyvinyl pyrrolidone and their multicolor cell imaging. *Nanotechnology* 25 (2014), 205604.

56.	S. Mandani, D. Dey, B. Sharma and T. K. Sarma; Natural occurrence of fluorescent carbon dots in honey. *Carbon* 119 (2017), 569.

57.	M. Sun, Y. He, W. Yang and M. Yin; A fluorescent perylene-assembled polyvinylpyrrolidone film: Synthesis, morphology and nanostructure. *Soft Matter* 10 (2014), 3426.

58.	P. Wu, W. Li, Q. Wu, Y. Liu and S. Liu; Hydrothermal synthesis of nitrogen-doped carbon quantum dots from microcrystalline cellulose for the detection of Fe^{3+} ions in an acidic environment. *RSC Adv.* 7 (2017), 44144.

59. Y. Liu, W. Duan, W. Song, J. Liu, C. Ren, J. Wu, D. Liu and H. Chen; Red emission B, N, S-co-doped carbon dots for colorimetric and fluorescent dual mode detection of Fe^{3+} ions in complex biological fluids and living cells. *ACS Appl. Mater. Interfaces* 9 (2017), 12663.

60. P. K. Sarkar, N. Polley, S. Chakrabarti, P. Lemmens and S. K. Pal; Nanosurface energy transfer based highly selective and ultrasensitive "turn on" fluorescence mercury sensor. *ACS Sens.* 1 (2016), 789.

61. I.-Y. S. Lee and H. Suzuki; Quenching dynamics promoted by silver nanoparticles. *J. Photochem. Photobiol. A* 195 (2008), 254.

62. S. Chandra, T. K. Mahto, A. R. Chowdhuri, B. Das and S. kumar Sahu; One step synthesis of functionalized carbon dots for the ultrasensitive detection of Escherichia coli and iron (III). *Sens. Actuators B: Chem.* 245 (2017), 835.

63. Y. W. Choi, G. J. Park, Y. J. Na, H. Y. Jo, S. A. Lee, G. R. You and C. Kim; A single schiff base molecule for recognizing multiple metal ions: A fluorescence sensor for Zn(II) and Al(III) and colorimetric sensor for Fe(II) and Fe(III). *Sens. Actuators B: Chem.* 194 (2014), 343.

64. B. Ke, W. Wu, L. Wei, F. Wu, G. Chen, G. He and M. Li; Cell and in vivo imaging of fluoride ion with highly selective bioluminescent probes. *Anal. Chem.* 87 (2015), 9110.

65. X. Yang, L. Xie, R. Ning, X. Gong, Z. Liu, Y. Li, L. Zheng, G. Zhang, B. Gao, Y. Cui, G. Sun and G. Zhang; A diketopyrrolopyrrole-based near-infrared sensor for selective recognition of fluoride ions. *Sens. Actuators B: Chem.* 210 (2015), 784.

List of Publications

1. **P. K. Sarkar**, S. Pal, N. Polley, R. Aich, A. Adhikari, A. Halder, S. Chakrabarti, P. Chakrabarti and S. K. Pal "Development and Validation of a Noncontact Spectroscopic Device for Hemoglobin Estimation at Point-of-Care", **Journal of Biomedical Optics** 22 (2017), 055006.

2. **P. K. Sarkar**, A. Halder, A. Adhikari, N. Polley, S. Darbar, P. Lemmens and S. K. Pal "DNA-based Fiber Optic Sensor for Direct *In-vivo* Measurement of Oxidative Stress", **Sensors and Actuators B: Chemical** 255 (2018), 2194.

3. **P. K. Sarkar**, N. Polley, S. Chakrabarti, P. Lemmens and S. K. Pal "Nano-Surface Energy Transfer Based Highly Selective and Ultrasensitive "Turn on" Fluorescence Mercury Sensor", **ACS Sensors** 1 (2016), 789.

4. **P. K. Sarkar**, A. Halder, N. Polley and S. K. Pal "Development of Highly Selective and Efficient Prototype Sensor for Potential Application in Environmental Mercury Pollution Monitoring", **Water, Air & Soil Pollution** 228 (2017), 314.

5. **P. K. Sarkar**, P. Kar, A. Halder, P. Lemmens and S. K. Pal "Development of Highly Efficient Dual Sensor Based on Carbon Dots for Direct Estimation of Iron and Fluoride Ions in Drinking Water", **ChemistrySelect** 4 (2019), 4462.

6. *A. Halder, **P. K. Sarkar**, P. Pal, S. Chakrabarti, P. Chakrabarti, D. Bhattacharyya, R. Chakraborty and S. K. Pal "Digital Camera Based Spectrometry for the Development of Point-of-Care Anemia Detection on Ultra-low Volume Whole Blood Sample", **IEEE Sensors Journal** 17 (2017), 7149.

7. *P. Kar, T. K. Maji, **P. K. Sarkar**, P. Lemmens and S. K. Pal "Development of a Photo-Catalytic Converter for Potential Use in the Detoxification of Cr(VI)

Metal in Water from Natural Resources", ***Journal of Materials Chemistry A*** 6 (2018), 3674.

8. *P. Kar, T. K. Maji, **P. K. Sarkar**, S. Sardar and S. K. Pal "Direct Observation of Electronic Transition-Plasmon Coupling for Enhanced Electron Injection in Dye-sensitized Solar Cells", ***RSC Advances*** 6 (2016), 98753

9. *N. Polley, **P. K. Sarkar**, S. Chakrabarty, P. Lemmens, and S. K. Pal "DNA Biomaterial Based Fiber Optic Sensor: Characterization and Application for Monitoring in situ Mercury Pollution", ***ChemistrySelect*** 1 (2016), 2916.

10. *A. Halder, M. Banerjee, S. Singh, A. Adhikari, **P. K. Sarkar**, A. M. Bhattacharya, P. Chakrabarti, D. Bhattacharyya, A. K. Mallick and S. K. Pal "A Novel Whole Spectrum-based Non-invasive Screening Device for Neonatal Hyperbilirubinemia", ***IEEE Journal of Biomedical and Health Informatics*** (2019), DOI: 10.1109/JBHI.2019.2892946.

11. *P. Pal, A. Halder, **P. K. Sarkar**, N. Polley, P. Basak, S. Chakrabarti, P. Chakrabarti, S. K. Pal "White Light Interferometry on Human Blood Film Using White Light Emitting Diode", ***IEEE*** 2017 2nd International Conference for Convergence in Technology (I2CT) (2017), 151.

12. *P. Pal, A. Halder, **P. K. Sarkar**, N. Polley, P. Basak, S. K. Pal "Development of a Fiber Optic Sensor for Online Monitoring of Thin Coatings", ***ADBU Journal of Engineering Technology*** 6 (2017), 00610604(05PP).

List of Book Chapter

1. *A. Halder, S. Singh, A. Adhikary, P. K. Sarkar and S. K. Pal, "Development of Spectroscopy-based Medical Devices for Disease Diagnosis in Low Resource Point of Care Setting", ***Bioelectronics and Medical Devices*** (2019).

List of International/National Conferences

1. "Development of Highly Selective and Efficient Prototype Sensor for Potential Application in Environmental Mercury Pollution Monitoring", ***Presented at International Conference iCAN2017***, held at Azara campus of Assam Don Bosco University, India, from 9th to 13th January 2017

2. "Development and Validation of a Noncontact Spectroscopic Device for Hemoglobin Estimation at Point-of-Care", ***Presented at 9th International Conference on "Advances in Science, Engineering and Technology" (ASET-17)***, held at Bangkok, Thailand, from 11th to 12th July, 2017.

3. "Nano-Surface Energy Transfer Based Highly Selective and Ultrasensitive "Turn on" Fluorescence Mercury Sensor", ***Presented at Sustainable Development Conference 2017***, held at Bangkok, Thailand, from 13th to 15th July, 2017.

4. "White Light Interferometry on Human Blood Film using White Light Emitting Diode", ***Presented at 2nd International for Convergence in Technology (I2CT 2017)***, held at Pune, India, from 7th to 9th April, 2017.

5. Attended "***Ultrafast Science 2015 (UFS-2015)***", held at the S. N Bose National Centre for Basic Science, Kolkata, India, during 19th to 21st November, 2015.

6. Attended "***Industry Academia Meet - 2018***", held at the S. N Bose National Centre for Basic Science, Kolkata, India, on 6th October, 2018.

*Publications are not included in the thesis